# Improvement of Space Debris Orbits

Inauguraldissertation
der Philosophisch-naturwissenschaftlichen Fakultät
der Universität Bern

vorgelegt von

**Emiliano Cordelli**

aus Italien

Leiter der Arbeit:
Prof. Dr. Thomas Schildknecht
Astronomisches Institut der Universität Bern
Dr. Alessandro Vananti
Astronomisches Institut der Universität Bern

# Improvement of Space Debris Orbits

Inauguraldissertation
der Philosophisch-naturwissenschaftlichen Fakultät
der Universität Bern

vorgelegt von

**Emiliano Cordelli**

aus Italien

Leiter der Arbeit:
Prof. Dr. Thomas Schildknecht
Astronomisches Institut der Universität Bern
Dr. Alessandro Vananti
Astronomisches Institut der Universität Bern

Von der Philosophisch-naturwissenschaftlichen Fakultät angenommen.

Der Dekan:
Bern, 31 July 2017
Prof. Dr. Gilberto Colangelo

# Declaration

I, Emiliano Cordelli, hereby declare that this thesis titled, "Improvement of Space Debris Orbits" and the work presented in it are my own. I confirm that:

- The contents of this dissertation are original.
- This work was done wholly or mainly while in candidature for a research degree at this University.
- Where any part of this thesis has previously been submitted for a degree or any other qualification at this University or any other institution, this has been clearly stated.
- Where I have consulted the published work of others, this is always clearly attributed.
- Where I have quoted from the work of others, the source is always given. With the exception of such quotations, this thesis is entirely my own work.
- I have acknowledged all main sources of help.
- Where the thesis is based on work done by myself jointly with others, I have made clear exactly what was done by others and what I have contributed myself.

Emiliano Cordelli
Bern, 31 July 2017

# Acknowledgements

Although there are a lot of people to whom I have to say thanks, I will try to keep this section brief and I hope that, in case I miss someone, he/she will forgive me.

First of all, I would like to acknowledge the Swiss National Science Foundation that through the grant 200020 157062 supported this work.

My special thanks and appreciations go to Prof. Dr. Thomas Schildknecht for giving me the opportunity to do my PhD thesis at the Astronomical Institute of the University of Bern, for giving me deeper insight in the space debris topic, for sharing with me his knowledge, for his availability and to be willing to find always the time to discuss with me. I want especially to thank him for the trust he put in me and my professional work.

I would like to acknowledge Dr. Alessandro Vananti for his supervision, for his patience when discussing my ideas for the thesis and when trying to teach me a different approach to solve problems.

I would like to thank Prof. Dr. Adrian Jäggi for his interest in my work, for having always found the time to help me understand and improve my results.

Many thanks go to Prof. Dr. Gerhard Beutler for his precious suggestions regarding the orbit determination and the interpretation of the results, his availability and for having saved me when lost in some mathematical derivation.

It is important for me to acknowledge Dr. Krzysztof Sośnica for his patience, the nice explanations and the introduction to the satellite laser ranging world; Dr. Andrea Grahsl for the suggestions, and the help provided while validating my results.

I would like to acknowledge Dr. Martin Ploner and Marcel Prohaska for the help and all the efforts spent in providing the data that I needed even if a bit “scared” (I understand) when seeing my phone-call.

I would like to thank Dr. Michiel Zittersteijn for his friendship, for his curiosity in the Italian culture (including the coffee) and the very good collegial work and support which made the atmosphere within the office very nice and cosy.

I would like to thank both Dr. Jiří Šilha for the advices and the nice, unfortunately for him, long discussions outside the office; and all the other members (past and present ones) of the Optical Astronomy group.

I would like to thank also Dr. Stefano Bertone and all the other institute members (present and past ones) not only for their availability and for being always willing to help me, but also for the nice atmosphere that they created around and outside the work environment.

How to forget my friends both the historical and the recent ones being always interested in my work, for their support and for the relaxing moments spent together. Please forgive me for not having addressed you personally.

Maintenant je vais essayer d’écrire quelques mots en français, en espérant pas faire trop d’erreurs.

Je voudrais remercier toute la famille d'Anaïs, en particulier Tristan, Bela et leurs familles pour les précieux conseils, pour leur aide et les bons moments que nous avons vécu ensemble. Je voudrais enfin remercier ma copine Anaïs pour sa patience pendant ces dernières années et encore aujourd'hui, pour sa confiance en moi, pour son soutien et la motivation qu'elle m'a donné quand j'en ai eu besoin.
Infine vorrei ringraziare la mia famiglia per la loro pazienza nei miei confronti (che deve essere stata non poca conoscendo il soggetto), per i sacrifici fatti e il supporto fornito durante tutti questi anni di studio.

# Abstract

The increasing amount of space debris requires huge efforts for the tracking networks in order to maintain the orbits of all the objects. The precise knowledge of the positions of space debris objects is fundamental for collision avoidance maneuvers performed by satellite operators and for future active debris removal missions. It is very well known that the accuracy of an orbit determination process depends on the kind of observables used, their accuracy, the length of the observed arc, the number of observations, the observer orbit, and the observer-target geometry of the observations.

In this thesis an in-depth study is carried out to understand how the mentioned parameters influence the orbit determination accuracy and how we can improve the quality of the estimated orbits. After a brief introduction on the least squares adjustment algorithm and on the way of propagating and manipulating the resulting covariance matrix, we will focus essentially on the influence of the object-observer relative geometry and of the use of different observables for the orbit determination of space debris.

The object-observer relative geometry is approached as an information gain problem and it is studied using simulations and covariance analysis. The main aim of the covariance analysis is to identify the optimal follow-up strategy as a function of the object-observer geometry, the interval between follow-up observations and the shape of the orbit. This analysis is applied to every orbital regime but particular attention is dedicated to the highly-populated space debris orbits. Furthermore, several particular cases are analyzed with this method: more than two follow-ups observations, the influence of a second observing station, and the introduction of the distance as second observable.

The study on the combination of different types of observables is carried out investigating the influence of addition of the laser range measurements to the classical optical astrometric observations in terms of improved accuracy of the determined orbit. In particular, after some validation tests to prove the effectiveness of the implemented algorithm, it will be shown how different kinds of observables influence the accuracies of the estimated orbital parameters. Then, the influence of the observation geometry is analyzed and finally the improvements achieved on the orbit prediction, for different orbital regimes, will be shown. All the mentioned tests are performed using real ranges from the International Laser Ranging Service (ILRS) stations and real angular/laser measurements provided by sensors of the Swiss Optical Ground Station and Geodynamics Observatory Zimmerwald owned by the Astronomical Institute of the University of Bern (AIUB).

# Contents

# List of Figures

# List of Tables

# Frequently Used Acronyms

| | |
|---|---|
| **ADR** | Active Debris Removal |
| **AIUB** | Astronomical Institute of the University of Bern |
| **AMR** | Area to Mass Ratio |
| **BSW** | Bernese GNSS Software |
| **CCD** | Charge Coupled Device |
| **CelMech** | Celestial Mechanics Software |
| **CMOS** | Complementary Metal Oxide Semiconductor |
| **CODE** | Center for Orbit Determination in Europe, AIUB |
| **CoM** | Center of Mass |
| **CRD** | Consolidated Laser Ranging Data Format |
| **DE** | Declination |
| **ECEF** | Earth Centered Earth Fixed |
| **ECI** | Earth Centered Inertial |
| **EOP** | Earth Orientation Parameter |
| **EPH** | Earth Perifocal system |
| **ESA** | European Space Agency |
| **ESASDT** | ESA Space Debris Telescope |
| **FoV** | Field of View |
| **GEO** | Geostationary Earth Orbit |
| **GLONASS** | *Globalnaya navigatsionnaya sputnikovaya sistema* or equivalently Global Navigation Satellite System |
| **GNSS** | Global Navigation Satellite Systems |
| **GPS** | Global Positioning System |
| **GTO** | Geostationary Transfer Orbit |
| **HTS** | NASA GSFC SLR Mission Contractor, USA |
| **IAG** | International Association of Geodesy |
| **IERS** | International Earth Rotation and Reference System Service |
| **ILRS** | International Laser Ranging Service |
| **ISS** | International Space Station |
| **ISON** | International Scientific Optical Network |
| **ITRF** | International Terrestrial Reference Frame |
| **JAXA** | Japan Aerospace Exploration Agency, JAPAN |
| **KIAM** | Keldysh Institute of Applied Mathematics |
| **LEO** | Low Earth Orbit |
| **LRO** | Lunar Reconnaissance Orbiter |

| | |
|---|---|
| **LSQ** | Least Squares |
| **LTT** | Light Travel Time |
| **MCC** | Mission Control Center, Russia |
| **MEO** | Medium Earth Orbit |
| **MJD** | Modified Julian Date |
| **MOD** | Mean (Equinox) of Date |
| **NEQ** | Normal Equations System |
| **NTW** | Normal, Tangential (or in-track) and Cross-track |
| **OD** | Orbit determination |
| **OE** | Orbital elements |
| **OPR** | Once-Per-Revolution |
| **PEF** | Pseudo-Earth Fixed |
| **POD** | Precise Orbit Determination |
| **RA** | Right Ascension |
| **RB** | Range Bias |
| **RAAN** | Right Ascension of the Ascending Node |
| **RH** | Relative Humidity |
| **RMS** | Root Mean Square |
| **RSW** | Radial, Along-track and Cross-track |
| **SGF** | NERC Space Geodesy Facility, United Kingdom |
| **SLR** | Satellite Laser Ranging |
| **SoR** | System of Reference |
| **STD** | Standard Deviation |
| **STM** | State Transition Matrix |
| **TEME** | True Equator Mean Equinox |
| **TOD** | True (Equinox) of Date |
| **TOF** | Time Of Flight |
| **UTC** | Universal Time Coordinated |
| **w.r.t.** | With respect to |
| **ZIMLAT** | Zimmerwald laser and astrometry telescope |
| **ZimSMART** | Zimmerwald small robotic telescope |

# Chapter 1

# Introduction

The first artificial satellite was launched in 1957; since then the satellite launch rate continuously increased reaching the point that in January 2017 5250 launches were performed bringing 7500 satellites in orbit [3]. Unfortunately, the space-race has a side product: orbital debris. At the moment there are more than 29000 objects with a diameter bigger than 10 cm [3], and more than 750000 objects with a diameter from 1 cm to 10 cm in the space around the Earth [3]; furthermore, according to estimates there are more than 166 million objects from 1 mm to 1 cm [3]. Among all these objects, only about 1400 are active satellites, all the rest is space debris. Space debris is any man made orbiting object which is not operational anymore with no reasonable expectation of assuming or resuming its intended function [4]. The space debris population includes discarded satellites, rocket bodies, mission-related objects, painting and insulation flakes, fragments created by collisions, and break up events [5].

The space debris problem was taken more seriously since 2009 when the collision between Iridium 33 and Cosmos 2251 occurred. Recent studies [6] and [7] proved that the space debris populations will continue to grow even if we stop to launch new satellites; this growth will be driven mainly by accidental collisions and breakups. Therefore, space debris constitutes a serious problem for manned and robotic missions, both humans and satellites. In the Low Earth Orbit region (LEO) the average speed for debris is about 8 km per second [8]. Because of the high velocities of the debris particles, the present shields, including those used on-board of the International Space Station (ISS), are able to protect spacecraft only from the smaller debris (less than 1 cm in size [5]). In order to ensure the long-term sustainability of outer space activities, the various agencies and institutions are facing this problem both from the bureaucratic side, developing guidelines for the satellite owners and manufacturers, and from the scientific side answering questions about the space debris population and its evolution. Studies on the evolution of the space debris population [7] and [9] showed the need of active debris removal (ADR) operations to preserve the environment for the future generations. Although the ADR will be necessary for the long-term sustainability, it is of fundamental importance for the current space activities to know and to understand as much as we can about the space debris problem.

The main aim of the space debris research is to find an answer to the most common questions about space debris: how many debris objects are there? What are the most populated regions? What are they made of? And how will this population evolve in the future? To answer these questions the most common approach consists of three main steps: the first is the discovery of

the objects [10], the second is their orbit determination [11] and the third is their characterization [12].
This work takes place in the second step of the chain, in particular once an object is discovered by mean of survey observations and classified as a space debris, to accomplish further study on it, it is necessary to improve its orbit. In particular, the main aim of this thesis is to study the ways to enhance the performance, in terms of accuracy, of the orbit determination (OD) process. The need of improving the OD accuracy is mainly due to two factors: the number of the objects and the type of instrument used to acquire the measurements. If on one hand we have to deal with a relatively high number of objects, on the other hand, the number of instruments which are able to observe them is limited. The only way to acquire the measurements needed to perform an OD of a space debris is via radar or telescope facilities. Both type of instruments have advantages and disadvantages. If radars can observe centimeter size object at 1000 km of altitude [13], the telescopes become the only instruments able to observe space debris at the higher altitude. If radars can provide both distance and direction measurements, the telescopes provide only direction angles. If radars can operate continuously, the telescopes observations are weather dependent and possible only during nighttime. At this point the need to optimize the observation strategy is evident. It is necessary to find methods which improve the results of the OD process and increase the maximum time interval in which the object has to be re-observed before losing it. Assuming that the dynamical model used to describe the orbital motion of an object is accurate enough, the OD accuracy depends essentially on 6 factors:

- the length of the observed arc,
- the number of the observations,
- the accuracy of the measurements,
- the type of observations,
- the temporal distribution of the observations,
- the object-observer relative geometry.

As we will see later in the course of the thesis, the length of the arc of observations has to be optimized as a function of the accuracy of the dynamical model used for the OD and the visibility of the observed object. Generally speaking, the more observations, the better is the OD accuracy. However, we do not have to underestimate the influence of the distribution of the measurements: observing always the same portion of the orbit does not ensure the precise knowledge of the object trajectory in the unobserved part of the orbit. The OD accuracy depends on the type of measurements, on their accuracy and on the type of information that they can provide directly. The achievable accuracy in the orbit estimation depends directly on the noise and the precision of the observations. Finally, according with the relative position of the object on its orbit and of the observer on the Earth the information retrieved during the OD process is different.
In this thesis we will treat the problem of the improvement of the OD accuracy analyzing the influence of all just mentioned factors but focusing mainly on the consequences of the object-observer relative geometry and of the different observables processed within a Least Squares adjustment (LSQ). After a generic introduction of the main algorithms typically used

for the OD (Chapter 2) we will analyze in more details the Least Squares adjustment method and its application to the space debris orbit determination. In particular, we will show the main parts, the main outputs and the main properties of the LSQ focusing especially on the properties of the normal equation system and of the covariance matrix.

One of the outputs of the LSQ is the covariance matrix, this gives information about the uncertainty of the estimated orbit and it is used as discrimination criterion to decide whether or not to perform new observations of an object. For this reason in the Chapter 3 we will describe how the covariance can be manipulated, propagated in time and what are the main characteristics of the propagated uncertainties. We will study also how certain factors, like the number of estimated parameters and the object-observer relative geometry, will influence the behavior of the propagated covariance.

Once proved the dependency of the performance of the OD algorithm on the observation geometry, an in-depth study is carried out via simulations and via the analysis of the covariance to identify the optimal sequence of follow-up observations and to understand which are the main geometry-dependent factors which influence the accuracy of the OD. This study is performed in Chapter 4 and applied to different typical observations scenarios and orbital regimes. With the same method we will study the influence of the number of observations, of the time distance between them. We will then analyze the OD results obtained when processing different observables (angular and range measurements) and when the observations come from more than one observatory.

Finally, in Chapter 5, we will analyze the benefits of adding laser range measurements to the classical optical astrometric observations. Kirchner et al. [14] have shown that with the new laser technologies it is possible to successfully track space debris, at least a certain category of them. After validation tests carried out to prove the effectiveness of the implemented algorithm, by means of only real data, we will show how the different observables influence the accuracy of the estimated parameters. We will investigate also the influence of the observation geometry and of the number of measurements. Particular attention is dedicated to the evaluation of the achievable accuracy with a relatively small number of observations spread over a short arc. These tests are performed using real ranges from the stations of the International Laser Ranging Service (ILRS) and real angular/laser measurements provided by sensors of the Swiss Optical Ground Station and Geodynamics Observatory of Zimmerwald owned by the Astronomical Institute of the University of Bern (AIUB).

# Chapter 2

# Least Squares Adjustment and Space Debris Orbit Determination

## 2.1 Introduction

One of the fundamental steps of the space debris research concerns the knowledge of the position of the objects. In facts, if one wants to characterize space debris, to know its rotational state or investigate the material it is made of, first of all one has to discover it, then one has to know precisely where it is and where it will be. We can say that the orbit determination (OD) processes, both the initial OD and the orbit improvement are fundamental pillars in this field. For simplicity from now on we will refer to orbit improvement simply by using OD.
Today several groups of estimators exist and are essentially based on the works of Kepler, Legendre and last but not least Gauss [15]. Of course, in this last 500 years, many innovations, modifications and adjustments to their algorithms were proposed and performed but the basic principles are still the same. The two main groups of algorithms commonly used in the orbit improvement are: the batch estimators (like the Least Squares method), and the sequential or recursive estimator (like the Kalman filters). Between them we find the group of the sequential-batch estimators which try to take the advantages of both mentioned algorithms.
The performance of all OD determination algorithms depends on some common factors like: the number of measurements, their accuracy, their distribution, the kind of observables and the object-observer relative geometry. Since the main aim of this thesis is the enhancing of the accuracy of the OD results, we will first of all briefly introduce the three main groups of estimators then we will analyze in detail the Least Squares (LSQ) adjustment and its properties. We will focus on this algorithm since it is the one on which all this thesis work is based.

## 2.2 Types of Estimator Algorithm

In the OD field, all the mentioned estimators are stochastic processes which estimate a set of unknown parameters (such as the classical orbital elements, the state vector, the equinoctial elements etc.) which minimize, very generally, the discrepancies between the computed and the real measurements. The difference among the three groups resides essentially in the way the observations are treated. The batch and the sequential-batch estimators process group of data (or batches) while the sequential ones update or correct the estimated parameters as soon as new observation is available. For convenience from now on we will refer to the classical orbital elements simply with orbital elements (OE).

### 2.2.1 Batch Estimator

The batch algorithms provide an estimate of the unknown parameters at a certain epoch and an associated covariance matrix which contains the uncertainty of the parameters and how they are related. Normally the batch estimators need iterations to converge on the optimal solution, especially if the investigated problem is non-linear. On the other hand, the numerical integration has to be performed only once per iteration. Since this type of algorithm processes batches of data, it is necessary to collect all the available data before performing the estimation. This limits the applicability of such algorithms only to post-processing since are computationally heavy and the restart of the algorithm every time that a new observation is available it is not efficient. Nevertheless, the post-processing has the advantage that one can profit of more precise information about time-varying parameters (e.g. the ballistic coefficients) [15] and then usually produces more accurate results. As an example, the atmospheric drag is a function of the atmospheric density that, as we will see in the Paragraph 5.4, can be modeled exploiting the parameters which describe the solar activity and the disturbances of the Earth's magnetic field. These parameters are obtained by processing other phenomena and are not available at the moment of the acquisition of the measurements. Another disadvantage of the batch estimator is the difficulty to model the uncertainties of the dynamical model [15]. On the other hand, it is common habit to introduce solve-for parameters which need to be estimated to remedy model deficiencies. Among the solve-for parameters there are, in general, scaling parameters to estimate the area-to-mass ratio (AMR), the ballistic coefficient and other empirical either constant or periodic and/or pseudo-stochastic accelerations to “complete” the dynamical model [15–17].

The family of the batch estimators includes the Least Squares algorithm which will be discussed in details later in Paragraph 2.3.

### 2.2.2 Sequential-Batch Estimator

As the name says, the sequential-batch estimators constitutes an hybrid solution between the batch and the recursive algorithms. These techniques process batches of data separately and then combine the obtained results using the Bayes theorem to update the state estimate and the related covariance [15]. For this reason, the sequential-batch techniques are also called Bayes filters. These techniques are often used to save time in the case that one has already processed a certain number of observations with a batch estimator and then new measurements become available. Therefore, instead of reinitializing a new batch estimator with old and new observations, we can use these kind of algorithms to update the previous solution. The main issues related to these techniques are due to the handling of the new data and to the propagation of the state estimate and its related covariance. For further details on this technique please see [15].

### 2.2.3 Sequential Estimator - The Kalman Filter

The last group of estimators is constituted by the sequential ones. Among them the most famous are the Kalman filters. These algorithms exploit the predictor-corrector mechanism to compute the best estimate of a time-varying process taking into account the noise of the observations and the uncertainties of the background models. These algorithms are very useful for problems where there is a continuous flux of measurements (e.g. attitude determination problems). The two main reasons that make popular these algorithms are the fact that the state estimate and its covariance are propagated until a new measurement is available and then updated; and the fact that all the information coming from the data history is stored within the covariance matrix, so the reprocessing of past data is not needed. If these can be considered advantages w.r.t. the batch estimators, on the other hand, it is difficult to find appropriate models for the process noise and they tend to ignore new data [15].
There are several versions of the Kalman filter, as in the case of the LSQ, the most used ones are: the Kalman filter applied to linear systems, the linearized, the extended and the unscented Kalman filters used for nonlinear problems. Being the OD determination problem nonlinear, the most used ones are the last three. The first two differ for their approach to the propagation: the first propagates the difference of the state about a nominal trajectory, the second uses each new estimates to generate a new reference trajectory [15]. Since sometimes the extended Kalman filter may not converge to the minimum variance solution [18], very often the unscented Kalman filter is used which calculate the covariance from the propagation of the perturbed states accurately selected around the correct one. This kind of algorithms is used to take into account in the propagation of the covariance that the error distributions in the OD are not Gaussian [19], and then it is essentially used for tracklet association and initial orbit determination problems [20, 21].

## 2.3 The Least Squares Adjustment

The OD problem is a particular case of parameters estimation: one has to determine the set of parameters (as the orbital elements, the equinoctial elements or the state vector) of a model of the phenomenon (the orbit dynamical model), which fit "best" a series of measurements. Since the problem is overdetermined, or rather the number of the observations is bigger than the number of parameters to estimate, we have to choose a criterion and set up a cost function to represent the "best" fit of the model w.r.t. the data. One possible criterion is to minimize the sum of the absolute values of the difference between the data and the computed values; or the one proposed by Gauss and Legendre where the sum of the squared difference has to be minimized (Least Squares) [18], which is by far the most used in the OD problems.
The basic formulation of the LSQ adjustment process is the observation equations visible in Eq. 2.1. Given a set $l$ of $n$ observations, this can be described by a functional model $f$, function of the vector $x$ made of $u$ unknown parameters (with $n > u$) plus the discrepancies $v$, called residuals, between the model and the measurements.

$$\mathbf{l} + v = f(\mathbf{x}) \tag{2.1}$$

It is assumed that the residuals have mean value equal to zero with a fixed standard deviation (STD) $\sigma$:

$$\begin{aligned} E[v] &= 0, \\ E[v^2] &= \sigma^2. \end{aligned}$$

In the case of linear systems, each observation can be expressed as a linear combination of the unknown parameters. Introducing the first design matrix $\mathbf{A}$ as the $n \times u$ partial derivatives matrix of the functional model w.r.t. to the unknown parameters, the Eq. 2.1 can be rewritten in matrix form as follows:

$$v = \mathbf{A}\mathbf{x} - \mathbf{l} \tag{2.2}$$

with

$$\mathbf{A} = \frac{\partial f(\mathbf{x})}{\partial \mathbf{x}}. \tag{2.3}$$

The least-squares cost function that has to be minimized is defined as follows:

$$J = \sum_{i=1}^{n} (A_i \cdot x_i - l_i)^2 = (\mathbf{A}\mathbf{x} - \mathbf{l})^T (\mathbf{A}\mathbf{x} - \mathbf{l}) \tag{2.4}$$

Assuming that the system of observations is positive definite the condition which minimizes $J$ is that its gradient w.r.t. $\mathbf{x}$ is equal to 0. This condition is verified if:

$$\left(\mathbf{A}^T\mathbf{A}\right)\mathbf{x} = \mathbf{A}^T\mathbf{l} \quad \text{or equivalently} \quad \mathbf{N} \cdot \mathbf{x} = \mathbf{b} \tag{2.5}$$

where:

- $\mathbf{N} = \left(\mathbf{A}^T\mathbf{A}\right)$,
- $\mathbf{b} = \mathbf{A}^T\mathbf{l}$.

The Eq. 2.5 is called “Normal Equations system” (NEQ). If $\mathbf{N}$ is regular, solving the NEQ w.r.t. $\mathbf{x}$ we obtain the set of parameters which minimizes the cost function $J$.

$$\mathbf{x} = \left(\mathbf{A}^T\mathbf{A}\right)^{-1}\mathbf{A}^T\mathbf{l} \tag{2.6}$$

The Equation 2.6 is valid when the unknown parameters and the observations are linearly related. Since in the OD problem the relations between the unknowns and the observations are not linear, the Eq. 2.1, must be approximated through a first-order Taylor series expansion around $\mathbf{x}_0$.

$$\mathbf{l} + v = f(\mathbf{x}_0) + \mathbf{A}\hat{\mathbf{x}} \tag{2.7}$$

where:

- $\mathbf{x}_0$ are the a priori values of the unknown parameters $\mathbf{x}$,
- **A** is again the first design matrix but evaluated as function of the a priori parameters, which reads as follow:

$$\mathbf{A} = \left.\frac{\partial f(\mathbf{x})}{\partial \mathbf{x}}\right|_{\mathbf{x}=\mathbf{x}_0}, \tag{2.8}$$

- $\hat{\mathbf{x}}$ are the unknown correction to add to the a priori value $\mathbf{x}_0$ so that $\mathbf{x} = \mathbf{x}_0 + \hat{\mathbf{x}}$.

Rearranging the Eq. 2.7 and introducing the term $\hat{\mathbf{l}} = \mathbf{l} - f(\mathbf{x}_0)$ usually called observed minus computed $(O-C)$ we obtain the observation equations for nonlinear systems:

$$v = \mathbf{A}\hat{\mathbf{x}} - \hat{\mathbf{l}} \tag{2.9}$$

The Equation 2.9, for nonlinear systems, is equivalent to the Eq. 2.2 for linear ones. The NEQ system and its solution can be derived analogously and look as shown in Eq. 2.10 and in Eq. 2.11:

$$\left(\mathbf{A}^T\mathbf{A}\right)\hat{\mathbf{x}} = \mathbf{A}^T\hat{\mathbf{l}}, \tag{2.10}$$

$$\hat{\mathbf{x}} = \left(\mathbf{A}^T\mathbf{A}\right)^{-1}\mathbf{A}^T\hat{\mathbf{l}}. \tag{2.11}$$

The main difference resides in the fact that we solve for corrections to be given to the a priori values, and we need to iterate the updating of the a priori value until when the new corrections values do not improve anymore the solution. It is important in this case to find a criterion to stop the iterations. Since we are looking for the solution which minimizes the residuals a good stop criterion can be made based on the changes of the value of the sum of the residuals. Practically, together with the mentioned criterion a maximum number of iterations is also allowed.
It must be said that the nonlinearity of the problem introduces some issues: we need an a priori estimate of the unknown parameters, and depending on the a priori values, the dynamic of the problem and the distribution of the observations, the LSQ is not always able to find a proper solution. In particular, two main convergence issues can occur: the first, the solution may diverge; and the second, the LSQ converges to a local minimum of the cost function which can be different from the true solution, as we will see in Chapter 5.

Until now all the observations were treated assuming that they have the same accuracy. Generally this is not the case, in fact very often one performs OD using either different kind of observables (e.g. direction angles and distances, range and range-rate, etc.) or the same observable but coming from different sensors. To take into account these differences we introduce the weight matrix **W**. The **W** matrix describes the stochastic model and is the inverse of the a priori variance-covariance information of the observations. It contains the relations between the measurements and it is also function of the measurements noise as shown in Eq. 2.12. So **W** is a positive definite symmetric matrix that for independent observations becomes diagonal. The elements of the diagonal matrix $\mathbf{Q_{ll}}$ are constituted by the square of the standard deviation $\sigma_i$ (variance) of the generic measurement $i$.

$$\mathbf{W} = \mathbf{K_{ll}}^{-1} = \sigma_0^2 \mathbf{Q_{ll}}^{-1} \tag{2.12}$$

where:

- $\mathbf{K_{ll}}$ is the cofactor matrix of the measurements [18],
- $\sigma_0^2$ is the a priori sigma of the unit weight,
- $\mathbf{Q_{ll}}$ is the covariance matrix of the observations.

Introducing the **W** matrix in the cost function $J$ and repeating the procedure described above, the solution of the NEQ for nonlinear systems in the case of weighted measurements reads as follows:

$$\hat{\mathbf{x}} = \left(\mathbf{A}^T \mathbf{W} \mathbf{A}\right)^{-1} \mathbf{A}^T \mathbf{W} \hat{\mathbf{l}}. \tag{2.13}$$

Together with the improvement of the estimated parameters, the other output parameters of the LSQ adjustment are:

- $\mathbf{K_{xx}}$ the a posteriori cofactor matrix of the estimated parameters, can be derived applying the error propagation law on the covariance matrix of the observations:

$$\mathbf{K_{xx}} = \left[\left(\mathbf{A}^T \mathbf{K_{ll}}^{-1} \mathbf{A}\right)^{-1} \mathbf{A}^T \mathbf{K_{ll}}^{-1}\right] \mathbf{K_{ll}} \left[\left(\mathbf{A}^T \mathbf{K_{ll}}^{-1} \mathbf{A}\right)^{-1} \mathbf{A}^T \mathbf{K_{ll}}^{-1}\right]^T = \left(\mathbf{A}^T \mathbf{W} \mathbf{A}\right)^{-1} = \mathbf{N}^{-1}. \tag{2.14}$$

- $v = \mathbf{A}\hat{\mathbf{x}} - \hat{\mathbf{l}}$ the estimate of the residuals.
- $m_0^2$ the a posteriori variance of the unit weight:

$$m_0^2 = \frac{v^{\mathbf{T}} \mathbf{W} v}{n - u} \tag{2.15}$$

where $n - u$ is the degree of freedom of the LSQ adjustment and it is valid only for $n > u$.

- $\mathbf{Q_{xx}}$ the a posteriori covariance matrix of the estimate parameters, where the square root of the elements on the main diagonal corresponds to the mean error of the estimated parameters. The off-diagonal terms reflect the correlation between the parameters.

$$\mathbf{Q_{xx}} = m_0^2 \left(\mathbf{A}^T\mathbf{W}\mathbf{A}\right)^{-1} = m_0^2\mathbf{K_{xx}} \tag{2.16}$$

- $\gamma_{ij}$ the correlation which can be retrieved from the covariance matrix as shown from Eq. 2.17. If $\gamma_{ij}$ exists, $-1 < \gamma_{ij} < 1$, the off-diagonal terms ($\gamma_{ij}$) can not be equal to 1 otherwise the covariance matrix would be singular and we would not be able to solve the NEQ system. However, if $\gamma_{ij} \approx \pm 1$ the two parameters are strongly correlated vice versa if $\gamma_{ij} = 0$ the parameters are not correlated. Being $Q_{xx,ij}$ the covariance term between the parameters $i$ and $j$, $Q_{xx,ii}$ and $Q_{xx,jj}$ the variances of parameters $i$ and $j$ respectively, their correlation reads as:

$$\gamma_{ij} = \frac{Q_{xx,ij}}{\sqrt{Q_{xx,ii} \cdot Q_{xx,jj}}}. \tag{2.17}$$

- Condition number of the correlation coefficients matrix. This number provides information about the robustness of the parameters estimation in the LSQ adjustment and about the consistency of the obtained covariance [22]. The condition number of the correlation coefficient matrix is defined as the ratio of its largest singular value to its smallest singular value [22]. To determine its value in our simulation first, we needed to apply the singular value decomposition [23] to the correlation matrix then, as said before, we took the ratio between the biggest and the smallest singular value. Parametric studies showed that a large condition number implies a lack of covariance consistency [22].

## 2.4 Properties of the NEQ

Starting from the basic formulas for the LSQ adjustment shown in the previous paragraph, several manipulations can be performed on the NEQ system. A general overview of these operations, which are important for the derivation of some results of this thesis, are reported in the next sections.

### 2.4.1 Stacking of NEQ Systems

The basic operation that can be done with NEQ systems is their stacking. Although it is commonly used in the satellite geodesy field [24, 25] this technique is also very useful to investigate how the distribution and the type of observations influence the accuracy of the estimated parameters (from now on we will refer to this kind of study simply with the information gain). This is the basic principle on which we based the analysis carried out in Chapter 4.

Stacking means the combination of common parameters coming from different NEQ systems in one single parameter in the resulting NEQ. It was proven that sequential LSQ adjustment leads to the same results as a common adjustment in one step, provided that the different observation series are independent [24]. Therefore we will briefly outline the basic formalism of this operation; for further details on the equivalence proof we refer to [24].
Assuming to have 2 statistically uncorrelated systems of observation equations (the extension to more than 2 NEQs is straightforward) function of the same unknown parameters $x$ we have:

$$\begin{cases} v_1 = \mathbf{A_1 x} - \mathbf{l_1} \\ v_2 = \mathbf{A_2 x} - \mathbf{l_2} \end{cases} \tag{2.18}$$

where $v_\mathbf{i}$, $\mathbf{A_i}$ and $\mathbf{l_i}$ with $i = 1,2$ are respectively the residuals vector, the first design matrix and the $O-C$ vector of the $i$th system. Knowing that $\mathbf{W_i}$ is the weight matrix of the $i$th system, the corresponding NEQ systems look as follow:

$$\begin{cases} \left(\mathbf{A_1}^T\mathbf{W_1 A_1}\right) \cdot \mathbf{x} = \mathbf{A_1}^T\mathbf{W_1} \cdot \mathbf{l_1} \\ \left(\mathbf{A_2}^T\mathbf{W_2 A_2}\right) \cdot \mathbf{x} = \mathbf{A_2}^T\mathbf{W_2} \cdot \mathbf{l_2} \end{cases} . \tag{2.19}$$

The superposition of the individual NEQ systems is defined as:

$$\mathbf{N_c} = \mathbf{N_1} + \mathbf{N_2} = \left(\mathbf{A_1}^T\mathbf{W_1 A_1}\right) + \left(\mathbf{A_2}^T\mathbf{W_2 A_2}\right) \tag{2.20}$$

$$\mathbf{b_c} = \mathbf{b_1} + \mathbf{b_2} = \mathbf{A_1}^T\mathbf{W_1} \cdot \mathbf{l_1} + \mathbf{A_2}^T\mathbf{W_2} \cdot \mathbf{l_2} \tag{2.21}$$

from which the common parameters $\mathbf{x}$ can be estimated from the combined NEQ.

$$\mathbf{N_c} \cdot \mathbf{x} = \mathbf{b_c}. \tag{2.22}$$

The just exposed technique of combining different NEQ systems is fundamental for the sequential-batch estimators, like for example the sequential LSQ adjustment.

### 2.4.2 Constraining of Parameters

It can happen that the observations available do not contain all the information needed to derive a solution. In this case, the NEQ is singular or almost singular. If this occurs, the **N** matrix is ill-conditioned therefore it should not be inverted since the inversion may produce large numerical errors. To remedy the rank deficiencies of the matrix, we need to introduce additional information, or constraints, into the LSQ. The constraining can be done in different way, but one of the most convenient methods of constraining is via the introduction of pseudo-observations with their appropriate weighting which reflects their accuracy. This procedure allows a reduction of the limitation to the degree of freedom of the parameters and avoids the degradation of the solution given by the setting of the conditions directly on the parameters [25]. Furthermore, the

constraints may also be applied to force the estimated parameters to assume a value within a restricted range.
The observation equations for the fictitious observations and their relative weights matrix is equivalent to that of the "real" observations in Eq. 2.9.

$$v_{\mathbf{h}} = \mathbf{H} \cdot \mathbf{x} - \mathbf{h} \tag{2.23}$$

$$\mathbf{W_h} = \sigma_0^2 \mathbf{Q_{hh}}^{-1} \tag{2.24}$$

where:

- $v_{\mathbf{h}}$ is the residual vector of the constraints,
- $\mathbf{H}$ is the first design matrix containing the partial derivatives of the fictitious observations w.r.t. the estimated parameters,
- $\mathbf{h}$ is the vector of the known fictitious observations,
- $\mathbf{Q_{hh}}^{-1}$ represents the dispersion matrix of the introduced pseudo-observations (constraints).

The NEQ system obtained for the pseudo-observations (Eq. 2.25) can be stacked as shown in the previous paragraph with the NEQ of the "real" observations to obtain the complete/constrained NEQ (Eq. 2.26).

$$\mathbf{H}^T \mathbf{W_h} \mathbf{H} \cdot \mathbf{x} = \mathbf{H}^T \mathbf{W_h} \cdot \mathbf{h} \tag{2.25}$$

$$\left(\mathbf{A}^T \mathbf{W} \mathbf{A} + \mathbf{H}^T \mathbf{W_h} \mathbf{H}\right) \cdot \mathbf{x} = \mathbf{A}^T \mathbf{W} \cdot \mathbf{l} + \mathbf{H}^T \mathbf{W_h} \cdot \mathbf{h} \tag{2.26}$$

Depending on the purposes of the LSQ and the estimated parameters several ways of constraining are possible. For the purposes of this thesis the most meaningful ones are the absolute and the relative constraining of the parameters [25].
The absolute constraint is used to force the estimated parameter $\mathbf{x}$ to a value $\mathbf{w}$. This can be done setting up the following pseudo-observation:

$$v_{\mathbf{h}} = \mathbf{x} - \mathbf{w}. \tag{2.27}$$

From which the Eq. 2.26 becomes:

$$\left(\mathbf{A}^T \mathbf{W} \mathbf{A} + \mathbf{W_h}\right) \cdot \mathbf{x} = \mathbf{A}^T \mathbf{W} \cdot \mathbf{l} + \mathbf{W_h} \cdot \mathbf{w}. \tag{2.28}$$

A particular application of this kind of constraining is the forcing of the estimated parameter to its a priori value, possible setting $\mathbf{w} = 0$ and adding the weights $\mathbf{W_h}$ to the NEQ.
The relative constraints are used to force the improvements of two parameters with respect to each other. Having two parameters $x_i$ and $x_j$, and the known value which relate them $w$, such constraint can be set up via the Eq. 2.29. Introducing $\sigma_w$ as the standard deviation (STD) of the

tie value $w$ the Eq. 2.30 shows the NEQ system of the constraint which, as shown before, must be stacked to the "real" observations NEQ.

$$v = x_i - x_j - w \tag{2.29}$$

$$\left(\frac{\sigma_0^2}{\sigma_w^2}\right) \cdot \begin{bmatrix} 1 & -1 \\ -1 & 1 \end{bmatrix} \cdot \begin{bmatrix} x_i \\ x_j \end{bmatrix} = \left(\frac{\sigma_0^2}{\sigma_w^2}\right) \cdot \begin{bmatrix} w \\ -w \end{bmatrix} \tag{2.30}$$

### 2.4.3 NEQ Normalization

This procedure is important to avoid numerical instabilities in the NEQ solution. In the previous paragraph we have just mentioned the problem of the bad conditioning of a matrix. In fact, as long as the $\det \mathbf{N} \neq 0$ the matrix is regular but the smaller the value of $\det \mathbf{N}$ is, the more unreliable is the solution for $\mathbf{x}$. In this case, we say that the matrix $\mathbf{N}$ is badly- or ill-conditioned; in particular, in such NEQ system a small change of $\mathbf{b}$ causes large relative changes in $\mathbf{x}$ [24]. The normalization is a particular transformation of the NEQ system whose aim is to scale the values of the matrix $\mathbf{N}$ so that the main diagonal is constituted by 1. As shown in [24] the normalization can be easily done applying the following equation:

$$\mathbf{B}^T \mathbf{N} \mathbf{B} \cdot \mathbf{x} = \mathbf{B}^T \cdot \mathbf{b} \tag{2.31}$$

where $\mathbf{B} = \operatorname{diag}\left(N_{ii}^{-\frac{1}{2}}\right)$ and $N_{ii}$ with $i = 1, ..., u$ is the $i$th element on the $\mathbf{N}$ matrix.

## 2.5 The Covariance Matrix and its Properties

Another product of the LSQ that will be extensively used during this thesis is the covariance matrix. As we have seen, the LSQ adjustment provides both the best estimate of the parameters which minimize the error and also the statistical confidence in the uncertainty of the answer [1]. The covariance matrix, defined by Eq. 2.16, contains the variances (squares of the STD) and the covariances of the estimated parameters. Together with $m_0$ it describes the closeness of the fit for the chosen dynamics [15]. Furthermore, the cofactor matrix indicates the observability of of the system. In order to be observable a linear dynamical system should fulfill the following criterion:

$$\delta \mathbf{x_k}^T \mathbf{K_{xx}} \delta \mathbf{x_k} > 0 \tag{2.32}$$

for all arbitrary real vectors $\delta\mathbf{x_k}$, at the time $t_k$ [26]. This condition requires that $\mathbf{K_{xx}}$ is symmetric and positive definite, which can be obtained only if $\mathbf{A}$ is full rank [26].
The covariance matrix indicates also which are the effects of the noisy data or of a certain parameter on the estimated ones [15, 26]. It is interesting to notice that the evaluation of the observability and the sensitivity of the system are not function of the availability of the real measurements but only of their partial derivatives w.r.t. the estimated parameters [15]. The validity of the model used to set up the observation equations can be easily checked via a model-test. Since for zero-mean Gaussian distributed noise on the measurements, the sum of the squares of the residuals should be $\chi^2$-distributed, then the ratio between the a posteriori and the a priori variances is close to 1. In particular being $z$ a $\chi^2$-distributed random variable with degree of freedom $n-u$, we have that:

$$\frac{m_0^2}{\sigma_0^2} = \frac{z}{n-u}. \tag{2.33}$$

If $n-u \gg 1$ and the ratio is not $\sim 1$, it means that either gross errors or outliers are present in the system, or there are deficiencies in the mathematical model [27].
The covariance matrix it is also fundamental to express the uncertainty w.r.t. different sets of parameters without solving a set-specific LSQ adjustment and to express the uncertainty evolution with the time. Sometimes, for numerical reasons as an example, it is better to determine an orbit w.r.t. a certain set of elements (i.e. either orbital elements, state vector or equinoctial elements) but for the applications another set of parameter is easier to use; e.g. for collision avoidance operation the uncertainty w.r.t. the state vector in radial, along- and cross-track components is more easily understandable than the uncertainty w.r.t. the orbital elements. Another goal of the LSQ modeling for OD is to predict the position of the observed object in the future. Unfortunately, since the dynamical model for the OD and propagation is just an approximation of the forces acting on an orbiting object, the estimated orbit has to be updated with new observations to keep it with a good level of accuracy. The question now is, when is the best time to re-observe an object? If on one hand the more observation the better, on the other, acquire observations which do not give a certain amount of improvement results in time-consuming activities for a generic observer. The use of the covariance matrix becomes essential to determine the optimal data span [18]. Generally speaking both these tasks can be accomplished via a similarity transformation of the covariance matrix as shown in Eq. 2.34.

$$\mathbf{Q_{yy}} = \mathbf{C} \cdot \mathbf{Q_{xx}} \cdot \mathbf{C}^T \tag{2.34}$$

where $\mathbf{Q_{yy}}$ and $\mathbf{Q_{xx}}$ are the output and input covariance matrices respectively, and $\mathbf{C}$ is the transformation matrix. The transformation matrix can be derived applying the linear-error theory [15] and in the case of transformations between different sets of parameters it corresponds to the partial derivatives matrix of the second set w.r.t. the first one; and in the case of uncertainty propagation $\mathbf{C}$ coincides with the state transition matrix (STM). Both these operations will be discussed in the next Chapter (3).

## 2.6 Orbit Determination of Space Debris

To determine the orbit of an object, the observation of its motion is required. The main types of observations used today are essentially three: the angular data, the range and the relative velocity measurements by measuring the Doppler effect.
Historically, the most ancient type of observations are the angular ones. In particular the Right ascension and the Declination (RA and DE), obtained observing the movement of an object w.r.t. the fixed stars, were used by Gauss to estimate the 6 orbital elements which fully describe an orbit. This set of angles express the position of an object in the celestial sphere. There are two types of RA and DE: the geocentric and the topocentric. The first are calculated in an equatorial coordinate system whose origin is in the center of the Earth (generally called Earth Centered Inertial - ECI) and essentially the RA is the longitude angle measured from the vernal equinox and the DE is the latitude angle measured from the celestial equatorial plane. The topocentric RA and DE use a plane parallel to the Earth equatorial plane but located at a particular site [15]. Another set of angular data is constituted by the Azimuth and the Elevation angles taken in the local-horizontal coordinate system. The RA and DE are extracted by processing the acquired images using an external star catalog [16], the azimuth and elevation can be measured directly on the mount of the instrument, being it a radar or a telescope.
The ranges are provided by radar or by laser systems and can be distinguished in two groups: one-way and two-way data. The one-way signals are measured either at the sensor location or on board the satellite while for the two-way ones the observing station sends a signal which has to be reflected or re-transmitted by the target. The ranges are determined converting the measured time of flight (TOF) of the electromagnetic signal.
The last group of measurements often used for the satellite OD are range rates. This measurement is derived from the Doppler shift, caused by the relative motion between object and observer, which alters the signal frequency traveling to and from the satellite. However, range and range rate especially for high altitude satellites are possible only through an active “collaboration” of the observed object. In fact, very often the satellite receives a signal and then retransmits it to the station.
Laser ranging techniques became popular since they provide very accurate measurements and do not require an active payload on board of the satellite. Laser range measurements are in fact possible thanks to the corner-cube retro-reflectors which reflect the light back parallel to the incoming beam.
At this point we may ask how we may determine orbits of space debris? A space debris is defined as: *“Any man-made object which is non-functional anymore without reasonable expectations that it will resume its intended function”* [13]. By definition a space debris it is not “collaborative”, and this will reduce the amount and the type of usable data for its OD.
The “Space Surveillance Network” (SSN) of the US Strategic Command (USSTRATCOM), a military entity of the USA, is the main provider of the orbits of large space debris. It consists of a global network of optical telescopes but mainly of narrow beams and phased array radars which collect and process continuously measurements in order to keep up to date the orbits of the observed objects [13]. Since the radar sensitivity decreases with the fourth power of the distance of the object, the application of radar techniques is strongly limited by the distance of the object. If on one hand we are able to track centimeter-size objects in the Low Earth Orbit (LEO) regime, it starts to be demanding the tracking of 1 meter-size object in the Geostationary Earth Orbit (GEO)

[13]. These are the main reasons why the estimated orbits of high altitude space debris are based on angular measurements provided by optical telescopes. Another big entity providing orbits of space debris in high-altitude orbits is the International Scientific Optical Network (ISON) managed by the Keldysh Institute of Applied Mathematics (KIAM) [28]. Other advantages of the optical telescopes are: the fact that the measurements are acquired passively exploiting the capability of the object to reflect the light of the Sun; and, being the angular resolution of a telescope $\propto \lambda/D$ where $\lambda$ is the wavelength and $D$ is the aperture diameter [15, 29], observing in the visual part of the electromagnetic spectrum allows us to obtain relatively small instruments with a high resolution and sensitivity. The main drawback of the use of optical telescopes is that the observations are weather dependent. Since the optical telescopes exploit the reflected light of the Sun their capability of collect light is directly proportional to their size, therefore faint objects can not be observed with small telescope. Despite that, an optical telescope of 1 m diameter is able to track an object of 10 cm in size in the GEO-regime. Practically a telescope whose mirror has a diameter of 1 m is able to track GEO objects that are 10 times smaller w.r.t. those trackable by the a USSTRATCOM radar system whose antenna have diameters between 34 and 36 m [13], this is the main reason why the USSTRATCOM tracks GEO objects mainly with optical telescopes. As we will see later, the OD accuracy depends on a lot of factors. Nevertheless, the angle-only orbit determination of space debris can produce accuracies better than 100 m [30]. Recently, several studies were performed to evaluate the influence of the range observables on the OD of space debris [31–33]. The tracking of space debris using laser techniques became possible thanks to the new generation of lasers with a high pulse energy (1 J) [34]. Further details on the space debris tracking using laser systems will be given in Chapter 5.

# Chapter 3

# Covariance Propagation

## 3.1 Motivation

The covariance matrix is one of the products of the LSQ adjustment. It gives information about the statistical reliability of the estimated parameters and consequently contains the uncertainties of the satellite position and velocity. Lastly, the satellite position uncertainty has become fundamental for different purposes. For catalog maintenance, as an example, it is needed to re-observe an object before the uncertainty becomes bigger than the field of view (FoV) of the instrument. For close-approach calculations the covariance is used to determine the collision probability and then to decide if the satellite has to maneuver or not [1].
It is then important to understand how the uncertainties of the estimated parameters evolve with time and how we can transform the covariance w.r.t. different representations of the state vector. The main aim of this chapter is to show how the covariance can be manipulated and then we will analyze the uncertainty evolution depending on different orbit determination scenarios and parameters.

## 3.2 Covariance Transformation

Depending on the applications, it is useful to transform the covariance matrix between different state representations. Figure 3.1 shows the main transformations between state vector descriptions. In particular, the figure shows the transformations between different sets of Cartesian coordinates (represented by the ellipses) and between different sets of parameters: Cartesian coordinates, classical osculating orbital elements, equinoctial elements and flight parameters (represented by rectangles) [1]. During this thesis the main transformations used are: between orbital elements and Earth Centered Inertial (ECI) Cartesian coordinates, between ECI and Earth Centered Earth Fixed (ECEF) coordinates, and between ECI and Radial, Along- and Cross-track components (RSW). For this reason, we will focus only on these transformations; however the others w.r.t.:

- the equinoctial elements,
- the flight (spherical) sets (geocentric latitude, longitude, flight-path angle from the local horizontal, azimuth, position magnitude and velocity magnitude) [1],

- the normal, tangential and cross-track components (NTW),
- the Pseudo Earth Fixed (PEF), which is similar to the ECEF but without considering the actual direction of the Earth's spin axis described by the polar motion;
- the Mean (Equinox) of Date (MOD),
- the True (Equinox) of Date (TOD),
- the True Equator Mean Equinox (TEME),

will not be treated but their application is analogous to what we will show and for further details please refer to [35, 15]. The difference between MOD, TOD, TEME and ECI resides only in the choice of the reference orientation of the Earth at a certain epoch. For completeness, when we refer to ECI we implicitly mean the J2000 reference system defined with the Earth's Mean Equator and Equinox at 12:00 Terrestrial Time on 1 January 2000. The $x$-axis is aligned with the mean equinox. The $z$-axis is aligned with the Earth's spin axis or celestial North Pole. The $y$-axis is rotated by 90° East about the celestial equator [26].

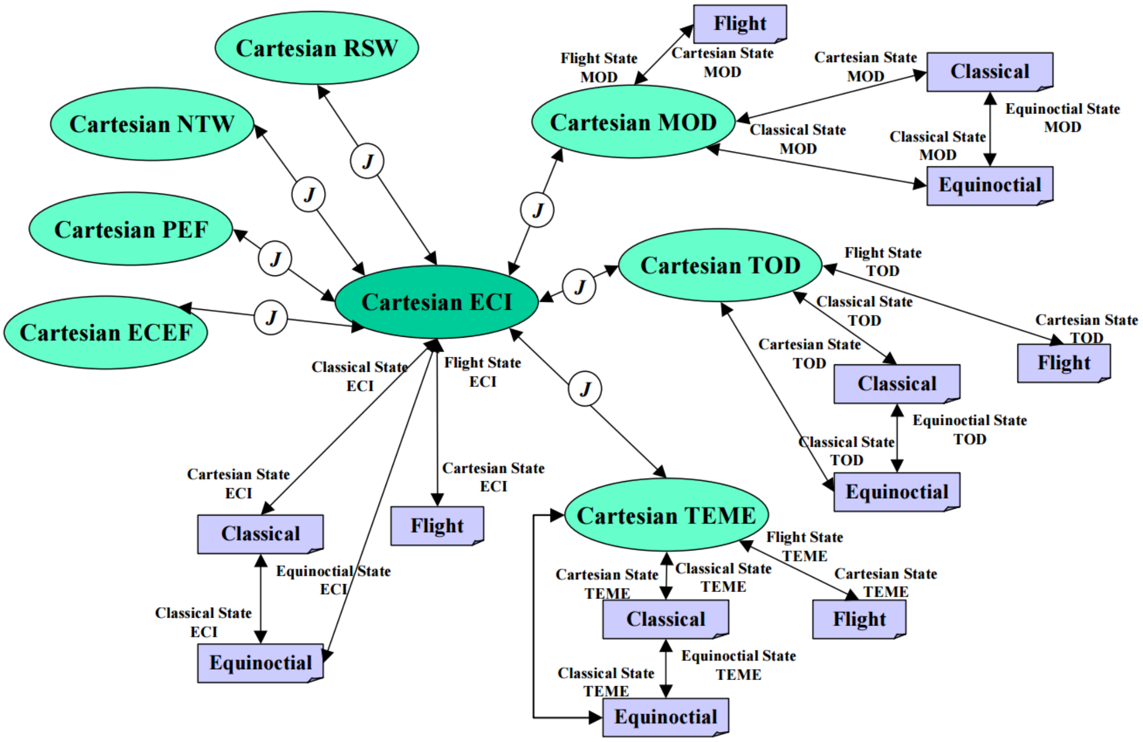

Figure 3.1 Main covariance transformations [1].

As said in the previous chapter, the covariance transformations can be derived by the application of the linear-error theory and result in a *similarity transformation* which follows the Eq. 2.34 [15]. For clarity, from now on when we will refer to a generic covariance transformation, without involving the propagation, we will use $\mathbf{J}$ to indicate the transformation matrix. The matrix **J** is simply the Jacobian matrix of the ending state w.r.t. the initial one [1]. Recalling for simplicity the transformation equation taking into account **J** and indicating with **y** the ending state and with **x** the initial one we have:

$$\mathbf{Q}_{\mathbf{yy}} = \mathbf{J}_{\frac{\mathbf{y}}{\mathbf{x}}} \cdot \mathbf{Q}_{\mathbf{xx}} \cdot \mathbf{J}_{\frac{\mathbf{y}}{\mathbf{x}}}{}^{T}, \tag{3.1}$$

where:

$$\mathbf{J}_{\frac{\mathbf{y}}{\mathbf{x}}} = \left[\frac{\partial \mathbf{y}}{\partial \mathbf{x}}\right]. \tag{3.2}$$

Generally speaking all the transformation can be performed applying the Eq. 3.1 only the values within **J** change. In the next paragraph we will shortly describe all the transformations used in this thesis.

### 3.2.1 Transformation between Orbital Elements and Cartesian Coordinates

Referring with the subscripts *OE* and *ECI* respectively to the orbital elements and to the Cartesian covariance matrix, respectively, the Eqs. 3.1 and 3.2 become:

$$\mathbf{Q}_{ECI} = \mathbf{J}_{\frac{ECI}{OE}} \cdot \mathbf{Q}_{OE} \cdot \mathbf{J}^{T}_{\frac{ECI}{OE}} \qquad \text{and} \qquad \mathbf{J}_{\frac{ECI}{OE}} = \left[\frac{\partial \vec{\mathbf{r}}}{\partial OE}, \frac{\partial \vec{\mathbf{v}}}{\partial OE}\right] \tag{3.3}$$

where:

- $\vec{\mathbf{r}} = [x, y, z]$ is the position vector in the ECI system with its corresponding vector components,
- $\vec{\mathbf{v}} = [v_x, v_y, v_z]$ is the velocity vector in the ECI system with its corresponding vector components,
- $OE = [a, e, i, \Omega, \omega, u_0]$ are the osculating orbital elements namely: semi-major axis, eccentricity, inclination, Right Ascension of the Ascending Node (RAAN), argument of perigee and argument of latitude at the osculating epoch;
- $\frac{\partial \vec{\mathbf{r}}}{\partial OE}, \frac{\partial \vec{\mathbf{v}}}{\partial OE}$ are the partial derivatives of the position and velocity components of the orbiting object w.r.t. the orbital elements whose derivation is shown later in Paragraph 4.2.3.

The partial derivatives of each state vector component w.r.t. each single orbital elements occupy the columns of the matrix **J**.
Numerical restrictions occur for certain values of the eccentricity and of the inclination where the derivatives (and the elements) start to be poorly defined, in particular this happens if the orbit is either nearly circular or nearly parabolic ($e < 0.00001$ and $e > 0.9999$), and if the orbit

is near equatorial ($i < 0.00001°$ and $180°-i < 0.00001°$) [1].
Finally, the inverse transformation from ECI components to orbital elements is obtained applying the following equations.

$$\mathbf{Q}_{OE} = \mathbf{J}_{\frac{OE}{ECI}} \cdot \mathbf{Q}_{ECI} \cdot \mathbf{J}^T_{\frac{OE}{ECI}} \qquad \text{and} \qquad \mathbf{J}_{\frac{OE}{ECI}} = \left[\frac{\partial OE}{\partial(\vec{\mathbf{r}}, \vec{\mathbf{v}})}\right] = \mathbf{J}^{-1}_{\frac{ECI}{OE}} \tag{3.4}$$

## 3.2.2 From ECI to RSW Components

The local orbital set of coordinates (RSW) is very useful since it allows us to visualize how the uncertainty is oriented along the orbit. An example of the different behaviors between ECI and RSW propagation will be shown later in Paragraph 3.4.1. This set of components can be easily obtained by a rotation applied to the ECI coordinates. In particular, being the unit vectors $\widehat{\mathbf{R}}$, $\widehat{\mathbf{S}}$ and $\widehat{\mathbf{W}}$ in the radial, along-, and cross-track directions defined as:

$$\widehat{\mathbf{R}} = \frac{\vec{\mathbf{r}}}{|\vec{\mathbf{r}}|}, \qquad \widehat{\mathbf{W}} = \frac{\vec{\mathbf{r}} \times \vec{\mathbf{v}}}{|\vec{\mathbf{r}} \times \vec{\mathbf{v}}|}, \qquad \widehat{\mathbf{S}} = \widehat{\mathbf{W}} \times \widehat{\mathbf{R}}, \tag{3.5}$$

arranging the direction vectors in the columns of the matrix $\left[\widehat{\mathbf{R}} \,|\, \widehat{\mathbf{S}} \,|\, \widehat{\mathbf{W}}\right]$ we obtain the rotation matrix from RSW to ECI coordinates systems. The matrix $\mathbf{J}$ describing the transformation of the covariance from ECI to RSW components becomes:

$$\mathbf{J}_{\frac{RSW}{ECI}} = \begin{bmatrix} \left[\widehat{\mathbf{R}} \,|\, \widehat{\mathbf{S}} \,|\, \widehat{\mathbf{W}}\right]^T & \mathbf{0}_{3\times3} \\ \mathbf{0}_{3\times3} & \left[\widehat{\mathbf{R}} \,|\, \widehat{\mathbf{S}} \,|\, \widehat{\mathbf{W}}\right]^T \end{bmatrix} \qquad \text{and} \qquad \mathbf{Q}_{RSW} = \mathbf{J}_{\frac{RSW}{ECI}} \cdot \mathbf{Q}_{ECI} \cdot \mathbf{J}^T_{\frac{RSW}{ECI}}. \tag{3.6}$$

As said, the matrix $\left[\widehat{\mathbf{R}} \,|\, \widehat{\mathbf{S}} \,|\, \widehat{\mathbf{W}}\right]^T$ represents a rotation. Since a rotation matrix is orthonormal, its inverse coincide with its transpose. Then the backward transformation from RSW to ECI is represented by the following matrix $\mathbf{J}$.

$$\mathbf{J}_{\frac{ECI}{RSW}} = \begin{bmatrix} \left[\widehat{\mathbf{R}} \,|\, \widehat{\mathbf{S}} \,|\, \widehat{\mathbf{W}}\right] & \mathbf{0}_{3\times3} \\ \mathbf{0}_{3\times3} & \left[\widehat{\mathbf{R}} \,|\, \widehat{\mathbf{S}} \,|\, \widehat{\mathbf{W}}\right] \end{bmatrix} \tag{3.7}$$

### 3.2.3 From ECI to ECEF Components

For completeness we will shortly describe the last transformation that will be implicitly used during this thesis: from inertial coordinates to Earth-fixed ones, namely from ECI to ECEF. To transform from, generally speaking, celestial frame (as ECI) to terrestrial frame (as ECEF), we have to take into account the Earth orientation model [15]. More specifically one has to consider the *Polar Motion* (*PM*) which defines the movement of the Earth's rotation axis w.r.t. the crust of the Earth [15], the *Precession* (*PR*) which describes the changes of the orientation of the equator w.r.t. the ecliptic [15], the *Nutation* (*NU*) which describes the oscillation of the Earth's rotation axis [15] and the *Sidereal Time* (*ST*) which accounts for the rotation of the Earth. We will not go through the details of the calculation of the $PM$, $PR$, $NU$ and $ST$ and their corresponding rotation matrices ($[\mathbf{PM}], [\mathbf{PR}], [\mathbf{NU}], [\mathbf{ST}]$), for these we refer to the *IERS Conventions* [36–38]. Introducing the Earth's rotation vector and its rate as $\vec{\omega}_{\oplus}$ and $\omega_{\oplus}$, the transformation of position and velocity between ECI and ECEF can be obtained from:

$$\vec{\mathbf{r}}_{PEF} = [\mathbf{ST}] \cdot [\mathbf{NU}] \cdot [\mathbf{PR}] \cdot \vec{\mathbf{r}}_{ECI}, \tag{3.8}$$

$$\vec{\mathbf{r}}_{ECEF} = [\mathbf{PM}] \cdot \vec{\mathbf{r}}_{PEF}, \tag{3.9}$$

$$\vec{\mathbf{v}}_{ECEF} = [\mathbf{PM}] \cdot \Big\{ [\mathbf{ST}] \cdot [\mathbf{NU}] \cdot [\mathbf{PR}] \cdot \vec{\mathbf{v}}_{ECI} - \vec{\omega}_{\oplus} \times \vec{\mathbf{r}}_{PEF} \Big\}. \tag{3.10}$$

As one can see, to pass from ECI to ECEF we need an intermediate step through the pseudo-Earth fixed reference system (PEF). The same mechanism applies to the covariance transformation therefore the matrix $\mathbf{J}$ and, consequently, the Eq. 3.1 reads as follows:

$$\mathbf{J}_{\frac{PEF}{ECI}} = \begin{bmatrix} \mathbf{D} & \mathbf{0} \\ \mathbf{wr} & \mathbf{D} \end{bmatrix} \qquad \text{and} \qquad \mathbf{J}_{\frac{ECEF}{PEF}} = \begin{bmatrix} [\mathbf{PM}] & \mathbf{0} \\ \mathbf{0} & [\mathbf{PM}] \end{bmatrix}, \tag{3.11}$$

$$\mathbf{Q}_{ECEF} = \mathbf{J}_{\frac{ECEF}{PEF}} \cdot \left[ \mathbf{J}_{\frac{PEF}{ECI}} \cdot \mathbf{Q}_{ECI} \cdot \mathbf{J}^{T}_{\frac{PEF}{ECI}} \right] \cdot \mathbf{J}^{T}_{\frac{ECEF}{PEF}}, \tag{3.12}$$

with:

$$\mathbf{D} = [\mathbf{ST}] \cdot [\mathbf{NU}] \cdot [\mathbf{PR}] \qquad \text{and} \qquad [\mathbf{wr}] = \omega_{\oplus} \cdot \begin{bmatrix} D_{21} & D_{22} & D_{23} \\ -D_{11} & -D_{12} & -D_{13} \\ 0 & 0 & 0 \end{bmatrix}. \tag{3.13}$$

Where $D_{ij}$ is the element of the $i$th-row and the $j$th-column of the matrix $\mathbf{D}$ with $i, j = 1, 2, 3$.

## 3.3 Covariance Propagation

There are two main methods of propagating the uncertainty: the first is stochastic and it is based on the Monte Carlo theory, the second is deterministic. During this work, for the propagation of the covariance matrix we utilized the analytical approach and we will compare the results obtained with different ways of calculating the state transition matrix. For completeness, we will briefly describe how the stochastic approach works.

### 3.3.1 Stochastic Propagation

This method is essentially based on the Monte Carlo theory. The core idea of this theory is the study of a generic system by empirically simulating it with a relatively huge number of samples. This approach is relatively simple and provides reliable results since it is based on the direct evaluation of the system. Very often is used as validation criterion for other methods. Being this a statistical method, it is computationally expensive, in facts the accuracy of the results depends on the number of samples: the higher is the number, the better are the results. Therefore the main drawback of this method is the computation time needed to perform the simulations which increases with the dimensions of the dynamic system [19].
The Monte Carlo theory is often applied to verify other methods for the covariance propagation [39, 40]. An example of how the Monte Carlo covariance propagation works is shown in the study of Sabol et al. [39].

### 3.3.2 Analytical Propagation

The analytical propagation of the covariance matrix can be done via the state transition matrix (STM). The STM propagates the deviations of the state vector from an epoch $t_0$ to an epoch $t$ [41]. In the field of the OD, we indicate with $\delta\mathbf{x}$ the vector of the corrections (or the deviations) to be applied to the estimated parameters. Hence, the STM allows to write the values of $\delta\mathbf{x}$ at a certain epoch $t$ as function of the value of $\delta x$ at time $t_0$:

$$\delta\mathbf{x}(t) = \Phi(t,t_0)\cdot\delta\mathbf{x}(t_0)\,. \tag{3.14}$$

Given two epochs $t_i$ and $t_j$, and indicating from now on, for simplicity, with $\delta\mathbf{x_i}$ and $\delta\mathbf{x_j}$ the values of the deviations at the respective time, the main properties of the STM are:

- $\Phi(t_i,t_i) = \mathbf{I}$ where $\mathbf{I}$ is the identity matrix,
- $\Phi(t_j,t_i) = \Phi(t_j,t_k)\cdot\Phi(t_k,t_i)$ where $t_k$ is a third epoch,
- $\Phi(t_j,t_i)^{-1} = \Phi(t_i,t_j)$

The equation for the covariance propagation can be easily obtained from the definition of the covariance. Indicating now with $\mathbf{Q_i}$ the covariance matrix at the time $t_i$ we have:

$$\mathbf{Q_i} \equiv E\left[\delta\mathbf{x_i}\delta\mathbf{x_i}^T\right]. \tag{3.15}$$

According to Eq. 3.14, $\delta\mathbf{x_i} = \Phi\left(t_i, t_j\right) \cdot \delta\mathbf{x_j}$ therefore we have:

$$\mathbf{Q_i} = E\left[\Phi\left(t_i, t_j\right) \cdot \delta\mathbf{x_j}\delta\mathbf{x_j}^T \cdot \Phi\left(t_i, t_j\right)^T\right]. \tag{3.16}$$

Since the STM is deterministic [26] we obtain:

$$\mathbf{Q_i} = \Phi\left(t_i, t_j\right) \cdot \mathbf{Q_j} \cdot \Phi\left(t_i, t_j\right)^T. \tag{3.17}$$

Fundamental for the deterministic propagation of the covariance is then the STM. The STM can be also used in the estimation process, especially when using sequential estimators like the Kalman filters. Here, the STM may be used to propagate the state vector from a measurement epoch to the successive one if the dynamical system is linear [18]. Usually in nonlinear systems, as in the case of orbit dynamics, the propagation of the state vector is performed via numerical integration, and the STM may be only used to evaluate the partial derivatives of the observations w.r.t. the state vector at a certain epoch [18]. In both cases, the calculation of the STM has to be very accurate. Several methods to determine the STM exist, the main are:

- Taylor series expansion of $e^{\mathbf{F}t}$,
- Padé series expansion of $e^{\mathbf{F}t}$,
- Inverse Laplace transform of $[s\mathbf{I} - \mathbf{F}]^{-1}$,
- Integration of $\dot{\mathbf{\Phi}} = \mathbf{F\Phi}$,
- Matrix decomposition method,
- Scaling and squaring (interval doubling) used with another method,
- Direct numerical partial derivatives using integration,
- Partitioned combinations of methods.

Where: $\mathbf{I}$ is the identity matrix, $s$ is the frequency parameter of the Laplace transform and $\mathbf{F}$ is the Jacobian matrix of a generic function $f$ w.r.t. a generic state vector $\mathbf{x}$ at a certain epoch. In the orbit determination/propagation case $f$ is the orbit dynamical model function of the state vector which could contain either the initial position and velocity or the initial osculating elements. During this work we performed some tests exploiting two of the mentioned methods to calculate the STM namely: the Taylor series expansion and the direct numerical evaluation of the partial derivatives. For details about the other methods refer to [18].

### STM Calculation - Taylor Series Expansion Method

For its simplicity the first method that we implemented was the Taylor series expansion of $e^{\mathbf{F}t}$. This method can be applied if the state dynamics are time invariant, so then **F** is constant, or it can be considered as time-invariant over the integration interval. Hence, its application to the orbital dynamics requires a small time integration step, whose size depends on the considered orbital regime. If the system is time-invariant the STM $\Phi(t)$ is equivalent to the exponential of the matrix $e^{\mathbf{F}t}$ and can be expanded through a Taylor series as follows [18]:

$$\Phi(t) = e^{\mathbf{F}t} = \mathbf{I} + \mathbf{F}\Delta t + \frac{(\mathbf{F}\Delta t)^2}{2!} + \frac{(\mathbf{F}\Delta t)^3}{3!} + \dots \quad \text{with} \quad \Delta t = t_i - t_j. \tag{3.18}$$

The output covariance matrix of a LSQ adjustment usually is either w.r.t. the state vector (position and velocity in the ECI coordinates) or w.r.t. the orbital elements. As said before, the transformation between the two state representations is relatively easy (and described in Paragraph 3.2.1) therefore we decided to evaluate both covariance propagations. It was then necessary to determine an **F** matrix for each representations.

For the propagation w.r.t. the orbital elements the derived **F** matrix (Eq. 3.19) contains the partial derivatives of the Gaussian perturbation equations (shown in Equations (3.20) to (3.25)) w.r.t. the orbital elements. For completeness, since the SATORB orbit determination estimate the argument of latitude as 6th parameter and the 6th parameter of the Gaussian perturbation equation is the perigee passing time, before propagating the covariance using this method we needed to perform a covariance transformation. In particular, we needed to convert the covariance from $[a, e, i, \Omega, \omega, u_0]$ to $[a, e, i, \Omega, \omega, T_0]$. The transformation matrix **J** is an identity matrix exception made for the last element of the main diagonal which contains the partial derivatives of $T_0$ w.r.t. $u_0$.

$$\mathbf{F} = \begin{bmatrix}
\frac{\partial \dot{a}}{\partial a} & \frac{\partial \dot{a}}{\partial e} & \frac{\partial \dot{a}}{\partial i} & \frac{\partial \dot{a}}{\partial \Omega} & \frac{\partial \dot{a}}{\partial \omega} & \frac{\partial \dot{a}}{\partial T_0} \\
\frac{\partial \dot{e}}{\partial a} & \frac{\partial \dot{e}}{\partial e} & \frac{\partial \dot{e}}{\partial i} & \frac{\partial \dot{e}}{\partial \Omega} & \frac{\partial \dot{e}}{\partial \omega} & \frac{\partial \dot{e}}{\partial T_0} \\
\frac{\partial \dot{i}}{\partial a} & \frac{\partial \dot{i}}{\partial e} & \frac{\partial \dot{i}}{\partial i} & \frac{\partial \dot{i}}{\partial \Omega} & \frac{\partial \dot{i}}{\partial \omega} & \frac{\partial \dot{i}}{\partial T_0} \\
\frac{\partial \dot{\Omega}}{\partial a} & \frac{\partial \dot{\Omega}}{\partial e} & \frac{\partial \dot{\Omega}}{\partial i} & \frac{\partial \dot{\Omega}}{\partial \Omega} & \frac{\partial \dot{\Omega}}{\partial \omega} & \frac{\partial \dot{\Omega}}{\partial T_0} \\
\frac{\partial \dot{\omega}}{\partial a} & \frac{\partial \dot{\omega}}{\partial e} & \frac{\partial \dot{\omega}}{\partial i} & \frac{\partial \dot{\omega}}{\partial \Omega} & \frac{\partial \dot{\omega}}{\partial \omega} & \frac{\partial \dot{\omega}}{\partial T_0} \\
\frac{\partial \dot{T}_0}{\partial a} & \frac{\partial \dot{T}_0}{\partial e} & \frac{\partial \dot{T}_0}{\partial i} & \frac{\partial \dot{T}_0}{\partial \Omega} & \frac{\partial \dot{T}_0}{\partial \omega} & \frac{\partial \dot{T}_0}{\partial T_0}
\end{bmatrix} \tag{3.19}$$

$$\dot{a} = \sqrt{\frac{p}{\mu}} \frac{2a}{1-e^2} \left\{ e \sin \nu f_R + \frac{p}{r} f_S \right\} \tag{3.20}$$

$$\dot{e} = \sqrt{\frac{p}{\mu}} \left\{ \sin \nu f_R + (\cos \nu + \cos E) f_S \right\} \tag{3.21}$$

$$\dot{T}_0 = -\frac{1-e^2}{n^2ae}\left\{\left(cos\nu - 2e\frac{r}{p}\right)f_R - \left(1+\frac{r}{p}\right)sin\nu f_S\right\} - \frac{3}{2a}\left(t-T_0\right)\dot{a} \tag{3.22}$$

$$\dot{i} = \frac{di}{dt} = \frac{r\cos u}{na^2\sqrt{1-e^2}}f_W \tag{3.23}$$

$$\dot{\Omega} = \frac{r\sin u}{na^2\sqrt{1-e^2}\sin i}f_W \tag{3.24}$$

$$\dot{\omega} = \frac{1}{e}\sqrt{\frac{p}{\mu}}\left\{-\cos\nu f_R + \left(1+\frac{r}{p}\right)\sin\nu f_S\right\} - \cos i\dot{\Omega} \tag{3.25}$$

where:

- $a$, $e$, $i$, $\Omega$, $\omega$, $T_0$ and $u$ are respectively the classical orbital elements plus the argument of latitude,
- $\mu$ is the Earth gravitational constant,
- $\nu$ and $E$ are the true and eccentric anomaly,
- $t$ is the time epoch,
- $p = a\left(1-e^2\right)$ is the semi-latus rectum,
- $n = \sqrt{\frac{\mu}{a^3}}$ is the osculating mean motion,
- $f_R$, $f_S$ and $f_W$ are the perturbing accelerations decomposed into the radial, along- and cross-track components whose partial derivatives are calculated numerically using the central difference method [15, 18].

The determination of the **F** matrix in the case of propagation of the covariance matrix w.r.t. the state vector is obtained by deriving the partial derivatives for the following equation:

$$\ddot{\mathbf{r}} = -\frac{\mu}{r^3}\vec{\mathbf{r}} + \vec{\mathbf{f}} \tag{3.26}$$

with $r = |\vec{\mathbf{r}}|$ and $\vec{\mathbf{f}}$ is the vector of the perturbing force in ECI components. Hence the **F** matrix in this case looks:

$$\mathbf{F}=\begin{bmatrix} 0 & 0 & 0 & 1 & 0 & 0 \\ 0 & 0 & 0 & 0 & 1 & 0 \\ 0 & 0 & 0 & 0 & 0 & 1 \\ \mu\frac{2x^2-y^2-z^2}{r^5}+\frac{\partial f_x}{\partial x} & \frac{3\mu xy}{r^5}+\frac{\partial f_x}{\partial y} & \frac{3\mu xz}{r^5}+\frac{\partial f_x}{\partial z} & \frac{\partial f_x}{\partial v_x} & \frac{\partial f_x}{\partial v_y} & \frac{\partial f_x}{\partial v_z} \\ \frac{3\mu xy}{r^5}+\frac{\partial f_y}{\partial x} & \mu\frac{2y^2-x^2-z^2}{r^5}+\frac{\partial f_y}{\partial y} & \frac{3\mu yz}{r^5}+\frac{\partial f_y}{\partial z} & \frac{\partial f_y}{\partial v_x} & \frac{\partial f_y}{\partial v_y} & \frac{\partial f_y}{\partial v_z} \\ \frac{3\mu xz}{r^5}+\frac{\partial f_z}{\partial x} & \frac{3\mu yz}{r^5}+\frac{\partial f_z}{\partial y} & \mu\frac{2z^2-x^2-y^2}{r^5}+\frac{\partial f_z}{\partial z} & \frac{\partial f_z}{\partial v_x} & \frac{\partial f_z}{\partial v_y} & \frac{\partial f_z}{\partial v_z} \end{bmatrix} \tag{3.27}$$

where:

- $x$, $y$, $z$, $v_x$, $v_y$ and $v_z$ are the position and velocity components in the ECI coordinates system,
- $f_x$, $f_y$ and $f_z$ are the perturbing forces decomposed into the ECI components whose partial derivatives are computed as in the previous case via the central differences method [15, 18].

We must remind that the Taylor series expansion is an approximation of the problem, thus to obtain more accurate results we can act on two parameters: the truncation order of the series and the time interval in which we assume **F** constant. We decided to truncate to the third order the Taylor series and we assumed that the **F** matrix can be considered constant for 5 and 1 seconds respectively for the case of OE and state vector propagation. The main consequence of such short time interval is, obviously, a huge increase of the computation time.

### STM Calculation - Direct Numerical Evaluation of Partial Derivatives Method

The second method used in this thesis for the STM calculation is based on the direct evaluation of the partial derivatives via their numerical integration. Being $t_j = t_0 + \Delta t$ where $\Delta t$ is a generic time interval, the STM can be written as follows:

$$\Phi\left(t_0+\Delta t, t_0\right)=\frac{\partial \mathbf{x}\left(t_0+\Delta t\right)}{\partial \mathbf{x}\left(t_0\right)}. \tag{3.28}$$

This formulation remains valid both for linear and nonlinear systems [18]. Furthermore, the implementation of this method is more convenient in our case since in SATORB the propagation of the partial derivatives and therefore of the state vector is performed by integrating the variational equations [16]. The mentioned program is used daily at AIUB for the OD of space debris and belongs to the CelMech software suite. Its original purpose is the generation of satellite orbits or their determination using tabular positions as pseudo-observations or astrometric positions as real observations [16]. During this thesis we made extensively use of SATORB which was modified in order to first propagate the covariance matrix and successively to handle the laser range measurements (see Chapter 5).
In SATORB, the partial derivatives of the position and velocity w.r.t. to the orbital elements are integrated using the collocation method [16], so to propagate the covariance we simply need to

extract the partial derivatives and build the STM. In this case, being the starting covariance w.r.t. the OE the propagation and the transformation are done in one single step, to obtain again the propagated covariance w.r.t. the OE we only need to apply the inverse transformation, see above in Paragraph 3.2.1.

### STM Calculation - Comparison of the Results

After checking the correctness of the implementation of the two methods for the calculation of the STM we decided to compare the results obtained propagating the covariance using the Taylor series expansion to evaluate the STM with those obtained using a STM directly evaluated by the numerical integration of the variational equations.

The comparison was carried out propagating the covariance w.r.t. the OE of a GPS-like orbit. First a synthetic series of continuous angular observations over 10 days of arc was generated, then an OD was performed and the osculating orbital elements were estimated at the beginning of the observation arc. The resulting covariance was then propagated over a total propagation time of 20 days using both the methods for the STM evaluation. The comparison is performed only on the following orbital elements: $a$, $e$, $i$, $\Omega$ and $\omega$ since the variational equation method propagates the uncertainty w.r.t. the argument of latitude and the Taylor series expansion w.r.t. the perigee passing time (respectively $u_0$ and $T_0$).

Figure 3.2 shows the comparison of the uncertainty propagation obtained exploiting the variational equations and the Taylor series expansion to calculate the STM. From now on we will use the term uncertainty to refer to the square root $\sigma$ of the variance of the estimated parameters.

Generally, there is a good agreement for the trends of the uncertainties; however the obtained results show important differences. These differences are probably due to: the truncation of the Taylor series expansion, the length of the time interval in which the matrix **F** can be considered constant, and to the complexity of the dynamical model and consequently the rising difficulties when evaluating the partial derivatives of the perturbing forces.

After this test we decided to keep, for the operational environment, only the propagation method which exploits the variational equations to calculate the STM. Summarizing, this choice was driven by three main factors:

- the linearization,
- the complexity of the equations,
- the computational time.

In particular the variational equations allow the determination of the total STM in one single step and therefore also the propagation of the covariance is performed by 2 matrix multiplications and produces more accurate results w.r.t. the Taylor series method. Furthermore, with this method, the only error introduced are those due to the numerical integration. On the other hand, the Taylor series needs to split the entire propagation period (which can be from few hours to several months) into small intervals whose size is given by the time interval in which the **F** matrix can be considered constant. This produces 720 STM determinations and consequently 1440 matrix multiplications for 1 hour propagation, which leads inevitably to an increase of the computation time. Furthermore, this approach introduces errors due to the truncation of the Taylor series. The Taylor approach needs the analytical derivation either of the Gaussian perturbation equations or of the basic two-body problem. For both, the Gaussian formulation and the two-body problem, to have more accurate results, one has to include the perturbing forces like the solar radiation pressure, the atmospheric drag, the third-body acceleration, the gravitational harmonics, etc. in the calculation of the **F** for the Taylor series expansion method for the STM evaluation. The analytical derivation of this partial derivatives is rather complicated and we overcome this problem via a numerical approximation using the central difference method, which has obviously introduced further approximation errors.

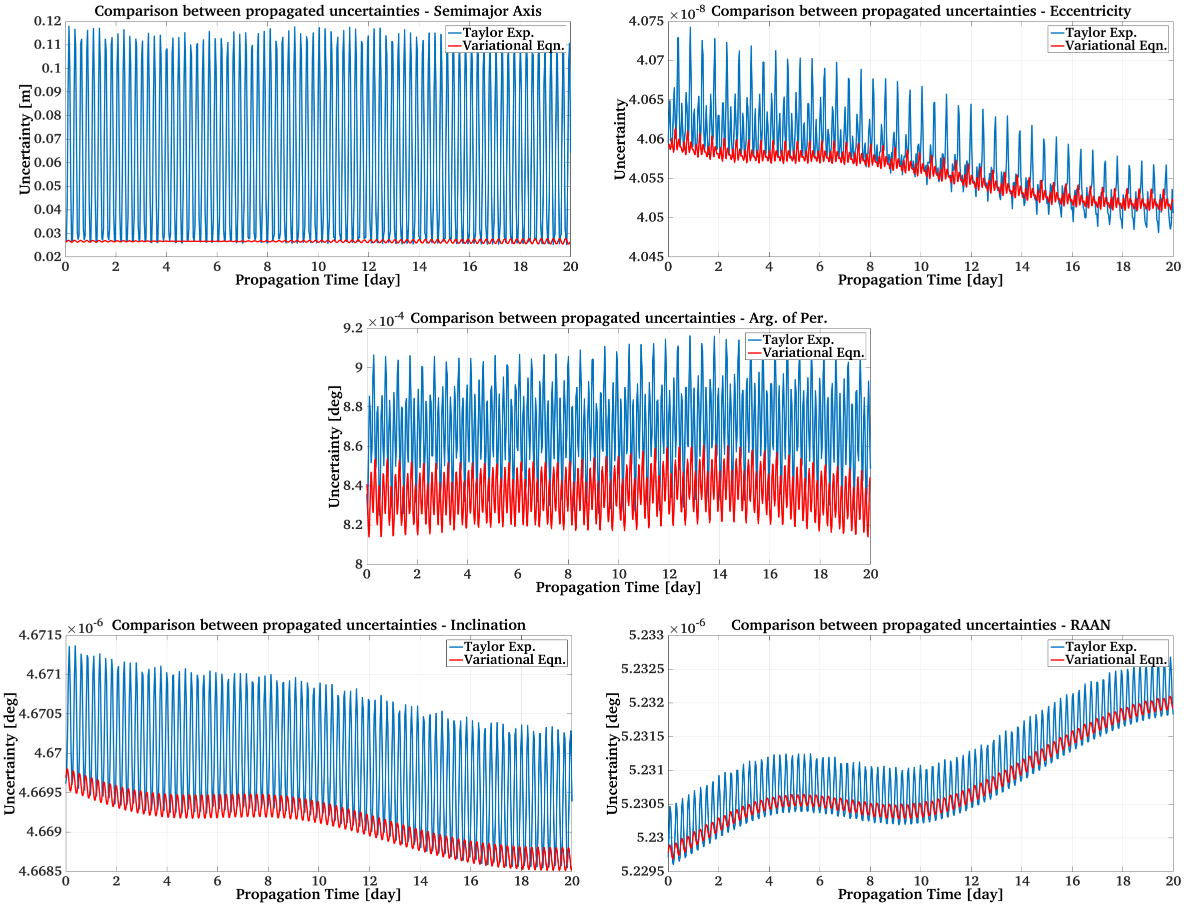

Figure 3.2 Comparison of the uncertainty ($\sigma$) propagation between the variational equation and the Taylor expansion methods to determine the STM.

## 3.4 Covariance Propagation Results

In this section, we will show some results of the covariance propagation. In particular, first we will show the characteristics and the different kind of information retrievable from the propagation of the covariance w.r.t. different state representations. Secondly, we will start a study to investigate the factors which influence the covariance propagation. In this paragraph the differences given by the number of estimated parameters will be showed and we verify that the covariance propagation depends not only on the variances themselves but also on the correlation coefficients [1]. This last simulation is the starting point of the study performed in Chapter 4.

### 3.4.1 Propagation w.r.t. Different State Representations

We will first show the comparison of the propagation between different state representations, namely OE and state vector, and between different state vector components, respectively ECI and RSW coordinates. More precisely, the propagation is always performed w.r.t. the ECI components and the uncertainties are then transformed w.r.t. the different state representations. This experiments is performed to illustrate the main features of the uncertainties propagation w.r.t. the different state representations. For this example we used an eccentric geosynchronous orbit where we simulated 10 continuous days of angular observations with a constant sampling from the European Space Agency (ESA) Space Debris Telescope (ESASDT) in Tenerife, and we performed an OD exploiting this set of measurements. The determined orbit and the related covariance are propagated for 200 days. Every 30 minutes a propagated covariance w.r.t. ECI components and the corresponding state vector are given as an output. For each epoch, these outputs are used to convert the covariance from ECI to RSW components and w.r.t. the orbital elements. Figure 3.3 and 3.4 show an excerpt, respectively 20 and 100 days of propagation, of the results obtained for a covariance propagation w.r.t. the state vector (in ECI and RSW coordinates) and w.r.t. the orbital elements (namely $a$, $e$, $i$, $\Omega$, $\omega$ and $u_0$).
In the first, the propagation of the uncertainty w.r.t. the state vector in different reference system, ECI and RSW, is shown respectively in Figure 3.3a and 3.3b. Looking at these figures, we can see some similarities; these are essentially due to the fact that, as seen in Paragraph 3.2.2, we can transform from ECI to RSW components simply via a rotation. The main similarity is visible in the general trend of the uncertainty which is decreasing during the first 5 days and then tends to increase, and in the fact that are present features which are repeating every orbital period. This "decrasing-increasing" trend is due to the fact that the first 10 days of uncertainty propagation fall within the time interval where observations were simulated and where the LSQ adjustment is performed. This occurs since the uncertainty propagation begins at the first observation epoch where also the orbit is estimated. The "decreasing-increasing" trend is due to the LSQ which fits best the measurements in the middle of the observations arc [26]. Nevertheless, the rotation between the two reference systems allows a better interpretation of the results. If in the case of ECI coordinates the uncertainty along $x$ and $y$ directions do not show particular differences, in the RSW, the three channels are completely separated showing that the uncertainty w.r.t. the orientation of the orbital plane ($W$ component) remains constant, while the total uncertainty is driven by the along-track component ($S$). Looking at the behavior of the uncertainties on the velocity components, in RSW, it is evident the correlation between the along-track position uncertainty and the radial velocity one. This second representation becomes very important in operational scenarios, like conjunctions, since it visually shows how the uncertainty ellipsoid is located w.r.t. the orbit.

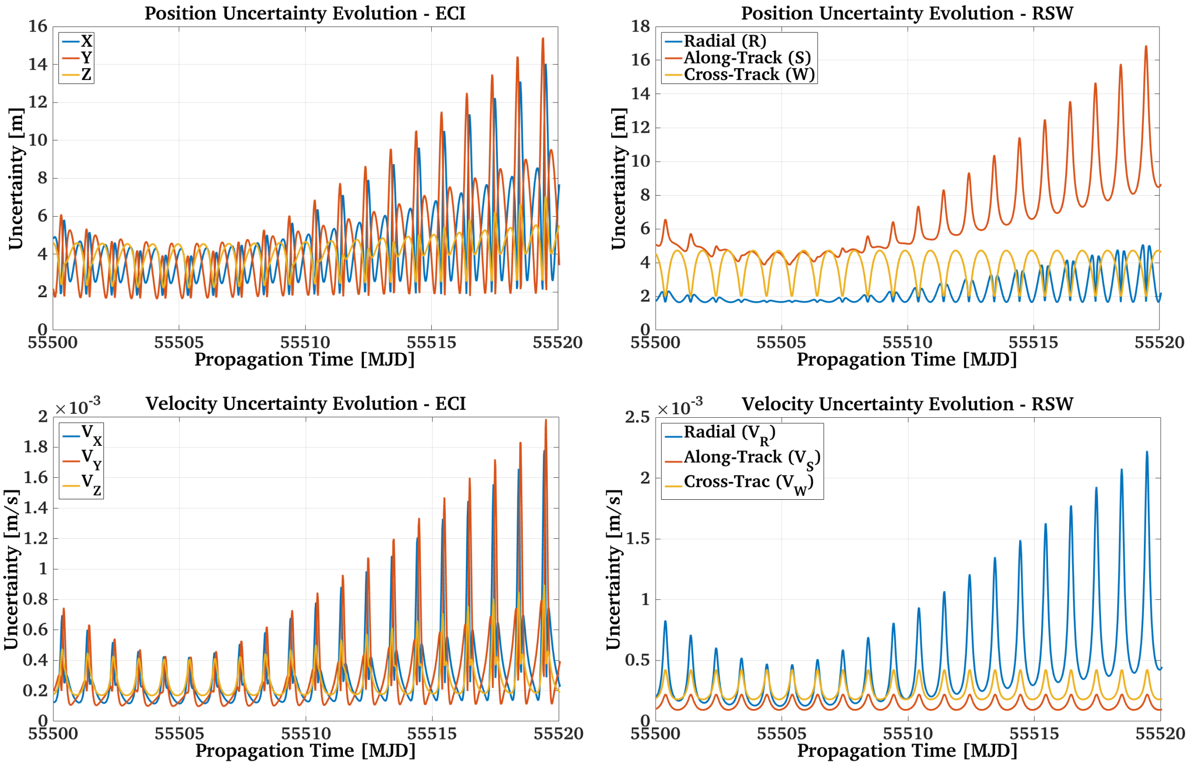

(a) Position and Velocity uncertainty in ECI

(b) Position and Velocity uncertainty in RSW

Figure 3.3 Comparison of the uncertainty propagation in ECI and RSW for an eccentric geosynchronous object. The first 10 days of propagation are performed within the “fit span”.

Depending on the application it is useful to transform the propagated covariance w.r.t. different state descriptions. For example, in Figure 3.3 it is easy to see the behavior of the uncertainties within the orbital period, while in Figure 3.4 the uncertainties w.r.t. the OE show the short, the medium and the long term features of the propagation. In Figure 3.4 we have in fact a total propagation period of 100 days, where the short term represents the uncertainty behavior within the orbital period, a medium term with roughly 25 days of period is visible, and finally a trend whose period is longer than 100 days. These trends are visible for all elements exception made for the argument of latitude that, consistently to what shown in Figure 3.3, contains mostly a divergent term consistent with the along-track uncertainty. This trend is due to the fact that any error in $a$ will result in a linear growing error in $u_0$.

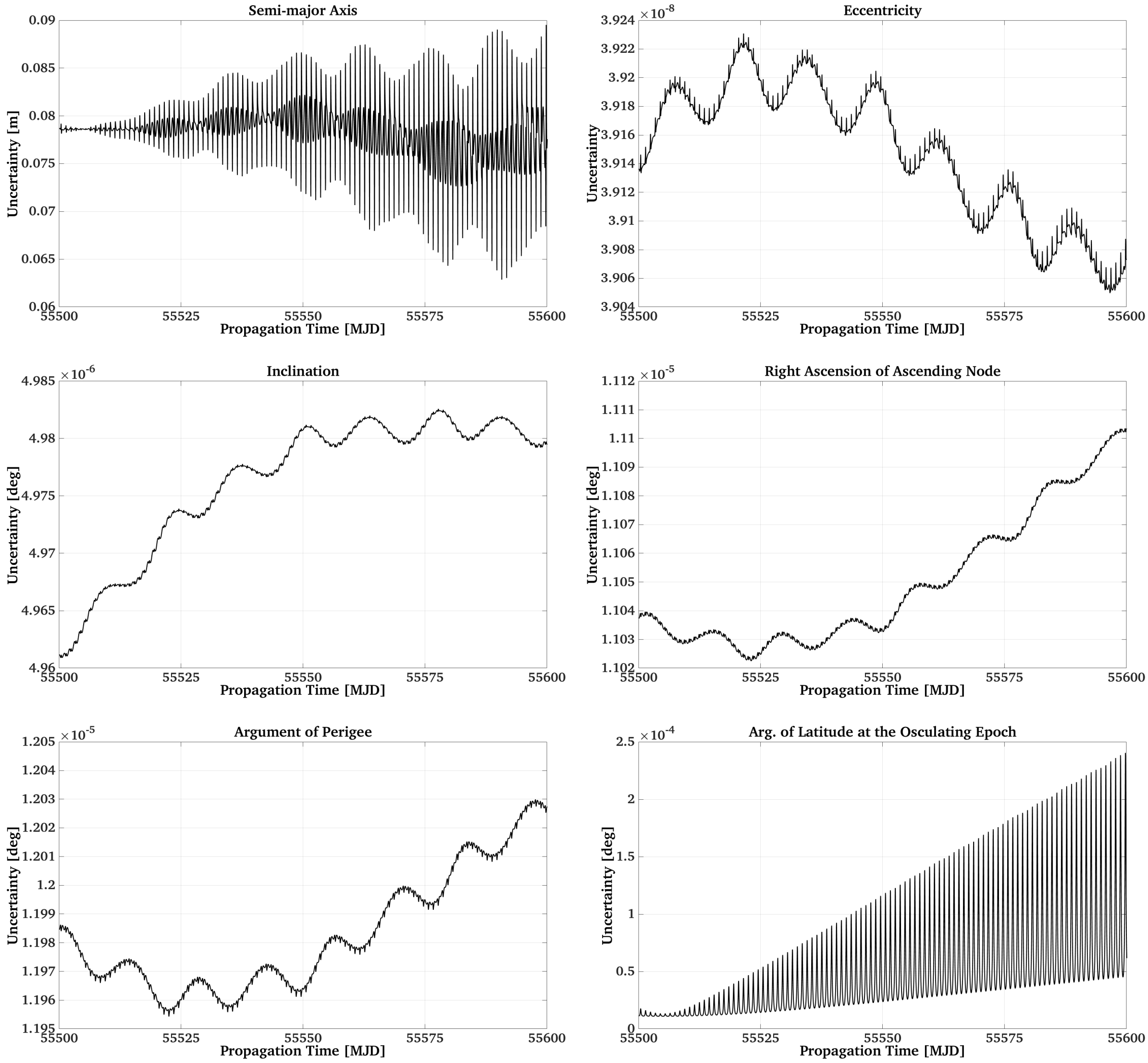

Figure 3.4 OE uncertainty propagation for an eccentric geosynchronous object.

### 3.4.2 Influence of the Estimated Empirical Parameters

In a general orbit determination problem is quite common to make use of dynamical and/or empirical parameters, which are further unknowns of the problem used to overcome the deficiencies of the physical model. The firsts are additional parameters which define the forces field; the seconds are determined empirically to absorb poorly modelled parts of the physical model [16, 17]. In the space debris OD environment the typically used dynamical parameters are:

- scaling parameter to estimate the area-to-mass ratio (AMR),
- scaling parameter to estimate the ballistic coefficient for the atmospheric drag,

while the typically used empirical parameters are:

- constant accelerations in radial, along- and cross-track directions,

- once-per-revolution (OPR) accelerations in radial, along- and cross-track directions.

These parameters, used to remedy the model deficiencies, will usually reduce the residuals on the observations and help getting (hopefully) a better orbit. To evaluate the influence of these parameters on the covariance propagation we decided to analyze two different kinds of orbits: a GPS and a GTO. To carry out this analysis we generated, for both cases, 10 days of continuous angular observations with a constant measurement sampling. An orbit determination is performed over the set of measurements estimating first simply the 6 orbital elements, then the OE together with the scaling parameter to improve the AMR, and finally the set of OE together with the once-per-revolution radial acceleration for the GPS while for the GTO also a constant along-track acceleration. In all cases the a posteriori errors per unit weight obtained at the end of the OD process are under 2 arcsec. The determined orbit and covariance are then propagated for 250 days for the GPS and for 150 for the GTO.
Figures 3.5 and 3.6 show the uncertainty behavior for the two considered objects. Figure 3.5 shows the uncertainty trends in RSW components for the GPS-like orbit, left-side graphs, and for the GTO-like orbit, right-side graphs, obtained for the 3 analyzed cases. Figure 3.6 shows, for an easier comparison, the modulus of the 3 components of the position uncertainty (indicated with 3D) obtained with the 3 set of estimated parameters within the same graph and a particular of the first 20 days of propagation. The figures clearly show that, within the LSQ process, the more parameters are used the faster the covariance grows with time. These examples were reported to show how a higher number of estimated parameters which produces the best “fit” (given by the lowest RMS) does not necessarily coincide with the most accurate orbit propagation. This phenomenon is due to the fact that the estimated parameters, if not properly modeled, do not describe correctly the physics of the forces acting on an orbiting object. Furthermore, it is interesting to notice how the general trends of the uncertainties change. Looking at the GPS case for example (left-side graphs), from an almost linear trend obtained estimating only the OE a quadratic behavior is obtained when estimating also the OPR accelerations in the radial direction (indicated with $R_C$ and $R_S$ in the graphs). Also interesting are the behaviors of the oscillation amplitudes obtained when estimating also the scaling parameter for the improvement of the AMR. We think that the long term changes in the uncertainty amplitude, visible in Figures 3.5c and 3.5d, are due to the motion of the Earth on its orbit and therefore of the motion of the orbital plane w.r.t. to the Sun. Consistently with the previous examples, the predominant error remains the along-track one while the “decreasing-increasing” behavior of the uncertainty propagation within the observation interval remains for all cases. The only differences are in their values which increase together with the number of estimated parameters. Finally it must be noticed that also the orbit of the object is playing a role in the uncertainty evolution. We can see that, exception made for the case of OD estimating only the 6th orbital elements, the uncertainties of the GTO-like orbit increase faster w.r.t. those of the GPS ones and even more faster if we increase the number of estimated parameters. The amplitude of the uncertainty oscillation is always bigger in the GTO case. Since the STM is function of the orbital elements, these phenomena are probably due to the eccentricity of the GTO orbit.

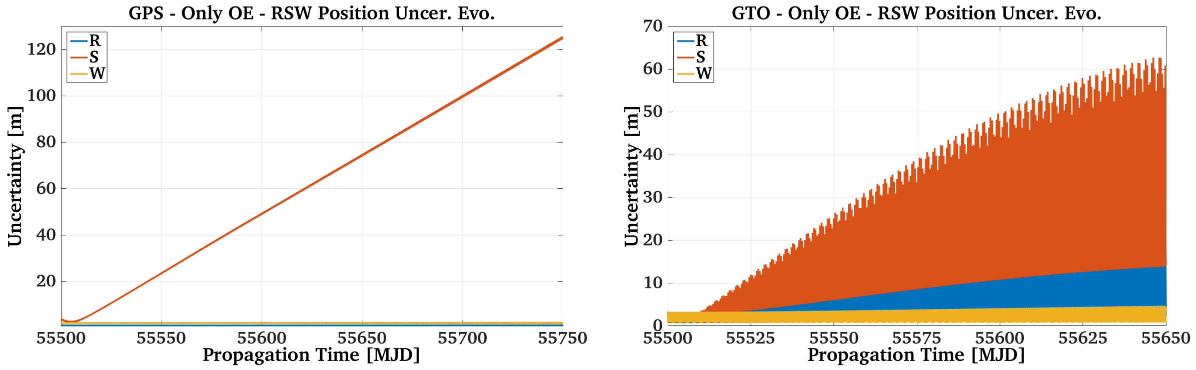

(a) GPS - Only orbital elements

(b) GTO - Only orbital elements

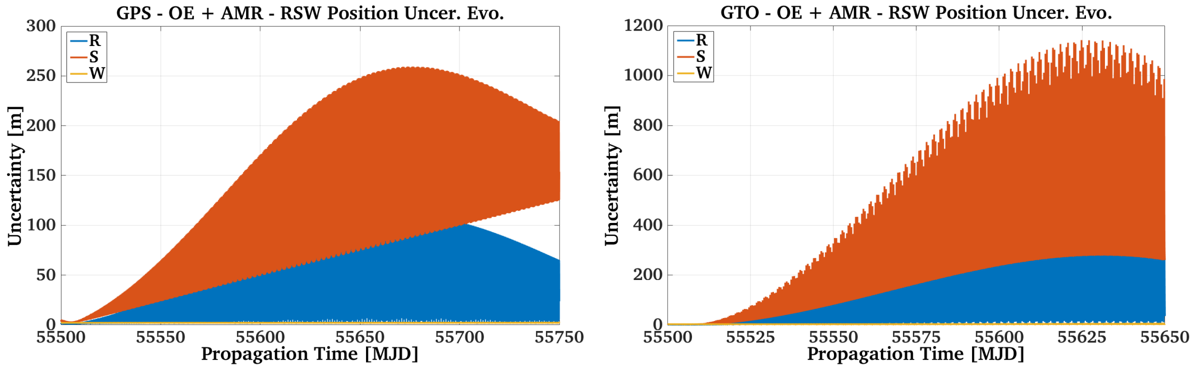

(c) GPS - OE and scaling AMR

(d) GTO - OE and scaling AMR

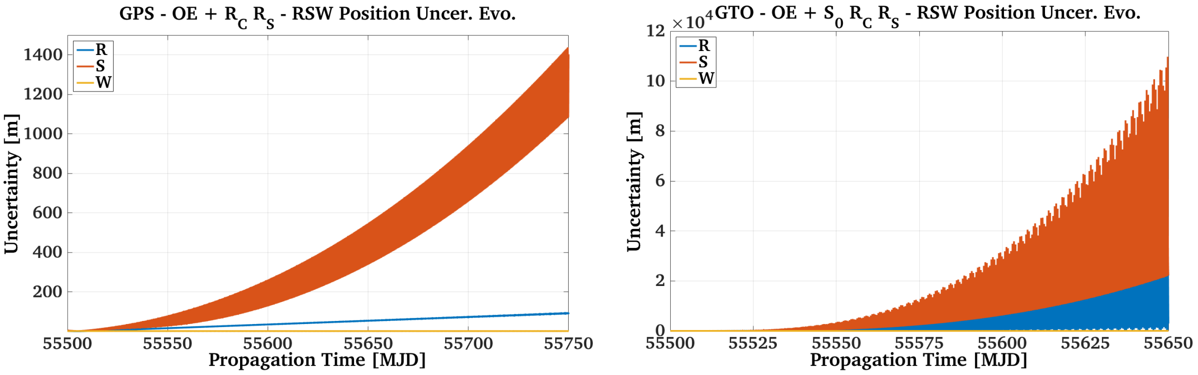

(e) GPS - OE and OPR $R$

(f) GTO - OE, constant $S$ and OPR $R$

Figure 3.5 RSW component uncertainty propagation, influence of the empirical parameters. For details see text.

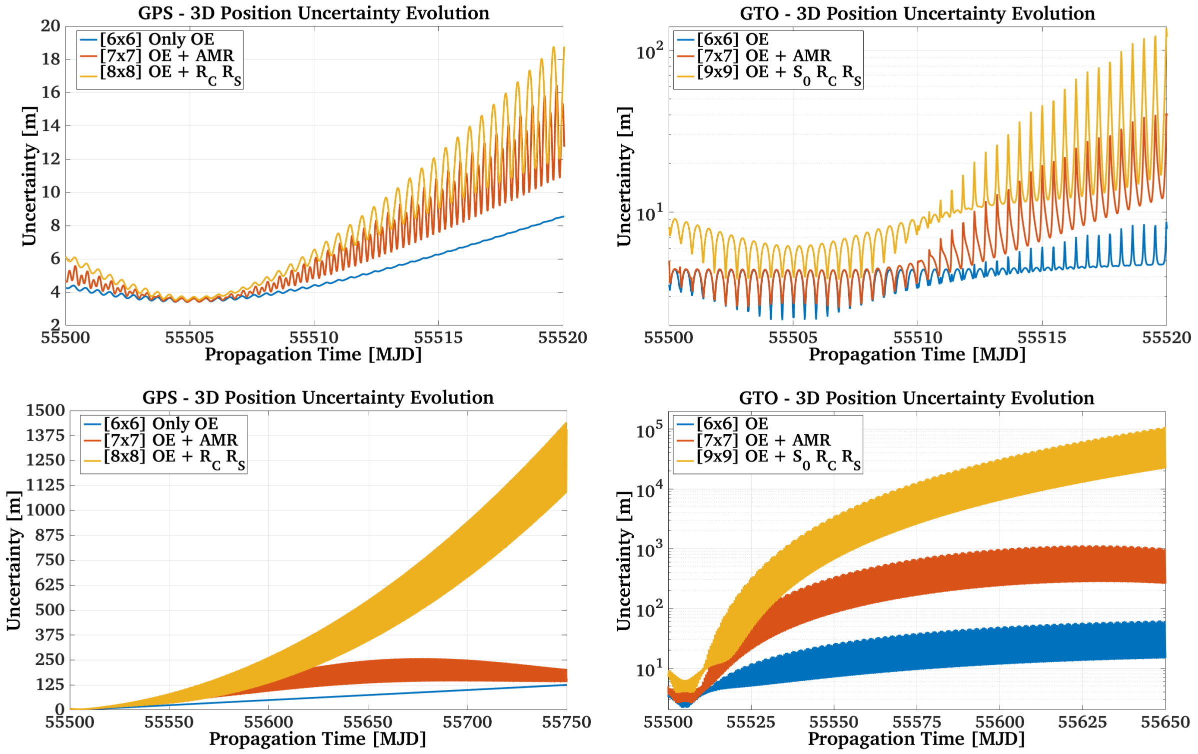

(a) GPS-like object

(b) GTO-like object

Figure 3.6 3D position uncertainty propagation, influence of the empirical parameters. For details see text.

### 3.4.3 Influence of Variance and Correlation Index

After the analysis of the influence of the empirical parameters, the next step was to understand how much the uncertainty propagation is influenced by the variances on the single parameters and by the correlation coefficients. In other words, we wanted to understand if the accuracy of an OD depends on the relative geometry between the observer and the object. We decided to verify this dependence via a Monte Carlo approach. First, we simulated a population of 40 objects distributed on slightly different orbits whose orbital parameters were:

- $a = 40000 \div 43000$ km,
- $e = 0 \div 0.02$,
- $i = 0 \div 10$ deg,
- $\Omega = 0 \div 360$ deg,
- $\omega = 0 \div 360$ deg,
- $u_0 = 0 \div 360$ deg.

We intentionally did not consider more objects since this was just an hypothesis exploration. For each object a reference orbit was generated and propagated over 10 days. Then, always

for each object, we simulated a set of observations made of 3 series (tracklets) of angular measurements (RA and DE) of 3 minutes length acquired from the ESASDT in Tenerife. Two series are consecutive (separated by 10 minutes) to simulate the discovery of the object, the third is separated by 2 hours w.r.t. the second to simulate the first follow-up. For each measurement we added a Gaussian distributed error with a standard deviation of 1 arcsec. The 3 tracklets are then used to perform an OD of the objects, the estimated orbit is then propagated and compared with the reference one. The results of this first simulation are shown in Figure 3.7a. The plot on the upper part of Figure 3.7a shows the difference between reference and estimated orbit in terms of angular distance in the sky for the first $\sim$ 4 hours of propagation displaying clearly the influence of the discovery and follow-up observations. The bottom-one shows the difference behaviors over the 10 days of propagation time. We can see how in the latter the features show different increasing rates and amplitudes of the differences w.r.t. the reference orbits, while they show the same periodicity with the orbital period.
This example is still too generic to extract a definitive conclusion, for this reason, a second one was carried out with the same methodology but in this case the population of the 40 objects belongs to the same orbit but are randomly distributed along it. The orbital elements used for this simulation are:

- $a = 40000$ km,
- $e = 0.02$,
- $i = 10$ deg,
- $\Omega = 20$ deg,
- $\omega = 30$ deg,
- $u_0 = 0 \div 360$ deg.

Analogously as for the previous case, the results of this simulation are shown in Figure 3.7b. Although the obtained behaviors are more similar, the differences are still quite big; this confirms that the accuracy of the OD and therefore the uncertainty propagation depends on the observation geometry. This topic will be studied in depth in the next chapter (4).

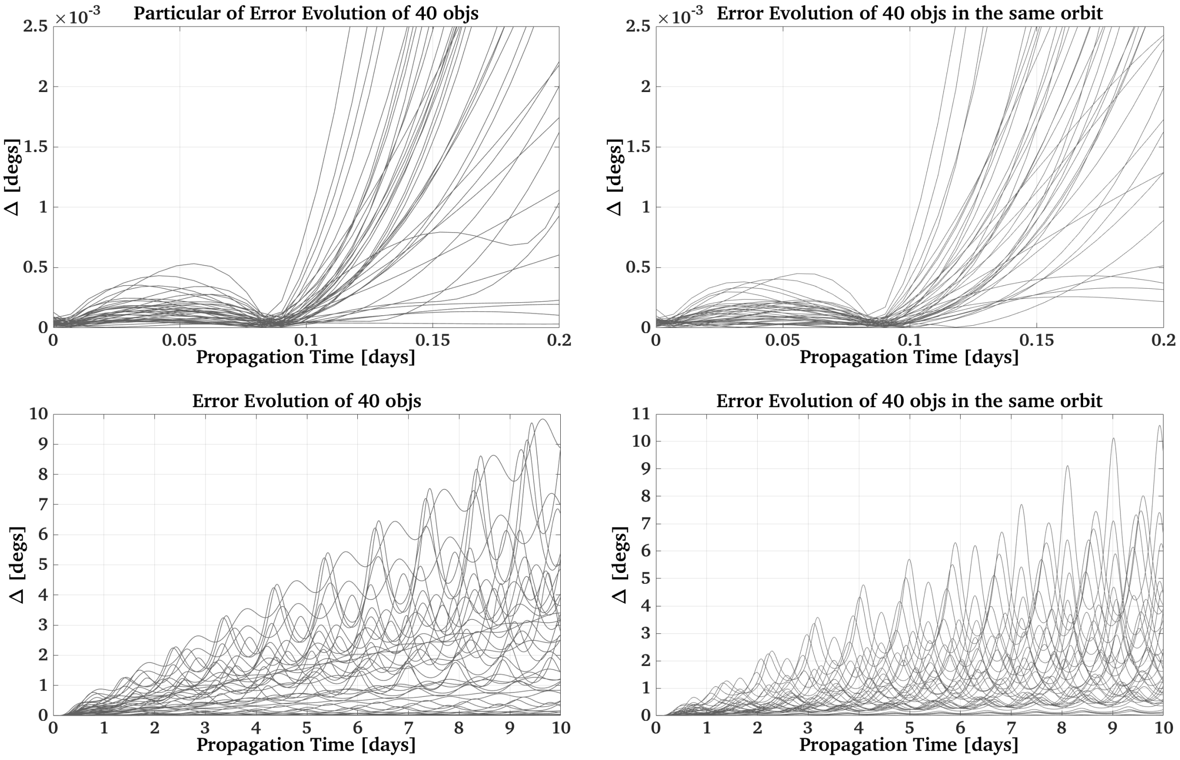

(a) Slightly different orbits (b) Same orbit

Figure 3.7 Monte Carlo simulation to show the influence of the observation geometry.

## 3.5 Summary

In this chapter we showed what transformations can be performed on the covariance matrix and we described and compared different methods which can be used to propagate it. The method based on the variational equations to compute the STM gives the most accurate results with the least computational efforts.

Successively, we described the characteristics of the covariance propagation w.r.t. different state representations. We started the analysis of the factors which influence the covariance propagation. We studied the influence of the number of estimated parameters focusing especially on the empirical accelerations usually used during the OD process and on the scaling parameter to determine the AMR. Essentially, the more parameters are estimated, the faster the uncertainty increases. A study was carried out to understand how much the orbit propagation is influenced by the variances and the correlation terms. This dependence was confirmed using Monte Carlo simulations. A more in depth study on the influence of the object-observer relative geometry is performed in the next chapter.

# Chapter 4

# Covariance Study to Optimize Follow-up Strategies

## 4.1 Motivation

In the space debris research, the precise knowledge of the number of objects and their position is a fundamental requirement. The orbit determination phase can be divided into two main steps: the first orbit determination and the orbit improvement. The first one is performed on the measurements resulting from a discovery campaign carried out by scanning certain regions of the sky to ensure that each object which cross the FoV of the telescope is observed several times during the same night [42]. While the orbit improvement is performed using the measurements obtained by planning regular observations of the object of interest, these additional series of observations are usually called follow-ups. Due to the huge amount of space debris and to the limitations of the telescopes, which can operate only when the weather conditions are good, it is necessary to optimize the time available for follow-up observations.

In this chapter we will describe a method, based on the analysis of the covariance matrix, to understand how the object-observer relative geometry influences the accuracy of the OD. This study will allow us to decide, in an operational scenario, how the follow-up observations should be distributed to obtain the best orbit and how the survey strategies could be optimized. We define the best orbit as the set of orbital elements with the lowest uncertainties, that maximizes the accuracy of the predicted positions of the object. In the first part of the chapter we describe the reasons that brought us to use the covariance matrix for this study and we will show the results of a theoretical study carried out to identify the main parameters which influence the results and how the problem can be simplified. Then, the results obtained from a simplified scenario will be shown. Afterwards, the complexity of the scenario is increased step by step showing in details the consequences on the results; in particular we will analyze first the influence of each estimated parameter on the results, and then the influence of the position of the observer. Once understood the basics, we will present the results obtained from the application of the covariance study to some typical observation scenarios and to some typical orbital regimes. Increasing gradually the complexity of the scenario we will study the case where two observers are observing the same target and the case where 3 series of observations are used. This last two scenarios are analyzed since the first allows us to understand how a network of observatories could improve the orbit determination while the second allows us to simulate a classical discov-

ery plus follow-up scenario. The last results presented are those obtained if we process together two kinds of observables, namely the classical angular measurements and the ranges.
Finally, we can say that we have carried out this analysis to be able to optimize the parameters estimation and to find the best combination of tracklets which gives the best orbit.

## 4.2 Theory

Depending on the number of objects to observe in the catalog, the survey strategy, the performance of the telescope system and of the software used to extract the measurements from an image, the number of observations per night per object, coming from the various observatories, is not constant. To carry out this study we choose the number of observations per object accordingly to what is provided by the AIUB observatory at the end of a standard observation night. Using the tools available at the Zimmerwald observatory, at the end of an observation night is not unusual to have, on average, two standard tracklets per observed objects. A tracklet is the result of a series of images acquired during a survey campaign or during a follow-up of an already cataloged object. We assume that a standard tracklet consists of e.g. 7 images, each one of them contains a triplet of data: a pair of angular measurements, one in Right Ascension and one in Declination (respectively RA and DE) and the time epoch when the measurements are collected. This means that for each tracklet one has 14 angular measurements, consequently, 28 observations per object, on average, from an observation night. Of course, these numbers can vary depending on factors like: the number of objects to observe in the catalog, the observation strategy and also, the information taken into account by the scheduler. For this study we assumed to have two good tracklets per observed object.
These two series of observations are then used to determine/improve the orbit of the object by means of a Least Squares adjustment (LSQ). The aim of this study is to analyze the output covariance of a LSQ process to understand how the relative geometry between the observer and the target object influences the accuracy of the estimated parameters. The covariance matrix or, to be more precise as we will see later in Paragraph 4.2.1, the cofactor matrix [27] is chosen as evaluation criterion because it contains the uncertainties of the estimated parameters. The partial derivatives are completely independent from the noise of the measurements and they are only functions of the geometric relation between the observer and the observed object. Since we are interested only in the influence of the geometry, we provide to the system the real/correct positions of the object for the calculation of the derivatives and no propagation of the covariance matrix is involved.
Together with the cofactor matrix we will make use also of the correlation indexes and the condition number (defined in Chapter 2) to explain the obtained results.

### 4.2.1 Cofactor Matrix

Recalling for simplicity the definitions already shown in Chapter 2, as one can see from Eq. 4.1, we chose the covariance matrix as the evaluation criterion because it contains the uncertainties of the estimated parameters as a function of the partial derivatives of the observations w.r.t. them and of the a posteriori error per unit weight.

$$\mathbf{Q} = {m_0}^2 \left[\mathbf{A}^T \mathbf{W} \mathbf{A}\right]^{-1} \tag{4.1}$$

$$\mathbf{K} = \left[\mathbf{A}^T \mathbf{W} \mathbf{A}\right]^{-1} \implies \mathbf{K} = \frac{\mathbf{Q}}{m^2} \tag{4.2}$$

in which:

$$\mathbf{A} = \frac{\partial \mathbf{obs}_i}{\partial \mathbf{x}_0}, \tag{4.3}$$

where:

- $\mathbf{Q}$ is the covariance matrix,
- $m_0^2$ is the a posteriori variance of the unit weight,
- $\mathbf{A}$ is the first design matrix,
- $\mathbf{W}$ is the weight matrix,
- $\mathbf{obs}_i = [RA_i; DE_i; \rho_i]$ are the $i$th measurements, the angular ones respectively Right Ascension and Declination, and the range where $i = 1, ..., n$, and $n$ is the number of measurement epochs,
- $\mathbf{x}_0 = [a, e, i, \Omega, \omega, 6\text{th}]$ are the orbital parameters.

Taking this into account, we do not need to solve the LSQ adjustment and feeding the systems with the correct values we avoid all “problems” related to the nonlinear LSQ like the initialization, the iterations and the convergence of the process on local minimum solution [15]. Since we are not going to solve the LSQ adjustment and in our study no real measurements with noise are involved it is more correct to talk about cofactor matrix [27]. The relation between covariance and cofactor matrix can be seen in Eq. 4.2. As one can see from Eq. 4.3, the cofactor matrix contains the partial derivatives of the observations w.r.t. semi-major axis, eccentricity, inclination, right ascension of ascending node, argument of perigee and the 6th parameter.
What we call from now on uncertainty values are not meant to be real values because we do not solve the LSQ and the analysis is performed without the employment of any measurement. So the vector of the residuals and then the a posteriori RMS can not be calculated. As consequence the obtained “uncertainties” are non-dimensional, to be more precise their dimension is the dimension of the parameter to which they refer divided by the square of the dimension of the residuals. On the other hand, the obtained uncertainty does not lose its importance as qualitative index indicating us which configuration of observation produces more accurate results.
In this chapter, we will consider first only the angular measurements as observations then we will introduce also the ranges (Paragraph 4.15). These partial derivatives are functions of the geometric relation between observer and observed object. This allows us to study both, the influence of the observation geometry and the influence of the different observables.

### 4.2.2 Choice of Parameters

As can be seen from Eq. 4.1 and Eq. 4.3, the output covariance of a LSQ adjustment is a $[6\times 6]$ matrix, function of the observer position and the orbit of the object. To simplify the problem, in order to isolate the contribution of each single component, it was decided to eliminate the effects associated to the observer, so in a first step an observer on the center of the Earth is used. The set of unknown parameters consists of: two parameters which describe the shape of the orbit (i.e. semi-major axis and eccentricity), two which describe the orientation of the orbital plane in space (i.e. inclination and right ascension of ascending node), one parameter for the orientation of the orbit in the plane (i.e. argument of perigee), and finally the 6th parameter which relates to the position of the object along the orbit at a particular time. Among them, the parameters describing the orientation of the plane in space are completely independent from the others, so negligible in a first analysis. The remaining parameters can not be excluded a priori because they depend on the chosen parametrization. There are several variables which can be used to express the 6th parameter: mean anomaly, eccentric anomaly, true anomaly, argument of latitude and perigee passing time, respectively $M, E, \nu, u_0$ and $T_0$. Among them, the historical one is the perigee passing time; in fact, using $T_0$, the dependencies between parameters have the structure described by Eq. 4.4 [16].

$$\begin{aligned} M &= M\left(a, T_0\right) \\ E &= E\left(M, e\right) \\ \nu &= \nu\left(e, E\right) \end{aligned} \tag{4.4}$$

Making use of this structure, the partial derivatives of true anomaly are function of $a, e$ and $T_0$. This parametrization has a big disadvantage for small eccentricity values; in fact if $e=0$, the orbit is circular, which means that we do not have any perigee and the $T_0$ can not be defined anymore. To overcome this problem, the most used solution is to define the argument of latitude at the time $t_0$. For circular orbit, exploiting the definition of osculating elements [16] , the user can set up arbitrarily an osculating time $T_{osc}$, with a certain $\omega$ and $\nu_0$, and solve the LSQ adjustment at this epoch. The disadvantage is given by the fact that the dependencies between parameters change accordingly with new parametrization as shown by Eq. 4.5. The analysis reported in this thesis were carried out using the parametrization with the argument of latitude because of the above mentioned reasons.

$$\begin{aligned} \nu_0 &= \nu_0\left(u_0, \omega\right) \\ E_0 &= E_0\left(\nu_0, e\right) \\ T_0 &= T_0\left(a, e, E_0\right) \end{aligned} \tag{4.5}$$

### 4.2.3 Build up of the Normal Equation System

As said in Paragraph 4.2.1, the cofactor matrix, shown in Eq. 4.2, is function of the weight and of the first design matrix. In this paragraph we will show how to calculate the matrices needed to build our cofactor matrix: first we will describe how to determine the first design matrix then, we will analyze the weight matrix.
As shown from Eq. 4.1 and Eq. 4.3, the covariance matrix is function of the partial derivatives of the observations w.r.t. the estimated parameters. At this point, since in the previous Paragraph (4.2.2) we explained the reasons of our parametrization choice, we can now determine the partial derivatives that will characterize the cofactor matrix. To simplify the calculation of the derivatives we decided to split them as shown in Eq. 4.6 [16].

$$\frac{\partial \mathbf{obs}}{\partial \mathbf{x}_0} = \frac{\partial \mathbf{obs}}{\partial \vec{\mathbf{r}}} \cdot \frac{\partial \vec{\mathbf{r}}}{\partial \mathbf{x}_0}, \tag{4.6}$$

where $\vec{\mathbf{r}}$ is defined as shown in Eq. 4.7. We have intentionally omitted the subscript $i$ since the following equations are valid for each observation epoch.

$$\vec{\mathbf{r}} = \vec{\mathbf{r}}_s - \vec{\mathbf{r}}_o = \begin{pmatrix} x \\ y \\ z \end{pmatrix} = \begin{pmatrix} x_s \\ y_s \\ z_s \end{pmatrix} - \begin{pmatrix} x_o \\ y_o \\ z_o \end{pmatrix} \tag{4.7}$$

Here $\vec{\mathbf{r}}_s$ and $\vec{\mathbf{r}}_o$ represent the position of the target object and of the observer whose coordinates in the inertial reference system are respectively $x_s, y_s, z_s, x_o, y_o$ and $z_o$. We reported only the coordinate of the positions since the measurements used in our orbit determination process does not depend on the target and/or observer velocities. At this point, defining $x, y$ and $z$ as shown in Eq. 4.7 we can determine the partial derivatives of our measurements w.r.t. $\vec{\mathbf{r}}$.
Recalling for clarity the definition of Right Ascension and Declination in the Eq. 4.8 and Eq. 4.9 and defining the range ($\rho$) as shown in Eq. 4.10 we have:

$$RA = \arctan\left(\frac{y}{x}\right), \tag{4.8}$$

$$DE = \arctan\left(\frac{z}{\sqrt{x^2+y^2}}\right), \tag{4.9}$$

$$\rho = \sqrt{x^2+y^2+z^2}. \tag{4.10}$$

We can now calculate the partial derivatives of RA and DE w.r.t. $\vec{\mathbf{r}}$ as follows:

$$\frac{\partial RA}{\partial \vec{\mathbf{r}}} = \begin{bmatrix} \frac{\partial RA}{\partial x} & \frac{\partial RA}{\partial y} & \frac{\partial RA}{\partial z} \end{bmatrix}^T$$

$$\frac{\partial RA}{\partial x} = -\frac{y}{x^2+y^2}, \quad \frac{\partial RA}{\partial y} = \frac{x}{x^2+y^2}, \quad \frac{\partial RA}{\partial z} = 0, \tag{4.11}$$

$$\frac{\partial DE}{\partial \vec{\mathbf{r}}} = \begin{bmatrix} \frac{\partial DE}{\partial x} & \frac{\partial DE}{\partial y} & \frac{\partial DE}{\partial z} \end{bmatrix}^T$$

$$\frac{\partial DE}{\partial x} = -\frac{x \cdot z}{\rho^2\sqrt{x^2+y^2}}, \quad \frac{\partial DE}{\partial y} = -\frac{y \cdot z}{\rho^2\sqrt{x^2+y^2}}, \quad \frac{\partial DE}{\partial z} = \frac{\sqrt{x^2+y^2}}{\rho^2}. \tag{4.12}$$

The partial derivatives of the ranges w.r.t. $\vec{\mathbf{r}}$ are:

$$\frac{\partial \rho}{\partial \vec{\mathbf{r}}} = \begin{bmatrix} \frac{\partial \rho}{\partial x} & \frac{\partial \rho}{\partial y} & \frac{\partial \rho}{\partial z} \end{bmatrix}^T$$

$$\frac{\partial \rho}{\partial x} = \frac{x}{\rho}, \quad \frac{\partial \rho}{\partial y} = \frac{y}{\rho}, \quad \frac{\partial \rho}{\partial z} = \frac{z}{\rho}. \tag{4.13}$$

Looking now at the remaining part of the Eq. 4.6, in particular the one which refers to the partial derivatives of $\vec{\mathbf{r}}$ w.r.t. the estimated parameters, we see that these are only function of the satellite position since from Eq. 4.7 we get:

$$\frac{\partial \vec{\mathbf{r}}_o}{\partial \mathbf{x}_0} = 0. \tag{4.14}$$

As one can see from [1], the satellite position coordinates in the inertial system of reference (SoR) can be obtained from its coordinates in the perifocal reference system ($\vec{r}_{EPH}$) using the following expression:

$$\vec{\mathbf{r}}_s = \mathbf{R} \cdot \vec{\mathbf{r}}_{EPH} \tag{4.15}$$

where $\mathbf{R}$ is the Euler rotation matrix [1]. The matrix $\mathbf{R}$ and the perifocal coordinates are defined by Eq. 4.16 and Eq. 4.17.

$$\mathbf{R} = \begin{bmatrix} \cos\Omega\cos\omega - \sin\Omega\sin\omega\cos i & -\cos\Omega\sin\omega - \sin\Omega\cos\omega\cos i & \sin\Omega\sin i \\ \sin\Omega\cos\omega - \cos\Omega\sin\omega\cos i & -\sin\Omega\sin\omega + \cos\Omega\cos\omega\cos i & -\cos\Omega\sin i \\ \sin\omega\sin i & \cos\omega\sin i & \cos i \end{bmatrix} \tag{4.16}$$

$$\vec{\mathbf{r}}_{EPH} = \begin{bmatrix} \frac{a\left(1-e^2\right)\cos\nu}{(1+e\cos\nu)} \\ \frac{a\left(1-e^2\right)\sin\nu}{(1+e\cos\nu)} \\ 0 \end{bmatrix} \tag{4.17}$$

From these equations and taking into account the dependencies shown in Paragraph 4.2.2 we can now calculate the derivatives of the satellite position w.r.t. the estimated parameters. Regarding the derivative w.r.t. the semi-major axis $a$ we have:

$$\frac{\partial \vec{\mathbf{r}}_s}{\partial a} = \mathbf{R} \begin{bmatrix} \cos E - e \\ \sqrt{1-e^2}\sin E \\ 0 \end{bmatrix} + a \cdot \mathbf{R} \begin{bmatrix} -\sin E \\ \sqrt{1-e^2}\cos E \\ 0 \end{bmatrix} \cdot \frac{\partial E}{\partial a}, \tag{4.18}$$

$$\frac{\partial E}{\partial a} = -\frac{na}{r}\left[\frac{3}{2a}(t-T_0) + \frac{\partial T_0}{\partial a}\right], \tag{4.19}$$

$$\frac{\partial T_0}{\partial a} = -\frac{3}{2an}\left[E_0 - e\sin E_0\right] = -\frac{3}{2a}\left(T_{osc} - T_0\right), \tag{4.20}$$

$$n = \sqrt{\frac{\mu}{a^3}}, \tag{4.21}$$

$$r = \frac{a\left(1-e^2\right)}{1+e\cos\nu}, \tag{4.22}$$

where $r$ is the geocentric distance of the satellite, $n$ is the mean motion, $\mu = 398600.4418$ km$^3$sec$^{-2}$ is the terrestrial gravitational constant, $t$ is the time, $E_0$ is the value of the eccentric anomaly at the osculating epoch where our LSQ is solved.
For the derivatives w.r.t. the eccentricity $e$ we have:

$$\frac{\partial \vec{\mathbf{r}}_s}{\partial e} = -a \cdot \mathbf{R} \begin{bmatrix} 1 \\ \frac{e\sin E}{\sqrt{1-e^2}} \\ 0 \end{bmatrix} + a \cdot \mathbf{R} \begin{bmatrix} -\sin E \\ \sqrt{1-e^2}\cos E \\ 0 \end{bmatrix} \cdot \frac{\partial E}{\partial e}, \tag{4.23}$$

$$\frac{\partial E}{\partial e} = \left[\sin E - n\frac{\partial T_0}{\partial e}\right] \cdot \frac{r}{a}, \tag{4.24}$$

$$\frac{\partial T_0}{\partial e} = -\frac{1}{n}\left[\frac{\partial E_0}{\partial e}(1-e\cos E_0) - \sin E_0\right], \tag{4.25}$$

$$\frac{\partial E_0}{\partial e} = -\frac{\sin \nu_0}{\sqrt{1-e^2}\,(1+e\cos\nu_0)}, \tag{4.26}$$

where $\nu_0$ is the true anomaly at the osculating epoch.
For the derivatives w.r.t. the inclination $i$ we have:

$$\frac{\partial \vec{\mathbf{r}}_s}{\partial i} = \frac{\partial \mathbf{R}}{\partial i}\cdot \begin{bmatrix} r\cos\nu \\ r\sin\nu \\ 0 \end{bmatrix}, \tag{4.27}$$

$$\frac{\partial \mathbf{R}}{\partial i} = \begin{bmatrix} \sin\Omega\sin\omega\sin i & \sin\Omega\cos\omega\sin i & \sin\Omega\cos i \\ -\cos\Omega\sin\omega\sin i & -\cos\Omega\cos\omega\sin i & -\cos\Omega\cos i \\ \sin\omega\cos i & \cos\omega\cos i & -\sin i \end{bmatrix}. \tag{4.28}$$

For the derivatives w.r.t. the Right Ascension of the Ascending Node $\Omega$ we have:

$$\frac{\partial \vec{\mathbf{r}}_s}{\partial \Omega} = \frac{\partial \mathbf{R}}{\partial \Omega}\cdot \begin{bmatrix} r\cos\nu \\ r\sin\nu \\ 0 \end{bmatrix}, \tag{4.29}$$

$$\frac{\partial \mathbf{R}}{\partial \Omega} = \begin{bmatrix} -\sin\Omega\cos\omega - \cos\Omega\sin\omega\cos i & \sin\Omega\sin\omega - \cos\Omega\cos\omega\cos i & \cos\Omega\sin i \\ \cos\Omega\cos\omega - \sin\Omega\sin\omega\cos i & -\cos\Omega\sin\omega - \sin\Omega\cos\omega\cos i & \sin\Omega\sin i \\ 0 & 0 & 0 \end{bmatrix}. \tag{4.30}$$

For the derivatives w.r.t. the Argument of Perigee $\omega$ we have:

$$\frac{\partial \vec{\mathbf{r}}_s}{\partial \omega} = a\frac{\partial \mathbf{R}}{\partial \omega}\begin{bmatrix} \cos E - e \\ \sqrt{1-e^2}\sin E \\ 0 \end{bmatrix} + a\mathbf{R}\begin{bmatrix} -\sin E \\ \sqrt{1-e^2}\cos E \\ 0 \end{bmatrix}\frac{\partial E}{\partial \omega}, \tag{4.31}$$

$$\frac{\partial \mathbf{R}}{\partial \omega} = \begin{bmatrix} -\cos\Omega\sin\omega - \sin\Omega\cos\omega\cos i & -\cos\Omega\cos\omega + \sin\Omega\sin\omega\cos i & 0 \\ -\sin\Omega\sin\omega + \cos\Omega\cos\omega\cos i & -\sin\Omega\cos\omega - \cos\Omega\sin\omega\cos i & 0 \\ \cos\omega\sin i & -\sin\omega\sin i & 0 \end{bmatrix}, \tag{4.32}$$

$$\frac{\partial E}{\partial \omega} = -\frac{na}{r}\frac{\partial T_0}{\partial \omega}, \tag{4.33}$$

$$\frac{\partial T_0}{\partial \omega} = -\frac{1}{n}\left[1 - e\cos E_0\right]\frac{\partial E_0}{\partial \omega}, \tag{4.34}$$

$$\frac{\partial E_0}{\partial \omega} = -\frac{\sqrt{1-e^2}}{1+e\cos \nu_0}. \tag{4.35}$$

For the derivatives w.r.t. the Argument of Latitude at the osculating time $u_0$ we have:

$$\frac{\partial \vec{\mathbf{r}}_s}{\partial u} = a\mathbf{R}\begin{bmatrix} -\sin E \\ \sqrt{1-e^2}\cos E \\ 0 \end{bmatrix}\frac{\partial E}{\partial u_0}, \tag{4.36}$$

$$\frac{\partial E}{\partial u_0} = -\frac{na}{r}\frac{\partial T_0}{\partial u_0}, \tag{4.37}$$

$$\frac{\partial T_0}{\partial u_0} = -\frac{1}{n}\left[1 - e\cos E_0\right]\frac{\partial E_0}{\partial u_0}, \tag{4.38}$$

$$\frac{\partial E_0}{\partial u_0} = \frac{\sqrt{1-e^2}}{1+e\cos \nu_0}. \tag{4.39}$$

Since the Argument of Latitude it is defined as shown in Eq. 4.40,

$$u_0 = \nu_0 + \omega \tag{4.40}$$

it is important to notice the relation between the derivatives of the eccentric anomaly $E$ w.r.t. $\omega$ and $u_0$, in particular we get:

$$\frac{\partial E_0}{\partial u_0} = -\frac{\partial E_0}{\partial \omega} \implies \frac{\partial E}{\partial u_0} = -\frac{\partial E}{\partial \omega} \tag{4.41}$$

Now we are able to determine the value of Eq. 4.6 for each observation epoch; in other words we are able to build the first design matrix **A**. To complete the set up of the normal equations system and then to be able to calculate our cofactor matrix, we need one last component: the weight matrix **W**. The weight matrix, in this study, is used only with merged measurements. In fact, since in this study, we focus only on the influence of the geometry we do not need the weight matrix when processing homogeneous measurements. During this study, also when we analyze the influence of a second observer, we assume that the accuracy of the observations from the two observers is the same.

The only case where the weight matrix is fundamental is when we evaluate the consequences of processing different kind of observables, i.e. angular and range measurements. In this case **W** is needed to normalize the contribution given by the derivatives of the ranges w.r.t. the angular

ones. This need can be easily proved by means of a dimensional analysis of the NEQ system with merged observables.
As defined in Chapter 3 and by adapting the generic form of the weight matrix to our case we have:

$$\mathbf{W} = \begin{bmatrix} w_{RA1} & 0 & 0 & \cdots & 0 & 0 & 0 \\ 0 & w_{DE1} & 0 & \cdots & 0 & 0 & 0 \\ 0 & 0 & w_{\rho 1} & \cdots & 0 & 0 & 0 \\ \vdots & \vdots & \vdots & \ddots & \vdots & \vdots & \vdots \\ 0 & 0 & 0 & \cdots & w_{RAn} & 0 & 0 \\ 0 & 0 & 0 & \cdots & 0 & w_{DEn} & 0 \\ 0 & 0 & 0 & \cdots & 0 & 0 & w_{\rho n} \end{bmatrix} \tag{4.42}$$

where $w_{RAi}, w_{DEi}$ and $w_{\rho i}$ are the weights for the $i$th RA, DE and range measurement respectively, with $i = 1, \ldots, n$. To be precise in our case, $w_{RA1} = w_{DE1} = \ldots = w_{RAn} = w_{DEn}$ and $w_{\rho 1} = \ldots = w_{\rho n}$. At this point, we need to determine the values for $w_{RA,DE}$ and $w_\rho$.
Consistently with the approach followed in Paragraph 5.5.1, we determined the weights between angular and range measurements relatively, in particular we have:

$$w_{RA,DE} = \frac{\sigma_0^2}{\sigma_{RA,DE}^2} \quad \text{and} \quad w_\rho = \frac{\sigma_0^2}{\sigma_\rho^2}, \tag{4.43}$$

where $\sigma_{RA,DE}$ and $\sigma_\rho$ are the measurement accuracies for the angles and the ranges, respectively. If we put $\sigma_0 = \sigma_{RA,DE}$ we obtain that:

$$w_{RA,DE} = 1 \quad \text{and} \quad w_\rho = \frac{\sigma_{RA,DE}^2}{\sigma_\rho^2}. \tag{4.44}$$

During this study the weights were calculated using the following values for the measurement standard deviations $\sigma_{RA,DE} = 0.5$ arcsec and $\sigma_\rho = 1.3$ m.

### 4.2.4 Study of Partial Derivatives

Once the parametrization was chosen, we decided to study the partial derivatives to have an idea of their influence on the results. Figures 4.1 and 4.2 show the behavior of the partial derivatives of RA, DE and $\rho$ w.r.t. the orbital elements, obtained for an object whose orbit is described by the following orbital elements: $a = 42164.173$ km, $e = 0.6$, $i = 30°$, $\Omega = 40°$, $\omega = 60°$ and $T_{osc} = 0$ sec. The observer's coordinates are: latitude 40° North, longitude 10° East and altitude 900 m.
As can be seen in Figures 4.1 and 4.2, all partial derivatives show periodic features over the orbital period, which in this case is also coincident with the sidereal day. There is only an exception for the derivatives w.r.t. the semi-major axis that show also a time dependency which

amplifies the periodic features. Looking at the analytical expression of the derivatives of the satellite position w.r.t. the semi-major axis, as shown in Eqs. 4.18-4.20, it was notice that these are the only ones which are proportional to the difference between the actual epoch and the osculating time, consequently the derivatives of the measurements w.r.t. $a$ keep this proportionality (see Eq. 4.45). During the analysis of the covariance matrix, the influence of different $T_{osc}$ was also studied; the variations caused by $T_{osc}$ are seen only in the uncertainties of the argument of latitude ($u_0$) without influencing the other parameters.

$$\left(\frac{\partial RA}{\partial a}, \frac{\partial DE}{\partial a}, \frac{\partial \rho}{\partial a}\right) \propto (t - T_{osc}) \tag{4.45}$$

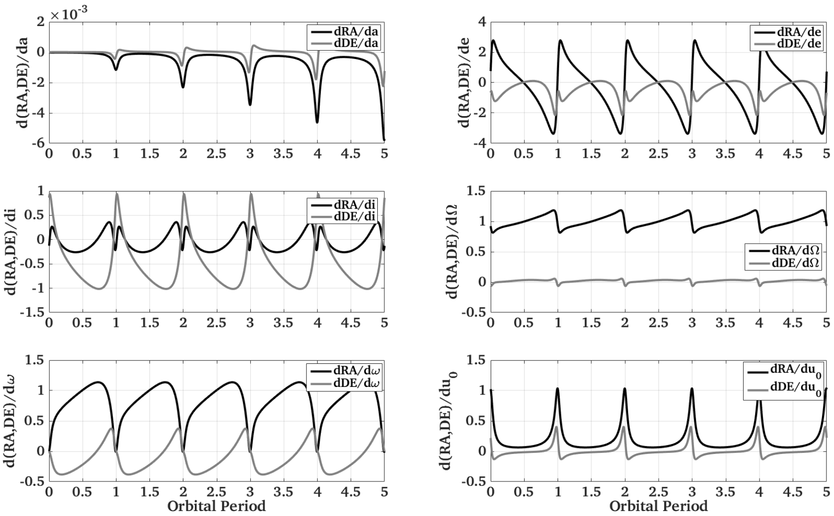

Figure 4.1 Behavior of RA and DE partial derivatives w.r.t. the orbital elements.

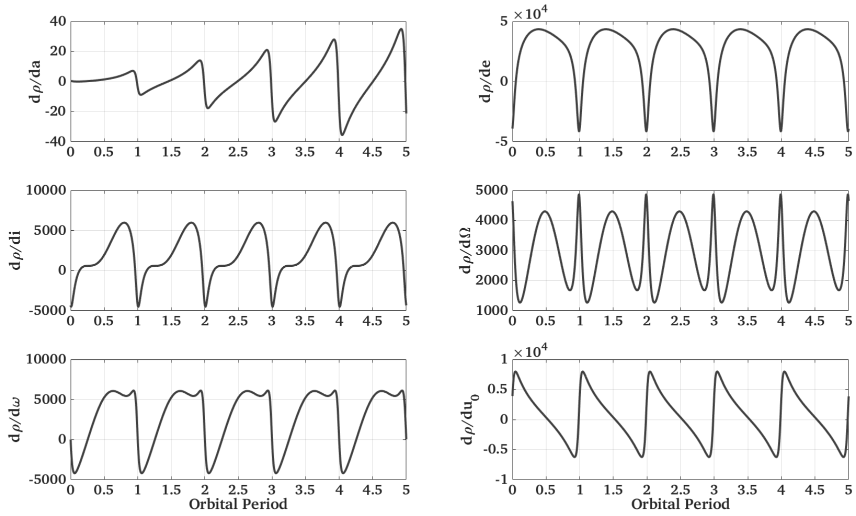

Figure 4.2 Behavior of range partial derivatives w.r.t. the orbital elements.

## 4.3 Simulation Set-up

The results which we are going to present are based on a limited number of observations. The main part of the results presented here were obtained using only two tracklets, each one consists of 7 triplets of measurements: two angles and one observation epoch (i.e. RA, DE and $t$), for a total number of 28 angular observations. Later on, when we will study some particular cases the number of observations used will change, more specifically, where studying the influence of a second observer a total of 4 tracklets are used; for the study of the follow-up influence 3 tracklets are used and finally to evaluate the influences of the ranges we will add to the usual 2 tracklets a variable number of ranges. Despite the change in the number of measurements, the basic principle of the simulation will remain the same. Details will be provided at the beginning of each Paragraph. However, during all simulations the time interval between the measurements within a tracklet is kept constant to 30 seconds.

We focus now, for simplicity, on the two tracklets case from a single observer. The simulations are performed in a way to cover all possible combinations of tracklets positions in the orbit. To do so, the first LSQ adjustment is performed positioning the first tracklet on the orbit perigee and the time interval between first and second tracklet is increased from 10 sec to 2 orbital revolutions with intervals of 2.5° in true anomaly; then, the same procedure is repeated positioning at each run the first tracklet 2.5° in true anomaly forward along the orbit. These scheme is adopted for all simulations carried out in this Chapter. For each couple of tracklets the last iteration of a LSQ adjustment is simulated and from the corresponding covariance matrix the square root of the terms in the main diagonal, the correlation coefficients and the condition number are stored. Since we are not interested in LSQ performances the correct orbital elements are given as input to the LSQ. It is possible to do this simplification because being a non-linear LSQ, the only requirement to find the minimum is that the initials value of the estimated parameters should be near to the global minimum values to converge to the correct solution [15].

## 4.4 First Results with Simplified Scenario

In order to simplify the problem and to identify the influence of the observation-geometry on each single estimated parameter the first set of results was obtained estimating a subset of the unknown parameters. In principle, if the parameters to be estimated are independent from each other, one could solve for each of them separately. Unfortunately, as we have seen in Paragraph 4.2.2, the orbital elements are not completely independent and the minimum number of parameters to be estimated depends on the chosen parametrization. Since we chose the following set of parameters: $a$, $e$, $i$, $\Omega$, $\omega$ and $u_0$, taking into account Eq. 4.5, we could separate them in only two groups. The first group concerns the parameters which describe the shape of the orbit and the position of the object along the orbit (namely $a$, $e$, $\omega$ and $u_0$); the second describes the orientation of the orbital plane in the space (namely $i$ and $\Omega$). Although this simplification was only partial, it allowed us to understand some basic features and characteristics of the problem. A further simplification that one can apply to the problem is related to the position of the observer.

In the first analysis the effect of an observer on the Earth's surface is neglected, so a geocentric observer is used. At the same time, only semi-major axis, eccentricity, argument of perigee and the argument of latitude are estimated. Figures 4.3, 4.4 and 4.5 show the results obtained for this simplified scenario for an orbit with: $a = 42164.173$ km, $e = 0.6$, $i = 30°$, $\Omega = 40°$, $\omega = 60°$ and $T_{osc}$ coincides with the epoch of the 1st observation (from now the osculating epoch will be indicated simply with $T_{osc} =$ 1st observation). The three figures show the three main results of our simulation. In Figure 4.3, the uncertainty maps obtained for the estimated parameters are reported. In Figure 4.4, a subset of the correlation maps are reported and finally Figure 4.5, the condition numbers map of the correlation matrix coefficients is shown. All the maps show the obtained results as a function of the tracklets position. In particular, the position of the 1st tracklet along the orbit can be read on the $y$-axis, while the position of the 2nd is displayed on the $x$-axis. Both positions are expressed in terms of true anomaly.

Before starting the discussion of the features visible in the maps it is important to highlight two particular regions of the obtained maps: the “period-line” and the “symmetry-line”. The subscript number indicates the number of the tracklet: $\nu_1$ indicates the first tracklet and $\nu_2$ indicates the second. The period-line is made by the points lying on the diagonal line whose extremes have coordinates $[\nu_2 = 360, \nu_1 = 0]$, $[\nu_2 = 720, \nu_1 = 360]$ which defines all tracklets whose positions are separated by one (or more) orbital period(s) in time. The symmetry-line consists of points lying on the diagonal line whose extremes have coordinates $[\nu_2 = 360, \nu_1 = 360]$, $[\nu_2 = 720, \nu_1 = 0]$ which defines all tracklets whose positions are symmetrical to the line of the apsides. Of course all the lines which are parallel to the one mentioned before with a distance multiple of 360° have the same meaning.

Each point of Figure 4.3 shows the logarithm (in base 10) of the square root of the uncertainty of the estimated parameters ($\log_{10} K_x$ with $K_x = \sqrt{K_{ii}}$ where $x$ is the generic estimated parameter coincident with the $i$th element on the main diagonal of matrix $\mathbf{K}$). Here, it is already possible to notice two important characteristics: the first is given by the fact that the features in the maps are completely different between the first and the second orbital revolution, more precisely when the time interval between the tracklets is smaller or bigger than the orbital period. The second is the $S$-shaped feature, associated with a high uncertainty area, which appears in the second revolution. The first effect is one of the consequences of the time dependency of some partial derivatives, while the $S$-shaped high uncertainty is occurring when the time interval between the tracklets is half an orbital period; both effects will be later discussed in details (respectively in the Paragraphs 4.5 and 4.6).

Looking at the $S$-shaped high uncertainty region it easy to see how for the eccentricity and the argument of perigee the features present some interruptions while for the semi-major axis the $S$ is continuous. Being this an elliptical orbit and the tracklets are acquired with a constant time sampling between observations, it is obvious that the arc length covered by the tracklets is depending on the tracklet position. Furthermore, the length of the arc between the single observations is not constant. The mentioned effects provide information regarding the eccentricity and the position of the perigee. In fact if one pays attention to the interruptions of the $S$ for the eccentricity, these are occurring when the first tracklet is on the perigee and the second is at the apogee (and vice versa). This tracklets combination maximizes the difference between the length of the arc covered by the tracklet.

Regarding the interruptions of the $S$ for the argument of perigee, these are occurring when the tracklets are symmetric w.r.t. the line of the apsides. In this case two symmetric tracklets with the same length are used, but the distances between the observations within the tracklet are first increasing then decreasing (or vice versa) in the same way. If we pay attention to the position

of the $S$-region, it is easy to see that thee minimum is not precisely on the half period distance between the tracklets, this is even more evident if we look at the interruptions for the eccentricity. As we will see later, this is a second effect of the time dependency.
For completeness also the uncertainty map for the argument of latitude ($u_0$) is reported in Figure 4.3, this parameter will not be always shown in this chapter because our interest is mainly focused on the geometric parameters. Furthermore, the uncertainties of $u_0$ are depending on the arbitrary time $T_{osc}$.

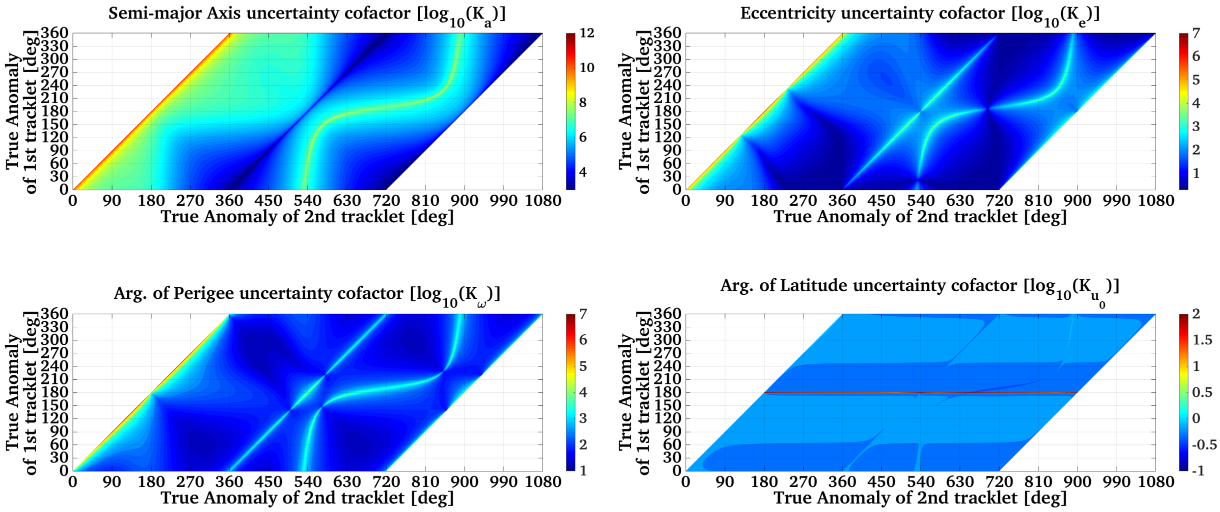

Figure 4.3 Uncertainty maps estimating only $a, e, \omega$ and $u_0$ with a geocentric observer.

Figure 4.4 shows the correlation maps obtained for the above mentioned scenario. The correlation index is calculated as shown in Eq. 2.17 and it tells us how strong any two parameters are correlated. In particular if $|\gamma_{ij}| \approx 1$ the two parameters ($i$ and $j$) are strongly correlated this means that any modification of one parameter will influence the other.
From Figure 4.4 is evident how the estimated parameters are strongly correlated. Some exceptions are present in these maps and coincide with the areas where the single parameters have their minimum uncertainty. For example if we look at the correlation between $a$ and $e$ or $a$ and $\omega$ the low correlation area are coincident with the period-line. This result is clearly understandable because if we observe an object twice in the same position with an interval between tracklets of one period, the semi-major axis is well defined. Other areas with low correlation values are occurring in the graph $a$ vs $e$ when the first tracklet is on the perigee and the second on the apogee, while for the map $a$ vs $\omega$ low correlations are occurring for tracklets symmetric to the line of the nodes. It is also important to highlight that the maps in Figure 4.4 show the maximum correlation value in the $S$-area with the only exception given by the points where each parameter has its own uncertainty minimum.

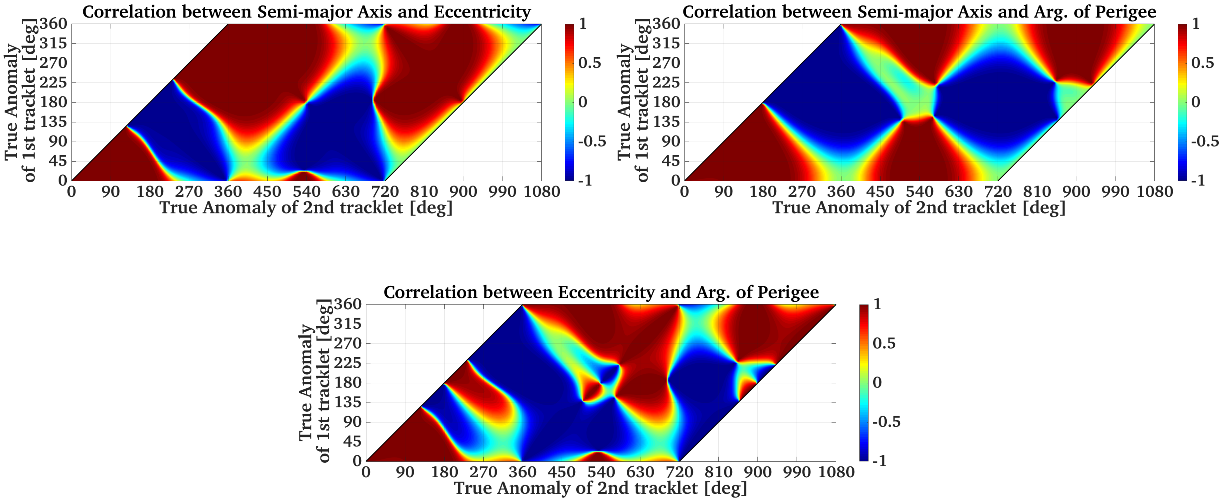

Figure 4.4 Correlation maps estimating only $a, e, \omega$ and $u_0$ with a geocentric observer.

The last part of the results is made by the condition number map of the correlation coefficients matrix shown in Figure 4.5. Each point of this map correspond to the condition number of the correlation coefficients matrix obtained for the couple of tracklets used in the LSQ. In Figure 4.5 it is possible to see a certain consistency between the high uncertainty areas shown in Figure 4.3 and the areas where the condition number is relatively high. The highest condition numbers are visible as expected for very short observation arcs and in the $S$-region. It is also interesting to notice how the condition number shows a relatively higher values for tracklets which are separated by one orbital period. Along the period-line it is easy to see that there are three interruptions of the higher values occurring when the tracklets are in the perigee and when the true anomaly is, in this case, $\nu_{1/2} = 140$ and $\nu_{1/2} = 220$ deg. Regarding the other two low condition number interruptions of the period-line these are due to the fact that we are resolving the LSQ with a subset of parameters. On the other hand, a very high condition number is visible for tracklets at the apogee: this is probably due to the arc covered by the tracklet that in this position is the shortest. In fact, it is possible to see how the condition number is decreasing going toward tracklets whose position is closer to the perigee.

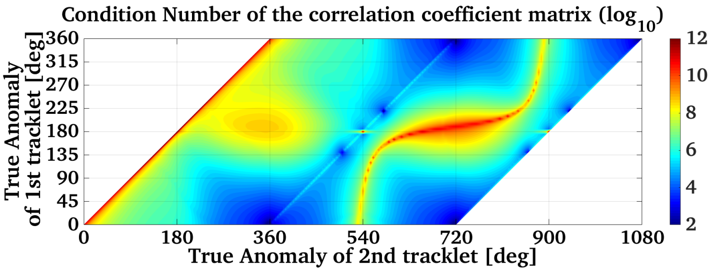

Figure 4.5 Condition number map of the correlation coefficients matrix estimating only $a, e, \omega$ and $u_0$ with a geocentric observer.

## 4.5 The S-Region

In Figure 4.3 it is possible to see an $S$-shaped area of high uncertainty values very sharp for the semi-major axis, the eccentricity and the argument of perigee. As anticipated in the previous paragraph this area is occurring when the distance in time between the tracklets is half of an orbital period. Looking now at Figure 4.4 it is evident that in the $S$-area the observations are distributed in a way that it is difficult to estimate correctly these three parameters, so in order to understand the cause of this $S$-shaped high-uncertainty area a simulation was performed fixing the argument of perigee in the first design matrix $A$. The results of this simulation are shown in Figure 4.6.

It is important to note that these results are not relevant for this study but at least they are helpful to find a possible explanation for the $S$-area. Looking at these results it is easy to see that from the $S$-region only two points are remaining, which coincide with the case where the position of the two tracklets is symmetric w.r.t. the line of the apsides with half a period distance. We think that the uncertainty on $a$ and $e$ is related to $\Delta t/\Delta\theta$ and this ratio is maximum for these particular points. We take a limit to $\Delta t = T/2$ because each symmetric positions w.r.t. the line of the apsides with $\Delta t > T/2$ is geometrically equivalent to the same positions after applying the $mod(\Delta t, T)$, where $T$ is the orbital period.

As seen before, if one estimates $a, e, \omega, u_0$ without fixing $\omega$, the above mentioned points disappear and instead of them we have the $S$-line containing all positions which are distant half a period in time. This is due to the fact that by varying $a, e$ and $\omega$ we can relate the generic situation of half a period distance between tracklets to the case of tracklets symmetric to the line of the apsides, just mentioned above.

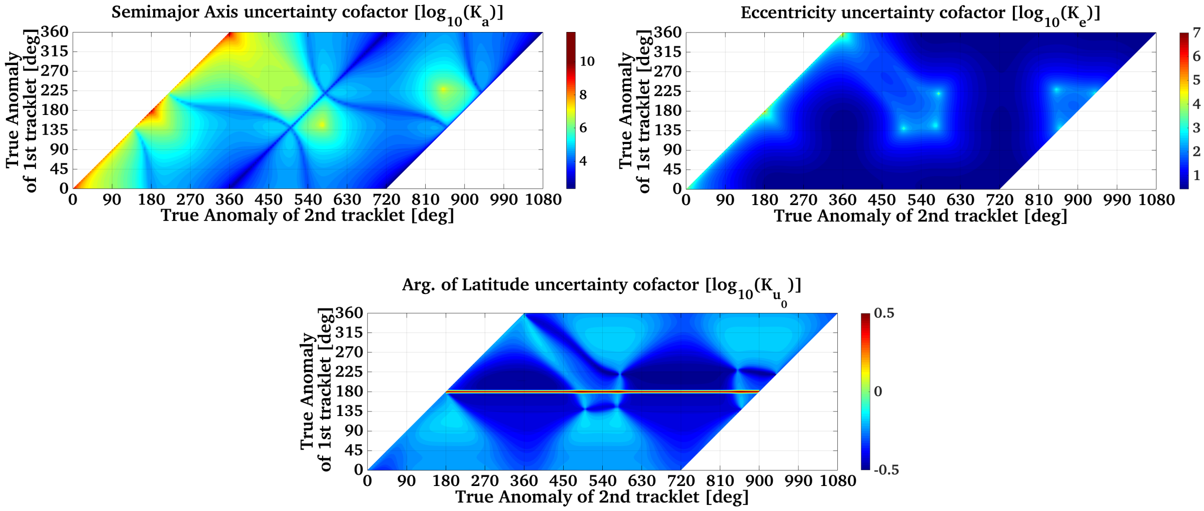

Figure 4.6 Uncertainty maps estimating only $a, e, \omega$ and $u_0$ with a geocentric observer but fixing $\omega$.

## 4.6 Influence of Time Interval

As expected from the analysis of the partial derivatives and then confirmed by previous results, the time interval between the tracklets has a big influence on the uncertainties of the estimated parameters. This effect can be highlighted comparing the results in Figure 4.3 with those in Figure 4.7, which are obtained with a distance in time between tracklets contained within 49 and 50 orbital revolutions.

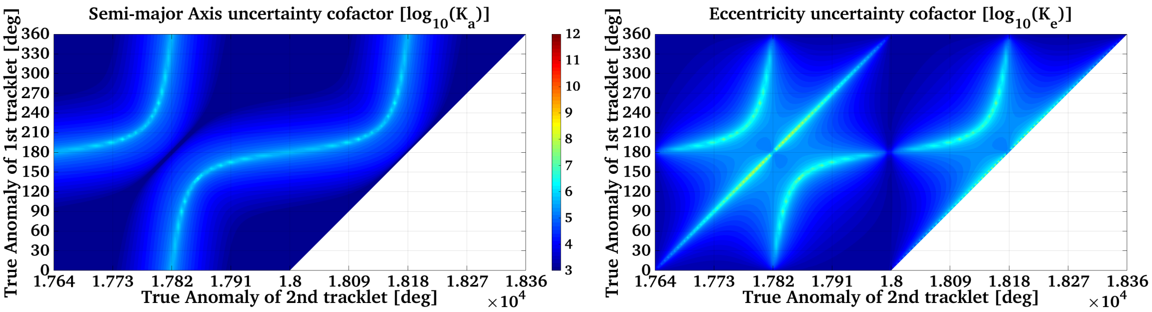

Figure 4.7 Uncertainty maps for $a$ and $e$ estimating only $a, e, \omega$ and $u_0$ with a geocentric observer with a maximum distance between tracklets of 50 orbital periods.

From this comparison it easy to see three main effects of the time distance between tracklets. The $S$-shaped high uncertainty for $a$, $e$ and $\omega$ is clearly visible from the 2nd period on. This does not mean that it is appearing only after one orbital revolution, but it is also present within the 1st period; the only difference is that in this case, this feature is hidden under higher uncertainty values. Secondly, the average values of the uncertainties tend to decrease while the time interval between tracklets increases (especially for the semi-major axis). Thirdly, the $S$-shaped high uncertainty is now precisely passing on the area where the tracklets are separated in time by half of an orbital period.

In Figure 4.8 it is possible to see how, especially for $a$, the average uncertainties are diminishing with time. It is also clear how the half-period feature is hidden within high uncertainty values when the time interval between tracklets is less than one orbital revolution. A possible explanation for these phenomena is in the behavior of the partial derivatives. In fact, as seen before, the partial derivatives of position w.r.t. the semi-major axis contains a direct dependency from the time, in particular $\partial \vec{\mathbf{r}}_{\mathbf{s}} / \partial a \propto (t - T_{osc})$, while the other derivatives are periodic over the orbital period. Despite the fact that the time is increasing linearly, we think that these effects are due to the order of magnitude of the time difference between the tracklets, which is growing from 0 sec up to $10^4$ sec within the 1st orbital period, then from $10^4$ sec to $10^5$ sec in the 2nd, and it will reach $10^6$ sec only after the 11th revolution.

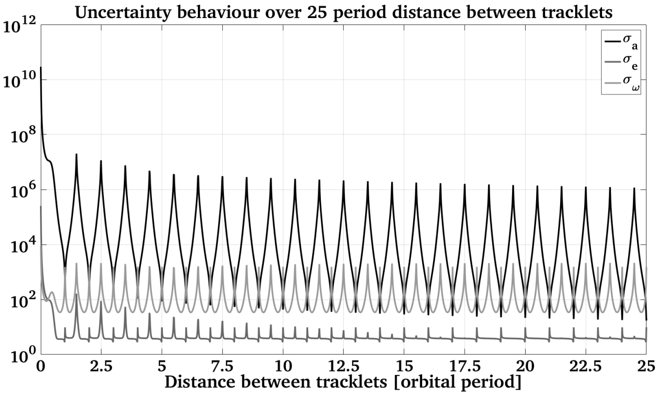

Figure 4.8 Behavior of the uncertainty of $a, e$ and $\omega$ obtained with the 1st tracklet on the perigee with a varying time interval of the 2nd up to 25 orbital revolutions.

## 4.7 Estimation of the Entire Set of Parameters

Once we understood the main features characterizing $a, e, \omega$ and $u_0$, the simulation was repeated including in the estimation process also the parameters which describe the orientation of the orbital plane in the space ($i$ and $\Omega$). Figure 4.9 shows the uncertainty maps obtained for the same orbit analyzed before ($a = 42164.173$ km, $e = 0.6$, $i = 30°$, $\Omega = 40°$, $\omega = 60°$ and $T_{osc} =$ 1st observation) with a geocentric observer.

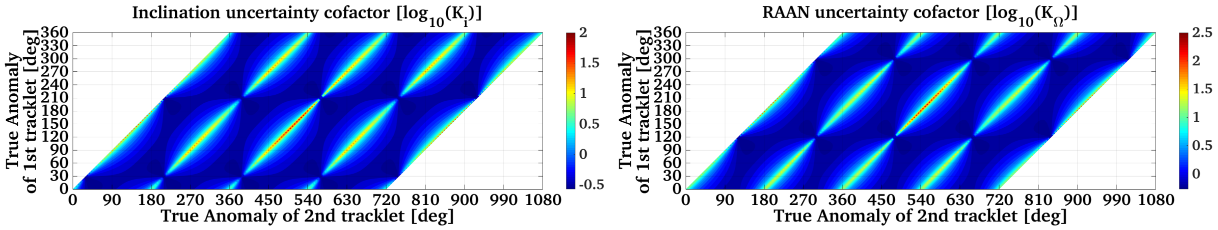

Figure 4.9 Uncertainty maps for $i$ and $\Omega$ estimating all 6 parameters with a geocentric observer.

The uncertainty maps of $i$ and $\Omega$ are characterized only by one main feature of high uncertainty values which includes all the positions with a difference in time of one (or more) orbital period(s) and which are separated by 180° in true anomaly. These high uncertainty areas can be explained considering the fact that the orientation of the orbital plane in the space is described by the direction of the angular momentum. At the same time this direction is also defined by the cross product of the directions of two position vectors. The cross product is undefined if the unit vectors involved are parallel or aligned which is precisely the case described just before. Each of these features presents two interruptions. To explain them it is necessary to have a look at the orbital parameters, in particular $\omega$, which in this case is equal to 60°. The line of the nodes intersects the orbit when the true anomaly is equal to 120° and 300°. Being the observer always within the orbital plane, the information regarding $\Omega$ is maximized if both observations are performed on the line of the nodes. The information about the inclination is maximized if the observations are performed at 90° of distance from the line of the nodes, in this case when $\nu$ of the 1st tracklet is equal to 30° and for the second tracklet $\nu = 210°$, or vice versa.

## 4.8 Topocentric Observer

Until now, the results shown were obtained using an unreal observer located at the center of the Earth. In the next section, the influence of a real observer on the Earth's surface is analyzed. Figure 4.10 shows the scenarios used to identify the contributions given by a topocentric observer. Two "standard" orbits are used to carry out this study and the results obtained using different observers displaced in longitude or in latitude are compared. The used orbits have the following orbital elements: $a = 42164.173$ km, $e = 0.6$, $i = 1°$ or 60°, $\Omega = 0°$, $\omega = 0°$ and $T_{osc}$ coincides with the time of 1st observation. As for the case of the geocentric observer, the simulations are performed analyzing all possible combinations between tracklets positions separated by 2.5° in true anomaly. The only difference is the observer position. In particular, the initial position of the observer is kept constant for the different 1st tracklet positions while for the second tracklet, the position of the observer is rotated accordingly with the time interval between tracklets and the Earth's angular velocity. The initial positions chosen for these simulations are shown in Table 4.1. It is important to note that being a geometrical study the real orientation of the Earth in the space is neglected. To better understand the results we set up the orbits so that their line of nodes/apsides are coincident with the $x$-axis of the generic inertial system and the Greenwich meridian is also aligned with the same axis at time $t = 0$.

| | **Longitude [deg]** | **Latitude [deg]** | **Geodetic altitude [m]** |
|---|---|---|---|
| Reference Observer | 0 | 0 | 0 |
| Longitude-displaced observer | 60 | 0 | 0 |
| Latitude-displaced observer | 0 | 50 | 0 |

Table 4.1 Observer's geodetic coordinates.

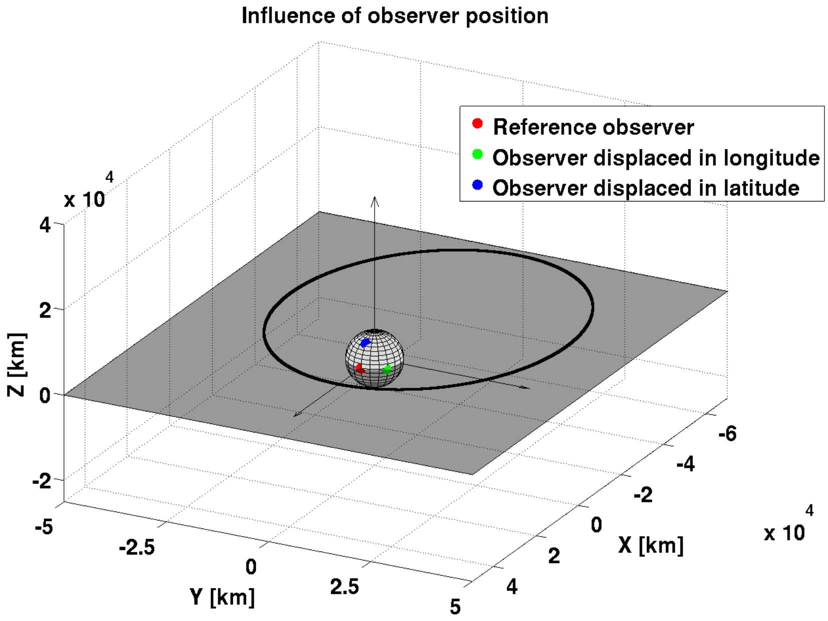

(a) Different observer positions with an equatorial orbit

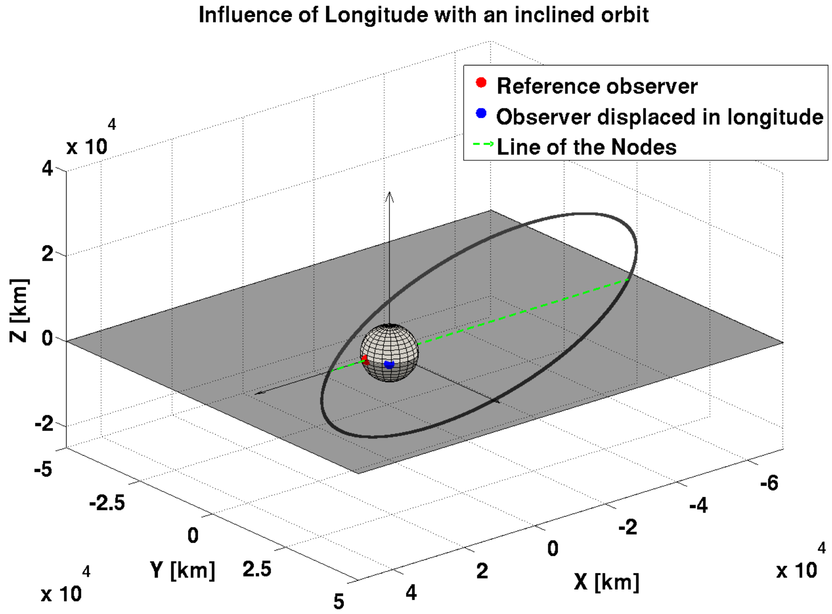

(b) Different observer positions with an inclined orbit

Figure 4.10 Scenarios used to evaluate the influence of a real observer.

### 4.8.1 Longitude Displacement of the Observer

In the first attempt, to isolate the contribution given only by the position of the observer, the simulations are performed using an almost equatorial orbit. To avoid the singularity of the used parametrization an inclination of 1° is used. In fact for $i = 0°$, $\Omega$ it is not defined anymore therefore also $\omega$ become undefined with this convention. The results obtained with a longitude displacement of the observer with an equatorial orbit are analyzed and no significant effects can be seen.

A “more” complicated scenario with $i = 60°$ is used to evaluate the effects of a longitude-displaced observer. The simulations are then repeated using the scenario described in Figure 4.10b, where the “Reference” observer, at the time of 1st tracklet, is within the orbital plane precisely on the line of the nodes, which in this case coincides also with the line of the apsides. Being a geosynchronous orbit, the observer will be again within the orbital plane every half of a revolution. For the observer displaced in longitude the 1st tracklet is acquired always outside of the orbital plane. The observer will be in the orbital plane only if the distance in time between the tracklets is equal to $1/3$ or $5/6$ of the orbital period. Figure 4.11 shows the results of this simulation and shows the comparison between only two parameters $a$ and $i$. Comparing the latter results with those obtained in the case of an equatorial orbit we can already conclude that the relative position of the observer w.r.t. the orbital plane has a huge influence on the results. In particular it is important to distinguish if the observer is always, systematically, or just “occasionally” within the orbital plane. Figure 4.11 shows the comparison between results obtained with an observer systematically inside the orbital plane w.r.t. that obtained by an observer just occasionally inside.

The Figures 4.11a and 4.11b show some common features like: the minimum uncertainty area on the period-line for $a$, the $S$-area with high uncertainties, the high uncertainties for tracklets whose angular distance is 180° for $i$. Focusing now on the uncertainty maps for $a$, it is possible to see few differences and one new feature. The main difference is in the uncertainty values in the $S$-area which are smaller if the observer is just occasionally within the orbital plane. The new feature that is not so sharp in this case, but will be more evident in the next paragraph, consists in a minimum value line for $a$ in the case where the tracklets have an angular distance of 180°. These two effects are due to the fact that observing from outside the orbital plane one is able to estimate the distance from the object.

Comparing the two inclination maps, it is easy to see that they are pretty different. In particular the one in Figure 4.11a shows two horizontal lines with low uncertainty values and an $S$-shaped low uncertainty area. The reason for this is that the two horizontal lines are occurring precisely when the true anomaly of the 1st tracklet is 90° or 270°; remembering that $\omega = 0°$ these two are the points of the orbit with the maximum angular distance from the line of the nodes. In the figure only the horizontal lines are present because they are relative to the 1st tracklet which is always acquired with the observer within the orbital plane; while if the 2nd tracklet is in the same positions the observer is outside the plane reducing the strength of this information. Regarding the $S$-area, it contains all the observations performed by the observer within the orbital plane.

Looking now at the inclination map of Figure 4.11b, the just mentioned features are not present anymore but only some minimum point-like areas can be observed. These areas are given by a compromise between distance of the observation from the line of the nodes and position of the observer w.r.t. the orbital plane. These higher average uncertainty values in this figure also mean that to determine $i$ and $\Omega$ it is better to have an observer within the orbital plane. It was decided not to show the maps for $e, \omega$ and $\Omega$ because we can extract the same conclusions just reported for $a$ and $i$.

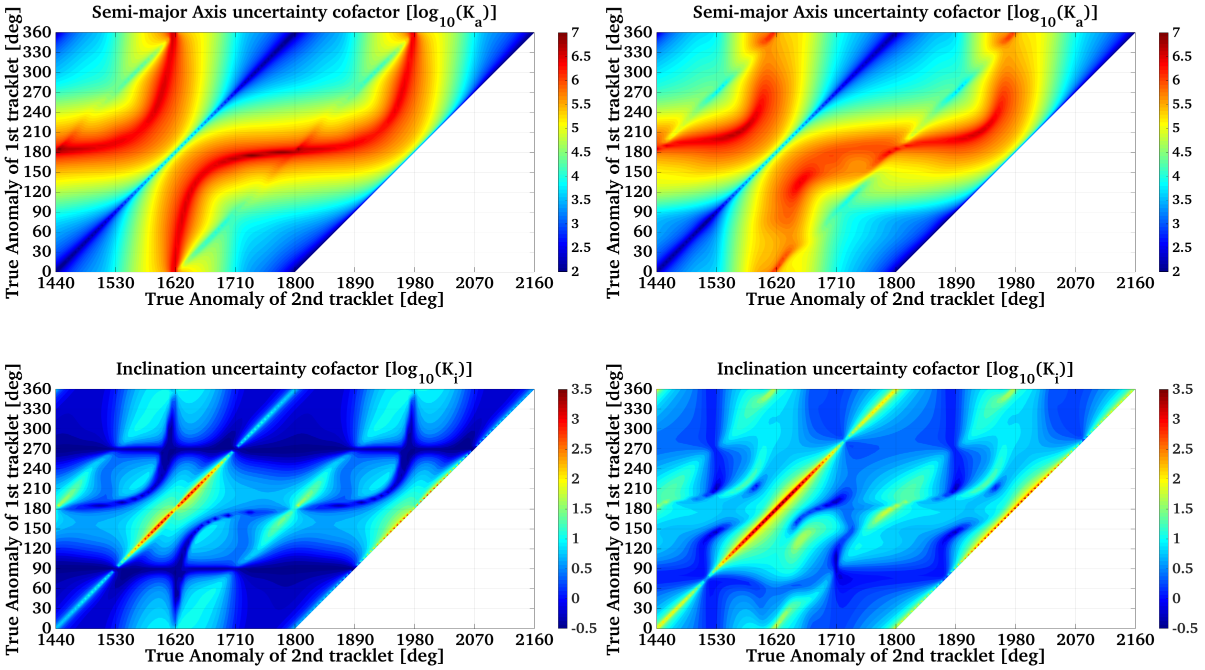

(a) Observer regularly within the orbital plane (b) Observer occasionally within the orbital plane

Figure 4.11 Comparison between uncertainty maps obtained for an inclined orbit with longitude-displaced observer.

### 4.8.2 Latitude Displacement of the Observer

To confirm the importance of the position of the observer w.r.t. the orbital plane, the case where the observer is always inside the orbital plane is compared with the case where it is always outside. The geosynchronous equatorial orbit is again used with an equatorial observer and the results are compared with those obtained with the same orbit but the observer was displaced by 50° in latitude (see Figure 4.10a). Figure 4.12 shows the uncertainty maps for $a, i$ and $\omega$ obtained with the equatorial observer and the ones obtained with a latitude-displaced observer (respectively in Figures 4.12a and 4.12b). In the uncertainty maps for $a$ it is clearly visible how the intensity of the $S$-area is strongly reduced by an observer outside the orbital plane. On the map of $e$ the same effect is noticeable. As for the previous paragraph, a diagonal line with low uncertainty values is appearing when the $\nu_2 - \nu_1 = 180°$; this effect can be explained by the fact that an orbit is a section of a cone. If one is observing the orbit from the apex of the cone (or from a circular section of the cone) and one is able to estimate the distances, exploiting the information within the tracklets, it is easier to determine the semi-major axis and the eccentricity. Comparing now the maps for the inclination we can see how the main features are kept. There is only a small reduction of the diagonal line with tracklets separated by 180°. The most important difference is that the average uncertainty values in the Figure 4.12b remarkably increased. This is well understandable because the inclination can be described measuring the distance of the object from the equatorial plane. Having a relatively small distance, given by 1° of inclination, this can be better measured if the observer is inside the orbital plane.

One interesting result is the difference between the maps for the argument of perigee. In the case shown in Figure 4.12a the classical $S$-shaped area is present, it is then important to notice that also a high uncertainty diagonal line is present for tracklets with angular distance of 180°. This feature is characteristic of $\Omega$ but is present also on $\omega$ because of the small inclination value. For $i \to 0$ it is difficult to define the line of the nodes and being the argument of perigee defined w.r.t. this line all the uncertainties of $\Omega$ are transferred also to $\omega$. The most interesting feature for the map of $\omega$ in Figure 4.12b is given by the fact that the $S$-area contains minimum uncertainty values. This can be explained by the fact that looking from outside the orbital plane we have an improvement given by the capabilities to estimate the distances. This is followed by an improvement also for the eccentricity estimation, and being able to estimate these two quantities, one is also able to decorrelate them from $\omega$. This effect can be seen looking at the relative correlation maps. Finally the increase of the average uncertainty values can be explained by the fact that looking from outside the orbital plane it is more difficult to determine precisely the distance between observations within a tracklet.

In conclusion, is it better to observe within or outside the orbital plane? There is not a unique answer to this question as we have just seen: the observer inside the orbital plane is gaining more information about the orientation of the orbital plane in the space, amplifying the effect given by the distance of the observations from the line of the nodes and reducing the average uncertainty values. Vice versa, observing from outside the orbital plane gives us information about distances that reduce the average error on $a$, strongly reduce the $S$-area for $a, e$ and $\omega$, and helps us decorrelate $\omega$ from $a$ and $e$.

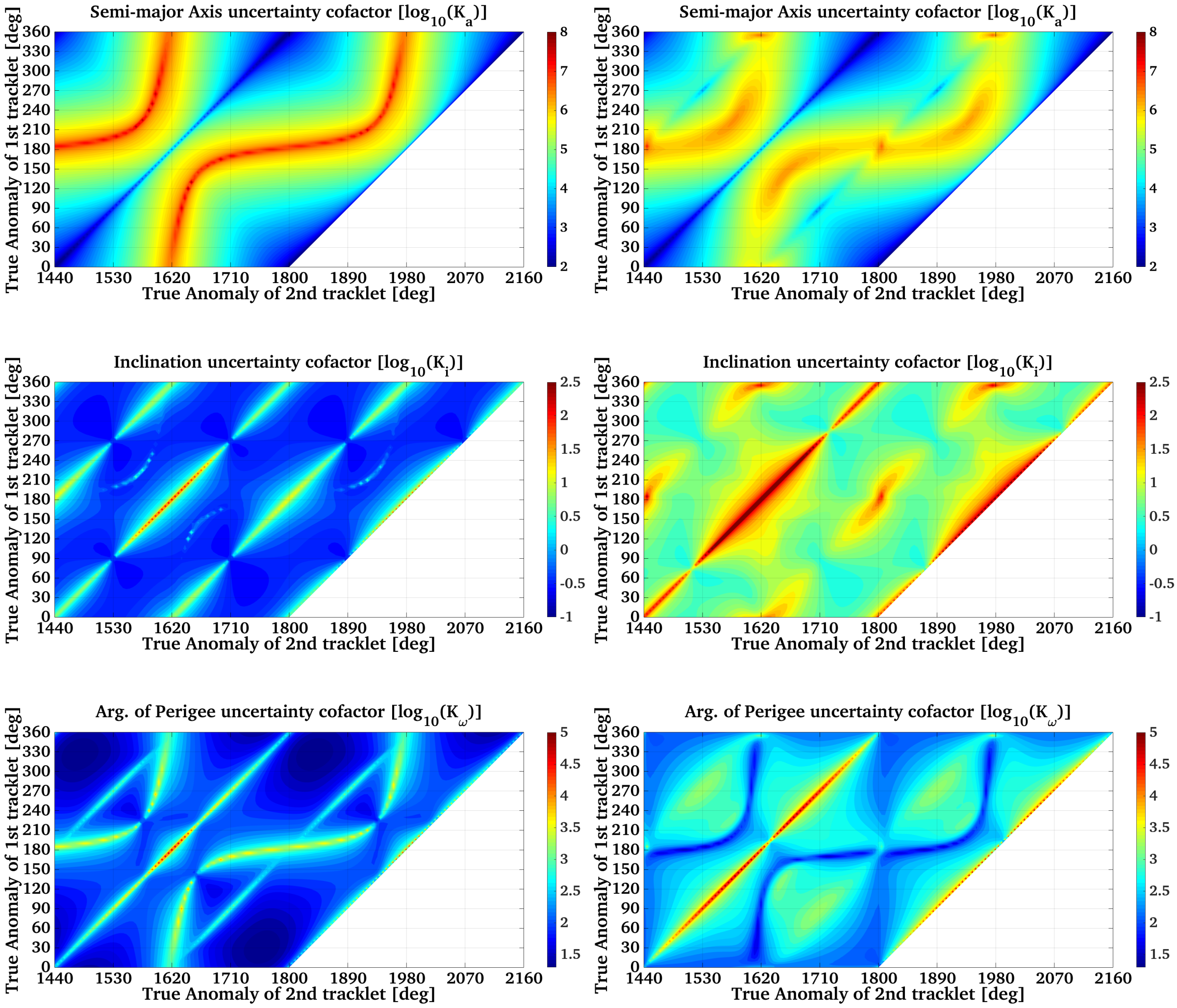

(a) Equatorial observer

(b) Latitude-displaced observer

Figure 4.12 Comparisons between uncertainty maps obtained for an equatorial orbit with an equatorial and a latitude-displaced observer.

## 4.9 Influence of Orbital Parameters

Once the main features in the results were studied, the analysis was repeated varying the orbital parameter of the reference orbit in order to understand their influences.

First, the influence of $u_0$ was studied: modifying $u_0$ is equivalent to change the osculating time $T_{osc}$, this means to solve the orbit determination problem for positions of the object along the orbit. This analysis showed that this parameter is affecting only the map of the argument of latitude while is not influencing at all the other geometric parameters.

The argument of perigee $\omega$ describes the orientation of the orbit within the orbital plane. Changing it, means to change the intersection points of the orbit with the equatorial plane producing only a translation of the minimum horizontal lines seen in Figure 4.9.

Repeating the simulations changing the position of the line of the nodes in the space (modifying $\Omega$) produces the same effect of a longitude displacement of the observer changing his relative position w.r.t. the orbital plane. In particular the observer will be inside or outside the orbital plane for different time distances between the tracklets reducing the strength of the $S$-area for $a$ and $e$ if the observer will be more outside the orbital plane and influencing the low uncertainty area for $i$ and $\Omega$.

One of the most interesting parameter is the inclination $i$, as anticipated before, the main effects are given when $i$ tends to 0. If $i = 0$, $\Omega$ is not defined. The main effects of this singularity is visible in the map of $\omega$ in Figure 4.12a. This because $\omega$ is defined w.r.t. the line of the nodes and then, it will show some characteristic features of $\Omega$. Additionally the closer $i$ is to 0 the fainter will be the characteristic $S$-area of $\omega$. Finally being $u_0 = \omega + \nu_0$, the main features of $\Omega$ are consequently transferred also to the argument of latitude. This phenomenon is also confirmed by the different correlation maps among $\Omega$, $\omega$ and $u_0$ which, in this case, do not show any feature and are constant at the maximum correlation value over all possible combinations of tracklets positions.

The eccentricity is the main responsible for the $S$-area, in particular if $e$ grows the $S$ tends to have the shape of two hyperbolas, while if $e$ decreases towards 0 (for circular orbit) the $S$ becomes a diagonal line for tracklets whose angular distance is 180° in true anomaly.

The last important effects are given by the variations of the semi-major axis which are related to the changing of the "Earth's parallax" angle, the length of the arc covered by the tracklet and the ratio between the Earth's rotation period and the orbital period. We define "Earth's parallax" as the angle $\theta = 2\arctan(R/r)$ where $R$ is the Earth's radius and $r$ is the geocentric distance of the object. This angle tells us how much the observation geometry can change due to the motion of the observer in the space. Increasing the semi-major axis means augmenting the distance of the object from the observer. This produces a general rise of the average uncertainty values especially for $a$ and $e$ since the beneficial effects of the Earth parallax and of the information within the tracklet are strongly reduced. In particular, if the object is enough distant from the Earth the effect given by the Earth's parallax and the fact that the observer is inside or outside the orbital plane is strongly reduced and the features of the maps become similar to those obtained for a geocentric observer which is always inside the orbital plane. Furthermore keeping constant the time interval between the observations within a tracklet during all simulations leads to a decrease of the arc covered by the tracklet if the semi-major axis increases, and produces a loss of information for $a$, $e$ and $\omega$. The main consequence of a shorter arc is an increase of the average uncertainty values especially for the just mentioned parameters. The ratio between the orbital period and the Earth's rotation is important because it will determine when an observer is within or outside the orbital plane. As seen before this is important for the high uncertainty $S$-shaped area.

## 4.10 Effect of the Rotation of the Earth

Another aspect that should be taken into account during the maps analysis is the rotation period of the Earth. In particular the ratio between the orbital period and the Earth rotation is important because it will determine when an observer is within or outside the orbital plane. Figure 4.13 shows the results obtained for the uncertainty maps of $a$ for two orbits which have the same values of $e, i, \Omega, \omega$ and $u_0$, but different $a$ values: $a = 20270.404$ km and $a = 42164.173$ km. These two values of $a$ were chosen in order to have, in the first case, three complete revolution of the satellite and, in the second case, one within the Earth's rotation period. This choice allowed us to have an observer within the orbital plane respectively every 1.5 and 0.5 orbital periods. This experiment confirms the fact that the $S$-area is characteristic of observations performed within the orbital plane. As shown in Figure 4.13a, the $S$ appears only when the distance between tracklets is 1.5 or 4.5 orbit revolutions.

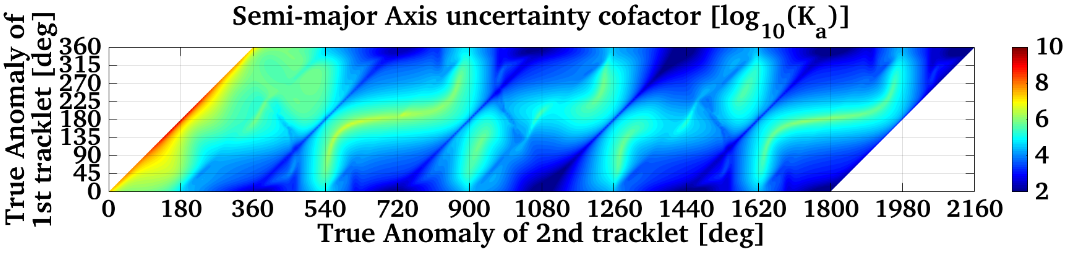

(a) $a = 20270.404$ km, 3 rev/day

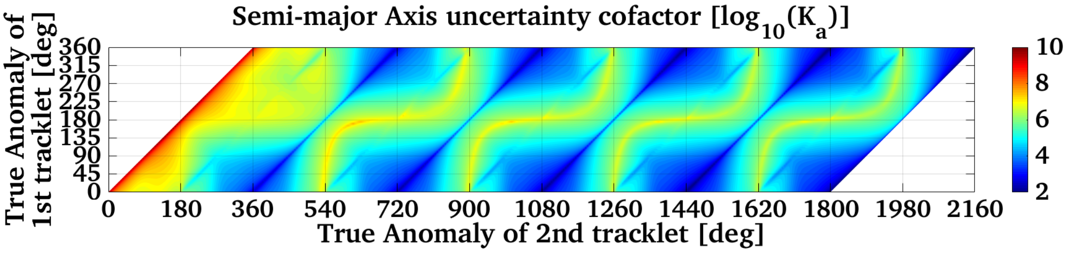

(b) $a = 42164.173$ km, 1 rev/day

Figure 4.13 Influence of Earth's rotation for the semi-major axis uncertainty map.

## 4.11 Application to Real Cases

Until now only a theoretical study was performed to highlight the influence of each single parameter on the accuracy of an orbit determination/improvement process. The main features are now known and the effect of the observer position is also known. The next natural step is to apply this method to a real scenario characterized by a real orbit with a real observer. For simplicity the simulations are carried out using a generic inertial system of reference. In this section we will show the results obtained for those orbital regions largely populated by satellites and then by space debris: the Low Earth Orbit regime (LEO), the Medium Earth Orbits (MEO), with the Molniya and the Geostationary Transfer Orbit (GTO) cases, and finally the Geostationary Earth Orbit (GEO) region.

### 4.11.1 LEO

To study the LEO case, we used the following orbital parameters: $a = 7707.627$ km, $e = 0.0008776$, $i = 66.125°$, $\Omega = 10.011°$, $\omega = 247.14°$ and $T_{osc} =$ 1st observation. The geodetic coordinates of the observing site are those of the Zimmerwald observatory namely: 46.8772° North, 7.4652° East and 951.2 m. Since the orbital period is only 112.238 minutes, for reasons of space, to display the uncertainty maps we needed to split them in two parts. The splitting was necessary to show the results obtained over an entire Earth's rotation period. The Figures 4.14 and 4.15 show respectively the obtained uncertainty maps for a time interval between the two tracklets from 10 seconds to 6.5 orbital revolution and from 6.5 to 13 orbital revolutions.

Comparing the Figures 4.14 and 4.15 it is interesting to notice that all the uncertainty maps show a trend of the general values of the uncertainties: from an average low value (exception made for the first orbital revolution), first they are increasing to have their maximum between the 6th and the 7th revolution to then decrease again. This trend of the average uncertainty values is due to the relative geometry between object and the observer, and in particular to the distance between the observer and the object. The only element in which this behavior is a bit dimmed is the semi-major axis because its uncertainty, as we have seen previously in Paragraph 4.6, decreases when the time interval between the measurements increases.

Since the orbit has a relatively low altitude we have fast changes in the observation geometry which lead to a more difficult interpretation of the maps. Starting from the figures describing the orientation of the orbital plane, respectively Figures 4.14c and 4.15c for the inclination and Figures 4.14d and 4.15d for RAAN, we can see how the low uncertainty areas for tracklets which are at the maximum and at the minimum distance from the line of the nodes (respectively for $i$ and $\Omega$) are still present, as well as the high uncertainty areas for tracklets separated by 180° and 360° in true anomaly. On the other hand, it is interesting to notice the appearance of low uncertainty areas for $i$ when the second tracklet is close to the apogee in Figure 4.14 and when it is close to the perigee in Figure 4.15. First of all, considering the position of the perigee, the just mentioned tracklet positions coincide with the farthest points w.r.t. the equatorial plane; while the change from apogee to perigee between the Figure 4.14c and 4.15c is probably due to the relative position of the observer w.r.t. to the orbit and the distance of the object from the observer. By looking at the geometry of the problem and at Figure 4.16c it is possible to see how the apogee of the orbit is closer to the observer position for tracklets whose separation in time is less than 12 hours (roughly 6.5 orbital revolutions which results are shown in Figure 4.14), vice versa the perigee is closer to the observer position for tracklets whose separation is bigger than 12 hours (results shown in Figure 4.15). At the same time, comparing the minimum distance between observer-apogee and observer-perigee, it is clear that the first is the shortest. The effect of this distance is also reflected in the maps: the uncertainty obtained when the 2nd tracklet is at the apogee, in Figure 4.14c, is lower than that obtained at the perigee in Figure 4.15c. For the RAAN, this phenomenon is less evident since the distance of the observer from the line of the nodes is more constant during the simulation interval.

Looking now at the maps of the semi-major axis (Figures 4.14a and 4.15a), of the eccentricity (Figures 4.14b and 4.15b) and of the argument of perigee (Figures 4.14e and 4.15e) we can see how the $S$-area is less defined and, due to the low eccentricity value of the orbit, is almost diagonal. Also for these maps, an interesting region is the horizontal low uncertainty values area which is occurring when the first tracklet is between 135° and 180° of true anomaly for $a$ and $e$, and between 90°and 135° of true anomaly for $\omega$. This position coincides with the closest distance between the object and the observer. Since the arc length of the tracklet is constant if measured from the geocenter, the length of the arc seen from the observer varies with the distance of the observer from the target. In particular, the closer the object the wider is the topocentric angle under which the object is observed. Since we use the topocentric RA and DE as measurement, the variations of their partial derivatives is bigger when the object-observer distance is shorter. This probably produces a gain of information useful to estimate $a$ and $e$. Due to the time dependency of the derivatives w.r.t. $a$, this improvement becomes more evident, in the map of the semi-major axis (Figures 4.14a and 4.15a), with the increase of the time interval between the tracklets and it is even more evident for observations separated by one or more orbital periods.

Looking now at the eccentricity maps (Figures 4.14b and 4.15b), we see a more constant horizontal low uncertainty area and in addition a vertical low uncertainty area is visible when the second tracklet is close to the apogee. The uncertainty values of the vertical lines are increasing with the object-observer distance.

Concluding with the analysis of the map of $\omega$ (Figures 4.14e and 4.15e), we can see how these maps have two main low-uncertainty areas. The first is due to the object-observer distance. In fact, the shorter the distance the wider is the arc seen from the observer and it is almost coincident with the low-uncertainty area seen for $e$ and $a$. The second are the classical low-uncertainty points which interrupt the high-uncertainty features visible in all maps related to $\omega$. These occur when the first and the second tracklet have the following positions in true anomaly: $\nu = 85°$ and $\nu = 265°$. As we know, these positions are determined by the eccentricity of the orbit and one couple of them corresponds to tracklets which are symmetric to the line of the apsides and separated by half of an orbital period. The second couple is obtained when the two tracklets are in one or the other position but separated by an integer number of orbital revolution. The last remark that we can do on these particular areas is regarding their values which are influenced, as all the other maps, by the object-observer distance. This phenomenon is much more evident for low-altitude orbits than for high-altitude ones since the relative change of this distance is smaller.

The behavior of the object-observer distance is shown in Figure 4.16. In particular, the Figure 4.16a we see the behavior of the distance for the first tracklet where it is interesting to see the minimum distance which is occurring when the true anomaly of the tracklet is between 135° and 180°. The Figure 4.16b shows the obtained map of the distances for the second tracklet as a function of the position of the first one. It is interesting to notice that in the first part of the graph the minimum distance is when the second tracklet is at the apogee while in the second part, due to the rotation of the Earth, the differences between maximum and minimum distance are smaller. This phenomenon leads to the appearance of a second low-uncertainty vertical line in Figure 4.15b when the second tracklet is at the perigee. It must be said that the values in this second line are higher than those visible when the second tracklet is at the apogee. Finally, Figure 4.16c shows the sum of the distances obtained for the two tracklets. Observing this last figure, it is easy to notice the correspondence between the minimum distance areas and the lowest-uncertainty spots, visible especially for the semi-major axis and the argument of perigee. At the same time the just mentioned correspondence is reflected also in the eccentricity and in the argument of latitude maps.

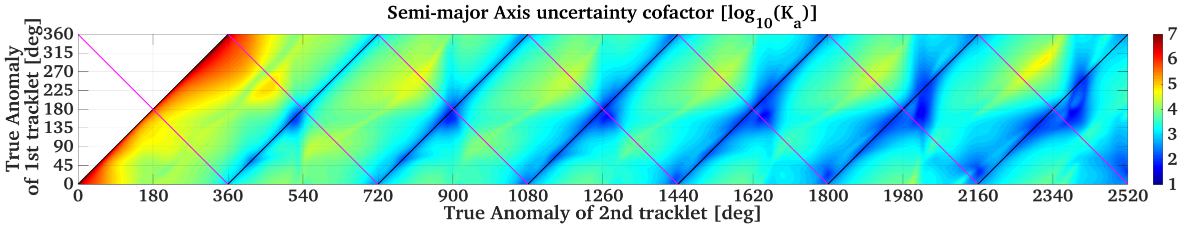

(a) Semi-major axis

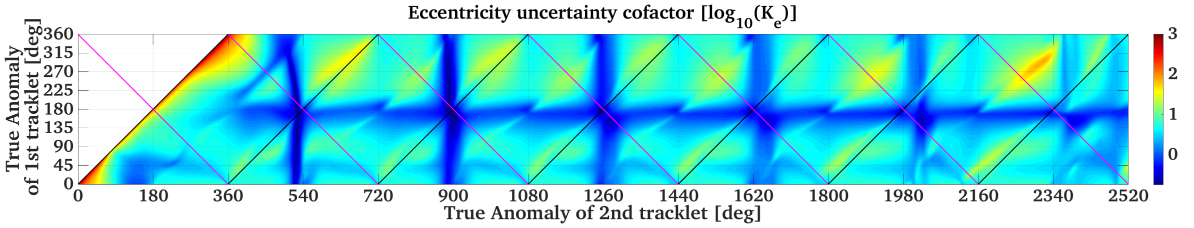

(b) Eccentricity

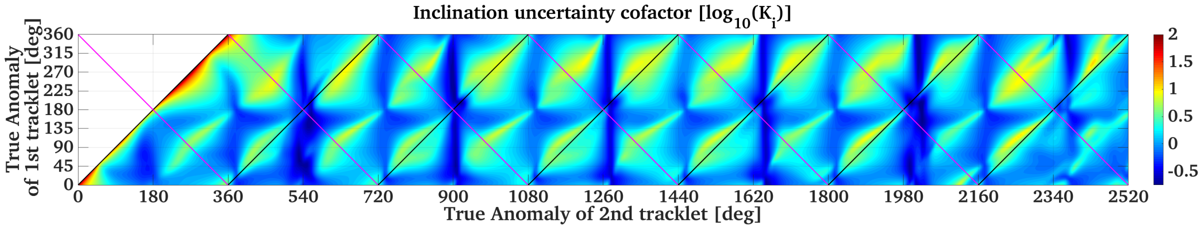

(c) Inclination

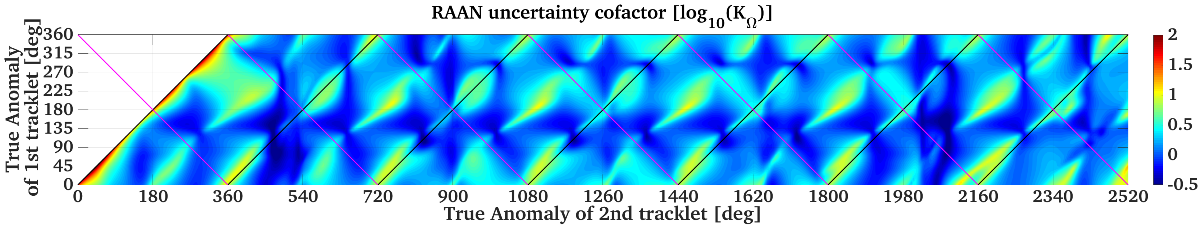

(d) Right Ascension of Ascending Node

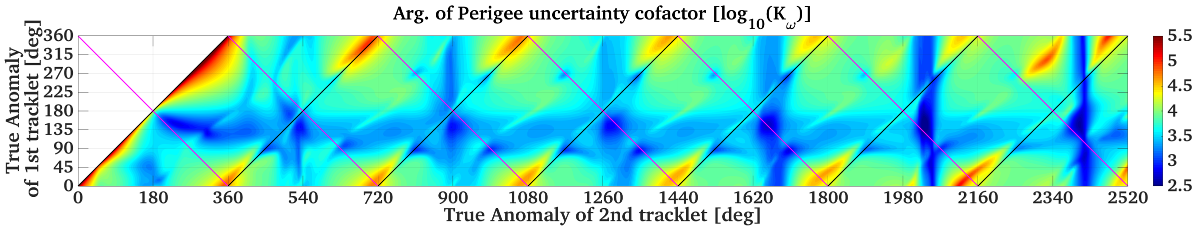

(e) Argument of Perigee

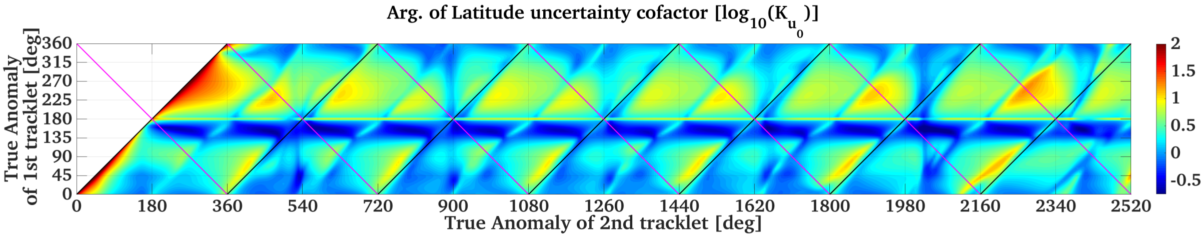

(f) Argument of Latitude

Figure 4.14 First part of the Uncertainty maps for LEO orbit observed from Zimmerwald.

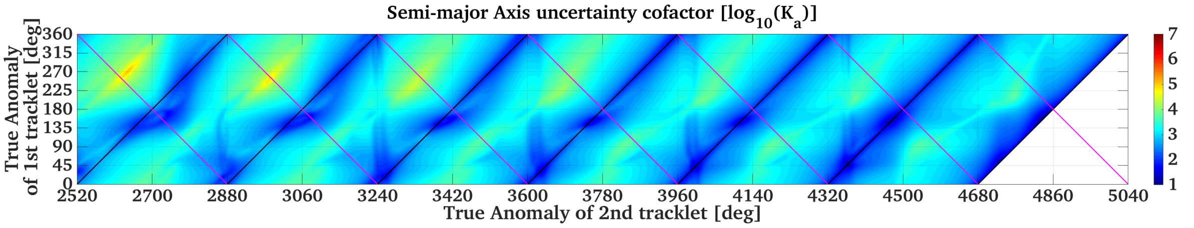

(a) Semi-major axis

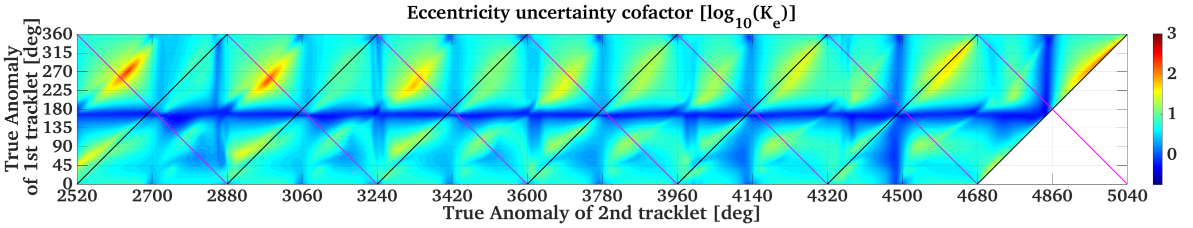

(b) Eccentricity

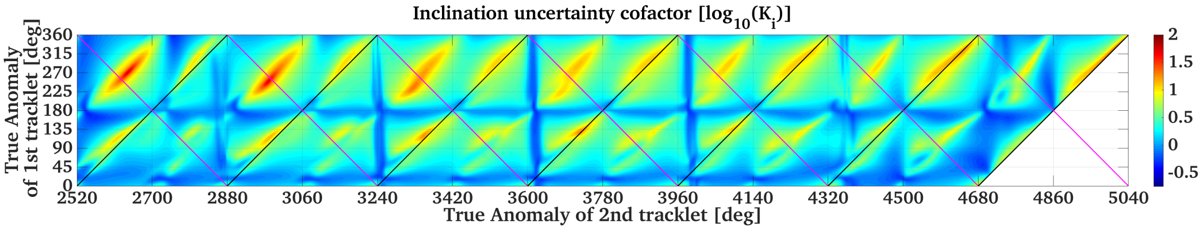

(c) Inclination

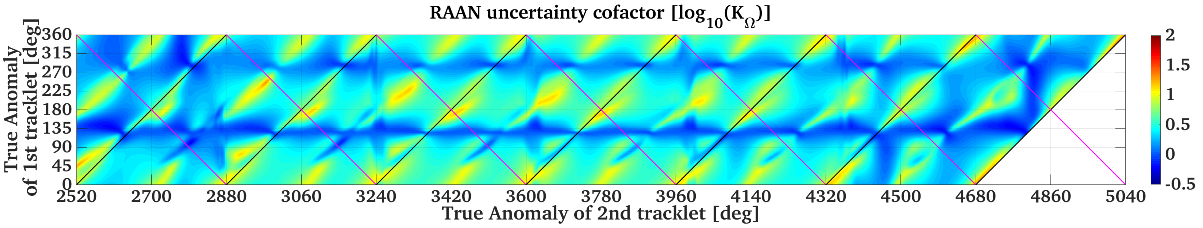

(d) Right Ascension of Ascending Node

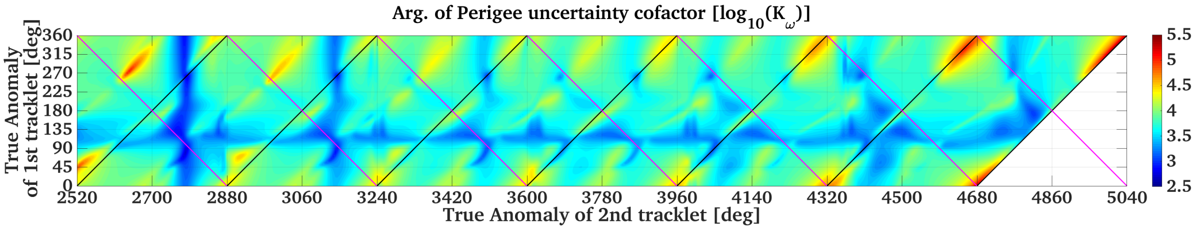

(e) Argument of Perigee

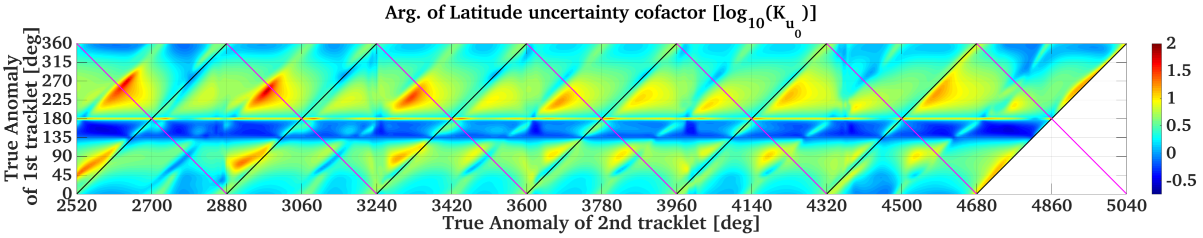

(f) Argument of Latitude

Figure 4.15 Second part of the Uncertainty maps for LEO orbit observed from Zimmerwald.

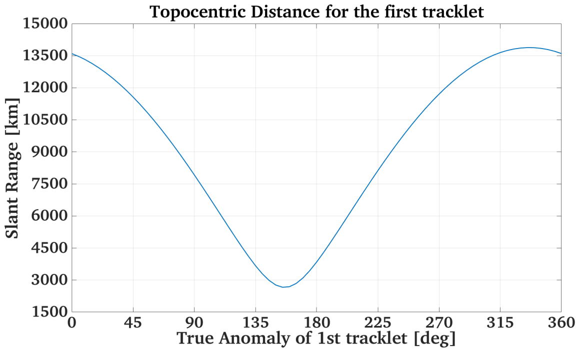

(a) Object-Observer Distance for the 1st tracklet

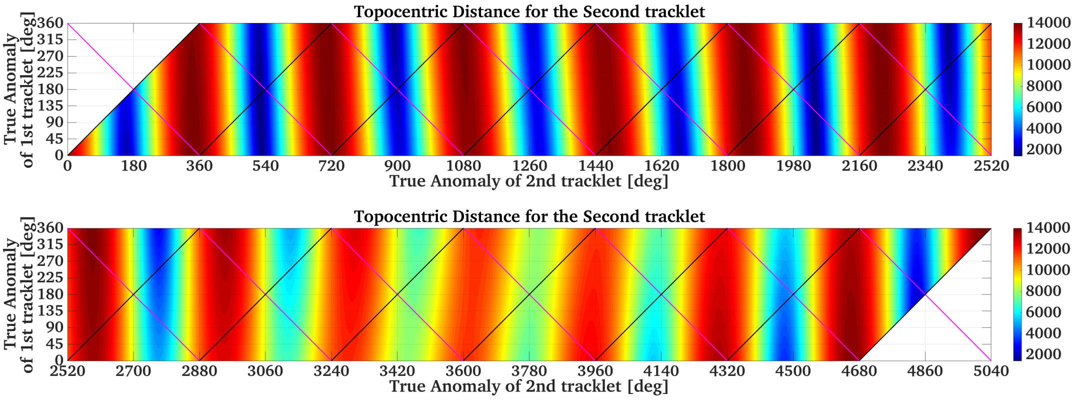

(b) Object-Observer Distance for the 2nd tracklet

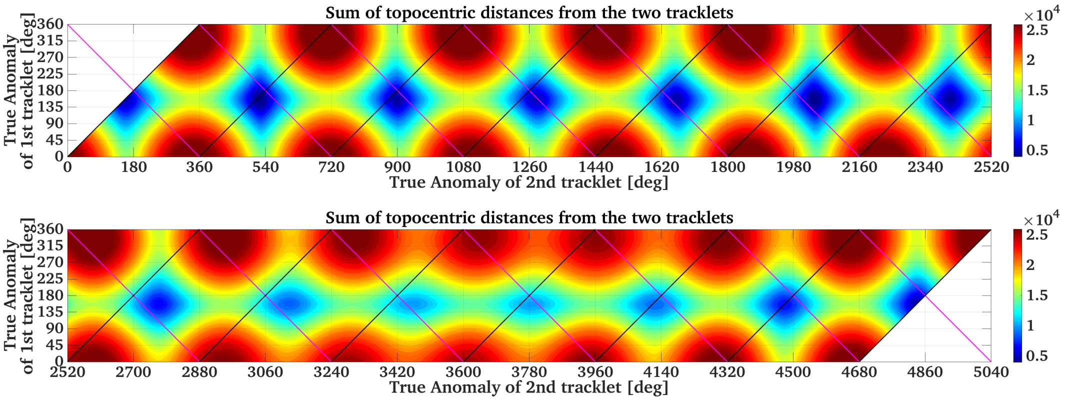

(c) Sum of the Object-Observer Distance for the 1st and 2nd tracklet

Figure 4.16 Topocentric object-observer distance for LEO orbit observed from Zimmerwald.

### 4.11.2 GTO

Another region with a high density of space debris is the Geostationary Transfer Orbit (GTO) region. This region becomes important since it contains the major part of discarded upper stages used to bring a geostationary satellite into orbit. We will analyze two examples for this kind of orbit also to highlight the influences of two parameters: the Right Ascension of Ascending Node and the Argument of Perigee (namely $\Omega$ and $\omega$).
The orbital parameters used for the first example are: $a = 24409.4$ km, $e = 0.7287$, $i = 6°$,

$\Omega = 0°$, $\omega = 226°$ and $T_{osc} =$ 1st observation. For the observer the Zimmerwald observatory is selected and a maximum distance of 2 orbital revolutions between the two tracklets is allowed. Figure 4.17 shows the uncertainty maps obtained for the first GTO-case. Although the results are difficult to interpret, it is still possible to see some main features like: the decrease of the values for the semi-major axis when the distance in time between tracklets increases, the $S$-area almost disappeared for $e$ and $\omega$ while for $a$ it is strongly reduced, and the presence of the minimum uncertainty diagonal line for tracklets separated by 180°. The latter two effects are both caused by the fact that the observer is always outside the orbital plane and by the non-synchronization between the orbital period and the Earth's rotation period. Looking at the uncertainty maps for $i$ and $\Omega$ it is possible to see how the diagonal lines for tracklets separated by 180°, even if still present, are strongly reduced. The high uncertainty area remains when the two tracklets are both close to the apogee. In these two maps it is also possible to see two horizontal lines of low uncertainty values, respectively when the 1st tracklet is between 30° and 60° for $i$ and between 300° and 330° for $\Omega$. Knowing that $\omega = 226°$ these regions coincide with the maximum distance from the line of the nodes, and the position of the line of the nodes, respectively. Then, it is important to notice how, due to a small inclination value, the feature of $\Omega$ are contaminating the maps of the argument of perigee and the argument of latitude.

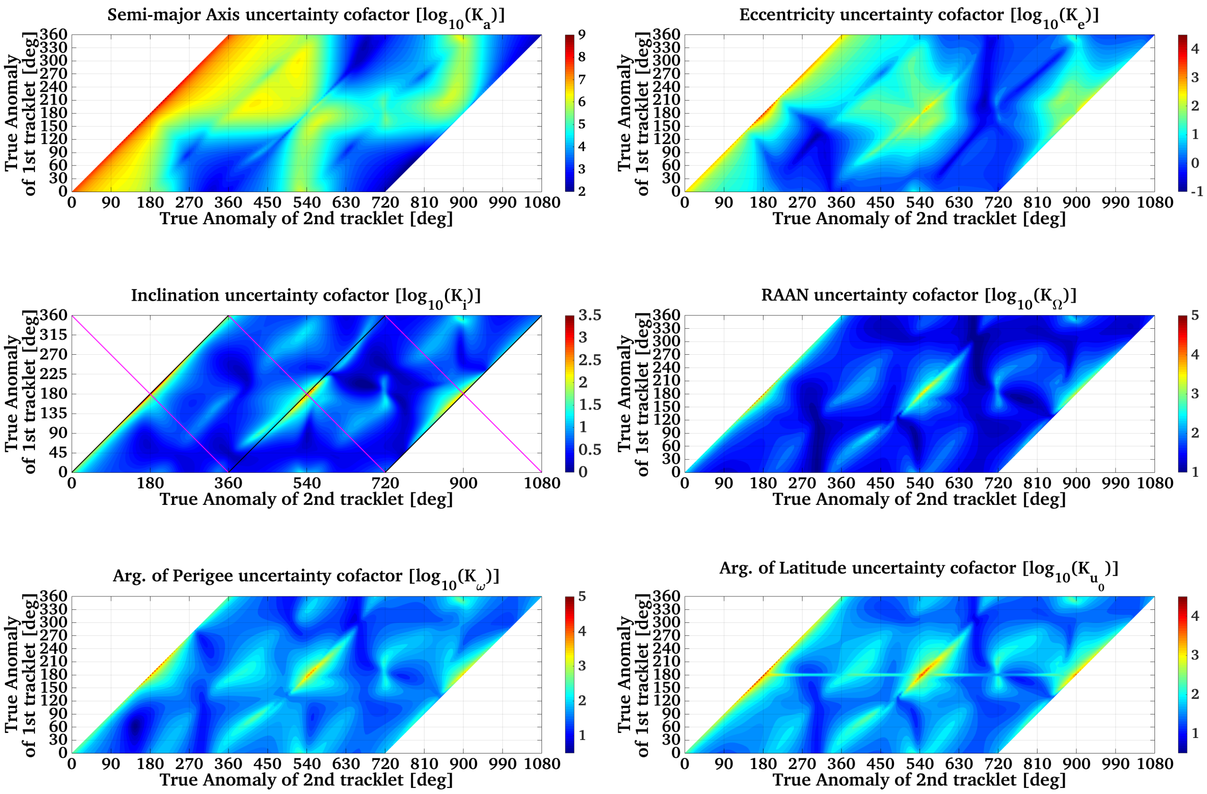
Semi-major Axis uncertainty cofactor [$\log_{10}(K_a)$]

Eccentricity uncertainty cofactor [$\log_{10}(K_e)$]

Inclination uncertainty cofactor [$\log_{10}(K_i)$]

RAAN uncertainty cofactor [$\log_{10}(K_\Omega)$]

Arg. of Perigee uncertainty cofactor [$\log_{10}(K_\omega)$]

Arg. of Latitude uncertainty cofactor [$\log_{10}(K_{u_0})$]

Figure 4.17 Uncertainty maps for 1st GTO orbit observed from Zimmerwald.

The second GTO case is obtained changing only the value for $\Omega$ and $\omega$. In this case we will then use: $a = 24409.4$ km, $e = 0.7287$, $i = 6°$, $\Omega = 226°$ and $\omega = 0°$. For completeness it must be said that the position of the observer and the time interval is precisely the same as in the

previous example, i.e. the observer is the Zimmerwald observatory and the time interval is 2 orbital revolutions.
Of course, there are a lot of similarities with the previous case (results in Figure 4.17). From the plot referring to the semi-major axis and the eccentricity for example it is easy to see the reduction of the *S*-area and the reduction of the diagonal line for positions separated by 180°. As expected the main effects due to the different value of $\Omega$ and $\omega$ are visible for the parameters which describe the orientation of the orbital plane. These effects can be seen comparing the results for $i$, $\Omega$, $\omega$ and $u_0$ shown in Figures 4.17 and 4.18. One of the consequences of the change in the orbital elements in the two GTO cases is that in the first case, the line of the apsides does not coincide with the line of the nodes. This has an influence first on the results obtained for the inclination. Looking at these two plots, respectively in Figures 4.17 and 4.18, one can see how the first graph shows an attenuation of the classical features seen until now and of the uncertainty values. In fact the diagonal lines of the tracklet separated by 180° and the one of the orbital period are fainter in the first case than in the second. On the other hand the low-uncertainty horizontal lines related to the maximum distance of the first tracklet from the line of the nodes (being $\omega = 0°$ the maximum angular distance from the lines of the nodes is obtained for $\nu_1 = 90°$ or $270°$), are much more visible in the second case than in the first one. It is interesting to notice the comparison among the uncertainty values obtained when both tracklets are acquired at the apogee (consequently separated by one orbital period). Here the values obtained in the first case are smaller than in the ones in the second and this is probably due to the fact that the apogee is not anymore in the Earth's equatorial plane. While the higher values of the second case are probably given by the sum of two effects: the high eccentricity of the orbit and the fact that the line of the nodes coincides with the line of the apsides. Comparing the plots which refer to $\Omega$ in the Figures 4.17 and 4.18 we can deduce the same conclusions as those obtained for the inclination. Also here the diagonal features from tracklets separated by 180°, despite strongly reduced, are still present but in the first case are less evident. The main difference between the two graphs is clearly visible in the plot for the argument of perigee where it is possible to see how the *S*-area is now a minimum uncertainty area due again to the observer position. This configuration is then characterized by the shortest tracklets along the orbit close to the line of the nodes. Finally, comparing the maps obtained for $\Omega$, $\omega$ and $u_0$ one can see huge similarities among them which are due to the relatively small inclination value which leads to a high correlation of these three parameters.

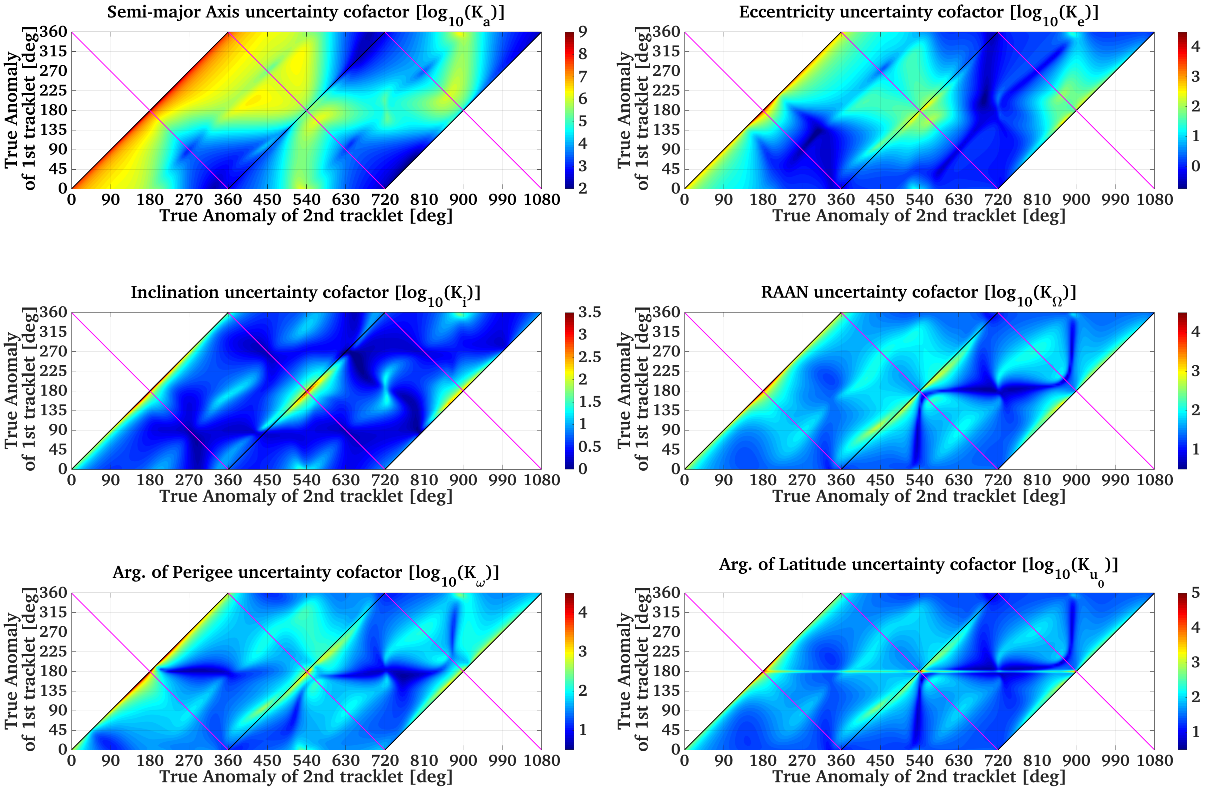

Figure 4.18 Uncertainty maps for 2nd GTO orbit observed from Zimmerwald.

### 4.11.3 Molniya

For this simulation the same scenario as described before is used changing only the orbital parameters of the orbit; in particular: $a = 26561.765$ km, $e = 0.7$, $i = 63.4°$, $\Omega = 278°$, $\omega = 270°$. As usual, also the results for the Molniya object show an $S$-shaped high uncertainty area for $a, e$ and $\omega$, in Figure 4.19. Comparing the $S$-area just obtained with that of the GTO, despite the similar shape of the orbit, in this case the $S$ is sharper and the average uncertainty is a bit higher. These effects are probably due to the fact that the orbit is synchronous with the Earth period and the higher inclination of the Molniya orbit reduces the distances of the orbital plane from the observer position. As for the GEO and GTO case, these results show also the diagonal line for tracklets separated by 180° of true anomaly typical of the observer always outside the orbital plane.

Looking now at the plot for $i$ and $\Omega$, it is interesting to notice how the different position of the perigee in space produces a shift of the horizontal low uncertainty lines. In particular, for the GTO case these lines have positions $\nu_1 = 90°$ and $\nu_1 = 270°$ for the inclination and, although not clearly visible, $\nu_1 = 0°$ and $\nu_1 = 180°$ for the RAAN; for the Molniya case is vice versa. This is due to the fact that $\omega = 270°$ , then the line of the nodes coincides with the line of the semi-latus rectum, while the apogee and the perigee are at the maximum angular distance from the equatorial plane. In these figures the high uncertainty diagonal lines for tracklets separated by 180° or 360° in true anomaly are also present. Finally, it is important to note two features which are visible in the graphs of $i$ and $\Omega$: one for the inclination and one for the RAAN. Regarding $i$, it is interesting to notice the presence of an $S$-shaped low uncertainty area coincident with half a period separation between tracklets. This is probably due to the orientation of the orbit in the space. Being the apogee and the perigee the furthest points from the equatorial plane, at least one of the two tracklets, which are separated in time by half a period, is far enough from this plane to clearly determine the inclination of the orbit. For the same reason the highest uncertainty areas for Ω are occurring for tracklets close to the apogee separated by one orbital period.

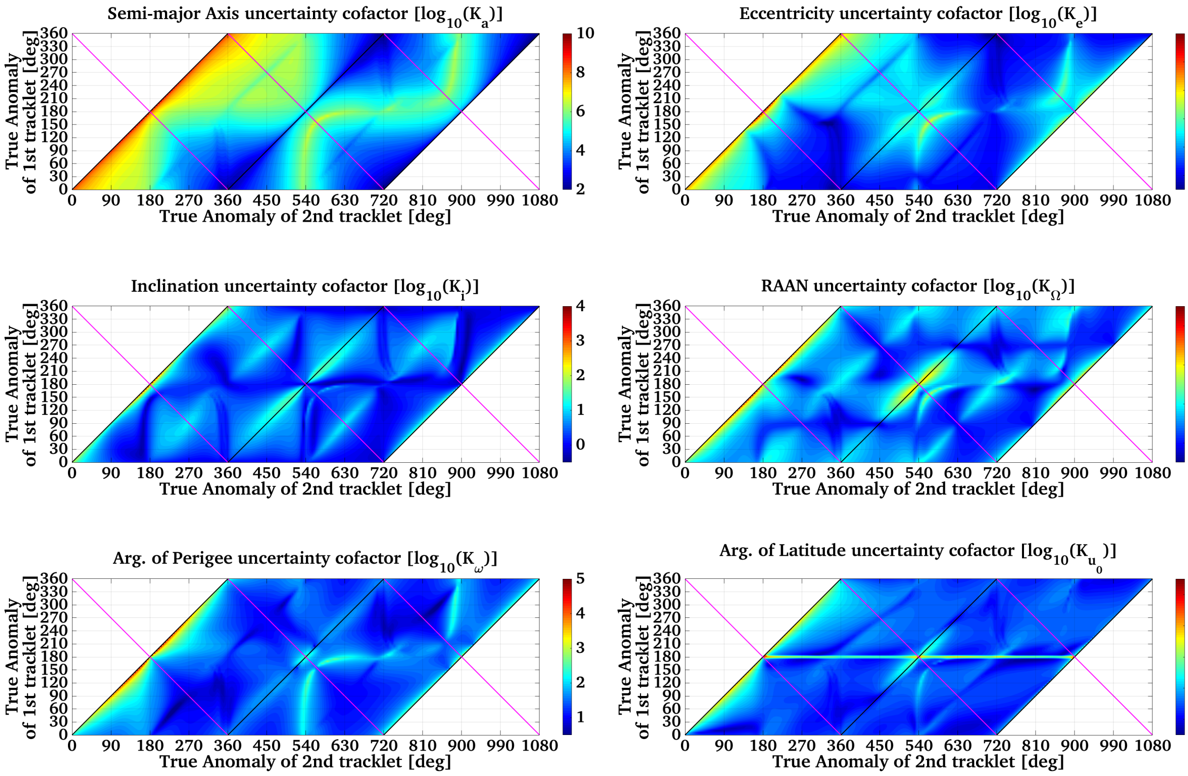

Figure 4.19 Uncertainty maps for Molniya orbit observed from Zimmerwald.

### 4.11.4 GEO

The orbital parameters used for this last set of simulations are: $a = 42164.173$ km, $e = 0.0005$, $i = 0.1°$, $\Omega = 270°$, $\omega = 0°$ and $T_{osc} =$ 1st observation. For the observer's position the Zimmerwald observatory is used. A maximum distance of 2 orbital revolutions between the two tracklets is allowed in this simulation. Figure 4.20 shows the results obtained for the just described scenario.

As we can see from the graphs referring to the semi-major axis, the eccentricity and the argument of perigee, being this an almost circular orbit, the $S$-area for $a, e$ and $\omega$ is now a diagonal line which is not yet precisely coincident with that of 180° angular distance between tracklets because of the time dependency shown in Paragraph 4.6. In these maps the diagonal line for the tracklets whose positions are separated by 180° in true anomaly is also present, this line is obtained by the fact that the observer is always outside the orbital plane. Looking at the uncertainty maps for $i$ and $\Omega$, the high-uncertainty diagonal lines for tracklets separated by 180° and 360° in true anomaly (which are more or less equivalent to half and to one orbital revolution) are clearly visible. It is interesting to notice that the 180° tracklets separation, although it is not the best configuration of observation for $i$ and $\Omega$, shows lower uncertainty values than the 360° tracklets separation due to the different geometry condition given by the observer position on the Earth's surface. Other consequences of the small eccentricity values can be observed in the average high uncertainties for the argument of perigee ($\omega$). In this case, despite the small inclination value, the argument of perigee keeps its main features while the uncertainties of $\Omega$ are directly transferred to $u_0$ which is completely correlated with it.

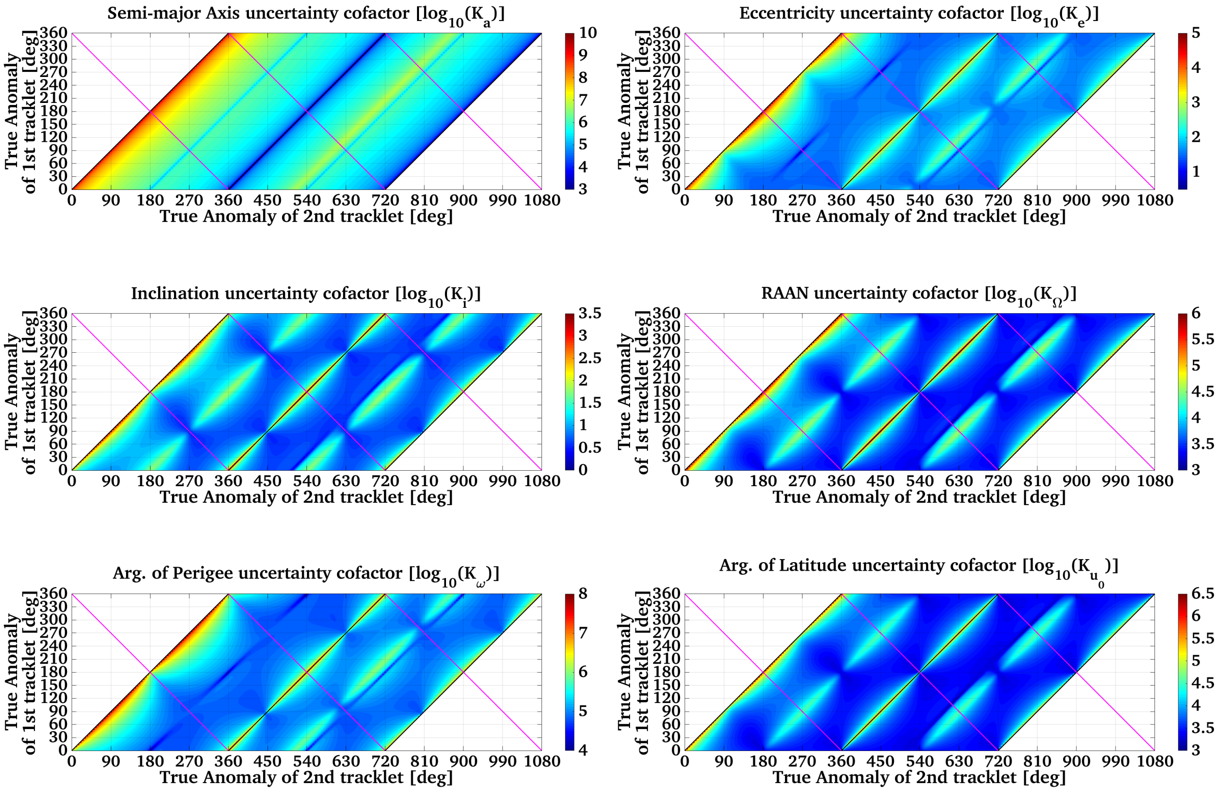

Figure 4.20 Uncertainty maps for GEO orbit observed from Zimmerwald.

## 4.12 Visibility and Night-Time

The current maps show also some impossible combinations of observations due to the visibility limits. For example if we consider the scenario described at the beginning of the Paragraph 4.8 where the perigee of the orbit is just at the zenith of the observer at time $t = 0$, it is obvious that all the 1st tracklet positions which are around the apogee are impossible to see because one should be able to look through the Earth. Are there some "forbidden" regions that is not possible to see in any case? How will the daylight time influence our maps? In fact it is always possible to find an orbit whose parameters fulfill my visibility criteria. For example, the results of two simulations were compared: in the first the orbital parameters described in Paragraph 4.8 were used, and in the second the same orbital elements were kept but $\omega$ was set to 180°, so that the apogee of the orbit was at the zenith at time $t = 0$. This comparison showed that the features present in the maps are precisely the same, the only difference are the uncertainty values which are slightly different due to the different distances of the object from the observer. It is possible then to conclude that the maps do not have forbidden regions but to apply them it is necessary to use a mask for the elevation limits and another one for the nighttime.

## 4.13 Second Observer

The results showed until now are obtained considering one single observer. The next step of this study will be the evaluation of the effects on the uncertainty maps given by a second observer. These series of tests were performed to simulate a network of telescopes and then to evaluate which improvements can be achieved. In order not to introduce a too much complicated scenario and to easy interpret the results we limited the number of observers to only two.

The introduction of a second observer posed the question: how the second observer should interact with the first one? There are two possible ways of interaction: the first is when the observers are acquiring measurements precisely at the same time of the same objects; the second is when the observers are more independent and they are observing the same object but with some delays between the measurements. The first case is described in the Paragraph 4.13.1, while the second is analyzed in the Paragraph 4.13.2.

### 4.13.1 Synchronous Observers

First we will analyze the case of “synchronous observers” in particular, we will evaluate the effects on the uncertainty maps given by a second observer which is observing the target object precisely at the same time as the first observer.

During these simulations it is necessary to take into account some constraints on the observer’s positions, in fact as an example we could not select observers which are on the opposite part of the Earth. Also in this case we performed a scan of all possible combinations of tracklets separated by 2.5° in true anomaly in the same way as described in the Paragraph 4.3. The only difference is that for this study two series of observations per observer, acquired at the same time, are used in the orbit determination process.

For an easier comparison of the results with those previously obtained we performed this study on the same "standard" geosynchronous orbit as that used in Paragraph 4.8. The following orbital parameters are used: $a = 42164.173$ km, $e = 0.5$, $i = 60°$, $\Omega = 0°$, $\omega = 0°$ and $T_{osc} =$ 1st observation. Two equatorial observers symmetrical to the Greenwich meridian are used, whose geodetic coordinates are: for the first Lat. 0°, Long. 45° West and Alt. 900 m; while for the second Lat. 0°, Long. 45° East and Alt. 900 m. The observation scenario is shown in Figure 4.21.

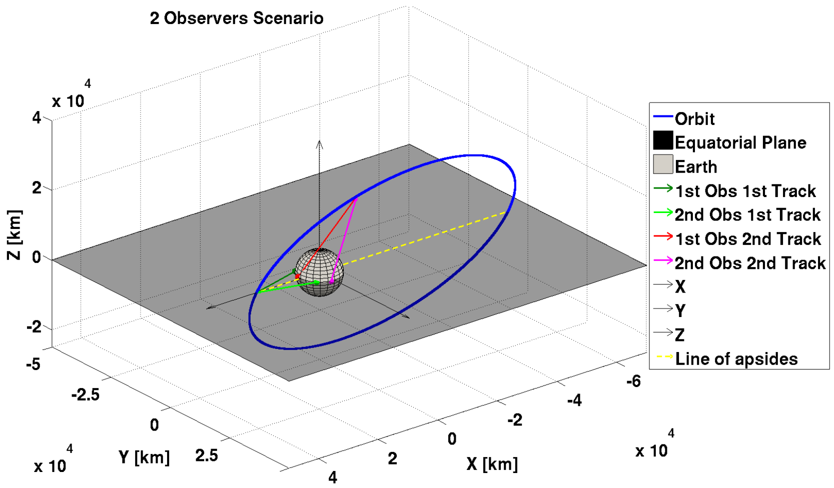

Figure 4.21 Simulation scenario with two observers symmetric to Greenwich meridian.

From Figure 4.22, especially for $a$, $e$ and $\omega$, it is easy to see how the typical features previously studied are still present. In particular it is still possible to see the effect of the time distance between the two tracklets, in fact the maps show different features for the 1st and the 2nd orbital revolution and the average error is decreasing while the time difference is increasing. The $S$-shaped high uncertainty area is still present, as well as the high uncertainty diagonal line for tracklets separated by 180° and 360° in true anomaly for $i$ and $\Omega$. However, some differences can be noticed w.r.t. the case of a single observer: first, the average uncertainty values are lower due to the capability of estimate the object distance and the higher number of observations, second some new features are appearing, like the high uncertainty spots close to the $S$-area for $a$, $e$ and $\omega$ or close to the diagonal line of tracklets separated by 180° for $i$ and $\Omega$. The main improvement given by a second observer is given by the fact that, knowing the observer position and the direction to the target object, it is always possible to estimate the distance of the object from the observers and also the object's geocentric position. The quality of the estimation of such distances is proportional to the parallax angle given by the pointing directions of the observers to the object position, the smaller this angle will be, the less accurate will be the distance estimation. The correspondence between the high uncertainty spots and the low parallax values is confirmed by Figure 4.23 which represents the sum of the parallax angles obtained for the first and for the second tracklets.

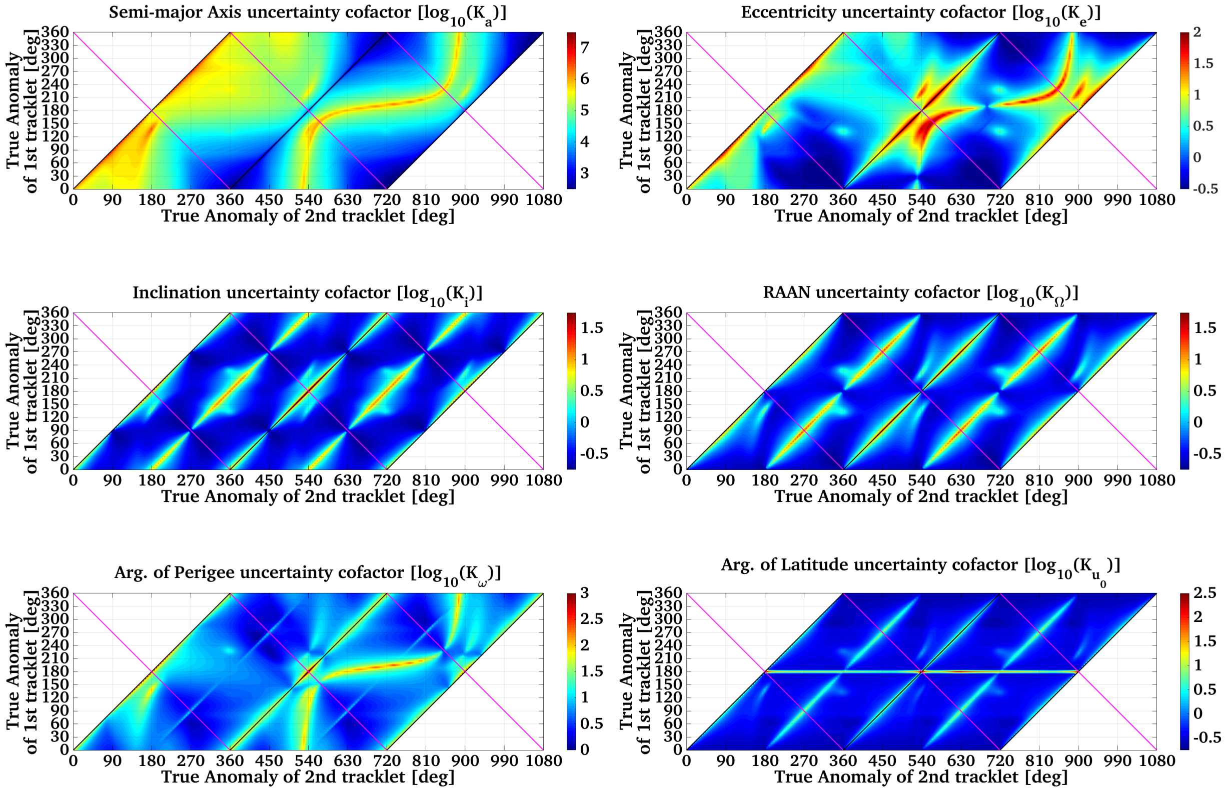

Figure 4.22 Two observers symmetric to the Greenwich meridian - Uncertainty maps for Geosynchronous inclined orbit.

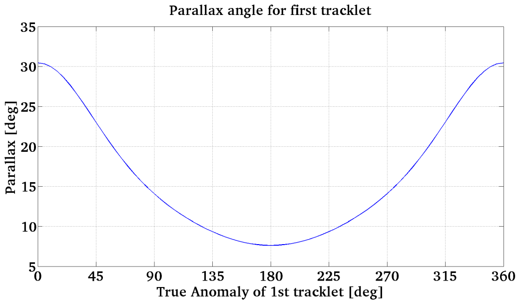

(a) Parallax for 1st tracklet

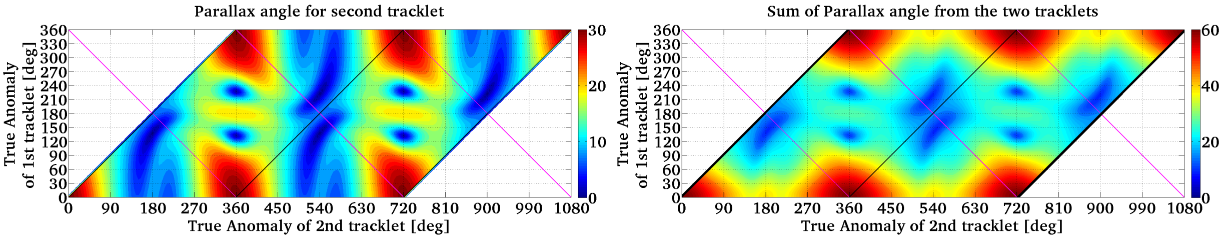

(b) Parallax for 2nd tracklet

(c) Map for total parallax (1st + 2nd)

Figure 4.23 Two observers symmetric to the Greenwich meridian - Parallax angles maps for Geosynchronous inclined orbit.

The most important result obtained by the introduction of the second observer is given by the capacity to estimate the distances. At the same time this improvement can be reduced by the dependency of the accuracy of the estimated parameters on the parallax of the observations. This quantity is, of course, dependent on the relative position between the observers and the object. To highlight this effect, the results of a second simulation are reported in the Figures 4.24 and 4.25. These results are obtained with the same scenario previously utilized, but changing the inclination of the orbit to make it equatorial ($i = 0.1°$). Only the maps of the semi-major axis and the eccentricity (namely those of $a$ and $e$) show significant changes. As one can see, instead of high uncertainty spots on the map, in this case some new features appeared which are intersecting the nominal $S$-area. The correspondence between these new features with those regarding the parallax angles is clearly visible in Figure 4.25c. Regarding the other orbital elements, we see that for the argument of perigee and the argument of latitude (respectively $\omega$ and $u_0$) the predominant features are as those visible for the RAAN ($\Omega$). At the same time in the maps obtained for $\omega$ and $u_0$ the $S$-area is barely visible. As said before, these phenomena are occurring since the orbit is equatorial and then one has the maximum correlation between $\Omega$, $\omega$ and $u_0$. Finally, regarding the inclination and the RAAN ($i$ and $\Omega$) we see that only the classical features given for tracklets which are separated by 180° of true anomaly and by an integer number of orbital period are visible. Since in this case both, the orbit and the observers ,are lying on the same plane, the orientation of the orbital plane in the space is well defined for almost all tracklets combinations except for the ones which are obtained when observing opposite parts of the orbit.

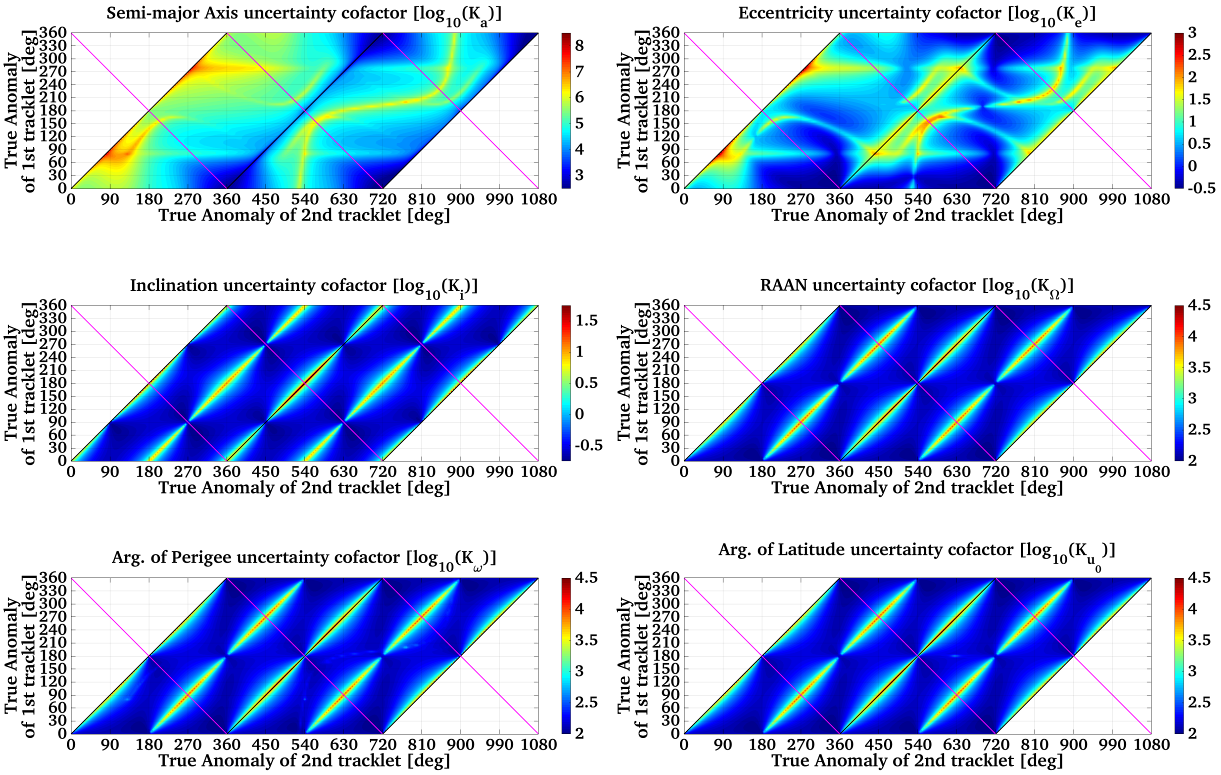

Figure 4.24 Two observers symmetric to the Greenwich meridian - Uncertainty maps for Geosynchronous equatorial orbit.

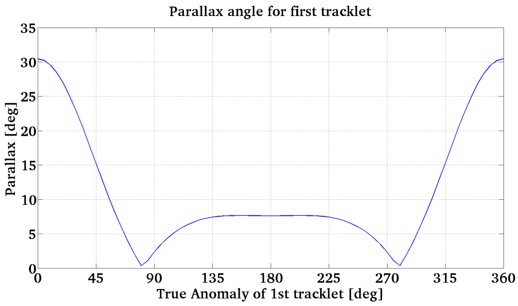

(a) Parallax for 1st tracklet

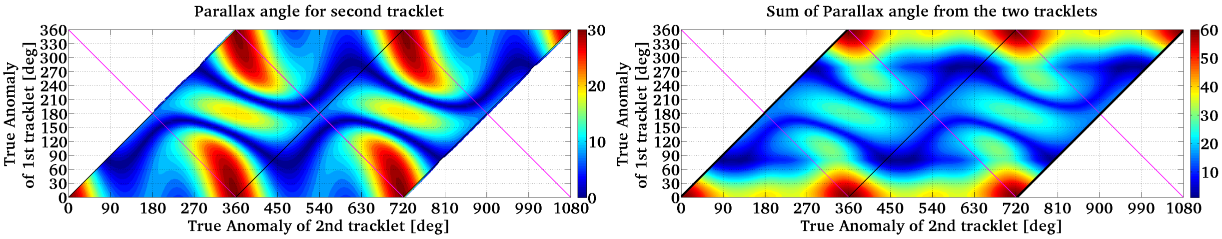

(b) Parallax for 2nd tracklet

(c) Map for total parallax (1st + 2nd)

Figure 4.25 Two observers symmetric to the Greenwich meridian - Parallax angles maps for Geosynchronous equatorial orbit.

For completeness the Figures 4.26a and 4.26b show the semi-major axis uncertainty map and the parallax map obtained using the same inclined geosynchronous orbit as in the first case, but in this case, the observers are in a symmetric position w.r.t. the Earth's equator, namely: 45° Lat. North and 45° Lat. South. As one can see from the figures, the parallax variations given by the tracklets combinations are smoother than those obtained previously and do not show highly pronounced particular regions. The obtained uncertainty maps do not show particular behaviors and the typical features analyzed until now are visible. For this reason we report only an extract of the results. It must be said that the only characteristic that can be noticed is the reduction of the obtained uncertainty values w.r.t. the one-observer case due to the increased amount of observations processed and the capability to estimate indirectly the distances exploiting the parallax angle and the known positions of the observers.

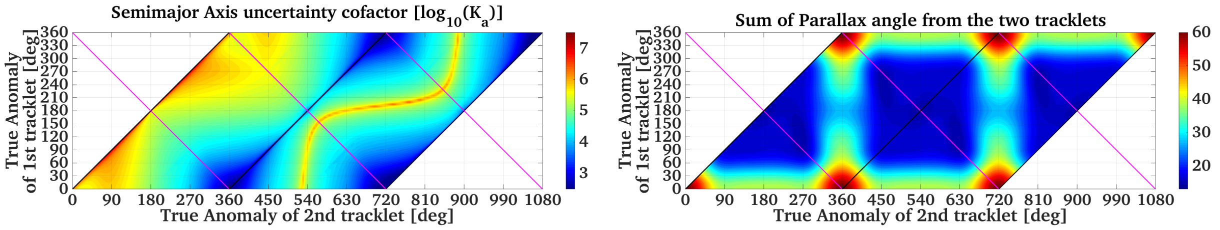

(a) Semi-major axis uncertainty map

(b) Map for total parallax (1st + 2nd)

Figure 4.26 Semi-major axis and Total Parallax for Geosynchronous inclined orbit observed from two observers symmetric to the Equator.

### 4.13.2 Non-Synchronous Observers

Another way of operating a network of telescopes is to let them work independently. To not complicate too much the scenario instead of selecting two observers whose positions are randomly distributed on the Earth and let them operate independently, we decided to keep the same observers, symmetric to the Greenwich meridian, as in the previous case and we analyzed the influence of a time delay between the observations of the observers. So we decided to increase step by step the time distance between the beginning of each tracklet of the second observer w.r.t. the beginning of the tracklets of the first one. In each simulation we used a constant delay between the tracklets of the two observers. The test orbit has the following orbital parameters: $a = 42164.173$ km, $e = 0.5$, $i = 60°$, $\Omega = 0°$, $\omega = 0°$ and $T_{osc}$ = 1st observation. The positions of the two observers have the following coordinates: for the first Lat. 0°, Long. 45° West and Alt. 900 m while for the second Lat. 0°, Long. 45° East and Alt. 900 m. The time delay between the observations was increased from 10 seconds to 45 minutes. Also in this case the simulations were performed in order to scan all possible combinations of tracklets separated by 2.5° in true anomaly as in the case of one observer over the orbit. These positions are used as reference to determine the positions of the tracklets of the second observer accordingly with the chosen time delay. Figure 4.27 shows the results obtained with a delay of 45 minutes between the observation of the two observers.

The simulations produced two kinds of results depending on the chosen time delay. If the chosen time distance is relatively small, let's say less than the length of the tracklet (in our case 210 seconds) and it is different from $k \cdot 30$ sec with $k = 0, 1, ..., 7$, we do not have coincident observations and then we can not estimate the distance of the object. At the same time, we see in the results almost the same features as shown in the Figure 4.22. Only the uncertainty values are slightly different. This is probably due to the fact that despite the "triangle" (between observers and object) is not closed perfectly, the observations of the two observers are close enough that, together with the known dynamical model of the orbit, the system could exploit this "approximated parallax-angle" to have a rough idea of the distance. At the same time, introducing a delay in the observations of the second observer, we increase slightly the length of the observed arc.

The second type of results are obtained when the tracklets of the two observers are not overlapping anymore. In this case, we have a conceptual change of the observation scenario. In fact the two observers are not interacting anymore and we have an increase of the observed portion of the orbit. This produces an information gain that is reflected by the reduction of the average uncertainty values, as shown in Figure 4.27. The main difference with the previous examples can be seen in the fact that their values are not symmetric anymore. Furthermore, as one can see especially from the maps of $e$, $i$, and RAAN, the classical behaviors of these maps are dimmed and bent. These deformation, asymmetries and even new features, as can be seen for the map of the inclination, are due to the variation of the angular distance of the tracklets of the two observers. In fact, since the delay is constant in time, according to the observed part of the orbit, the angular distance between the tracklet of the first observer w.r.t. that of the second is changing. If we are observing close to the apogee the same time delay corresponds to a small angle and a shorter portion of the orbit observed with the consequent increase of the uncertainty. Vice versa observing close to the perigee the observed portion of the orbit increases giving more information for the correct estimation of the parameters. To better understand these results and the just mentioned phenomenon, in the Figure 4.28 we report the values of the true anomaly of the tracklet of the second observer as a function of the position of the tracklet of the first one and the selected time delay.

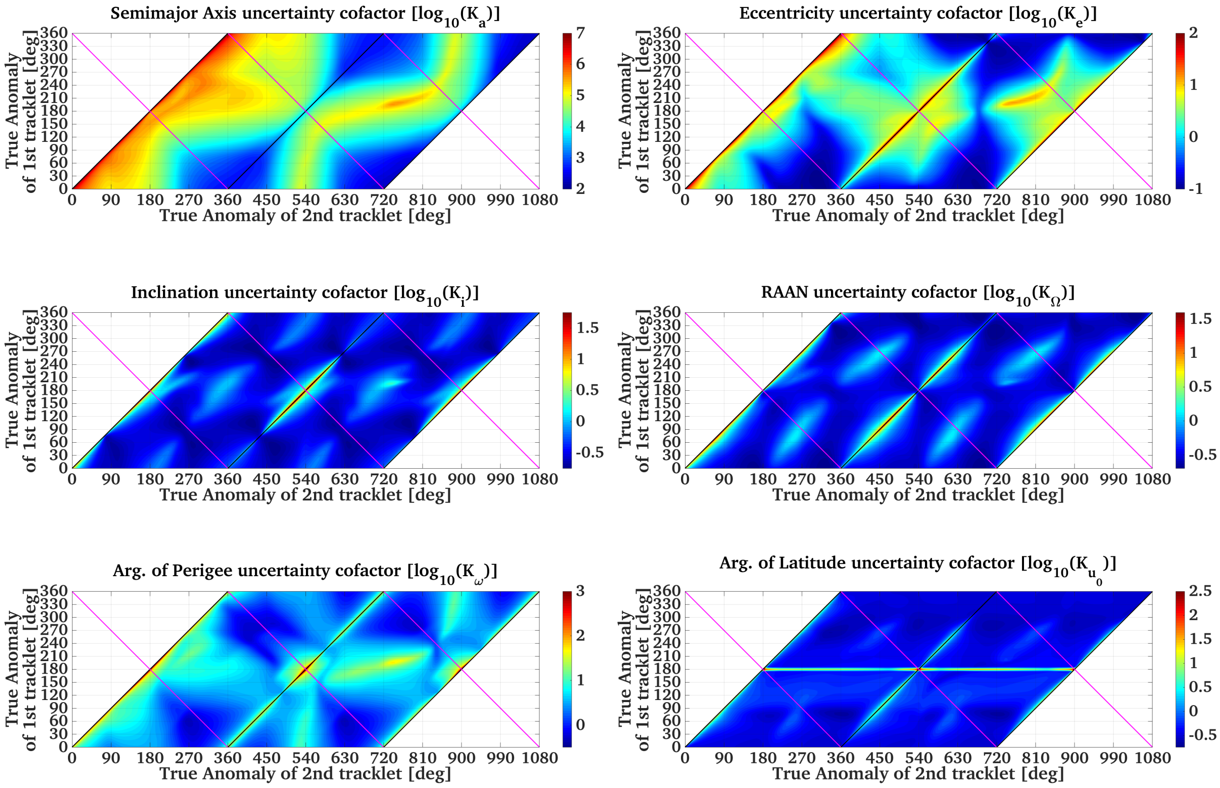

Figure 4.27 Two not synchronized observers symmetric to Greenwich meridian - Uncertainty maps for Geosynchronous inclined orbit.

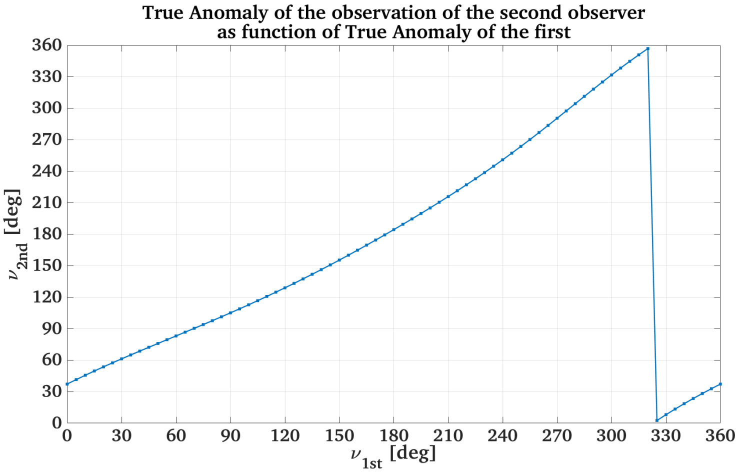

Figure 4.28 True Anomaly of the object at the time of the observation of the second observer as a function of the observation position of the first one for the case of a Geosynchronous inclined orbit observed from two non-synchronized observers (45 minutes distance between the observation of the 1st and 2nd observer) symmetric to the Greenwich meridian.

## 4.14 Discovery and First Follow-up

The last results are obtained using three tracklets in the simulation of our orbit determination problem. This scenario was introduced since it is representative of a classical discovery and first follow-up scenario as it is common habit to have during the regular observations at the AIUB. In particular, this kind of observation scheme is principally used at the AIUB when operating the ESA Space Debris Telescope in Tenerife (ESASDT). Since the time available to the AIUB to operate the ESASDT is limited one has to ensure that the determined orbit is good enough to reobserve the newly discovered object in the future from the Zimmerwald observatory.

Usually when the ESASDT and, more in general, when a telescope is used to discover new objects, the survey observations are scheduled in a way that every single object is observed at least two times within the same night. The time distance between the first two series of observations is fixed and usually depends on the orbital regime of the target (e.g. LEO, MEO and GEO) and on the survey plan. The pictures acquired by the ESASDT [43] are processed almost in real time, a first orbit is determined and then a second and a third series of so-called follow-up observations are scheduled within the same night.

We decided to analyse the 3-tracklets case to simulate this kind of scenario: we fixed the time distance of the first and second tracklet to simulate the results of a survey and then we evaluated how the position of the follow-up (third tracklet) will improve our orbit determination as a function of its time distance from the second one. A scheme of the just mentioned observation scenario is visible in Figure 4.29.

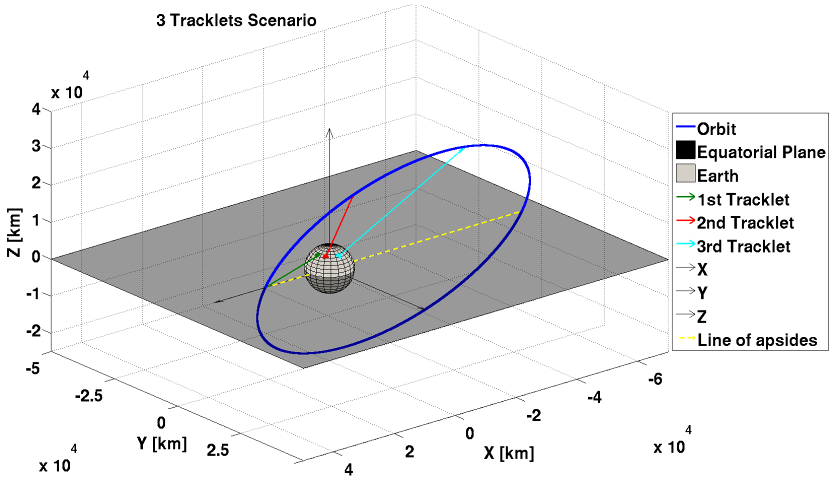

Figure 4.29 3 tracklets from a single station Scenario.

The simulated observation scenario consists of a geosynchronous eccentric orbit with a single observer on the Earth's surface. The Zimmerwald observatory is used as the observer position while the used orbital parameters are: $a = 42164.173$ km, $e = 0.5$, $i = 60°$, $\Omega = 8°$, $\omega = 180°$ and $T_{osc}$ = 1st observation. As said before, for this simulation the time distance between the 1st and the 2nd tracklet is kept constant to 2 hours, while the distance of the 3rd one is varying from 10 seconds up to 2 orbital revolutions. As for the other cases, the observer position at the epoch of the first observation is kept constant while all the other positions (respectively for the remaining observations of the 1st tracklet and those for the 2nd and the

3rd) are determined consistently with the Earth rotation rate and the time distance from the just mentioned observation epoch. Also in this case, the simulation is performed in order to analyze all possible combinations of tracklets positions separated by 2.5° in true anomaly.
Figure 4.30 shows the results obtained for the 3 tracklets case. As usual, the position of the 1st tracklet is represented in the $y$-axis while in the $x$-axis the position of the 3rd is shown. The position of the 2nd tracklet is roughly coincident with the first visible position of the 3rd tracklet, this because the minimum time distance between the latter two is 10 seconds (e.g. $\nu_1 = 0°$, $\nu_2 = 81.557°$ and $\nu_3 = 81.631°$). As one can see from the uncertainty map obtained for the semi-major axis, the use of a third tracklet strongly reduces the average uncertainty values in comparison to those obtained for the case using only two tracklets. Despite that, as for the previous cases, the uncertainty tends to decrease with the increase of the time distance between tracklets. Also the $S$-area is still visible but strongly reduced consistently to the higher number of observations and to the fact that the observer is always outside of the orbital plane. The part of the map where the $S$-area is sharper coincides with the case where the positions of the first two tracklets are close to the apogee because the slower the object the shorter is the arc between the first two tracklets. It is still possible to see the minimum uncertainty diagonal line coincident with one period separation between first and third tracklet. It is interesting to notice that also another minimum line is appearing in this map and it coincides with the orbital period distance of the third tracklet from the second.
Looking at the maps obtained for the eccentricity and the argument of perigee, as in the case of the semi-major axis, it is still possible to identify the residuals of the classical $S$-area of half a period distance between observations and at the same time, the features which in the map of $a$ are minima regions, in the map of $e$ and $\omega$ are high uncertainty regions. This because when the third tracklet is coincident with one of the first two it loses some useful information for the determination of $e$ and $\omega$. In the map of $e$, two horizontal lines of minimum uncertainty appeared for positions of the first two tracklets which are symmetrical w.r.t. the line of the apsides.
Finally, looking at the maps obtained for $i$ and $\Omega$, it is possible to see how, for positions of the 3rd tracklet which are coincident with one of the previous two, there is a loss of information which produces high uncertainty values. This loss is even more evident in the inclination map, for tracklets whose positions are close to the apogee; these positions are, in fact, coincident with the lines of the nodes. Both maps show two horizontal lines of minimum uncertainty, these appear when either the 1st or the 2nd tracklet is at the maximum angular distance from the line of the nodes (for $i$) or is on the line of the nodes (for $\Omega$).

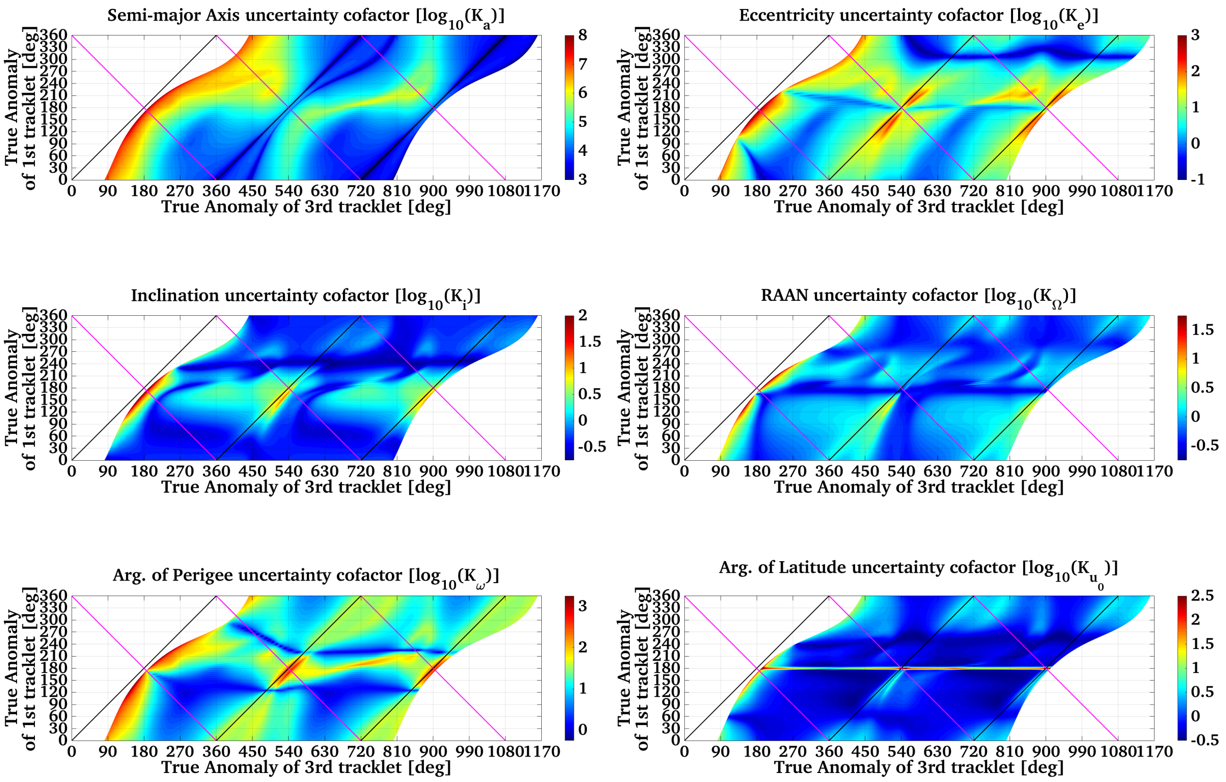

Figure 4.30 3 Tracklets - Uncertainty maps for Geosynchronous orbit observed from the Zimmerwald observatory.

## 4.15 Angular and Range Measurements

The last analysis is performed to study the influence of the range measurement when processed together with the angular ones. It was decided to carry out this study since the ranges are regularly used to determine an orbit [15]. In particular, the range measurements can be obtained either from radar facilities and usually are processed together with the steering angles of the radar (i.e. azimuth and elevation) or from laser facilities [2]. Usually the ranges obtained by laser facilities, due to their high accuracy, are used for geodetic purposes. Since the capability of collecting range measurements via laser systems depends essentially on the capability of the target object to reflect the light toward the laser station and due to the accuracy of the laser measurements, many studies are focusing on the tracking and processing of laser measurements to determine the orbit of space debris [34, 31].

As we will see in the next chapter (5), the main reasons that motivated scientists to study the applicability of the laser technologies for the orbit determination of space debris are the fact that laser measurements are: less dependent on the size of the target, very precise and the laser systems are cheaper than the radar ones. For these reasons, we decided first to investigate the influence of the ranges on an orbit determination process based on the classical angular measurements, then in Chapter 5 we will analyze the results obtained with real measurements. As before, to easily understand and interpret the results, we focused our study in a relatively simple scenario: only two series of observations from the same observer are taken into account.

Each observation series consists, as usual, of 7 of angular observations ($RA$, $DE$) and 3 ranges ($\rho$) with their corresponding epochs ($t$). As we will see in Chapter 5, due to the high precision of the laser measurements, to process correctly laser and angular measurements and to be able to discriminate the effects of each observable it is fundamental to limit the number of processed ranges and to use the proper weights on the observables within the LSQ adjustment. We decided to limit the number of ranges to 3 per series. We time tagged the ranges with the epoch of the first, the fourth and the last angular measurement of the tracklet. As previously shown in Paragraph 4.2.3, to process consistently the two types of observables, it was necessary to relatively weight the partial derivatives of the ranges w.r.t. those of the angular measurements. The weights values are determined consistently with the method proposed in Paragraphs 5.5.1 and 5.5.2. The weights are calculated using the following values for $\sigma_{RA,DE} = 0.5$ arcsec and for $\sigma_\rho = 1.3$ m. As usual, the Zimmerwald station is used as observing site and the orbit of the target has the following orbital parameters: $a = 26561.765$ km, $e = 0.7$, $i = 63.4°$, $\Omega = 278°$, $\omega = 270°$ and $T_{osc} =$ 1st observation. To easily compare the results, we decided to use precisely the same Molniya-orbit that was analyzed previously in Paragraph 4.11.3.
Figure 4.31 shows the uncertainty maps obtained for the just described scenario. Comparing the obtained maps with those in Figure 4.19 we can see a significant general reduction of the uncertainty values. For the semi-major axis, for example, the maximum values are roughly two orders of magnitude smaller than those obtained processing two angular tracklets. The main improvements are visible on the $S$-region and especially toward the apogee of the orbit along the direction of the symmetric positions w.r.t. the line of the apsides. The improvements on this region are even more evident if we compare the eccentricity uncertainty maps. A high uncertainty area for short time distances between the observations when the position of the first tracklet is between 135° and 225°, which almost disappeared in the eccentricity map of Figure 4.31. Being the orbit very eccentric and these observations taken closer to the apogee, the arc covered by the tracklet is very short as also the distance among the observations within the tracklets. Thus dealing with angles only the system has more difficulties to estimate correctly the eccentricity, which is partially overcome by the distance information given by the ranges.
It is interesting to notice how the ranges are helping also in the estimation of the orientation of the orbital plane. Comparing the uncertainty maps obtained for the inclination we can notice a strong reduction on the uncertainty values for tracklets closely spaced in time and for those belonging to the $S$-area which are separated by half of an orbital period. The tracklets belonging to this region have positions either spaced far apart on the orbit or enough distant from the Earth's equatorial plane. These characteristics are favorable to the estimation of $i$ and this effect is amplified by the ranges. The same improvements are also visible for the RAAN where the highest uncertainty area corresponds to the tracklet combinations whose positions are close to the apogee and are separated by one orbital period. These positions coincide, in the analyzed case, to the farthest point from the line of the nodes.
The last maps which we will analyze are those related to the argument of perigee. Here, the improvements given by the range produce even a change in the features for tracklets whose time separation is within the first orbital period. First, an important reduction of the uncertainty values is visible; second, coherently with the results obtained for the eccentricity, a huge improvements is visible towards the apogee of the orbit and finally a low uncertainty $S$-area is appearing.

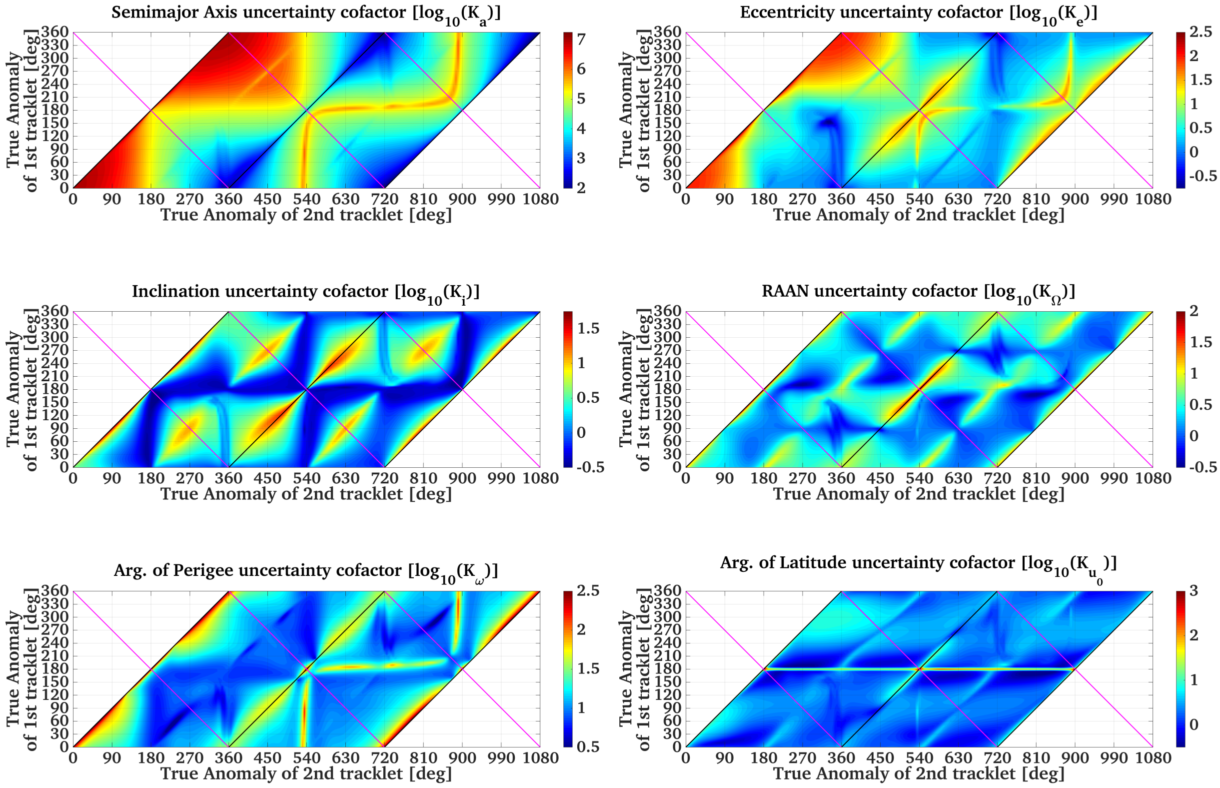

Figure 4.31 Merged Measurements - Uncertainty maps for Molniya orbit observed from the Zimmerwald observatory.

Another analysis can be done comparing the correlation and the condition number maps obtained processing two tracklets of angles with or without the ranges, shown respectively in the Figures 4.32b and 4.32a. Since the main effects of the ranges are visible for the semi-major axis, the eccentricity and the argument of perigee, we decided to report only the correlation maps related to these parameters. Figure 4.32a shows the correlation maps for $a$ and $e$, $a$ and $\omega$ and finally for $e$ and $\omega$. The maps reflect the effect already highlighted for the uncertainty maps. The decrease of the average uncertainty values in the estimation produces, in general, a major decorrelation between the parameters. Looking at the correlation maps between semi-major axis and eccentricity and between $a$ and $\omega$, the ones obtained processing both angles and ranges show more structured features which before were hidden within the high correlation part. Furthermore it is possible to see a reduction of the high correlation areas towards the apogee of the orbit and in the short time separation between the tracklets, respectively in the maps of $a$ and $e$ and in that of $a$ and $\omega$. The most prominent changes are visible in the $e$ and $\omega$ correlation map, where the information on the distances produce a strong decorrelation between the two parameters, especially for tracklets which are symmetric to the line of the apsides. Finally, the diminution of the condition number by roughly one order of magnitude all over the map confirms the importance of the ranges in the orbit estimation considering short arcs of observation.
The results shown until now were obtained using 2 tracklets of observations constituted by 7 angular and 3 range measurements. As said before, the ranges are coincident with the 1st, the 4th and the 7th angular observations of each tracklets. For the same scenario we performed also a simulation using a different placement of the ranges w.r.t. the angles (e.g. ranges placed on the

1st, 2nd and 3rd angular measurement). These results will not be reported since they are pretty much the same as those shown in the Figures 4.31 and 4.32. In particular, no significant changes are visible in the features of the map, but only the uncertainty values are slightly different. To be precise only the average uncertainty values all over the map of the semi-major axis show a noticeable, although small, increase. This is probably due to the length of the arc covered by the ranges which is maximized when positioning the ranges on the first and last angular observation. The same scenario was also used to test the influence of the number of ranges within the tracklets. The number of ranges was varied from the minimum of 1 to the maximum of 7. The epoch of the ranges was taken always coincident with those of the angles. Also for this analysis we will not report the results since essentially no changes in the features of the maps can be noticed. Only the uncertainty values are changing: in particular they decrease as the number of ranges increases. As expected, the main changes are noticeable, first for the map regarding the semi-major axis, then for the eccentricity and the argument of perigee, and finally the smallest changes are occurring for the argument of latitude and the parameters which describe the orientation of the orbital plane (namely $i$ and $\Omega$). Other changes can be seen in the values of the correlation maps between $a$ and $e$, and between $e$ and $\omega$. These maps shows a growing capability of the system to decorrelate the parameters when increasing the number of the ranges. All these changes in the maps are due essentially to the increment of the number of processed measurements. As obvious, the higher the number of observations the better is the accuracy of the results. This trend is also reflected by the condition number map whose values are also decreasing. For completeness, it must be said that, if on one hand a higher number of observations produces better results, on the other, the amount of improvement is limited by the observation geometry and even more by the portion of orbit observed. The evidence of this phenomenon can be seen in the fact that the change of the uncertainty values is minimal and will be also proved by means of real measurements subsequently in Paragraph 5.6.2.

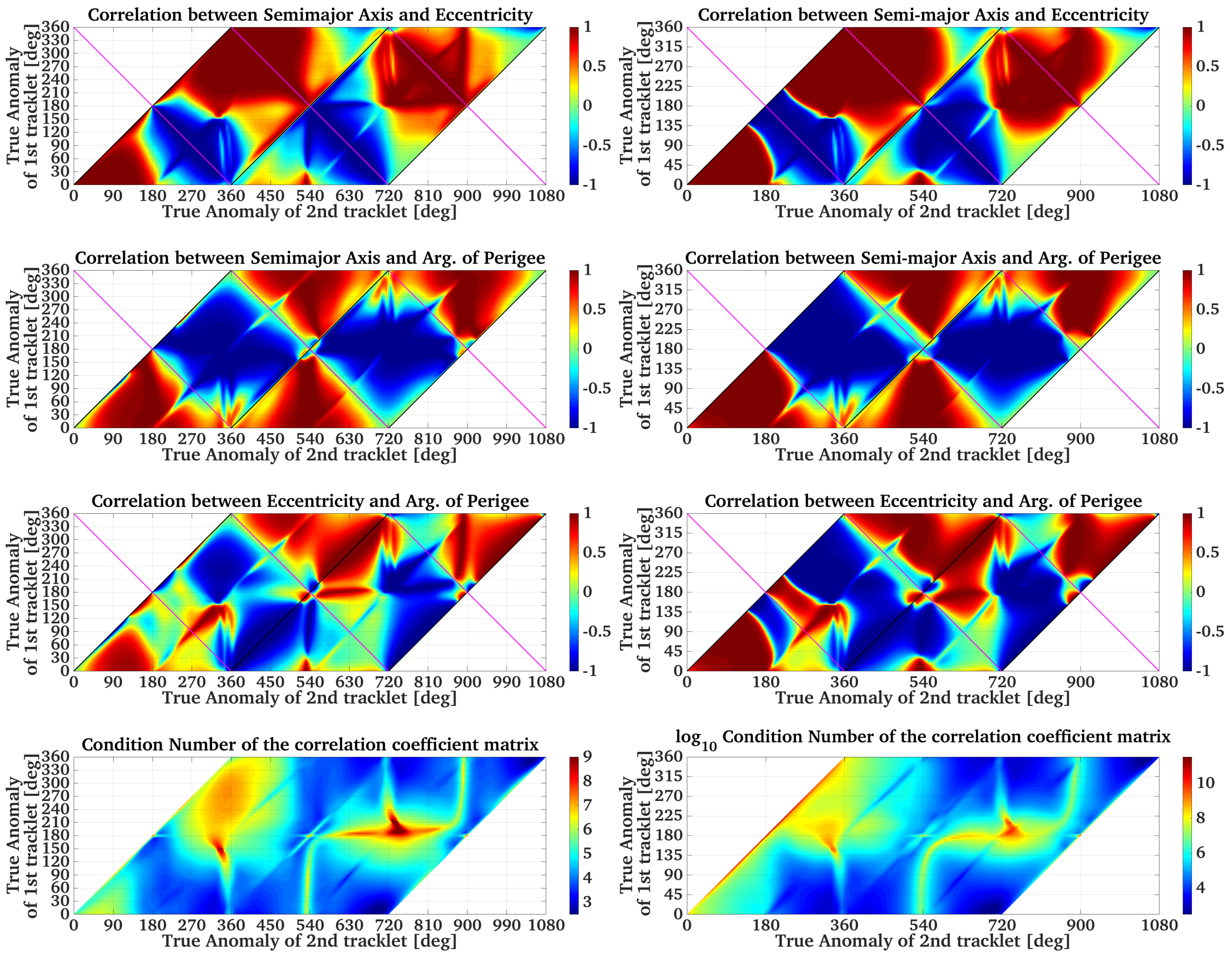

(a) Angles and ranges

(b) Only angles

Figure 4.32 Comparisons between the correlation and the condition number maps for the Molniya orbit obtained processing range and angular measurements with those obtained by processing only angles.

## 4.16 Conclusions

In this chapter, a study was presented to highlight the dependency of the accuracy of the results achievable from an orbit determination on the object-observer relative geometry. This study was performed analyzing the covariance matrix obtained from the simulation of a LSQ adjustment process. In particular, we simulated an orbit determination/improvement problem, in which we evaluated the influences of the position along the orbit of some observations series (2 or 3 tracklets, 4 only in the case with two observers) on the accuracies of the estimated parameters. The relative position of the two series of observations were chosen in order to cover all possible combinations of tracklets positions separated by 2.5° in true anomaly. Tests were carried out using intervals between tracklets smaller than 2.5° but the narrower sampling did not show further features. The results of the simulations allowed us to create an uncertainty map for each estimated parameter, which shows the uncertainties as a function of the position of the first

series of observations and the separation in time between the series.
At the beginning, this analysis was performed for a simplified scenario without estimating the complete set of parameters using an observer in the center of the Earth. Such simplification of the problem allowed us to better understand what kind of results are achievable, the influence of the time interval between tracklets and what the limitations of the parametrization are.
Then we introduced the parameters which describe the orientation of the orbital plane in the space.
Subsequently an observer on the Earth's surface was introduced in the LSQ process. This study was repeated for different observer positions and different kinds of orbit. This first part of the study allowed us to understand which are the main factors which influence the accuracies of the estimated parameters. The key factors are:

- the time interval between tracklets, especially the effect on $a$, $e$, and $\omega$ if the observations are performed within the 1st orbital period or in the successive ones if performed with 1.5 orbital period of time distance ($S$-region).
- the object-observer topocentric distance,
- the parallax angle due to the movement of the observer in the space,
- the relative position of the observer w.r.t. the orbital plane, it was shown the effect on $a$, $i$, and $\Omega$ of the observations performed by an observer within the orbital plan w.r.t. those performed by one outside.
- the distance of the observations from the line of the nodes and the line of the apsides, which effects are evident in $i$ and $\Omega$.

Successively, more complex scenarios are analyzed. The case of two observers which are observing the same object is studied first; secondly, the case of three series of observations is analyzed and thirdly the consequences of using also range measurements are analyzed. Apart from the obvious improvements given by the higher number of observation processed, the main advantages given by the second observer can be summarized in the capability to estimate distances of the object from the observers. This effect is quite evident in the case of synchronous observers and it is directly proportional to the amplitude of the parallax angle given by the pointing directions of the observers to the object position.
The case of two observers who are not observing the target at the same time was also studied. This examples showed a trend in the achievable accuracy: if the time delay between the two observers is relatively short we have a reduction of the parallax effects. This reduction is proportional to the time delay between the two observers. On the other hand, if the time delay increase we have an improvement in the achievable accuracy given by the wider arc of orbit covered by the observations and by the combination of the effects already seen in the single observer case.
The analysis of the case with three series of observations showed that the main effects, noticed in the case of the two tracklets, are amplified by the relative combinations between the third and first or the second tracklet. These features occur respectively when the first two tracklets are in symmetric positions w.r.t. the line of the apsides and when one of the first two tracklets is at the maximum or minimum distance from the line of the nodes.

In the last test, the introduction of the range measurements showed how this different kind of observable helps the system in the estimation of $a$, $e$ and $\omega$, especially for short time distance between the series of observations.
Finally, it is worthwhile to mention the secondary effects on the uncertainty of the parameters given by:

- the angular distance between tracklets,
- the difference between orbital period and sidereal day,
- the total number of observations,
- the length of the tracklets and the distance between intra-tracklet observations,
- the inclination of the orbit,
- the eccentricity of the orbit,
- the length of the arc of orbit covered by the tracklet.

This study can be applied to more general situations, where more than two series of observations are available in order to optimize the survey/follow-up strategy for a given orbit or orbital regimes. However, it is important to notice that, since the uncertainty maps are “object-specific”, it is not possible to obtain a unique conclusion. Nevertheless they help understand which are the key factors and how they influence the OD accuracy. Furthermore the maps show where to observe a second time in order to minimize the uncertainty on the unknown parameters, based on the position of the first observation. Therefore they can be useful, depending on the needs of the users, to evaluate the gain of information given by a certain observation geometry.

# Chapter 5

# Fusion of Laser Ranges and Angular Measurements

## 5.1 Introduction

It is very well known that the accuracy of an orbit determination (OD) depends on: the number of observations, the length of the observed arc [44, 45], the observation geometry [46] and the accuracy of the observations. Therefore to improve the OD accuracy one can optimize the observation strategy, increase the number of observations and the length of the observed arc, and/or use different observables in addition to the classical angular measurements. It is quite common in the OD process to use range measurements together with the angular ones. The first kind of measurement can be provided by radar and by laser facilities. The main limit of the first is the size of the targets, while the main limit of the second is the weather dependency. Recent studies showed the possibility of successfully track space debris objects with 1 m level precision [14].

In this chapter we investigated the influence of merging the laser range and the angular measurements in the OD process. First, a description of what we need to take into account to process SLR measurements correctly is given. Then, we will show the results of the validation tests of our OD tool. Afterwards the issue of the different measurements relative weighting in the Least Squares LSQ adjustment will be addressed. Finally we will report the results obtained by merging real range and angular measurements in different scenarios for different orbital regimes. These tests were performed to identify the influence of the observation geometry, of the length of the observed arc and the effect of different kinds of observables on the estimated OE. For the tests only real data are used: the angular and part of the laser measurements were provided by the sensors of the Swiss Optical Ground Station and Geodynamics Observatory Zimmerwald owned by the AIUB, while the other ranges were provided by ILRS stations.

For convenience, the following list reports all the nomenclature used in this chapter:

- $c$ speed of light,
- $\Delta t_r^s$ light travel time,
- $\rho$ one-way range between the observatory and target at time $t_r$,
- $t_r$ time epoch of received time tied to UTC,

- $\delta_{rel}$ relativistic correction,
- $\delta_{ltt}$ light travel time correction,
- $\delta_{rot}$ correction due to the Earth's rotation and satellite motion in the inertial system,
- $\delta_r$ correction due to station eccentricity w.r.t. the reference point,
- $\delta_{RB}$ station range bias,
- $\delta_{CoM}$ satellite Center-of-Mass correction or satellite laser array offset,
- $\delta_{atm}$ atmospheric (tropospheric) signal delay,
- $\varepsilon$ remaining systematic or random system errors,
- $\vec{\omega}$ Earth's angular velocity vector in the inertial system,
- $\vec{\mathbf{r}}$ satellite position vector in the inertial system,
- $\dot{\vec{\mathbf{r}}}$ satellite velocity vector in the inertial system,
- $\vec{\mathbf{r}}_{\mathbf{r}}$ station position vector in the inertial system,
- $\dot{\vec{\mathbf{r}}}_{\mathbf{r}}$ station velocity vector in the inertial system,
- $a$ semi-major axis,
- $e$ eccentricity,
- $i$ inclination,
- $\Omega$ Right Ascension of Ascending Node,
- $\omega$ Argument of Perigee,
- $A/M$ Area to Mass Ratio,
- $\mathbf{x}$ vector of adjustment to the a priori values of the parameters to be estimated,
- $\mathbf{A}, \mathbf{A}^T$ First Design Matrix of observation partial derivatives w.r.t. the parameters to be estimated and its transpose,
- $\mathbf{W}$ weights matrix of the observations,
- $\mathbf{l}$ difference between the observations and the computed ones as a function of $\mathbf{x}$,
- $w_i$ weight of he $i$th measurement,
- $n$ number of observations,
- $\sigma_0$ a priori errors of the parameters to be estimated,
- $\sigma_\alpha$ standard deviation of the angular measurements,

- $\sigma_r$ standard deviation of the range measurements,
- $E$ error either in radial or along- or cross-track component,
- $u$ amplitude of the error sinusoid,
- $\theta$ angular rate of the error sinusoid,
- $t$ time,
- $\gamma$ phase of the error sinusoid,
- $m$ error drift,
- $q$ error offset,
- $M$ mean anomaly.

## 5.2 Satellite Laser Ranging

The Satellite Laser Ranging (SLR) is one of the geodetic techniques which started to be used intensively for OD purposes 50 years ago. It is the only geodetic technique which performs measurements in the visible part of the electromagnetic spectrum. The *"Satellite Laser Ranging and the Lunar Laser Ranging use short-pulse lasers and state-of-the-art optical receivers and timing electronics to measure the two-way time of flight (TOF) (and hence distance) from ground stations to retroreflector arrays on Earth orbiting satellites and the Moon"* [2]. The SLR products are mainly used for precise orbit determination (POD), for the determination of the Earth's gravity field [47], and for the estimation of geodynamical parameters such as the polar motion, the estimation of the station coordinates and the tectonic motions [41]. The SLR activities are organized and coordinated by the International Laser Ranging Service (ILRS) which provides laser data and their derived products to support the various research activities.

### 5.2.1 Main Characteristics

The main components of the SLR system are represented in Figure 5.1. The figure shows both the main components and the observation principle. The SLR system is made of two main components: the ground and the space segment. The ground segment includes: a high energy pulsed laser, an accurate time interval counter, a precise photon detector and a telescope. The two most used type of laser is the Neodym-YAG-Laser (Yttrium-Aluminum-Granat) [47]. This laser emits in the infrared part of the spectrum but to increase the efficiency of the detections the frequency is usually doubled to obtain the classical green light (532 nm for Nd:YAG) [27]. Usually lasers differ for their pulse-rate: the new generation of lasers emit pulses at high frequency and low energy, e.g. 0.4 mJ at 2 kHz; the traditional ones have a lower pulse-rate with a higher energy, e.g. 20 – 100 mJ at 10 Hz [2]. The high-frequency lasers produce higher precision data due to the shorter length of the pulses and the higher number of measurements per normal point while the high-energy ones have a better signal-to-noise ratio [47]. As we will see more in details later, the data derived from laser systems are distance measurements converted from time interval measurements. The other main components of the ground segment are the time interval counters and the detectors: the time interval counters are used to accurately measure the time-of-flight (TOF) of the laser-pulse, these are started by the outgoing laser beam and are stopped when the detectors identify the weak return signal (few or single photons). The usual accuracy of the time interval counters is of the order of 10 picoseconds [2]. The last component is the telescope which has to be fast and precise since it needs to track LEO satellites and the width of the laser beam is relatively small (e.g. $< 30$ arcsec for the SLR system of the Zimmerwald observatory). Since this is a general overview of the laser systems we will skip all other additional components of the ground segment: the kind of detectors, the ultra-stable clocks, the safety systems, the narrow-band filters and the components needed to have daytime observations; for further information refer to [47].

The other main component of the SLR systems is the space segment. Another big advantage of the SLR techniques is that they do not need an active payload on board of the satellite. The entire space segment is then reduced to a retroreflector or to an array of them. The retroreflector is a device which reflects the light back to its source with a minimum of scattering [48]. The retroreflectors which are widely used on board of satellites are the corner cubes. These are made of three mutually perpendicular intersecting flat and square surfaces, which reflect the laser light back directly towards the source, but slightly shifted [49]. There are three main kinds of corner cubes retroreflectors as shown in [50]. These can be classified as: hollow corner cubes, back-coated solid corner cubes and uncoated solid total internal reflection (TIR) corner cubes. All have different characteristics, their advantages and disadvantages. As said most satellites carry on board corner cubes but there are some exceptions: satellites like BLITS and METEOR-3M have a spherical glass retroreflector [2].

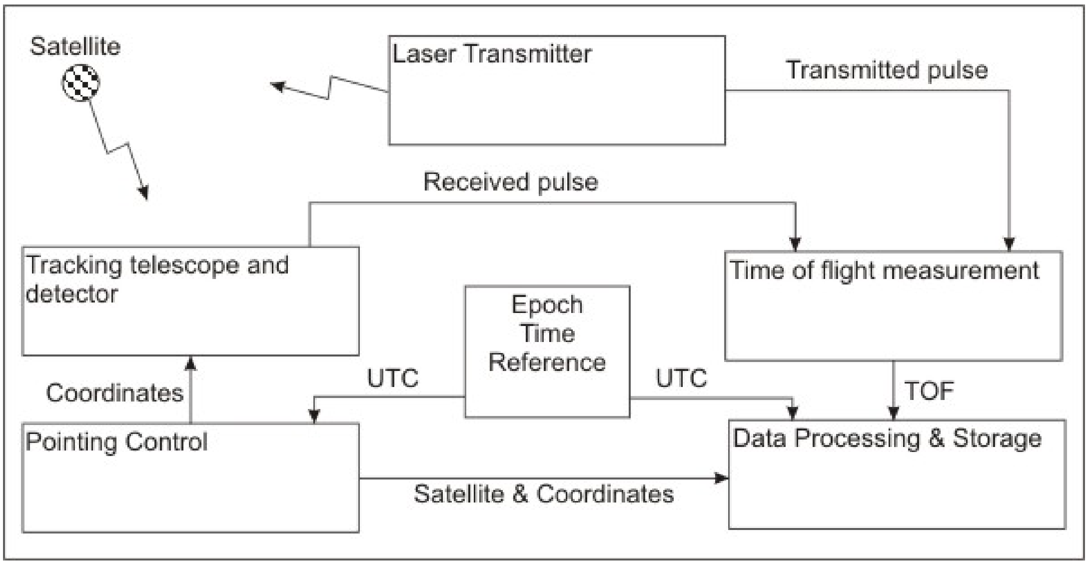

Figure 5.1 Basic scheme of the SLR system [2].

### 5.2.2 How It Works

The basic SLR measurement is the round trip travel time of a laser pulse between the station and the satellite and back to the station. This time measurement is then converted to a distance by multiplication with the speed of light. To achieve the desired level of accuracy of the SLR-products the measurements need to be corrected for several effects due to the propagation through the atmosphere, the general relativity, the relative motion between the satellite and the station. For the space debris orbit determination case, some of these errors and/or biases can be neglected, however a detailed description of the needed and applied corrections will be given in Paragraph 5.3.2.

One of the advantages of the SLR systems is that the measurements are done on ground and the satellite is a completely passive system. This means that the station starts the time interval counter when the pulse is sent and stops it when the pulse is received back after the reflection on the satellite. The main consequence is that there is no need to synchronize the clocks of the station with that of the satellite, as it is mandatory when one deals with GNSS measurements [51]. For completeness, it must be said that in most of the cases the SLR are two-ways ranging but there are also cases in which one-way ranging is used, e.g. in case of the Lunar Reconnaissance Orbiter (LRO) [2].

The two-ways light travel time ($\Delta t_r^s$) can be expressed as the sum of the time needed by the pulse sent from the station to reach the satellite ($\Delta t_1$) and the time needed by the pulse to reach the station, once reflected, to reach the station again. We can then express the light travel time as:

$$\Delta t_r^s = \Delta t_1 + \Delta t_2 = \frac{1}{c}\left[\left|\vec{\mathbf{r}}\left(t^s\right) - \vec{\mathbf{r}}_{\mathbf{r}}\left(t^s - \Delta t_1\right)\right| + \left|\vec{\mathbf{r}}\left(t^s\right) - \vec{\mathbf{r}}_{\mathbf{r}}\left(t^s + \Delta t_2\right)\right|\right], \tag{5.1}$$

where $t^s$ is the pulse reflection epoch. If we expand the receiver position at the different time epochs in the Eq. 5.1 via a Taylor series, and we neglect the higher order terms of the expansion we obtain the following expressions:

$$\vec{\mathbf{r}}_{\mathbf{r}}\left(t^s - \Delta t_1\right) \approx \vec{\mathbf{r}}_{\mathbf{r}}\left(t^s - \frac{1}{2}\Delta t_r^s\right), \tag{5.2}$$

$$\vec{\mathbf{r}}_{\mathbf{r}}\left(t^s + \Delta t_2\right) \approx \vec{\mathbf{r}}_{\mathbf{r}}\left(t^s + \frac{1}{2}\Delta t_r^s\right). \tag{5.3}$$

Assuming that $\Delta t_1 \simeq \Delta t_2$, then substituting the equations 5.2, 5.3 in the Eq. 5.1 and solving (neglecting the second and higher order terms of the Taylor series expansion) w.r.t. the two way light travel time ($\Delta t_r^s$), we obtain the relation between the measured time and the positions of the satellite and of the station at time $t^s$.

$$\Delta t_r^s = \frac{2}{c}\left|\vec{\mathbf{r}}\left(t^s\right) - \vec{\mathbf{r}}_{\mathbf{r}}\left(t^s\right)\right| \tag{5.4}$$

from which we have the basic observation equation for the SLR measurements:

$$\Delta t_r^s = \frac{2}{c}\left(\rho + \delta_{rel} + \delta_{atm}\right) + \frac{1}{c}\delta_{RB} + \varepsilon. \tag{5.5}$$

### 5.2.3 SLR Data

As just said, the laser ranging data consist in a time measurement of the laser pulse round-trip between the laser-pulse generator and the target satellite. There are two main kinds of derived ranging data: the full-rate and the normal points data [2].

The full-rate data are the original observations plus corrections. These were the primary SLR product till mid 1980's [2]. They are essentially the registration of the time epochs and the flight times of each single laser pulse generated by the station plus some parameters which give information about the station, the laser characteristics and the atmospheric parameters (i.e. temperature, pressure and relative humidity). Since the amount of collected data is relatively big, even more if we think about the new generation of high-frequency lasers, and the measurements are correlated especially within a short time distance, the full-rate data are usually used to generate the normal points which are the main SLR products since late 1980's. On the other hand the full-rate data are still used for specialized analyses like co-location analysis, Fizeau effect, center-of-mass algorithm development [2].

The normal points range measurements are generated by an averaging algorithm of the full-rate data collected over a certain time interval. The normal points are also called quick-look data since they are generated directly by the station shortly after the end of the satellite pass and transmitted to the data centers. Briefly the normal point formation process is divided in two main steps: the formation of range residuals from a trend function and data screening, and the real normal point formation. In the first part, the prediction residuals are generated differentiating the observations with the predictions. Then, a first screening to remove outliers is performed. The systematic trends of the prediction residuals are removed with a trend function, then the fit residuals of the trend function on the prediction residuals are calculated and the outliers are eliminated. The estimation of the trend function and of the fit residuals is iterated until the process converges. In the second part, the fit residuals are divided into fixed time intervals (usually called bins) whose size depends on the satellite processed. For each bin, the mean value of the fit residuals is calculated. Then, the nearest observation to the mean epoch of the bin with its fit residual is located, and the normal point is computed as the difference of the observation and its fit residual and summing the mean fit residuals value. Finally, the Root Mean Square (RMS) of the accepted fit residuals is computed for each bin. The normal points are then stored in a file with a particular format called Consolidated Range Data (CRD). Details about the CRD format is decribed in the appendix B.1.1. It must be said that the bin size or the standard normal point time interval is derived by the assumption of linearity of the measurements w.r.t. their predictions. For this reason the bin size is different for each satellite and it depends from its altitude. Therefore, for the lower satellites we will have short bin sizes which go from the 5 seconds of GOCE, CHAMP and GRACE to the 15 seconds of Cryosat-2 and Jason-2. The bin size for the MEO region varies from the 2 minutes of the LAGEOS satellites to the maximum of 5 minutes for GLONASS, GPS, IRNSS and ETALON satellites. For more detailed information about the SLR data and the normal points formation please refer to the International Laser Ranging Service website [2].

### 5.2.4 International Laser Ranging Service (ILRS)

The International Laser Ranging Service is a space geodetic service of the International Association of Geodesy (IAG) which was established in September 1998. The ILRS collects, archives, analyses and provides global satellite and lunar ranging data and their related products to support geodetic and geophysical research activities [2]. The service develops the necessary global standards and specifications, and coordinates a network of about 50 stations around the world (as shown in Figure 5.2).
The SLR and the lunar ranging data are mainly used to generate the following data products and to support a variety of scientific and operational applications [2]:

- Detection and monitoring of tectonic plate motion, crustal deformation, Earth rotation, and polar motion
- Modeling of the spatial and temporal variations of the Earth's gravitational field
- Determination of basin-scale ocean tides
- Monitoring the variations of the coordinates of the center of mass of the total Earth system (solid Earth-atmosphere-oceans)
- Establishment and maintenance of the International Terrestrial Reference System (ITRS)
- Detection and monitoring of post-glacial rebound and subsidence
- Station coordinates and velocities of the ILRS tracking systems
- Centimeter accuracy satellite ephemerides
- Fundamental physical constants
- Lunar ephemerides and librations
- Lunar orientation parameters
- Support the monitoring of variations in the topography and volume of the liquid Earth (ocean circulation, mean sea level, ice sheet thickness, wave heights, etc.)
- Calibration of microwave tracking techniques
- Picosecond global time transfer experiments
- Astrometric observations including determination of the dynamic equinox, obliquity of the ecliptic, and the precession constant
- Gravitational and general relativistic studies

For more detailed information about the ILRS products and activities please refer to the ILRS web page [2].

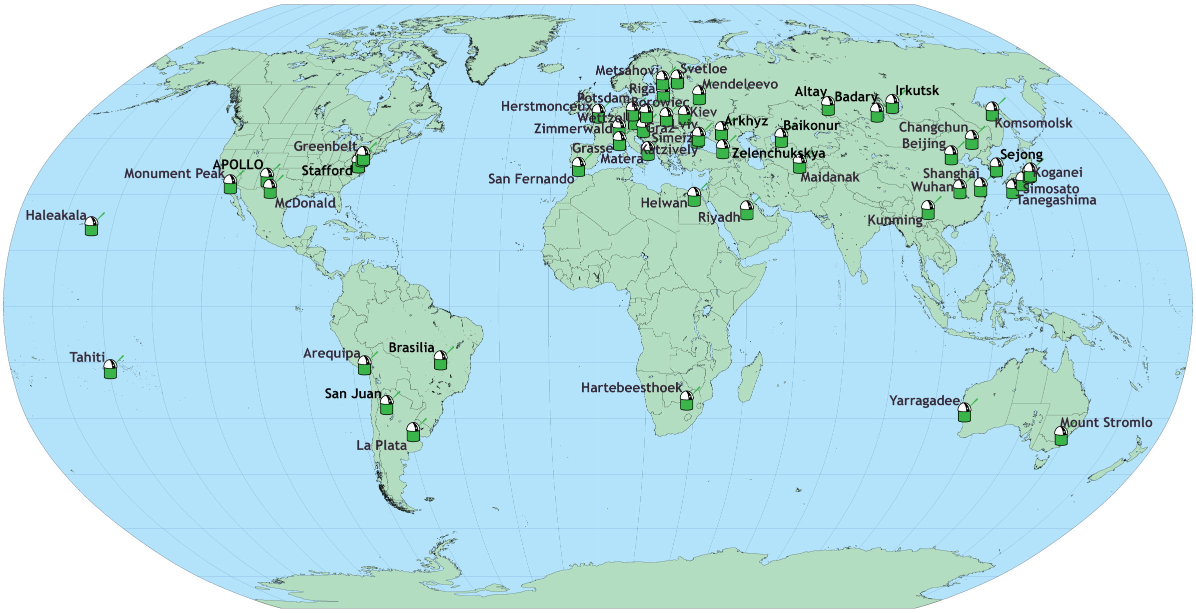

Figure 5.2 ILRS network [2].

### 5.2.5 SLR Limitations and Application to Space Debris

One way to improve the accuracy of predicted orbits to avoid unnecessary collision avoidance maneuvers is to use high precision measurements like the laser ranges. The success of the SLR technique for OD purposes is mainly due to the fact that the measurements do not need an active payload on board of the satellite and due to the very high accuracy of the derived ranges ($\sim 1$ mm) [15]. These are the two main reasons why the laser technique is also suitable for the OD of space debris.

Unfortunately, there are some limitations. The first limiting factor is given by the weather conditions. Since we exploit the visible part of the electromagnetic spectrum, we are able to observe only when the sky is clear. The second limiting factor is given by the capability of the target to reflect the laser pulse back to the station. For a generic object to be trackable by a laser system it has either to be quite big and rather low in altitude or it has to carry on-board retroreflectors array should be visible from the station. This means that the target should have either a stabilized and/or favorable attitude or it is entirely covered by retroreflectors (i.e. the case of geodetic satellites like LAGEOS, ETALON, LARES, etc.).

In the space debris field, the LEO upper-stages, due to their size, are suitable target for this kind of experiments. Nevertheless the proof that the attitude of the object has to be favorable even if the object carries a retroreflector was shown by the study of Silha et al. [52]. In this study, the estimation of the tumble axis direction of ENVISAT was confirmed by the fact that the satellite passes at the East w.r.t. the Zimmerwald station did not produce any laser returns since the retroreflector was not visible.

To exploit the high precision of the laser data it is necessary to apply correctly the Center of Mass ($CoM$) correction which is possible only if one knows the shape of the target, the displacement of the retroreflectors array w.r.t. the center of mass and the attitude of the target. This will inevitably limit the achievable OD accuracy in the space debris case.

The last requirement/limitation of the SLR systems is given by the aperture of the laser beam and the field of view (FoV) of the detector. These two apertures are relatively small, e.g. the aperture at the Zimmerwald observatory is $\leq 30$ arcsec [2] and the FoV of the detector is smaller and changes from night- to day-time observations.

This requires very precise ephemerides to be able to keep the object within the FoV. This last characteristics make the usage of the SLR techniques in the space debris field quite controversial. In fact, why should we use SLR measurements to improve the space debris orbit when the available ephemerides are already good enough to hit the object? Recent studies have shown the possibility to track space debris with lasers exploiting the images acquired by a CCD, CMOS or a tracking cameras to correct the pointing offset of the telescope w.r.t. the target position [32, 33].

It must be said that, due to their high precision, several applications of the SLR measurements in the space debris domain are possible. In this thesis we focus on the achievable improvements by using laser ranges in the OD process. The studies of Silha and Kucharski [52, 53] showed the possibility of the employment of laser measurement for the attitude determination of defunct satellites.

## 5.3 Implementation of the Software

The CelMech tool [16], in particular the part of the software called SATORB, which is used daily at the AIUB for OD, was able to handle only the classical RA and DE angular measurements. The first part of this work was dedicated to implement the capability to handle correctly the SLR measurements. To exploit all the advantages given by the high precision range measurements two main aspects of the tool needed to be improved: the first is related to the satellite orbit modeling, and the second to the corrections to be applied to the measurements.

The list of Perl scripts and Fortran subroutines modified and implemented for the SLR and angular measurements processing with their descriptions are reported in the Appendix A.

### 5.3.1 Background Models

The physical models used in the processing of the SLR data are summarized in Table 5.1 and were chosen consistently with those used by the Bernese GNSS Software (BSW) [54]. The table includes all the models used during the studies presented in this chapter. It must be said that, according to the analyzed case, the settings on the models are changed and more in general, some forces are neglected. As an example, for the gravity field, we considered up to degree and order 40 for orbiting objects whose altitudes are higher than 5000 km. But for LEO satellites, with altitudes less than 2000 km we increased the considered terms of the gravity field up to degree and order 70. Furthermore, when processing MEO and GEO satellites we disabled the atmospheric drag and the Earth's Albedo. Finally, it must be said that despite it is common habit in the precise orbit determination (POD) field to estimate empirical accelerations to compensate for deficiencies of the models [17, 55], all the orbit determination results shown in this chapter were obtained without estimating any empirical parameters. We intentionally renounced to the usage of the empirical parameters and pseudo-stochastic pulses since we were not interested in the achievement of the most accurate orbit, but we wanted to investigate the influence of the different observables in the parameters estimation.

Table 5.1 Models used for the processing of SLR and angular measurements.

| Type of Model | Description |
|---|---|
| Tropospheric delay | Mendes-Pavlis delay model with FCULa mapping function [56] |
| Atmospheric drag | Using MSISe90 model (only for LEO satellites) [57] |
| Relativistic Corrections | General relativity corrections<br>Shapiro effect according to IERS Conventions 2003 [37]<br>Schwarzschild acceleration<br>Lense-Thirring effect<br>Geodetic precession (DeSitter effect) [38] |
| Solar Radiation Pressure | Direct radiation: applied with a fix radiation pressure coefficient $C_R = 1.13$<br>Earth's Albedo (only for LEO satellites) |
| Tidal Forces | Solid Earth Tide Model [37]<br>Pole Tide Model [37]<br>Ocean Pole Tide [38]<br>Love numbers for ocean tides - FES2004 [58] |
| Loading Corrections | Ocean tidal loading: FES2004 [58]<br>Atmospheric tidal loading: Ray and Ponte [59] |
| Earth Gravity Field | EGM2008 [60] |
| Third Body | Earth's Moon, Sun<br>JPL Ephemerides DE200 [61] |
| Earth orientation parameters | IERS08 [62] |
| Subdaily pole model | IERS Conventions 2010 [38] |
| Nutation Model | IAU2000 [63] |
| Ocean Tide model | FES2004 [58] |
| Geodetic Datum | ITRF2008 [64] |
| Numerical Integration | Integration order: 12, Initial step size: 120 seconds, Number of iteration per step 1, Maximum error per Velocity component: $1 \cdot 10^{-10}$ m/sec, Collocation method [16] |
| Gravitational Constant ($\mu$) | 398600.4415 $\mathrm{km}^3 \cdot \mathrm{sec}^{-2}$ |
| Speed of Light ($c$) | 299792458 m/sec |
| Earth equatorial radius | 6378.137 m |

### 5.3.2 Correction of the Measurements

The second main part of the implementation consisted in the correct handling of the laser range measurements and the application of the needed corrections. The extended formula of SLR observations reads as follows [47]:

$$\frac{1}{2}c\Delta_r^s = \rho + \delta_{rel} + \delta_{ltt} + \delta_{rot} + \delta_r - \delta_{RB} + \delta_{CoM} + \delta_{atm} + \varepsilon, \tag{5.6}$$

where:

$$\delta_{rot} = \frac{\dot{\vec{\mathbf{r}}} + \vec{\omega} \times \vec{\mathbf{r}}}{c} \cdot (\vec{\mathbf{r}}_{\mathbf{r}} - \vec{\mathbf{r}}), \tag{5.7}$$

$$\delta_{ltt} = -\frac{(\vec{\mathbf{r}} - \vec{\mathbf{r}}_{\mathbf{r}})\left(\dot{\vec{\mathbf{r}}} - \dot{\vec{\mathbf{r}}}_{\mathbf{r}}\right)}{c}. \tag{5.8}$$

The term $c\Delta_r^s$ represents what is really measured by the station. It contains the effective geometrical distance between the station and the satellite ($\rho$) at time $t_r$ with a series of additional terms. The above mentioned corrections can be divided in three groups: the ones due to the signal propagation (i.e. $\delta_{rel}$, $\delta_{ltt}$ and $\delta_{atm}$), the ones related to the station which usually are constant over a longer period and do not depend on the target (i.e. $\delta_r$ and $\delta_{RB}$) and the last ones related to the satellite and its motion (i.e. $\delta_{CoM}$ and $\delta_{rot}$).
According to the theory of general relativity, the speed of light depends on the strength of the gravitational potential along its path. In our case, the Earth's gravity field produces a delay (Shapiro effect [37]) which is taken into account in the term $\delta_{rel}$. The $\delta_{ltt}$ corrects the aberration due to the movement of the station and of the target. It is generally called *light travel time* (or simply *light time*) since the light path is not a straight line between the the two objects [15]. The last correction of the first group, i.e. $\delta_{atm}$, corrects the delay in the propagation of the laser-pulse due to the atmosphere, more precisely to the troposphere. Usually this correction is divided in two components: a zenith path delay and a mapping function. They depend on the air temperature, the atmospheric pressure, the relative humidity and the observation direction which influences the "amount" of atmosphere crossed by the pulse. There are different tropospheric models to determine the delay of the signal in the visual part of the electromagnetic spectrum. The most used for the SLR measurements are those developed by Marini and Murray [65] and by Mendes and Pavlis [56]. In particular, the latter it is the one which is recommended by the ILRS and provides better results since it takes into account the hydrostatic and the non-hydrostatic components of the zenith delay and, within the mapping function, the refraction of the light due to the water vapor in the atmosphere.
The $\delta_r$, called *eccentricity*, accounts for the difference in position between the station reference point coordinates and the intersection between the elevation and the azimuth axis of the telescope which is the point from where the range is measured. The range bias ($\delta_{RB}$) contains the delays due to instrumental problems of the station or incorrect calibration measurements which should be constant over a satellite pass or for longer time periods. The biases can be corrected by using the ILRS SINEX data handling file which contains the time interval in which the station is affected by the bias and the amount of the bias [66].
The last group of corrections contains the $\delta_{rot}$ which compensates for the relative motion between target and station in the inertial frame and it must be applied if the setup of the observation

equations is done in an Earth fixed frame [47]. The final correction $\delta_{CoM}$ is needed to refer the measured range to the Center-of-Mass (CoM) of the target. This is needed since the laser pulse is reflected from the retroreflectors array on the surface of the satellite while its orbit refers to its CoM. For "simple" geodetic satellite the CoM it is approximately the radius of the sphere while for complex-shaped satellite (like TOPEX, GLONASS, etc.) this correction is defined by a three-components vector in the satellite-body reference frame. During our experiments, this correction will be applied only in the validation case for geodetic satellites. For all other cases this correction will be neglected since it is function of the shape and of the attitude of the object which are usually unknown parameters for space debris.

### 5.3.3 Modification to the LSQ

Finally, to complete the implementation of the SLR measurements in our tool it was necessary to adapt the part of SATORB responsible for the building of the normal equation system. In particular, the implementations concerned the partial derivatives of the new observable w.r.t. the parameters to estimate and the relative weighting of the different observables. Since the validation tests were performed using homogeneous measurements (only ranges), the problem of the relative weighting when processing together angles and ranges will be addressed in details later in Paragraph 5.5.1. The explanation of the adaptation of the specified subroutines is given in the Appendix A.

Regarding the partial derivatives of the observables w.r.t. the unknown parameters also the SATORB software uses Eq. 4.6.

Since the part of the derivatives of the target position w.r.t. the unknown parameters was already handled by the software, we needed to take care only of the implementation of the partial derivatives of the range measurement w.r.t. the satellite position. The implemented derivatives are the same showed in Eq. 4.2.3.

## 5.4 Validation

To check the correctness of our implementation we divided the test in two parts: the first concerning the application of the range-corrections and the second concerning the OD results. The validation of the ranges corrections was performed comparing the ranges, before and after their application, with those provided by the Bernese GNSS Software Version 5.2 [54].

The solution of our OD process was validated comparing the ephemerides obtained by the propagation of the orbit determined with real laser measurements (publicly available on the ILRS [2]) with the satellite positions provided by the ILRS. This comparison was repeated for four different satellites belonging to different orbital regimes, namely LARETS, LAGEOS 1, ETALON 1 and GLONASS 123. As can be seen from Table 5.2, the first belongs to the LEO regime while the others to the MEO.

Table 5.2 Orbital Elements of the satellites used for the validation.

| Orbital Elements | Larets | Lageos 1 | Etalon 1 | Glonass 123 |
|---|---|---|---|---|
| COSPAR ID | $03042F$ | $76039A$ | $89001C$ | $10041B$ |
| $a$ [km] | 7059.78 | 12265.2 | 25501.2 | 25505.4 |
| $e$ | $2.071 \cdot 10^{-4}$ | $4.467 \cdot 10^{-3}$ | $1.902 \cdot 10^{-3}$ | $3.567 \cdot 10^{-3}$ |
| $i$ [deg] | 97.896 | 109.898 | 64.114 | 64.892 |
| $\Omega$ [deg] | 11.148 | 133.163 | $-152.988$ | $-35.241$ |
| $\omega$ [deg] | 9.688 | 150.832 | 203.517 | 166.867 |
| $A/M$ [$m^2$/kg] | $1.5 \cdot 10^{-3}$ | $6.9 \cdot 10^{-4}$ | $1.04 \cdot 10^{-3}*$ | $2.90 \cdot 10^{-2}*$ |

$^*$ Estimated

### 5.4.1 Validation of Range Corrections

The validation of the ranges was performed comparing the values of the corrected range with those provided by the Bernese GNSS software. This comparison was performed evaluating each single correction at a time and excluding all the other possible sources of errors as those given by: the propagation, the dynamical model and the orbit estimation part. To exclude the influence of the parameters estimation we carried out the comparison during the first set up of the normal equation system (NEQ). In principle, the a priori orbital elements are used to generate the orbit which is propagated till the measurement epoch to calculate the observation residuals (observed minus computed, $O-C$). Already at this point some differences could be introduced by the orbit propagation. Two are the main causes of the error introduced by the propagation: the main component is due to the background model, which is not completely equivalent to the one adopted in the BSW, and the numerical integration part.
Although the integration method used by SATORB and by BSW is the same, in both cases we use in fact the collocation method to integrate the variational equations [16], in the BSW we use a fix step-size for the integration while in SATORB we use a variable step-size optimized as a function of the order of the integration polynomial and of the tolerance error on the satellite velocities. Of course, the difference due to the numerical integration are smaller than those given by the background model. On the other hand, tests showed that over 7 days of propagation already more than 20 cm of position error can be accumulated. To overcome this problem, we used the satellite coordinates provided by the BSW as input to the subroutine responsible for the application of the corrections (namely *RGCORR.f* see Appendix A). We were then able to check the correctness of the propagation of the station coordinates, the right application of the Earth orientation parameters (EOP) and of the corrections of the measurements. Since we exploited the same subroutines of the BSW to calculate the corrections, it was enough to compare the correctness of their inputs and finally the range before and after the application of the corrections.
For this reason in Table 5.3 we report an example of the results of this comparison. As previously said, it is common use in the BSW to calculate first the geometric range and then apply the corrections so that it can be compared with the real observation. First the comparison of the station coordinates (after the propagation and the application of the station eccentricity) is proposed, then we checked the obtained pole coordinates and true sidereal time of Greenwich which

will be used by *TOPSTA.f* to apply the relativistic and the light-travel-time corrections. The correction due to the tropospheric delay is applied within *TROPOS.f* which needs as inputs the station, the satellite coordinates, the laser wavelength and the weather data at the measurement epoch (namely temperature, relative humidity and atmospheric pressure). The range-bias and CoM corrections are read directly from a file. We report also the measurement time fraction used to “complete” the numerical propagation and then to correct the satellite position. Finally, the geometrical and the corrected ranges are shown. We can see how the values in the table are very close to each other, in particular, apart from the differences due to rounding, we have sub-millimeters difference in the station coordinates and between the ranges confirming that the application of the corrections is correct.

Table 5.3 Validation of the laser range corrections.

| Parameter | | SATORB | BSW |
|---|---|---|---|
| Station Coor. [m] | X | 4331283.376556 | 4331283.376160 |
| | Y | 567550.031096 | 567550.031410 |
| | Z | 4633140.429627 | 4633140.429704 |
| Pole Coor. [rad] | X | $4.264447763888022 \cdot 10^{-7}$ | $4.264447763888022 \cdot 10^{-7}$ |
| | Y | $2.205209272933186 \cdot 10^{-6}$ | $2.2052092729331858 \cdot 10^{-6}$ |
| True Sidereal Time [rad] | | 1.81847311072601 | 1.8184731107260097 |
| Meas. Time fraction [sec] | | $8.765667 \cdot 10^{-5}$ | $8.765700 \cdot 10^{-5}$ |
| Geo. Range [m] | | 7543515.5756690 | 7543515.5753968 |
| Corr. Range [m] | | 7543572.1095809 | 7543572.1093140 |

### 5.4.2 Factors Influencing the Orbit Determination Accuracy

The accuracy of the OD results depends on: the arc-length covered by the observations, the number of observations, their accuracy and the relative position of the object along its orbit w.r.t. the observer position. The relative observer-object geometry is, of course, influenced by the stations positions and the satellite orbit. The ILRS network is made of roughly 50 sites not homogeneously distributed and mainly located on the northern hemisphere, so it is not possible to have a homogeneous observation coverage of the satellites orbits. Furthermore the visibility of a satellite is influenced by its altitude and inclination. Especially for the LEO satellites, the visibility is the main factor that limits the amount of observations that can be collected [67]. On the other hand, having high-altitude satellites as in the upper MEO and GEO regions (from 20000 to 40000 km of altitude), which have very broad visibility windows, does not mean more observations since, in this case, the power of the laser of the station is the main limit for collecting observations. Summarizing, the altitude and the inclination of the orbit together with the distribution of the observing stations constitute a trade-off for the achievable OD accuracy. If on one hand, the visibility is limiting the accuracy, on the other hand the altitude is limiting the number of measurements. The best compromise in terms of number of observations and orbit coverage is given for the LAGEOS satellites which will be used as first validation scenario. The OD accuracy is also influenced by the altitude of the satellite since it determines the dynamical model of the forces used in the OD. LEO satellites are more sensitive to the higher degree and orders of the gravity field, to the atmospheric drag and the radiation of the Earth in terms of albedo and thermal radiation. Satellites at higher altitudes are more sensitive to the correct modeling of the solar radiation pressure. There are several methods to counteract the effect of the mismodeling like the set-up of empirical accelerations or scaling parameters for the estimation of the AMR and the ballistic coefficient. For completeness, we have to say that in all the OD performed in this study no empirical accelerations are used and no scaling parameters are estimated. Only in the case of Glonass 123 and Etalon 1 the AMR was estimated in a 6 months observation period, then the obtained value was used in the validation part, while the AMR of the Larets and Lageos 1 satellites were taken from [67].

The above mentioned factors drove the choice of the length of the observation arc, in particular we needed to select an amount of observations not too spread over time in order not to accumulate mismodeling effects but at the same time not too short in order to guarantee a good coverage of the orbit and not to be affected too much by the relative object-observers geometry. Since there are no specific guidelines about the selection of the arc-length we needed to determine it. First of all, we took the epoch of the positions given by the ILRS, this was used as our central time interval for the OD. Then, keeping the reference ephemerides in the middle of our arc of observations, we increased the time interval from which we collected the laser measurements used for the OD from 1 day up to 1 month (for the Etalon 1 case). At this point, an OD process was performed, and the determined orbit was used to generate the ephemerides within the fit span. The positions obtained at the same epoch of those provided by ILRS were stored and then compared. During these tests, all the available stations in the CRD-file were used and only a manual screening to remove the outliers was performed on the available observations.

### 5.4.3 Lageos Orbit Determination

The first validation test was performed on the Lageos 1 satellite. This was chosen because its altitude, about 6000 km, is a sort of compromise, since it is not too high to be reachable from almost all SLR stations and it has a nice visibility window which allows a pass length over a single station of more than 30 minutes. At the same time, its orbit is less sensitive to the higher terms of the gravity field (the gravity field used for the OD is up to degree and order 40 [47]) and is not influenced by the atmospheric drag. Table 5.4 reports the results obtained from the validation tests using Lageos 1 observations. In the first column, the observations arc-length is shown. In the second, the number of observations (normal points) used in the OD is reported. In the last three we report the mean position differences w.r.t. three ILRS analysis centers (namely SGF, JAXA and HTS), obtained from the comparison of 4 days of ephemerides generated within the fit span. For completeness, in the bottom part of the table we report the mean position difference between the centers, obtained averaging the difference between the ephemerides provided by the different centers.

Table 5.4 Lageos 1 results of validation tests.

| Arc-length | Num. of obs. | Mean Position Difference w.r.t. | | |
|---|---|---|---|---|
| | | SGF [m] | JAXA [m] | HTS [m] |
| 1 Day | 297 | 0.94 | 1.90 | 1.50 |
| 3 Days | 870 | 0.84 | 1.47 | 1.22 |
| 5 Days | 1427 | 0.81 | 1.36 | 1.14 |
| 7 Days | 2044 | 0.81 | 1.41 | 1.15 |
| 9 Days | 2553 | 0.83 | 1.17 | 1.05 |
| 11 Days | 3023 | 0.72 | 1.25 | 0.99 |
| 13 Days | 3595 | 0.71 | 0.91 | 0.82 |
| 15 Days | 4095 | 0.68 | 0.94 | 0.80 |
| 19 Days | 5034 | 0.78 | 1.03 | 0.93 |
| 23 Days | 5992 | 0.74 | 1.23 | 0.97 |
| | Mean position Difference between centers [m] | | | |
| SGF Vs HTS | 0.47 | | | |
| SGF Vs JAXA | 0.95 | | | |
| HTS Vs JAXA | 0.79 | | | |

As one can see from Table 5.4, the best OD results were obtained with the 15 days observation arc; in this case we have the minimum position differences w.r.t. the different centers and more important, the distance of our results is of the same order of magnitude as the distance between the centers themselves. It is easy to see also the “parabolic” behavior of the mean error that shows higher values for short arcs in which the observations are not enough and the geometry is not very good. At the same time, the error increases as the arc is getting longer; this is probably due to the deficiencies of the dynamical model and to the fact that we did not compensate them using empirical accelerations. These effects are even more evident in the following example, the Larets case.

### 5.4.4 LEO Orbit Determination

Table 5.5 shows the results obtained for 5 days of ephemerides comparison for the Larets satellite case. The number of observations used for the test is way smaller than the Lageos 1 case; this is due to the short visibility windows of the satellite mainly caused by its low altitude ($\sim$ 700 km). Furthermore, to process satellites at this altitude, one needs to increase the coefficients of the gravity field model (up to degree and order 70) and needs to take into account the atmospheric drag that is no longer negligible. Despite these modifications and improvements of the dynamical model, the mismodeling effects appears earlier than in the Lageos 1 case. In fact, the mean error increases again already after 7 days. Another evidence of the effect of a more complex dynamical model are the higher values of the obtained position differences both w.r.t. the centers and among themselves (from $\sim 1$ m of the Lageos 1 case to $> 10$ m).

Table 5.5 Larets results of validation tests.

| Arc-length | Num. of obs. | Mean Position Difference w.r.t. | | |
|---|---|---|---|---|
| | | SGF [m] | MCC [m] | HTS [m] |
| 1 Day | 102 | 16.12 | 64.34 | 109.77 |
| 3 Days | 290 | 14.41 | 56.21 | 83.60 |
| 5 Days | 529 | 12.95 | 47.40 | 67.32 |
| 7 Days | 835 | 11.43 | 39.27 | 66.47 |
| 8 Days | 942 | 11.88 | 39.43 | 65.93 |
| 9 Days | 1008 | 12.57 | 40.42 | 65.48 |
| 11 Days | 1199 | 14.17 | 41.16 | 64.30 |
| 13 Days | 1372 | 17.14 | 46.28 | 63.60 |
| | Mean position Difference between centers [m] | | | |
| HTS Vs MCC | 83.77 | | | |
| HTS Vs SGF | 77.13 | | | |
| SGF Vs MCC | 34.98 | | | |

### Modification Done for the Atmospheric Drag

When processing LEO satellites it is fundamental to consider the air drag in the satellite background model. The SATORB tool uses the MSISe90 atmospheric model to determine the atmospheric density, in particular the atmospheric density is calculated as a function of the solar flux and geomagnetic indices [57]. In SATORB there was the possibility to specify the average solar flux and geomagnetic index as input in the graphical interface. Since the solar flux constant changes from day to day and the geomagnetic indices are given with a 3 hours sampling, we wanted to evaluate the consequences of these approximations when processing observations distributed over an arc of several days. To do this comparison we needed to implement in SATORB the capability to use correctly these indices in particular, the MSISe90 model needs the daily solar flux index plus the average solar flux index of the last 90 days, the daily geomagnetic index, the 3 hours geomagnetic indices until 9 hours before the measurement epoch, the average of the 3 hours indices from 12 to 33 hours before the current epoch and the average of the 3 hours indices from 36 to 59 hours before the measurement epoch [68]. These procedure was implemented within *GTSFGMI.f.* Successively, we performed 3 different OD determinations on the same measurements for the same satellite (i.e. LARETS): the first neglecting the atmospheric drag, the second using the previous configuration of SATORB which uses the average indices and the last using the just mentioned implementation for the indices. As usual, after the OD the obtained orbit is integrated over the arc of observations and the generated ephemerides are compared with those provided by the OD centers (namely HTS, MCC and SGF). The resulting coordinate differences are shown in Figure 5.3. The OD was performed over an arc of 9 days of observations and the reported ephemerides coincide with the last 4 days of the observation arc. As shown in Figure 5.3, the average distance of the estimated orbit in the case where the effect of the atmospheric drag is neglected is bigger than 120 m for the entire propagation period w.r.t. all centers. The distance becomes smaller if we consider the atmospheric drag, in particular the average error w.r.t. the SGF center becomes 22.6 m if we consider the average indices given as input in the SATORB mask (as before the modification) and decreases to 9.7 m when the geomagnetic and the solar flux indices are applied properly. Apart from the case of the comparison w.r.t. MCC where the average error in both cases remains the same, also the comparison w.r.t. HTS shows an improvement of roughly 16 m for a correct use of the geomagnetic and solar flux indices.

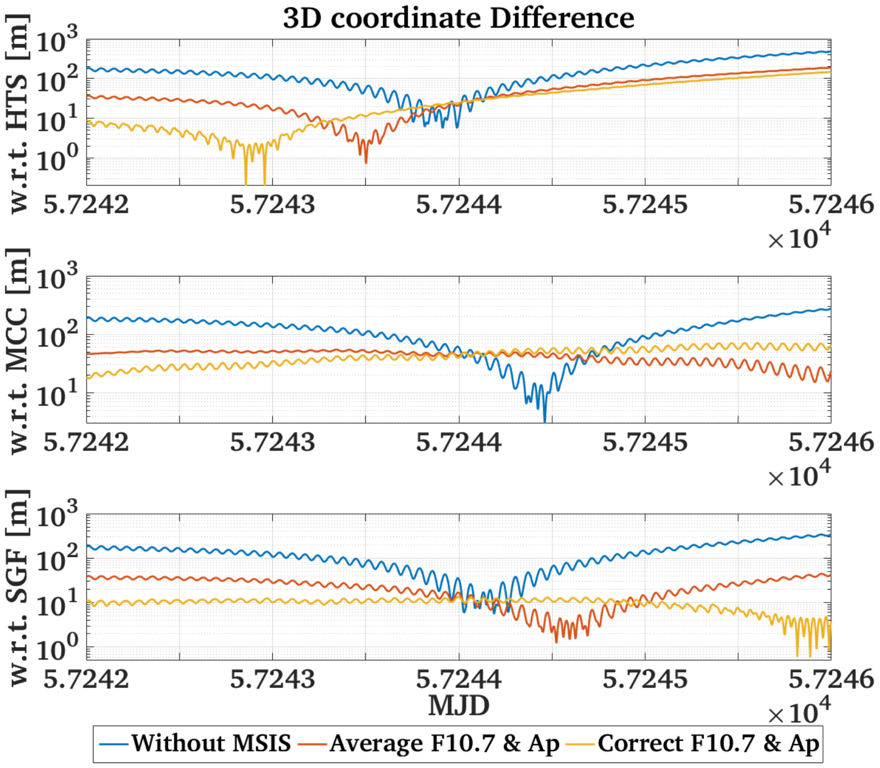

Figure 5.3 Evaluation of the influence of the geomagnetic and solar flux indices in the OD process.

### 5.4.5 Higher Altitude MEO Orbit Determination

The results of the validation test for the last orbital regime are shown in the Tables 5.6 and 5.7. For the MEO case we decided to report the results obtained for two different satellites, Etalon 1 and Glonass 123. The first is a classical geodetic satellite and, as in the previous cases, we have at our disposal all the needed information to be able to determine the level of accuracy available for this orbital regime. The second is a 3-axis stabilized navigation satellites with a more complex shape. This satellite was used to evaluate the consequences in the achievable accuracies when neglecting the attitude and the CoM corrections.
Although the satellites at $\sim$ 20000 km of altitude have nice visibility windows, the number

of observations available is even smaller than in the LEO case. This is essentially due to two main factors: the normal point bin size (5 minutes) and the fact that only a subset of stations belonging to the ILRS are able and focus on the tracking of high satellites. The main effects of the stations tracking capabilities are a smaller number of available observations and a poor distribution of the observations along the orbit. Although the dynamical model is simpler w.r.t. the previous cases, these factors reduce the achievable accuracy in the OD. In fact, the average error is higher than that obtained for Lageos 1. Since the AMR was not available in this case, we were obliged to estimate it before conducting the tests; to do so we took a relatively long arc of observation ($\sim$ 6 months) and we performed an OD estimating the AMR scaling factor as empirical parameter. The estimated AMR was then used as a priori value in the validation test and it was not further refined. As one can see from Table 5.6, the best results are obtained for an arc-length of 11, 13 days and the obtained mean error is of the same order of magnitude as the difference between the two centers. As we have seen before, the mean error increases again starting from 13 days. At the same time, it is possible to see that the error remains stable around 3.2 m. This effect suggests that the poor relative object-observer geometry and the smaller number of observations are the main causes of the limit in the OD accuracy and not the deficiencies in the dynamical model as in the previous cases.

Table 5.6 Etalon 1 results of validation tests.

| Arc-length | Num. of obs. | Mean Position Difference w.r.t. | |
|---|---|---|---|
| | | SGF [m] | HTS [m] |
| 3 Days | 71 | 2.99 | 2.91 |
| 5 Days | 135 | 3.47 | 3.05 |
| 7 Days | 189 | 3.56 | 3.07 |
| 9 Days | 302 | 3.15 | 2.47 |
| 11 Days | 377 | 2.82 | 2.45 |
| 13 Days | 468 | 2.86 | 2.50 |
| 15 Days | 527 | 3.10 | 2.73 |
| 19 Days | 634 | 3.17 | 2.73 |
| 23 Days | 734 | 3.39 | 2.96 |
| 27 Days | 869 | 3.24 | 2.84 |
| 31 Days | 995 | 3.19 | 2.70 |
| | Mean position Difference between centers [m] | | |
| SGF Vs HTS | 3.28 | | |

The last validation test, whose results are shown in Table 5.7, was carried out on a Glonass satellite which is in the same orbital regime as Etalon 1 (see Table 5.2). This test was carried out because in the case of Etalon 1 we do not care about the attitude of the satellite, since it is a sphere, and then the application of the CoM correction is relatively easy. For the case of a Glonass satellite we did not apply the CoM correction since it is time dependent and its correct application require the knowledge of the attitude of the satellite. This choice was made since for a generic space debris, we do not have any information about its attitude, about the position of the retroreflector, or about which part of the space debris reflects the laser pulse, therefore we can not estimate precisely the AMR. This test was carried out to evaluate how much these deficiencies will affect the OD results. In this case, 3 days of satellite positions every 15 minutes were provided by the CODE center. These ephemerides are obtained from the processing of radio-frequency measurements, therefore completely independent from the SLR ones. As in the Etalon 1 case, the number of usable observations is limited by the altitude of the satellite and the used AMR was estimated fitting 2 months of SLR observations. Although we used a mean AMR value and we did not apply the CoM correction, the best OD produced results whose accuracy is comparable to the Etalon 1 case.

Table 5.7 Glonass 123 results of validation tests.

| Arc-length | Num. of obs. | Mean Position Difference w.r.t. CODE [m] |
|---|---|---|
| 3 Days | 64 | 8.25 |
| 5 Days | 114 | 3.85 |
| 7 Days | 166 | 3.42 |
| 9 Days | 219 | 2.92 |
| 11 Days | 252 | 3.79 |
| 13 Days | 316 | 5.85 |
| 15 Days | 374 | 6.71 |

### 5.4.6 Comparison of SATORB Propagation versus BSW Propagation

The last validation test was performed comparing the ephemerides generated by the propagation of the results of an OD process carried out with SATORB with those generated by the BSW. The comparison was performed again using the measurements of Lageos 1 satellite. For the test, the same set of measurements, spread over 7 days of observation arc, were given as input to SATORB and the BSW, the OD was then performed without the use of any empirical accelerations and without estimating any scaling parameters. The determined orbits were then integrated over the fit span in the Earth Centered Inertial system (J2000) to generate a 2 minutes sampling set of ephemerides. The comparison of the two sets of ephemerides is shown in Figure 5.4. In particular, the left graph shows the radial, along- and cross-track differences of the generated ephemerides while the right graph shows the modulus of the three components. The "decreasing-increasing" behavior of the 3D distance is a consequence of the LSQ estimation which gives the best fit in the middle of the observations arc. Although the average distance, over the propagation period, is about 0.88 m which is of the same order of that obtained w.r.t. the different centers, we were expecting a smaller distance. To find out the reason of such distance we decided to split the problem again between OD part and orbit propagation. To test the orbit propagation we compared the ephemerides generated propagating the same set of orbital elements. This test produced the results shown in Figure 5.5 where it is clearly visible how the differences starting from a sub-millimeter level reach the 5 m level after 7 days of propagation. We can then confirm that the difference between SATORB and the BSW are mainly caused by the propagation part. As said before, two are the main components of the propagation error: the background model and the errors cumulated within the numerical integration. Tests where we changed the order of the integrating polynomial and the tolerances on the velocity error showed that over 7 days of propagation the differences introduced by the numerical integration is $\sim 16$ cm. We can then conclude that the differences between the SATORB and BSW results are essentially given by the background models. Further investigations are needed to find out which part of the background model causes these differences. However among the possible causes we have: the number of planets of the solar system considered for the third body perturbation forces, the correct application of the tidal forces, loading corrections and possibly also some small problems due to the EOP. Since for our study the achieved level of accuracy can be considered sufficient we did not further investigate the reasons of these differences, nevertheless one has to take into account that this problem has to be solved for future, more precise, applications.

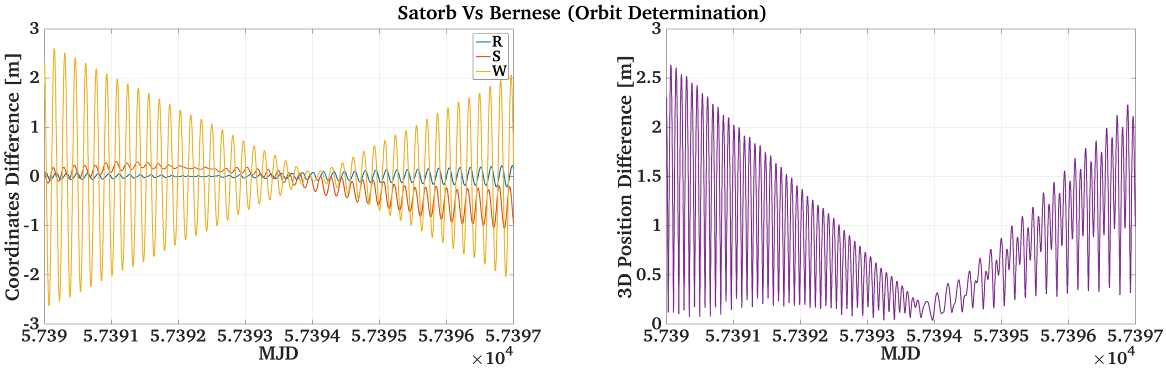

Figure 5.4 Comparison of the ephemerides obtained integrating the results of a SATORB OD with those of a BSW OD.

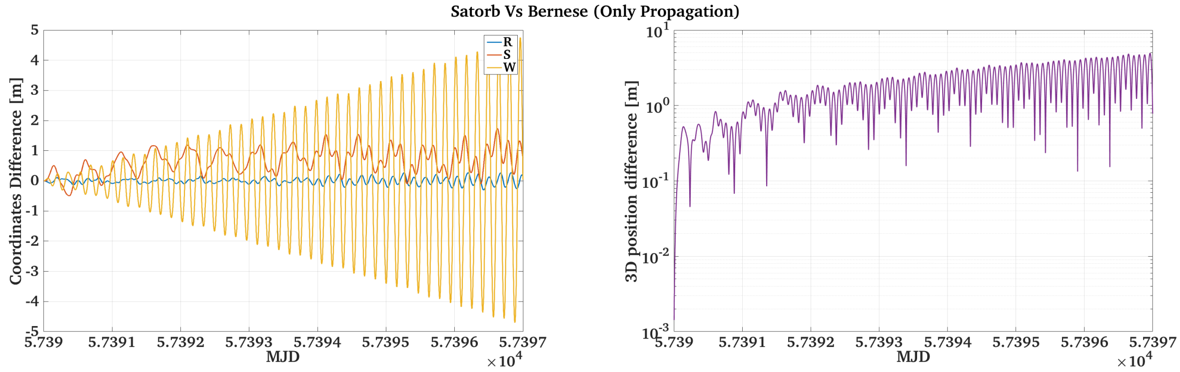

Figure 5.5 Comparison of SATORB and Bernese GNSS Software propagation starting from the same orbital elements.

## 5.5 Simultaneous Processing of Angular and Range Measurements

Before merging the ranges with the angular measurements, we needed to face the problem of their weighting within the normal equation system. The weighting of the different observations becomes necessary since the two observables have very different accuracy [26]. In this case, we need to make the system able to get the advantages of both measurements without ignoring one or the other.

### 5.5.1 Observables Relative Weighting

First of all we will recall for convenience the solution equation of a LSQ adjustment.

$$\mathbf{x} = \left(\mathbf{A}^T \mathbf{W} \mathbf{A}\right)^{-1} \mathbf{A}^T \mathbf{W} \mathbf{l}, \tag{5.9}$$

where the weight matrix is:

$$\mathbf{W} = \begin{bmatrix} w_1 & \cdots & 0 \\ \vdots & \ddots & \vdots \\ 0 & \cdots & w_n \end{bmatrix} \tag{5.10}$$

and each single weight is obtained by

$$w_i = \frac{\sigma_0^2}{\sigma_i^2} \quad \text{with} \quad \sigma_i^2 = \sigma_\alpha^2, \sigma_r^2. \tag{5.11}$$

Now, if one sets up $\sigma_0 = \sigma_\alpha$ we obtain a relative weight between the two observables where all angular measurements are weighted with 1 and the ranges are weighted proportionally to the ratio between the two standard deviations.

At this point, we calculate the relative weights using an initial guess value for the standard deviations of each observable. Typical value for the ZIMLAT telescope are of 0.5 arcsec for the angular measurements [45] and 1.5 cm for the normal point [2]. Since the astrometric accuracy are instrument dependent and the normal point accuracy are satellite and station dependent, the rough values of 1 arcsec for the angular ones and, of 3 cm for the SLR measurements were used. The selection of these values produces the following weights values: $w_\alpha = 1$ and $w_r = 2.6 \cdot 10^{-8}$.

Several tests were performed comparing the OD results obtained with only angular, only SLR and with merged measurements provided by the Swiss Optical Ground Station and Geodynamics Observatory Zimmerwald (from now on called simply Zimmerwald observatory). In particular, the evaluation was made comparing the ephemerides generated from different OD cases w.r.t. those obtained from a reference OD scenario. The reference orbit was obtained processing all available measurements both angular and laser from all available stations spread over a time period which contains the one for the study case. The reference orbit was then integrated, starting from the 1st observation epoch, over the entire fit span to generate the reference ephemerides. Several OD were carried out changing both the length of the observations arc (from 1 to 5

nights) and the observation geometry (e.g. only night measurements, or only angular during the nighttime and SLR during the daytime). These tests showed almost no difference between the cases of merged measurements and those using only SLR. This indicated that the angular measurements did not play a huge role in the OD process.
The suspicion was confirmed after a second series of tests. For these tests, only the observations (both angular and SLR) acquired from the Zimmerwald observatory for a specific satellite were used in the OD. At each run of OD we kept the observations used constant and we varied the SLR weights in a way to simulate STD values going from 1 mm up to 15 km. The standard deviation of the angular measurement was kept constant to 1 arcsec. The choice of these STD values to determine the weights for SLR measurements was made on purpose in order that the system will consider as little as possible those measurements. The OD results are then used to generate the ephemerides which will be then compared with the reference ones. An extract of the results, considering only 3 days of propagation, obtained from these tests is shown in Figure 5.6. In this example, the test was performed using Lageos 1 observations acquired in 5 days only during the night time. The differences in radial, along-track and cross-track components are obtained comparing the ephemerides generated from the determined orbit w.r.t. the reference ones. Figure 5.6 shows only the results obtained using the following a priori STD to calculate the weights: 5 mm, 5 cm, 50 cm, 5 m, 50 m, 500 m, 5 km. The figure contains also the results obtained from an OD with only SLR and only angular measurements which are respectively under the red/cyan and the yellow curves.

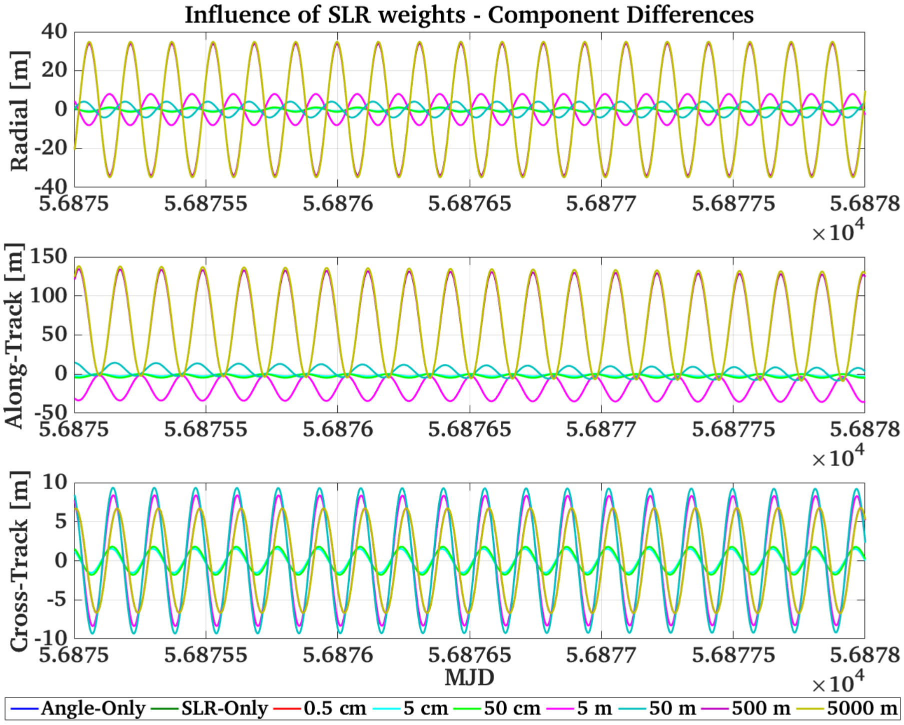

Figure 5.6 Position difference in Radial, Along- and Cross-track components obtained with different weighting of SLR measurements.

Unfortunately, from these results, it is not possible to define the most appropriate weight to give to the SLR measurements so that the system can profit from the benefits of the two kinds of observables. To answer this question, it was decided to characterize the errors curves exploiting their shape. In fact, if we consider a reasonable propagation length as the one in Figure 5.6 (i.e. 3 days), the shape of the differences among the components can be described by a biased drifting sinusoid, as shown by Eq. 5.12, neglecting the change of amplitude over time.

$$E = u \sin(\theta t + \gamma) + mt + q \tag{5.12}$$

It was decided to characterize the error in the RSW directions as a function of its amplitude, its drift and its offset, respectively $u$, $m$ and $q$. For simplicity, to estimate these parameters first a straight line was fitted through the differences between the ephemerides components and the total position error, the inclination and the offset of the line coincide with the drift and offset of the error ($m$ and $q$). Then the straight line is subtracted from the measured error to de-trend it and finally the amplitude was calculated as shown in the following equation:

$$u = \frac{\max[E - (mt + q)] - \min[E - (mt + q)]}{2}. \tag{5.13}$$

Figure 5.7 shows the drift, the offset and the amplitude of the error in the RSW components and the total position error obtained comparing the reference ephemerides with those generated by an OD varying the weights for the SLR measurements. In these plots are also indicated, with the horizontal green and red line, the drift, the offset and the amplitude of the error obtained using only angular and only SLR measurements in the OD. As expected, the results of the OD coincide with the laser-only solution in the case of low STD for range measurements (higher weight). On the other hand, increasing the STD on the SLR measurements, after a transition phase, the solutions tend toward the one obtained with the angles-only case. For all cases, the main component of the error is, as expected, in the along-track direction since the radial components of the error is constrained by the range measurements. The cross-track error is surprisingly small also in the SLR-only case. This effect is probably due to the fact that a good a priori orbit is used to initialize the LSQ and the orbital plane is determined indirectly exploiting the high precision of the SLR measurements and the exact knowledge of the observer position. These factors and the 5 nights of observations allow enough geometry changes that allow the correct identification of the orbital plane. In the cases of merged observations, the angular ones are of fundamental importance in the estimation of the orbital plane. As one can see from the comparison of the offsets and the amplitudes on each direction, the difference between the laser-only and the angles-only solution is less pronounced in the cross-track component than in the other directions.

The tests with different weights on the SLR measurements were repeated for different orbital regimes and different observation scenarios for the same object. In all these tests the transition phase between the laser-only and the angles-only solutions showed different behaviors confirming that the cause of it should be seen in the different relative geometry changes in combination with the weight given to each measurement.

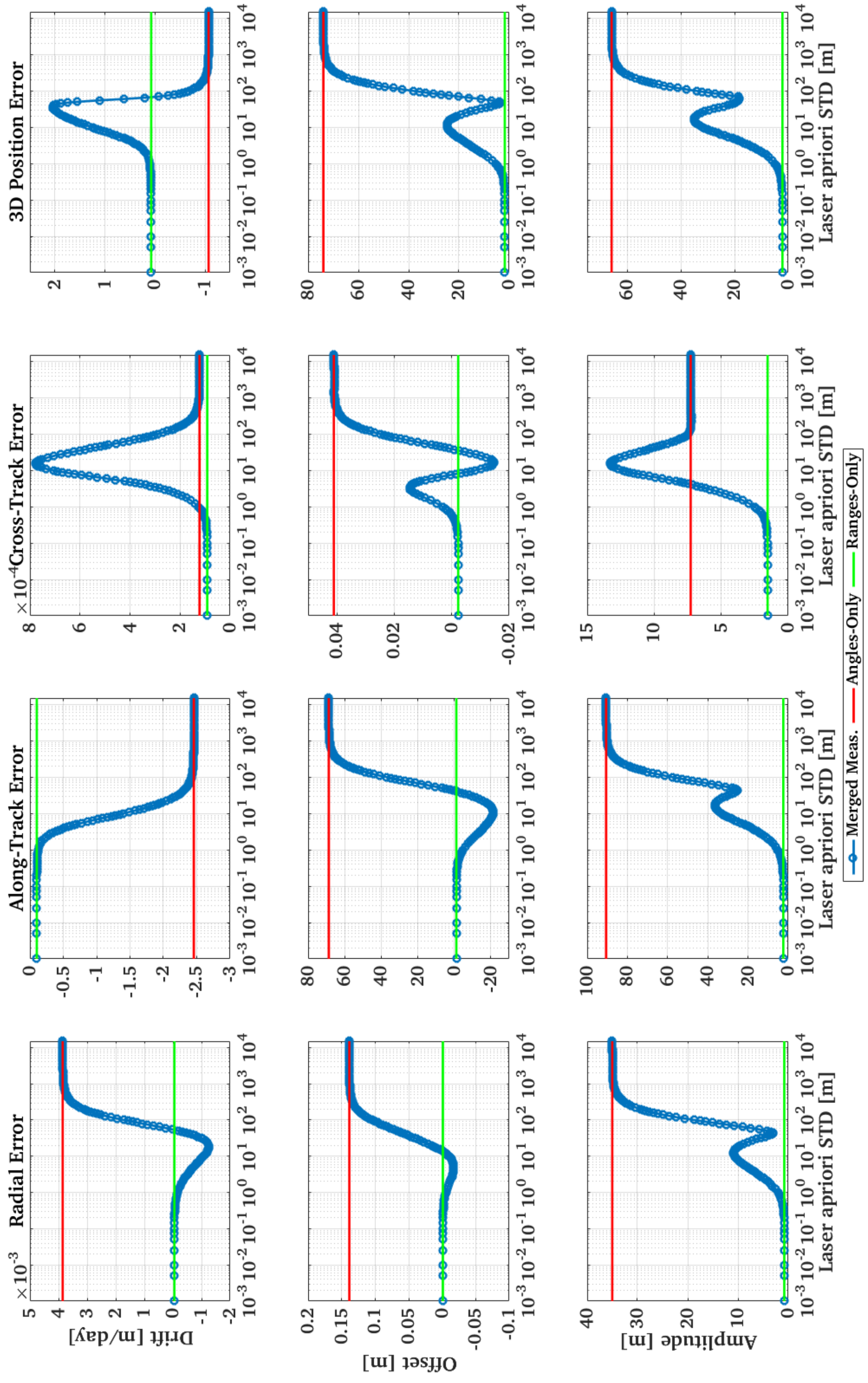

Figure 5.7 Results of error characterization for the runs varying the weights on SLR measurements.

### 5.5.2 Weights Determination

Finally coming again to our first question, these tests showed that the STD of 1 arcsec and 3 cm, respectively for the angular and the SLR measurements used for the weight determination, produced a solution almost coincident with the one obtained processing only ranges in the OD. It was then necessary to use other values to determine the weight in a more proper way. This problem was addressed both from the side of the angular and of the SLR measurements.
The astrometric accuracy of the Zimmerwald telescopes was estimated exploiting the observations acquired over satellites whose position is very well known and publicly available (i.e. GPS and GLONASS satellites). In particular, the astrometric positions in RA and DE of GNSS satellites are routinely acquired at the Zimmerwald observatory. These are then compared with the RA and DE coordinates calculated by precise ephemerides provided by CODE. As previously said, CODE is one of the GNSS analysis center which provides the orbits of GNSS satellites with accuracy in the order of 1.5 cm, which corresponds to an angle smaller than 0.0002 arcsec [69]. Due to their high precision and to the fact that they are estimated processing microwave observations (and thus completely independent from the telescope measurements) we can consider the orbits provided by CODE as the "truth". Figure 5.8 shows the position differences in terms of RA and DE for several GPS satellites observed in the night of 25th October 2015. As one can see the average difference in position between observations and CODE ephemerides is below 1 arcsec, only a few outliers can be seen. Usually, these position differences are used for the determination and then the calibration of the time bias of the observation system [70]. Figure 5.9 shows the time bias of the ZIMLAT telescope-system obtained from November 2014 to October 2015 where we can see how the value of the time bias remains always below 10 ms and the median value is about 2.4 ms over the entire period. The residuals obtained at the end of the time bias calibration process can be used to estimate the astrometric accuracy of the system itself. Figure 5.10 shows an extract of the residuals of the time bias calibration obtained for the ZIMLAT and ZimSMART telescopes which are daily used at the Zimmerwald observatory. After having screened the outliers from the residuals of the calibration process using the Median Absolute Deviation method [71], the resulting astrometric accuracies obtained for the Zimmerwald telescopes over 6 months of data are summarized in Table 5.8. In particular, the $2\sigma$ and $3\sigma$ values refer to the threshold, of respectively 2 and 3 time the median absolute deviation value, used to exclude the outliers. The screened data are successively averaged to obtain the values shown in the table.

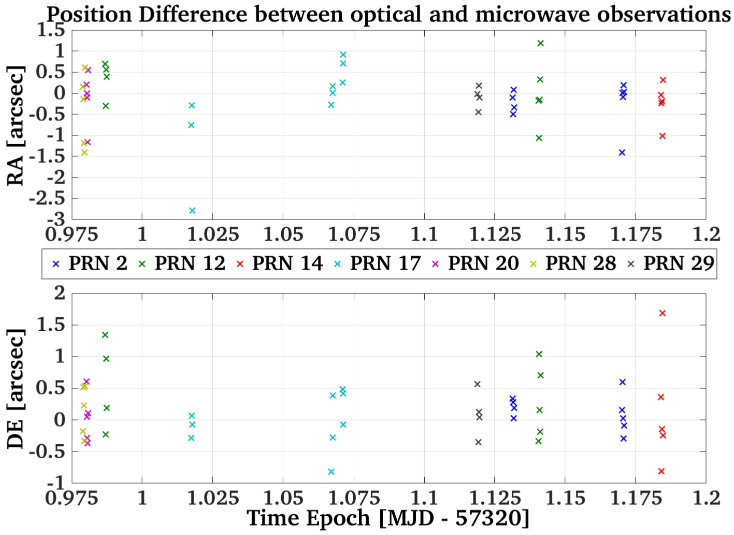

Figure 5.8 Comparison between RA, DE coordinates obtained from optical and microwave observation.

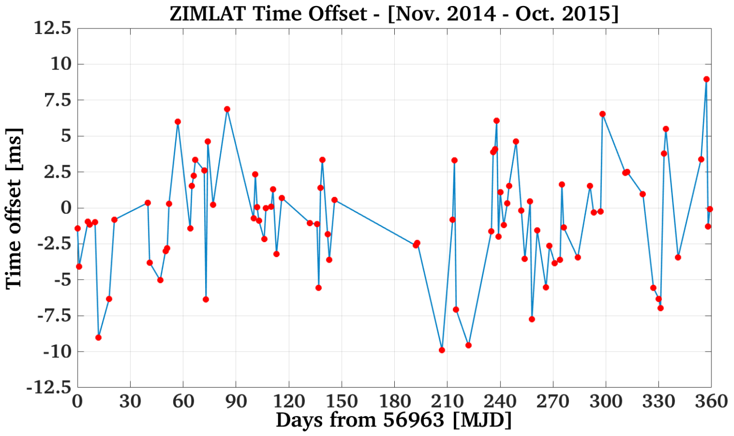

Figure 5.9 One year Time Offset obtained for the ZIMLAT telescope.

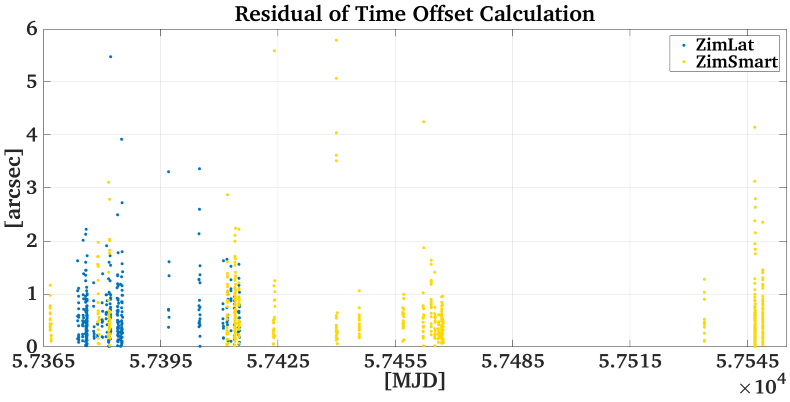

Figure 5.10 Angular Residuals after the time offset calibration.

Also for the SLR measurements we decided to extract the values used for the weight calculation from experimental data. In particular, we used the resulting a posteriori RMS per unit weight obtained at the end of the OD performed with only SLR measurements. Furthermore, this OD process was carried out without the estimation of any empirical force and of any scaling parameter. In this case, we do not have a unique value that can be used for all the following experiments since, as seen in Paragraph 5.4, the OD accuracy depends on the orbit altitude. It was then necessary to estimate a value per orbital regime. To do that an OD was performed taking into account all the available SLR observations over the time interval which gave, for the analyzed orbit, the smallest average position difference in Paragraph 5.4.
Since the tests shown in the following paragraphs are using angular observations which come exclusively from the Zimmerwald observatory, we can already say that the value used for the angular measurements in the weight determination is 0.5 arcsec while, the one used for the ranges will be specified for each case that will be analyzed. The selected astrometric accuracy correspond to the worse accuracy obtained in Table 5.8.

Table 5.8 Astrometric accuracy of Zimmerwald telescopes.

| Telescope | Mean astrometric accuracy [arcsec] | |
|---|---|---|
| | $2\sigma$ | $3\sigma$ |
| ZIMLAT | 0.46” | 0.50” |
| ZimSMART | 0.41” | 0.45” |

## 5.6 Orbit Determination Results

At this point, we are ready to analyze the influence of the SLR measurements on an OD process based on angular measurements. With these tests we tried to understand the influence of the relative observer-object geometry, the number of observations and number of follow-ups. These tests were repeated for different orbital regimes to investigate the influence of the different observables on each orbital parameter. It must be said that the main part of the results showed in the following paragraphs refers to the Lageos 1 satellite. This choice was made since, as we have seen in Paragraph 5.4, this satellite-orbit combination gives the best compromise in terms of visibility and number of observations allowing us to play easily with the different observation geometries. Finally, always for different orbital regimes, we will show the achievable improvements of an OD with 3D measurements (RA + DE + ranges) w.r.t. the angles-only solution and how the use of 3D measurements will allow us to save time for future catalog maintenance application. The just mentioned topics will be addressed separately in the following sections.

### 5.6.1 Influence of the Arc Length

The first series of tests was performed to evaluate the influence of the length of the observed arc. Only the observations (both SLR and angular) acquired by the Zimmerwald observatory for a total of 5 days of observations spread over 18 days will be used. For this experiment, only the SLR observations acquired during the night-time after the first angular measurements are taken into account (the measurements time epoch is within the $MJD - 0.25$ and $MJD + 0.25$ of the observation night). This choice was made to simulate an active tracking of space debris. The considered object is the Lageos 1 satellite, so the STD used to determine the weight of SLR measurements is 55 cm (together with 0.5 arcsec for the angles). As mentioned before, this RMS is obtained from an OD performed using only normal points spread over an observation arc of optimal length. The OD is carried out without using any empirical acceleration to compensate the deficiencies of the dynamical model. It must be said that 55 cm of RMS for a LAGEOS orbit is a very high value compared with geodetic standards [47]. Nevertheless we decided to use this value for several reasons: for consistency w.r.t. our solutions, for the differences highlighted in Paragraph 5.4.6, and for the fact that such high level of accuracy was not needed to carry out the following studies.

This test was carried out performing an OD covering an increasing observation arc from one pass up to 5 observation nights. For each observation arc an OD is performed first, using only angular measurements (2D), then merging angles and ranges, and finally for completeness with ranges-only (1D). For each OD the ephemerides were generated and compared with those obtained from the reference orbit. The comparison period is coincident with the reference orbit which starts 8 days after the last observation night and lasts 5 days. This time distance was chosen on purpose to evaluate what was the committed error for the target object after roughly one month from the first observation. The reference orbit was generated performing an OD using all possible laser observations over 5 days from all available stations to get rid, as much as possible, of geometry dependencies. These observations were provided by the ILRS.

The mean error of the ephemerides generated by the OD results w.r.t. the reference ones are summarized in Table 5.9. In the table, it is possible to see: the number of observations used in the OD separated by type (1D for SLR and 2D for RA and DE), the errors separated by components (radial, along-track and cross-track, namely R, S and W) and the total position error in meters obtained for different arc-lengths. In the 2D observations counting we counted the number of epochs for which a couple of RA, DE measurements is available. We did not report the number of observations used in the OD with 3D measurements as it is given by the sum of the number of 1D and 2D observations.

Table 5.9 Results of the influence of the arc-length test for Lageos 1.

| Days of Obs. | | 1Pass | 1 | 2 | 3 | 4 | 5 |
|---|---|---|---|---|---|---|---|
| # of obs. | 1D | 14 | 50 | 57 | 100 | 134 | 169 |
| | 2D | 18 | 59 | 63 | 83 | 97 | 101 |
| R [m] | 1D | 60.5 | 0.61 | 0.50 | 0.74 | 0.83 | 0.80 |
| | 2D | 19.7 | 16.4 | 13.1 | 17.0 | 21.9 | 22.0 |
| | 3D | 4.10 | 0.43 | 0.54 | 0.89 | 1.06 | 1.06 |
| S [m] | 1D | $2.0 \cdot 10^4$ | 15.8 | 13.9 | 3.92 | 3.41 | 1.65 |
| | 2D | $1.9 \cdot 10^3$ | $2.5 \cdot 10^3$ | 53.2 | 34.5 | 44.5 | 44.7 |
| | 3D | $3.0 \cdot 10^3$ | 55.6 | 12.2 | 2.90 | 2.56 | 2.32 |
| W [m] | 1D | 47.9 | 11.6 | 11.5 | 9.67 | 0.74 | 8.52 |
| | 2D | 23.1 | 11.8 | 8.14 | 7.73 | 17.0 | 6.80 |
| | 3D | 10.7 | 11.3 | 11.4 | 9.59 | 9.27 | 8.42 |
| Total [m] | 1D | $2.0 \cdot 10^4$ | 20.2 | 18.7 | 10.9 | 10.4 | 8.88 |
| | 2D | $1.9 \cdot 10^3$ | $2.5 \cdot 10^3$ | 56.4 | 42.6 | 54.3 | 54.6 |
| | 3D | $3.0 \cdot 10^3$ | 57.0 | 17.3 | 10.5 | 10.1 | 9.11 |

1D = SLR, 2D = RA & DE, 3D = SLR + RA & DE,

With these tests we would like to focus the attention on the comparison between the results obtained with the classical angular-only case and the one with 3D measurements. The ranges-only case was added for completeness and to have a general overview that allowed us to understand better the other results. Furthermore the sometimes more precise orbit obtained in the 1D case was possible because, for convenience, we used the SLR measurements to improve an already good a priori orbit. This is the only reason why it was possible to obtain the convergence of LSQ especially in the 1-pass case. In fact, in this case, being the ranges one dimensional measurement, if the geometry, given by a second station, or the angular measurements are not available, it is impossible to estimate the orbital plane. Despite the good a priori orbit, the ranges-only solution (1D), shows the highest errors of the entire set of tests.
Looking now at the error components, there are two main remarks that can be done: first, the error component on the along-track direction is the biggest among the three (especially for the 1-pass case); second, the smallest cross-track error is obtained for the 2D case. The main reason of the first can be easily explained if we look at the 1-pass case: here, the radial component is constrained by the measurements themselves but at the same time the observed arc is too short to estimate correctly the semi-major axis, the eccentricity and the perigee passing time. These parameters are so correlated in this case that they can be adjusted to fit perfectly the measurements but, at the same time, these are not enough to ensure the correctness of the estimation. The second effect can be explained by the nature of the used observables. In fact, the astrometric positions are just directions in the inertial frame, so even a series of them allows a relatively easy identification of the orbital plane orientation (namely $i$ and $\Omega$). The nature of this observable has another consequence: being only a direction, a single couple of RA and DE does not give any information about the distance of the object. This quantity can be in any

case estimated combining series of astrometric positions with the corresponding epoch. This phenomenon is reflected directly in the higher error obtained in the radial direction.
From these tests it is already possible to notice the huge impact of the SLR measurements on the orbit accuracy especially for the shortest arcs. Looking at the 1-night arc, for a total of two satellite passes, we have an improvement of two orders of magnitude from roughly 2.5 km of error to just 57 m. Then, always comparing the 2D case with the 3D one, increasing the arc the error is dropping down from roughly 2 arcsec (at the Lageos 1 altitude, 1 arcsec $\simeq$ 29 m) to less than 0.5 arcsec. The only exception to this trend is for the 1-pass case where the error of the merged solution, still remaining of the same order of magnitude, is bigger than the angles-only case. This is probably due to the fact that the number of observations for the 1D and 2D cases is almost the same, but being the laser ones much more precise than the angular the LSQ converges on a local minimum solution. Finally, one can see that due to the high number of SLR measurements, to the geometry changes obtained in the 18 days of observation arc and the $\simeq$ 6.4 revolution per day of the satellite, the 1D solution is of the same order of magnitude than the 3D one and, for the case of 5 nights, it is even slightly better. Observing the value of the errors for the 1D and 3D case, we can make one last consideration. Starting from 3 nights there are not substantial changes in the error values. This is, probably, the precision limit with that geometry configuration before the error starts to increase again due to mismodelling effects.

### 5.6.2 Influence of the Number of Measurements

In the previous Paragraph (5.6.1), we considered all the observations coming from one station but limited to a certain period of the day. Already in this scenario the SLR observations, probably due to their high number, play a big role especially with the increase of the observation arc. In the following tests we want to reduce this effect and see the influence of a handful of SLR measurements (per pass) associated with angular ones. This test was performed to simulate a more realistic environment of debris tracking where, due to the shape of the object and its attitude, it is not possible to have the same amount of observations as for a regular geodetic satellite, even if the target carries a retroreflector on board. To do it, the previous test was repeated using just a small fraction of the observations available, as can be seen from Table 5.10. As in the previous case, the observations used were acquired only from the Zimmerwald observatory.

Table 5.10 OD Results for Lageos 1 varying the arc-length using sparse range measurements.

| Days of Obs. | # of Obs. | | Mean error w.r.t. the reference orbit | | | |
|---|---|---|---|---|---|---|
| | 1D | 2D | R [m] | S [m] | W [m] | Total [m] |
| 1Pass | 3/14 | 18 | 30.62 | 4614 | 25.03 | 4614 |
| 1 | 6/50 | 59 | 3.11 | 1144 | 9.64 | 1144 |
| 2 | 7/57 | 63 | 0.693 | 3.48 | 12.95 | 13.76 |
| 3 | 11/100 | 83 | 2.40 | 27.10 | 13.08 | 30.85 |
| 4 | 12/134 | 97 | 4.39 | 25.02 | 8.72 | 27.44 |
| 5 | 13/169 | 101 | 4.88 | 30.02 | 9.09 | 32.27 |

The second column of Table 5.10 shows the number of SLR measurements used over those available. Comparing the obtained results with those shown in the last line of Table 5.9, we can see, as expected, that except for the 2 observation nights case, the error w.r.t. the reference orbit increases due to the reduction of the number of observations. At the same time it is important to notice that this is not so crucial. In fact, again with the exception of the 1 night case, the errors remain of the same order of magnitude. This experiment confirms the advantage of using SLR ranges. Excluding the 1-pass case, although we used just a tenth or even less of the observations available, we were able to obtain results at least two times better than in the angles-only case; this factor is of importance if one wants to optimize the observation time.
From the previous example we have seen that a higher number of observations produces better results. Is it always like this? In principle yes but, at the same time, the distribution of the observations and the relative object-observer geometry are also very important. In the following Figure 5.11 and Table 5.11 the ephemerides distance w.r.t. the reference orbit are shown. These were obtained from an OD using only the observations, for the Lageos 1 satellite, coming from the Zimmerwald observatory. In these runs only the observations coming from one satellite pass are taken into account. The total length of the pass is about 40 minutes. While the ranges are homogeneously distributed over the entire pass, the angular ones are concentrated in the middle of it and cover only 5 minutes of the pass. The difference among each runs relies in the number of range measurements considered and their distributions. In the figure each color is associated with a different number of ranges taken into account in the OD process: from 0 (angles-only) to 19, that was the maximum number available for the selected pass. There are two lines that refer to the same number of ranges used, namely “Mer. 3 s, m, e” and “Mer. 3 rng”. In these runs only three ranges are used, the difference between the two is in the distribution of those measurements over the pass. In the first, the ranges are one at the beginning, one in the middle and one at the end of the angular measurements. In the second, are just the first three ranges available after the first epoch of the angular measurements. In all the other cases, the considered ranges are selected in chronological order since the first angular measurement. The only exception is given by the “Mer. all obs.” case, where all the observations available in the pass are considered and then even those before the angular ones.
Figure 5.11 and Table 5.11 show the effects of the distribution of the observations. As one can see, the best solution, in this case, is given adding 3 ranges, one at the beginning, one in the middle and one at the end of the series of angular measurements. The solution obtained using all ranges available (“Mer. all obs”), which coincides with the longest observed arc in this case, is more or less comparable with that obtained using only two ranges (“Mer. 2 rng”). The obtained errors, in these cases, are respectively $\simeq 4$ and $\simeq 5$ times bigger w.r.t. those obtained for the best solution (“Mer. 3 s,m,e”). The angle-only solution, due to the very short arc, gives the biggest error while the others, increasing the number of used ranges, produce better results getting close to the best solution but then they tend again toward the solution obtained using all observations available. This behavior is probably due to the fact that adding more ranges, due to their better distribution over the relatively short arc considered for the OD and their higher precision make the LSQ converge on a local minimum solution.
The same behavior is visible in Table 5.11. There, the effect of the range measurements can be seen comparing the radial component of the error (third column) obtained in the angles-only and in the 1-range solution, respectively reported in the third and forth row of the table. Only one range produces an improvement of two orders of magnitude. The same jump in the error is

visible comparing the one with the two ranges solution. Afterward, the improvements are less pronounced.
Concluding this section, we can say that the number of ranges used in the OD process is of fundamental importance together with their distribution and the object-observer relative geometry which we suppose is the main cause of the obtained plateau in the position error w.r.t. the reference orbit. Nevertheless, as shown in Table 5.11, the angular observations are fundamental in the determination of the orientation of the orbital plane in the space. In fact, comparing the error components obtained in the merged cases with those obtained in the angle-only case, the cross-track error show the smallest improvement.

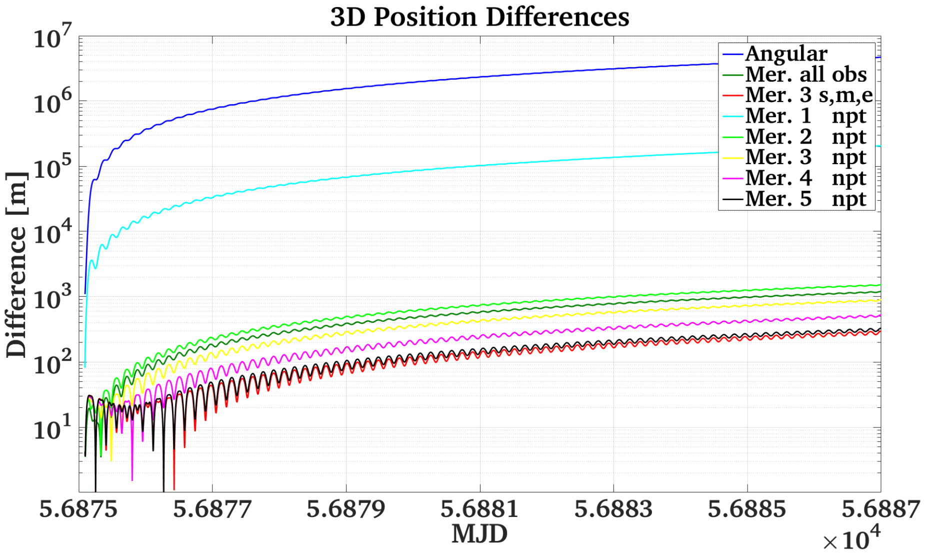

Figure 5.11 Ephemerides difference, w.r.t. the reference orbit, obtained with 1 pass of Lageos 1 orbit varying the number of used SLR measurements.

Table 5.11 OD Results from 1 pass of Lageos 1 from Zimmerwald observatory varying the number of used SLR measurements.

| # of Obs. | | Mean error w.r.t. the reference orbit | | | |
|---|---|---|---|---|---|
| 1D | 2D | R [m] | S [m] | W [m] | Total [m] |
| – | 41 | $5.925 \cdot 10^5$ | $3.263 \cdot 10^6$ | 604.1 | $3.324 \cdot 10^6$ |
| 1 | 41 | 995.7 | $1.461 \cdot 10^5$ | 83.55 | $1.461 \cdot 10^5$ |
| 2 | 41 | 7.42 | 1068 | 12.23 | 1068 |
| 3 | 41 | 6.33 | 620.2 | 12.14 | 620.8 |
| 3* | 41 | 5.20 | 194.9 | 12.07 | 193.3 |
| 4 | 41 | 5.63 | 356.9 | 12.10 | 357.9 |
| 5 | 41 | 5.26 | 217.6 | 12.07 | 218.9 |
| 19*[1] | 41 | 6.02 | 838.5 | 6.17 | 838.7 |

* 1 at the beginning, 1 in the middle and 1 at the end of the pass (s, m, e, in the Figure 5.11)

*[1] All available ranges

### 5.6.3 Influence of the Object-Observer Relative Geometry

Until now, both angular and laser measurements were provided by the Zimmerwald observatory. In this paragraph, we want to highlight the consequences of the relative object-observer geometry in the accuracy of OD results. Since we did not want to feed the system with synthetic observations, the angular measurements used in the following tests were provided by the Zimmerwald observatory while, the range measurements were provided by three SLR stations (namely Graz, Matera and Mt. Stromlo whose coordinates are given in Table 5.12).

These stations were chosen because they are among the most productive stations of the ILRS network, consequently there were more data available for the geometry tests and they are able to track even high altitude satellites. In the first series of tests we want to show the influence of a displacement of the station which provides ranges, while in the second we want to show the effects introduced by combining the angular measurements with the SLR ones provided by more stations. For the following test the data of the Glonass 123 satellite are used.

As mentioned in Paragraph 5.5.1, being this object in a MEO orbital regime, the $\sigma_r = 1.3$ m is used to determine the weight for the range measurements. This value coincides with the a posteriori RMS obtained from the OD performed over the arc of observations with the optimal length. This object was chosen especially for the reduced number of measurements available w.r.t. the Lageos 1 satellite. As usual, the tests were performed comparing the ephemerides obtained by an OD using a subset of measurements with those generated by a reference OD. To generate the reference solution we used 18 days of observations from all available stations both angular and SLR. The orbit so determined was then integrated over the fit span to generate the reference ephemerides. For the OD tests we used all angular measurements from the Zimmerwald station and all SLR measurements from the selected station/s available within the 18 days of arc. For both series of tests the time interval used for the comparison of the ephemerides coincides with the fit span used in the various ODs. Finally, for an easier comprehension of the following results, we report in Figure 5.12 the distribution of the observation within the fit span of the stations considered for the experiments.

Table 5.12 Coordinates of the stations used in the tests.

| Station | Geodetic Coordinates | | |
|---|---|---|---|
| | Latitude[°] | Longitude[°] | Elevation [m] |
| Zimmerwald | 46.8772 N | 7.4652 E | 951.2 |
| Graz | 47.0678 N | 15.4942 E | 495.0 |
| Matera | 40.6486 N | 16.7046 E | 536.9 |
| Mt. Stromlo | 35.3161 S | 149.0099 E | 805.0 |

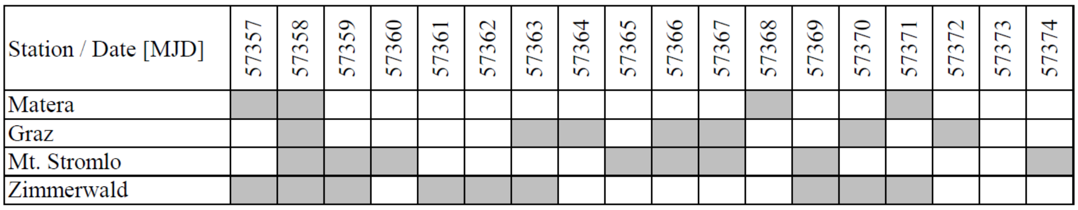

| Station / Date [MJD] | 57357 | 57358 | 57359 | 57360 | 57361 | 57362 | 57363 | 57364 | 57365 | 57366 | 57367 | 57368 | 57369 | 57370 | 57371 | 57372 | 57373 | 57374 |
|---|---|---|---|---|---|---|---|---|---|---|---|---|---|---|---|---|---|---|
| Matera | ▨ | ▨ | | | | | | | | | | ▨ | | | ▨ | | | |
| Graz | | ▨ | | | | | ▨ | ▨ | | ▨ | ▨ | | | ▨ | | ▨ | | |
| Mt. Stromlo | | ▨ | ▨ | ▨ | | | | | ▨ | ▨ | ▨ | | ▨ | | | | | ▨ |
| Zimmerwald | ▨ | ▨ | ▨ | | ▨ | ▨ | ▨ | | | | | | ▨ | ▨ | ▨ | | | |

Figure 5.12 Distribution of the observation used to study the object-observer relative geometry for the selected station.

### One Station Angular Data and One Station SLR, Different Relative Geometry

With this series of tests we wanted to see how data from a SLR station located somewhere else on the Earth impacts our solutions. Comparing the coordinates of the Zimmerwald observatory w.r.t. those of the other stations (see Table 5.12), one can see that Graz was chosen as representative of the effect of a shift in longitude and Matera as a generic shift both in latitude and in longitude. Both stations share with Zimmerwald almost the same visibility window for the considered satellite (Glonass 123) and then we can have angular and SLR measurements which are collected almost at the same time. The third station, Mt. Stromlo, was chosen since it does not share the visibility window with Zimmerwald and then will provide a completely different observation geometry.

The summary of the obtained results is reported in Table 5.13. The table shows the mean position difference and the mean difference of the osculating orbital elements. The mean differences in the radial, along- and cross-track directions are obtained, as usual, averaging the difference of the propagated positions w.r.t. the reference ones. The mean differences of the osculating orbital elements are determined averaging the difference of the osculating elements obtained by converting the generated state vectors at each available epoch. For completeness, the results obtained with an angles-only OD and the number of measurements used in the various OD processes are also reported. As one can see, the best solution is obtained merging the angular measurements coming from Zimmerwald with the SLR ones coming from Graz whose average total position error is less than 7 m.

Table 5.13 OD Results for one station angular and one SLR with different geometries.

| 10041B | | Angle-Only | Zimmer. & Matera | Zimmer. & Graz | Zimmer. & Mt. Stromlo |
|---|---|---|---|---|---|
| # of Obs. | 1D | – | 31 | 33 | 61 |
| | 2D | 63 | 63 | 63 | 63 |
| Mean Pos. Error [m] | R | 43.2 | 0.382 | 0.403 | 1.271 |
| | S | 90.3 | 13.60 | 2.165 | 12.58 |
| | W | 7.10 | 7.762 | 6.239 | 1.294 |
| | Tot. | 108.5 | 16.79 | 6.909 | 12.90 |
| Orbital Elements Mean Error | $a$ [m] | 0.389 | $9.404 \cdot 10^{-2}$ | $1.559 \cdot 10^{-2}$ | $7.990 \cdot 10^{-2}$ |
| | $e$ | $1.83 \cdot 10^{-6}$ | $1.200 \cdot 10^{-8}$ | $1.500 \cdot 10^{-8}$ | $3.400 \cdot 10^{-8}$ |
| | $i$ [°] | $2.38 \cdot 10^{-5}$ | $1.520 \cdot 10^{-5}$ | $1.270 \cdot 10^{-5}$ | $4.300 \cdot 10^{-6}$ |
| | $\Omega$ [°] | $8.30 \cdot 10^{-6}$ | $2.530 \cdot 10^{-5}$ | $1.990 \cdot 10^{-5}$ | $1.600 \cdot 10^{-6}$ |
| | $\omega$ [°] | $3.22 \cdot 10^{-2}$ | $3.484 \cdot 10^{-4}$ | $3.414 \cdot 10^{-4}$ | $1.144 \cdot 10^{-3}$ |
| | $M$ [°] | $3.22 \cdot 10^{-2}$ | $3.294 \cdot 10^{-4}$ | $3.286 \cdot 10^{-4}$ | $1.171 \cdot 10^{-3}$ |

Looking now at each single error component, we can notice that the errors in the radial direction obtained for the Matera and Graz case are comparable while the one obtained in the Mt. Stromlo case is 3 times bigger. On the other hand, in the Mt. Stromlo case one has the smallest cross-track error. Similar assessments can be done observing the mean error on the osculating elements. If one analyzes separately the parameters which describe the orientation of the orbital plane (namely $i$ and $\Omega$) and those which describe the orbit shape and the position of the object along the orbit (namely $a$, $e$, $\omega$ and $M$), we can see that the Mt. Stromlo case presents the lowest error for $i$ and $\Omega$ and the biggest for $\omega$ and $M$. The latter two parameters are, together with $a$ and $e$, the main responsible for the error in the along-track direction. We think that the smaller error in the orientation of the orbital plane and the higher one in the along-track directions is probably due to the different geometry. Comparing the Graz case with the Mt. Stromlo one, we can see that in the first, the observations are concentrated in one part of the orbit. In this case, the ranges and the higher density of observations improve the estimation of the semi-major axis. In the second, the bigger spatial distributions of the observations along the orbit will constrain better the orientation of the orbital plane. Finally, the interpretation of the difference between the Matera and the Graz case is more difficult. Comparing the error components we can see a larger error in the along-track direction of the Matera case w.r.t. the Graz one. Although the two cases have almost the same number of observations, probably, this higher error is due to the worse distributions of them over the considered arc. In the Matera case, just in the middle of the observation arc there are 9 days of gap where no measurements are available, while in the Graz case, the SLR measurements are more homogeneously distributed and no such big gaps are present. This worse distribution of the observations is probably the cause of the higher error in the semi-major axis which leads to the just mentioned difference in the results.

### One Station Angular Data and More than One SLR station

The previous tests showed the results achievable exploiting the ranges provided by one single station, in this section we analyze the impact on the OD given by observations from more than one SLR station. We wanted to face this problem because it is very well known that ranges, being one-dimension measurements, do not provide any information about the orientation of the orbital plane (at least not directly). At the same time, as it is common use in the geodetic community, using more than one station we can remedy to this deficiency. In particular, if we take one station whose position is known and a range, the satellite could be on every point on a sphere centered on the station with radius equivalent to the measured range. At this point, adding a second station whose position it is also known we constrain the satellite to move on the intersection of the two spheres. Adding now a second range for each stations we are able to identify the orbital plane. This series of tests was carried out using a combination of the observations used in the previous paragraph for the Glonass 123 satellite. In these tests we compared the results achievable using two SLR stations with those obtained adding also the angular measurements and finally with those obtained by all 4 stations together. It was possible to estimate an orbit starting from 2 SLR stations because their coordinates are known and an a priori orbit is used as input in the LSQ adjustment. These tests were performed also to highlight the benefits given by the angular measurement in the OD.

Table 5.14 shows the obtained results. As usual, in the first rows of the table the name of the test and the number of observations used, separated by kind, are reported. The “Graz & Matera” and the “Matera & Mt. Stromlo” are those tests carried out without using angular observations. Furthermore, the results of the test “Graz & Mt. Stromlo” performed using only SLR measurements are not reported as they will be similar to those of the “Matera & Mt. Stromlo” case. These two test cases show how the processing of ranges produce high accuracy results in the radial and along-track directions but at the same time, being the range one dimensional, show higher error in the cross-track component. Consequently the estimation of the orientation of the orbital plane is less accurate. However, the interaction given by a second station brings down the error to an acceptable level.

Looking now at all results, the obtained overall errors are relatively small for all cases. In fact, they are at least one order of magnitude smaller than the angles-only case (see Table 5.13) and the maximum average error over 18 days is 11.53 m.

Using a relatively large number of ranges we are able to reduce a lot the error in the radial and along-track directions.

Looking now at the error in the cross-track direction, we can see a smaller improvement w.r.t. the cases shown in the previous paragraph. Furthermore there are no cases for which a second or even a third SLR station improves the solution in this direction (between the series of tests shown in Table 5.13 and Table 5.14, the smallest cross-track error is obtained for the “Zimmerwald & Mt. Stromlo” case). We suppose that this is due to the bigger number of SLR measurements w.r.t. the angular one. This effect can also be seen looking at the case where the measurements provided by the 4 stations are processed together (“Graz, Matera, Mt. Stromlo & Zimmerwald” case). Against the expectations, this case did not produce the best results in terms of position error w.r.t. the reference ephemerides. As one can see from the Table 5.14, we obtained the smallest error in the radial and along-track directions but the overall position displacement is driven by the difference in the cross-track direction. This is probably caused by the fact that the ranges, due the their higher number, drive the LSQ solution but, at the same time, only 3 SLR stations do not provide enough geometry change to identify precisely the orbital plane.

One last thing which is interesting to highlight can be seen from the comparison of the "Graz, Mt. Stromlo & Zimmerwlad" case with the "Graz, Matera & Zimmerwald" one. These two examples show the smallest error in the cross-track direction. Furthermore looking at the error on the orbital elements, the first shows the smallest error in the inclination while the second in the RAAN. As it was anticipated previously, the displacement of the SLR stations and their number have an impact in the OD results especially in the accuracy of the parameters describing the orientation of the orbital plane. As for the "Zimmerwald & Mt. Stromlo" case (of the previous paragraph), the "Graz, Mt. Stromlo & Zimmerwald" one confirms the importance in the estimation of $i$ and $\Omega$ of the observations located in places diametrically opposite along the orbit. In the latter case, this effect is strengthened by the introduction of the Graz station.

The "Graz, Matera & Zimmerwald" case, instead, shows that two SLR stations, which are sharing almost the same visibility window with the satellite and can acquire measurements almost at the same time, will set stronger constraints to the orbital plane via the triangulation of ranges w.r.t. to the single SLR station case. At the same time, this constraint is weaker than the just above mentioned case since the displacement of the two stations and the introduced parallax w.r.t. the orbital plane are relatively small.

Finally, one could ask: why the "Matera, Mt. Stromlo & Zimmerwald" case, although their geometry is similar, produces slightly worse results than the "Graz, Mt.Stromlo & Zimmerwald" one? We suppose that, as said in Paragraph 5.6.3, the reason lies in the huge data gap of measurements coming from the Matera station.

The just showed tests highlighted the importance of object-observer relative geometry in the estimation of orbital parameters. They show also the importance of the angular measurements in the case where not a large number of SLR stations provide measurements. On the other hand, they indicate us the tendency of the LSQ adjustment to follow the higher precision range measurements that, in the case where they are not enough to observe homogeneously an orbit, may result in not optimal results.

Table 5.14 OD Results obtained by merging ranges from more than one station.

| 10041B | | Graz & Matera | Matera & Mt. Stromlo | Graz, Mt. Stromlo & Zimmerwald | Matera, Mt. Stromlo & Zimmerwald | Graz, Matera & Zimmerwald | Graz, Matera, Mt. Stromlo & Zimmerwald |
|---|---|---|---|---|---|---|---|
| # of Obs. | 1D | 64 | 92 | 94 | 92 | 64 | 188 |
| | 2D | – | – | 63 | 63 | 63 | 63 |
| Mean Pos. Error [m] | R | 0.930 | 0.672 | 0.575 | 0.698 | 0.673 | 0.447 |
| | S | 5.60 | 1.63 | 1.51 | 6.24 | 1.85 | 1.20 |
| | W | 7.66 | 9.49 | 2.61 | 8.62 | 4.69 | 5.99 |
| | Tot. | 10.06 | 9.83 | 3.30 | 11.53 | 5.37 | 6.26 |
| Orbital Elements Mean Error | $a$ [m] | $1.3 \cdot 10^{-2}$ | $1.4 \cdot 10^{-2}$ | $6.8 \cdot 10^{-3}$ | $5.4 \cdot 10^{-2}$ | $1.6 \cdot 10^{-2}$ | $1.1 \cdot 10^{-2}$ |
| | $e$ | $4.6 \cdot 10^{-8}$ | $2.9 \cdot 10^{-8}$ | $2.3 \cdot 10^{-8}$ | $3.5 \cdot 10^{-8}$ | $2.5 \cdot 10^{-8}$ | $2.1 \cdot 10^{-8}$ |
| | $i$ [°] | $2.6 \cdot 10^{-5}$ | $9.8 \cdot 10^{-6}$ | $8.0 \cdot 10^{-6}$ | $1.3 \cdot 10^{-5}$ | $1.6 \cdot 10^{-5}$ | $9.9 \cdot 10^{-6}$ |
| | $\Omega$ [°] | $9.4 \cdot 10^{-6}$ | $3.6 \cdot 10^{-5}$ | $5.1 \cdot 10^{-6}$ | $3.0 \cdot 10^{-5}$ | $4.5 \cdot 10^{-6}$ | $2.1 \cdot 10^{-6}$ |
| | $\omega$ [°] | $5.5 \cdot 10^{-4}$ | $5.1 \cdot 10^{-4}$ | $5.5 \cdot 10^{-4}$ | $4.1 \cdot 10^{-4}$ | $5.5 \cdot 10^{-4}$ | $3.1 \cdot 10^{-4}$ |
| | $M$ [°] | $5.6 \cdot 10^{-4}$ | $4.9 \cdot 10^{-4}$ | $4.6 \cdot 10^{-4}$ | $4.1 \cdot 10^{-4}$ | $5.5 \cdot 10^{-4}$ | $3.1 \cdot 10^{-4}$ |

## 5.6.4 Discovery and Follow-ups Scenarios Simulation

We have just illustrated the effects of the object-observer relative geometry, of the number of observations, of the length of the observed arc and the importance of the right weights selections within the LSQ adjustment. But, in the end, what are the benefits of the SLR measurements in terms of achievable orbit accuracy? And in the space debris field, what are the improvements, for example, for catalog maintenance applications? To illustrate these effects in the next examples we will compare the OD results obtained using one or two nights of angular observations with those adding a very small number of ranges. As usual, the ephemerides generated after an OD are then compared with those obtained from a reference orbit. Only a very small number of observations are taken into account in these tests so that we simulate the classical scenario of object discovery and first follow-ups (acquired in the same and in the following night). This choice was made as this way of operating is usually adopted at the AIUB and, especially for the GEO case, the obtained results could be easily compared with those shown in [44] to highlight the benefits given by the ranges. These tests were repeated for different orbital regimes (namely LEO, MEO and GEO).

### LEO

One good candidate for the kind of analysis carried out for the LEO regime is TOPEX POSEIDON (92052A). This satellite, which carries a retroreflectors array, was built to measure the

surface topography and was decommissioned in 2006. This satellite, with its 2400 kg of mass and its fast spin period ($\sim$ 10 sec), is one of the case studied in the space debris field [72].
For the analysis of this case we used only the observations provided by the Zimmerwald observatory acquired during three consecutive passes of the satellite from one single night. In particular, we have an astrometric series for each pass and two ranges series belonging to the first two passes. The results of the tests and the precise number of used observations are summarized in Tables 5.15 and 5.16. Since in this case we did not have enough observations to generate a good reference orbit, the analysis was performed comparing the propagated ephemerides obtained from the computed orbit with those provided by the ILRS centers. In particular, we compared the ephemerides obtained from $\sim$ 7 days of propagation starting from the first observation epoch, which is also the epoch were we estimated the orbit. The time interval between two successive ephemerides positions is 1 minute. Due to the lack of observations it was not possible to estimate a laser-only orbit and as a consequence the value of $\sigma_r$. We decided to use the value of $\sigma_r = 1.7$ m obtained for the LARETS case. Knowing that, for TOPEX, the distance from the center of the retroreflector array and the CoM is $\sim$ 1.42 m [2] the uncontrolled attitude motion of the satellite cause an error in the range that should be absorbed by the chosen $\sigma_r$ value. The value of $\sigma_\alpha$ is kept constant to 0.5 arcsec.

Table 5.15 Results of the OD tests for the LEO satellite in the 1 pass case.

| 92052A Mean Position Error [m] | | Angle-Only Circular | Angle-Only 6 ele. | All angles, 2 ranges | 1 angle, all ranges | 16% of ranges | Merged All Meas. |
|---|---|---|---|---|---|---|---|
| 1 Pass | Obs* | $-/3$ | $-/3$ | $2/3$ | $21/1$ | $4/3$ | $21/3$ |
| | R | $2.655\cdot10^4$ | $8.397\cdot10^6$ | $3.989\cdot10^5$ | 5561 | 113.7 | 1258 |
| | S | $5.391\cdot10^5$ | $4.929\cdot10^6$ | $2.122\cdot10^6$ | $2.388\cdot10^5$ | $2.308\cdot10^4$ | $1.059\cdot10^5$ |
| | W | 246.2 | $1.248\cdot10^5$ | 794.5 | 1197 | 418.8 | 861.9 |
| | Tot. | $5.399\cdot10^5$ | $1.030\cdot10^7$ | $2.164\cdot10^6$ | $2.389\cdot10^5$ | $2.308\cdot10^4$ | $1.059\cdot10^5$ |

[*] Number of observations respectively 1D/2D

Table 5.16 Results of the OD tests for the LEO satellite in the 2 and 3 passes case.

| 92052A Mean Position Error [m] | | Angle-Only | Ranges-Only | 16% of ranges | Merged All Meas. |
|---|---|---|---|---|---|
| 2 Passes | Obs* | −/20 | 59/− | 10/20 | 59/20 |
| | R | 180.0 | 184.2 | 147.2 | 159.4 |
| | S | 8023 | 644.0 | 528.0 | 509.7 |
| | W | 263.7 | 291.1 | 228.7 | 234.6 |
| | Tot. | 8034 | 789.1 | 641.8 | 634.9 |
| 3 Passes | Obs* | −/25 | 59/− | 10/25 | 59/25 |
| | R | 110.5 | 184.2 | 148.5 | 159.2 |
| | S | 1336 | 644.0 | 472.1 | 474.7 |
| | W | 346.8 | 291.1 | 235.0 | 239.7 |
| | Tot. | 1412 | 789.1 | 598.1 | 607.9 |

* Number of observations respectively 1D/2D

As usual we want to compare the results obtained by the classical angles-only solution with those using merged measurements varying the number of ranges used in the OD. Furthermore we want to report, for completeness, the results obtained by the ranges-only OD. For the satellite considered, this kind of experiments was not always possible especially for the 1-pass case. We decided to split the results in two tables: in the first (Table 5.15), the results obtained for the 1-pass case are shown, and in the second (Table 5.16), the ones obtained for the 2- and 3-passes cases are reported. Since the observed part of the orbit, in the 1-pass case, is too short to perform a LSQ to determine the orbit only one type of measurements we needed to change the method to calculate the orbit. For the “Angle-Only” case we used the Gauss-method as described in [16], in particular we reported the case where only a circular orbit was estimated and the case with the estimation of the entire set of orbital parameters (namely “Angle-Only Circular” and “Angle-Only 6 ele.”). These results are obtained processing an extremely short arc of observation made of only 1 tracklets constituted by 3 measurement epochs. The results in the “Angle-Only Circular” column were obtained estimating only the semi-major axis, the inclination, the RAAN and the argument of latitude (respectively $a$, $i$, $\Omega$ and $u_0$) assuming $e = 0$ and $\omega = 0$.
For the “Ranges-only”, we were obliged to use a minimum number of merged observations to be able to estimate an orbit. In particular, for the 1-pass case, we decided to report the results obtained with all ranges available plus the minimum number of angular observation to ensure the LSQ convergence (the “1 Angle, All Ranges” case). We also reported the results obtained using all angular measurements available plus the minimum number of ranges (the “All Angles, 2 ranges” case). As one can see from the Table 5.16 the workarounds used in the “Angle-Only Circular”, “All angles, 2 ranges” and “1 angle, all ranges” cases were not necessary for the 2/3-passes scenarios, so they were not replicated. The last two columns of the tables show the

results obtained using only $1/6$ of the ranges and using all measurements available. As for the other cases no empirical parameters are used during the OD process. On the other hand, since the object is still influenced by the effects of the atmosphere, we used the MSISe90 model to determine the atmosphere density and to model the atmospheric drag [16]. Finally, due to its fast attitude dynamics (tumbling period $\sim$ 10 sec [72]) we could not use the nominal value of AMR. We estimated the AMR fitting all available observations (both ranges and angular) coming from 1 week of observations from different laser stations. The observation arc used to determine the AMR was chosen in a way that the observations used for our tests are in the center of this arc. As said before, once estimated the AMR the ODs for the next tests were performed without estimating any empirical forces/parameters.

Starting now from the angles-only examples in the 1-pass case shown in Table 5.15, we report a comparison between the results obtained by the application of the Gauss-method to estimate the complete and the reduced set of orbital elements. As one can see, the total error obtained estimating the circular orbit is 2 orders of magnitude better than those obtained estimating the full set of parameters. This is due, obviously, by the fact that the observed arc is extremely small and the target object is in an almost circular orbit (the true eccentricity is $\simeq 4 \cdot 10^{-4}$).

The case “All angles, 2 ranges” was reported since it represents the minimum number of observations (with a majority of the angular ones) for which the LSQ converges. The total observation time interval is about 6 minutes which does not allow for a good OD but one can already see the improvements given by the ranges. The radial error decreased by 1 order of magnitude w.r.t. the “Angle-only 6 ele.” case. Looking at the “1 angle, all ranges” case we can see how the accuracy of the ranges produces an improvement of 2 orders of magnitude w.r.t. the angles-only case. In particular, the main improvements are visible for the radial component (3 order of magnitudes better) and secondarily for the along-track error. At the same time this example shows the importance of the angular observations. The obtained error in cross-track component is roughly 1.5 times bigger than in the “All angles, 2 ranges” case where a significantly smaller number of observations is used, the observed arc is shorter and 2 more angular measurements were used. As for the previous examples we decided also to evaluate the influence of the number of observations w.r.t. the length of the observed arc keeping constant the number of angular observations considered (namely the cases: “All angles, 2 ranges”, “16% of Ranges” and “Merged All Meas.”). In the “All angles, 2 ranges” case we just used the first two ranges measurements available, in the “16% of Ranges” one we used a subset of ranges homogeneously distributed over the entire pass and finally, the “Merged All Meas.” case considers simply all the measurements available for that satellite pass. These three examples show the importance of the distribution of the observations. In fact, as one can see by the comparison of the “All angles, 2 ranges” case against the “16% of Ranges” one, the addition of only 2 ranges, with a different distribution over the arc, improves the solution by 2 orders of magnitude. Adding further measurements leads to a degradation of the solution. As for the example shown in Paragraph 5.6.2, this degradation is due to the fact that the OD fits nicely the observations over the observed arc which is too short to describe correctly the shape of the real orbit.

Looking now at the 2-passes examples shown in Table 5.16 we can see how, due to the length of the arc observed and therefore the higher number of observations available, we were able to carry out an OD using a LSQ adjustment even with only one type of measurements. It must be said that the convergence of the LSQ algorithm, and therefore the improvement of the orbit, using only range measurements is probably due to the fact that the orbit used to initialize the algorithm was near the true orbit. The highest improvement in the accuracy of the solution can be see observing the angles-only case where the error now is 4 order of magnitude smaller w.r.t. its analogous in the 1-pass case. As expected, the main component of the error is the along-track one which depends on the estimation of the semi-major axis, the eccentricity, the argument of perigee and the perigee passing time. These parameters, except the semi-major axis, are difficult to estimate if the observations are taken with a distance of one orbital period. In the ranges-only case the along-track component is 10 times smaller than the angles-only case. This is due to the nature of the observables which helps in the estimation of the just mentioned parameters. The comparison of the merged cases is another evidence of the importance of the distribution of the observations: as one can see, the results obtained with one sixth of the available observations are comparable to those obtained using all of them.

Looking at the results of the 3-passes cases shown in Table 5.16, it must be said that the ranges-only results were just copied from the 2-passes case, for an easier comparison, since we did not have any ranges from the third pass. Considering now the angles-only case it is possible to see how the further addition of observations still improves the results. Performing the same comparison with the merged cases, a much smaller improvement is visible. There are two probably main reasons: the first is the fact that no other ranges are added w.r.t. the 2-passes cases, the second is given by the object-observer relative geometry. The information gained from the geometry is limited by the fact that only one station provides measurements and the considered arc is relatively short, in fact the total observation arc is only 4 hours.

The same plateau and the reduction of the improvements, in the results accuracy, given by the introduction of the range measurements with longer observation arcs can be seen also in Figure 5.13. The figure shows the behavior of the total position error of the propagated orbit w.r.t. the reference ephemerides. Each plot shows the comparison between the results obtained by an OD using homogeneous and merged measurements together with the observation epochs. The epochs of each measure are identified with the green vertical lines for the ranges, and with the red ones for the angles. Note that the first two plots are in a logarithmic scale while the latter in a linear one.

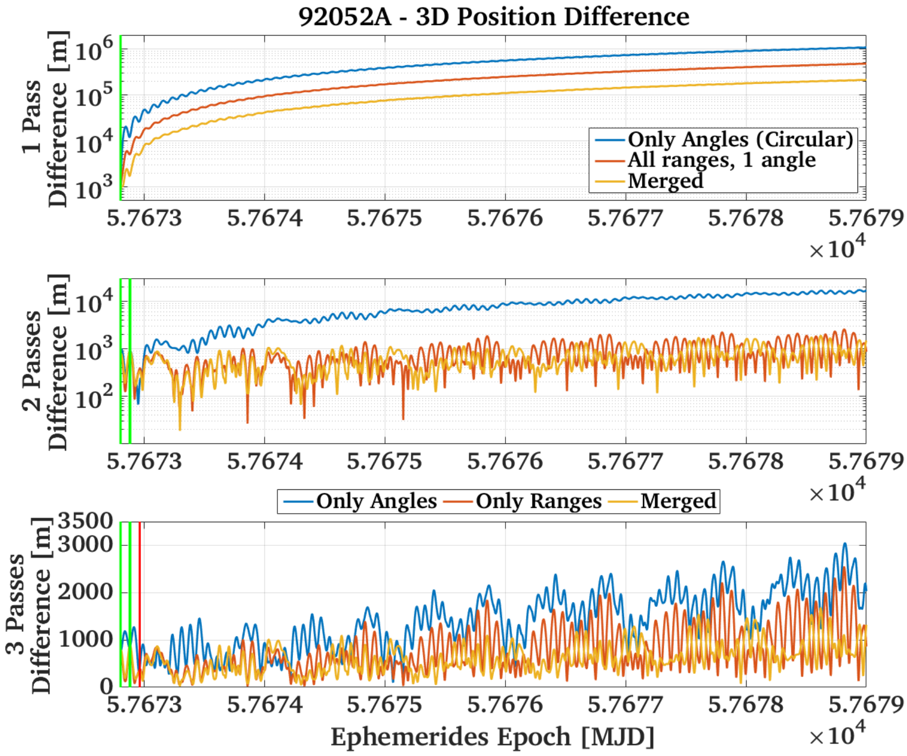

Figure 5.13 Behaviour of the 3D position errors and distribution of the used observations resulting from the OD tests for the LEO case.

### MEO

For the MEO orbital regime test scenario, we used two consecutive nights of observations where a total of 4 angular tracklets (3 of them during the first night) were acquired from the Zimmerwald observatory and 4 range measurements (again 3 during the first night) were acquired from the Graz station. The precise number of used observations can be seen in Table 5.17. The satellite used for this test is the Glonass 125 (11009A).

As usual, at the end of each OD process, the ephemerides are calculated from the obtained orbit and then compared with those of a reference one. In this case, the positions of the object were generated starting from the first measurement epoch and propagated for the next 6 days with a sampling of 1 position every 5 minutes. The reference orbit was determined processing all the data, both angular and ranges, available over a period of 13 days which includes the just mentioned propagation period. This orbit is then integrated over the fit span to generate the reference ephemerides.

As in the tests with the Glonass 123, also here, the value of $\sigma_r = 1.3$ m is used to determine the weights on the ranges, while the $\sigma_\alpha$ is kept constant to 0.5 arcsec. For each ephemeris epoch, the calculated state vector is converted to the correspondings set of osculating orbital elements which are also compared with the reference ones. Table 5.17 shows the average position and elements differences obtained over the 6 days of propagation. Figure 5.14 shows the behaviors of the position difference during the propagation time together with the distribution of the

observations. In particular the red vertical lines show the position of the angular measurements and the green the SLR ones. Looking at the results obtained with the “1 night” case, it is easy to see the huge jump in accuracy using merged measurements. As can be seen from the Table 5.17, the use of only 3 ranges allows an improvement of 3 orders of magnitude (passing from roughly 200 km to 600 m). This huge difference is driven by the error in the along-track component which is mainly caused by the error in the estimation of the semi-major axis ($\sim$ 4 km) together with the error in the eccentricity, argument of perigee and mean anomaly.
The error in the estimation of these parameters is strictly related to the kind of observables used and to the length of the observed arc. In fact the angular measurements do not provide directly information about the distance of the object. Adding at this point even a couple of ranges provides the needed distance information to strongly constrain the semi-major axis (the error in this case is $\sim$ 11 m) and as direct consequence reducing also the along-track error to $\sim$ 612 m. In this way we obtained results which are comparable in accuracy to those given by two nights of observations. These results are of fundamental importance for catalog building and maintenance applications. Looking at the angles-only case we can say that probably, we would have lost the object (of course depending on the field of view of the telescope used), while in the second case, the obtained final error is $\sim$ 1.3 km which is, for the considered object, less than 14 arcsec after 6 days. On the other hand, these results confirm the fundamental importance of the angular measurements in the estimation of the orbital plane. In fact, looking at the errors obtained for the inclination and the RAAN, we can see that in all 4 cases they are of the same order of magnitude.
Finally, looking at the bottom plot of Figure 5.14 we can see how the addition of the ranges, for the two nights of observations case, produces a final error still twice better than the angles-only case. This small improvement is probably due to the small number of used ranges, and to the small geometry changes between the object and the observers. The small geometry changes are caused by an interaction of the orbital period of the observed object ($\sim$ 11 hours and 20 minutes) and the distance between the observations which are roughly 1 day apart.

Table 5.17 Results of the OD tests for the MEO case.

| 11009A | | 1 Night | | 2 Nights | |
|---|---|---|---|---|---|
| | | Angles-Only | Merged | Angles-Only | Merged |
| # of Obs. | 1D | – | 3 | – | 4 |
| | 2D | 10 | 10 | 14 | 14 |
| Pos. Error [m] | R | 5171 | 11.65 | 36.79 | 5.309 |
| | S | $2.246 \cdot 10^5$ | 612.4 | 455.8 | 220.3 |
| | W | 159.4 | 52.25 | 26.74 | 24.17 |
| | Tot. | $2.248 \cdot 10^5$ | 619.4 | 462.6 | 224.1 |
| Orbital Elements Error | $a$ [m] | 3843 | 10.88 | 8.929 | 4.178 |
| | $e$ | $1.439 \cdot 10^{-4}$ | $4.130 \cdot 10^{-7}$ | $1.796 \cdot 10^{-6}$ | $1.080 \cdot 10^{-7}$ |
| | $i$ [°] | $8.70 \cdot 10^{-5}$ | $2.35 \cdot 10^{-5}$ | $3.58 \cdot 10^{-5}$ | $2.17 \cdot 10^{-5}$ |
| | $\Omega$ [°] | $6.318 \cdot 10^{-4}$ | $3.150 \cdot 10^{-4}$ | $9.560 \cdot 10^{-5}$ | $9.060 \cdot 10^{-5}$ |
| | $\omega$ [°] | 5.631 | $3.150 \cdot 10^{-2}$ | $1.149 \cdot 10^{-1}$ | $2.244 \cdot 10^{-2}$ |
| | $M$ [°] | 5.128 | $3.021 \cdot 10^{-2}$ | $1.140 \cdot 10^{-1}$ | $2.200 \cdot 10^{-2}$ |

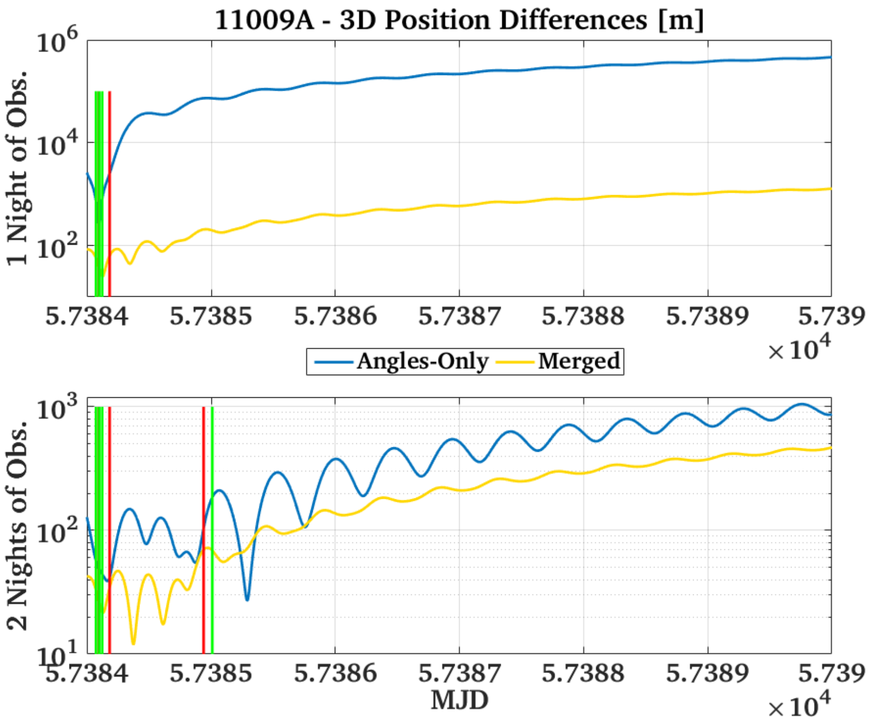

Figure 5.14 Behavior of the 3D position errors and distribution of the used observations resulting from the OD tests for the MEO case.

## GEO

The last orbital regime that we wanted to investigate is the geostationary one. This region is one of the most exploited, it presents also a higher density of space debris. The satellite used for these tests is the IRNSS1A (13034A). As in the previous case (MEO), we will compare the position and orbital elements, generated after an OD performed over a maximum of two nights of observations, with those coming from a reference orbit. The reference orbit was determined processing all the data, both angular and ranges, available over a period of 22 days. Since the satellite used for this experiment is an active one, this period coincides with the time interval between two maneuvers. The reference orbit is then integrated over the fit span to generate the reference ephemerides with a sampling frequency of 1 position every 5 minutes. The fit span includes the subset of measurements used for the following tests. The orbit determined using the subset of observations are then propagated for 4 days for the comparison with the reference ephemerides.

The angular data are provided, as in the previous cases, by the Zimmerwald observatory, while the ranges by Hertsmonceux (United Kingdom). Also in this case the weights on the SLR measurements are determined using $\sigma_r = 1.3$ m. We would like to highlight that, in this case, the usual comparison is made using SLR measurements which were available only for the first night of observation. This was probably due to the rising difficulties of the SLR stations in tracking high altitude satellites. It is also important to notice that, in this case, w.r.t. the MEO one, a higher number of angular observations was available. A total of 3 tracklets spread over 3 hours were available for the first night and another 2 consecutive ones for the second night. Looking at Table 5.18, as for the MEO case, adding the 2 ranges produces a jump of 3 orders of magnitude in the mean error that will ensure the recovery of the object, as we will see in Paragraph 5.6.5, even after 4 weeks. In the angles-only case, as previously shown by Musci et al. in [44], a follow-up in the successive nights becomes mandatory. Comparing quickly the results shown by Musci et al. in [44] for the same orbital regimes we can say that 1 night of observations made by 3 tracklets and 2 ranges provides the same accuracy achievable with 4 (angular-only) follow-ups spread over 3 observation nights.

Looking now at the bottom graph of Figure 5.15, we can see how the behavior of the errors is completely different from those shown before. In fact, in this case, the error sinusoidal component is more pronounced than the drifting one. Furthermore, from the vertical green and red lines, it is easy to see how the smallest error occurs close to the observed part of the orbit. This effect is due to the distribution of the angular measurements which are precisely one day apart and the orbital period of the object that, being a GEO satellite, is coincident with the sidereal day. As main consequence this observation distribution improves strongly the estimation of the semi-major axis but at the same time, as shown in [46], does not give enough information to estimate correctly the eccentricity of the orbit. This effect, even if less pronounced, is also visible for the two nights case with merged measurements. In this case the ranges together with the distance information increase also the geometry changes. Since they are acquired a bit more than two hour later than the last angular observation, they help constrain both the semi-major axis and the eccentricity reducing the amplitude of the error oscillations (see elements error in Table 5.18). Consequently, improving the estimation of $a$ and $e$, the ranges have strong effects even in the estimation of the argument of perigee and the mean anomaly, as can be seen looking at the error for $\omega$ and $M$.

Another consequence of the distribution of the observations can be seen in the parameters which describe the orientation of the orbital plane. Looking at the distributions of the angular measurements they are spread over 3 hours during the 1st night of observations, and the time distance between the 1st and the last tracklet is about 24 hours. As shown in [46] for GEO objects, series of angular observations in the same part of the orbit, since the arc covered by the tracklet is relatively small, do not provide enough information to determine correctly $i$ and $\Omega$. This effect can be easily seen from the error value reported in Table 5.18: the errors for $i$ and $\Omega$ are relatively high and stay on the same order of magnitude (especially $i$) for the angles-only cases. In this case the ranges help also the estimation of these parameters ($i$ and $\Omega$) enlarging the observed portion of the orbit. The arc observation increases in fact from 3 to 5 hours. This last test shows the strength of the SLR measurements: looking at the last column of Table 5.18, even a small number of ranges (only 2) produces an improvement of the average error from roughly 2 arcmin to 2 arcsec.

Table 5.18 Results of the OD tests for the GEO case.

| 13034A | | 1 Night | | 2 Nights | |
| --- | --- | --- | --- | --- | --- |
| | | Angles-Only | Merged | Angles-Only | Merged |
| # of Obs. | 1D | – | 2 | – | 2 |
| | 2D | 19 | 19 | 33 | 33 |
| Pos. Error [m] | R | $7.193\cdot10^{5}$ | 486.8 | 5436 | 86.07 |
| | S | $5.219\cdot10^{6}$ | 9017 | $1.698\cdot10^{4}$ | 199.6 |
| | W | $8.992\cdot10^{3}$ | 50.99 | 703.9 | 20.87 |
| | Tot. | $5.282\cdot10^{6}$ | 9056 | $1.850\cdot10^{4}$ | 234.3 |
| Orbital Elements Error | $a$ [m] | $2.793\cdot10^{5}$ | 497.2 | 61.71 | 6.729 |
| | $e$ | $4.997\cdot10^{-3}$ | $1.822\cdot10^{-6}$ | $8.270\cdot10^{-5}$ | $3.089\cdot10^{-6}$ |
| | $i$ [°] | $4.921\cdot10^{-3}$ | $3.190\cdot10^{-5}$ | $1.387\cdot10^{-3}$ | $4.500\cdot10^{-5}$ |
| | $\Omega$ [°] | $3.997\cdot10^{-2}$ | $2.207\cdot10^{-4}$ | $1.407\cdot10^{-3}$ | $9.800\cdot10^{-6}$ |
| | $\omega$ [°] | 22.93 | $2.995\cdot10^{-1}$ | 5.032 | $1.760\cdot10^{-2}$ |
| | $M$ [°] | 16.75 | $2.865\cdot10^{-1}$ | 5.055 | $1.771\cdot10^{-2}$ |

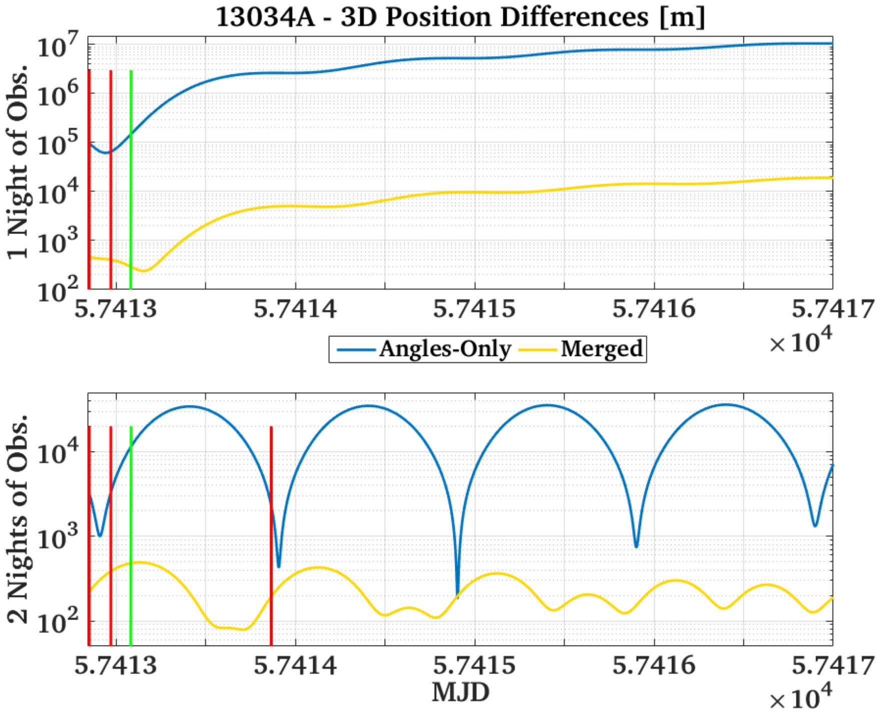

Figure 5.15 Behavior of the 3D position errors and distribution of the used observations resulting from the OD tests for the GEO case.

### 5.6.5 Error Evolution with Time

With the last tests we want to compare the influence of few SLR measurements in a short observation arc on the time needed by an observed object to go outside of the FoV of a telescope. This time interval it is important for an observer since if it does not want to lose an object, it has to acquire new measurements to improve its orbit before it leaves the FoV of the telescope. The maximum time interval available before losing the object will be called recovery period. In the following tests we will highlight the benefits of the use of SLR measurements in terms of length of the recovery period for an observed object. We want to compare the time needed by an observed object to go outside of the FoV of a telescope. For these tests we used the FoV of the Zimmerwald telescopes, namely ZIMLAT and ZimSMART. The first has a FoV of $\simeq 26$ arcmin while the second $\simeq 3.5$ deg; consequently, we will consider an object as lost when the vectorial sum of the errors in the along- and cross-track directions, w.r.t. the reference orbit, is greater than the half of the FoV. This comparison will be made between results obtained from an OD with different kinds of observables, number of observations, lengths of the observed arc and for different orbital regimes. Particular emphasis is given to the comparison between the angles-only case and the merged one in order to highlight the improvements of the SLR measurements w.r.t. the results achievable with the actually used angular observations method. This test is of fundamental importance for catalog maintenance. The increase of the recovery time allows a more relaxed observation schedule with a smaller number of required observations permitting the tracking of a bigger number of objects. The test will be performed mainly on short observation arcs using a very small number of ranges to better simulate the space debris observation case. Table 5.19 shows the time interval needed by the propagated orbit to go outside the FoV for the first time for the different cases analyzed. We report the smallest time interval needed to go outside the FoV since it can happen that, due to the observation geometry, certain OD produce results like those shown in the bottom graph of Figure 5.15. In this case the object, before getting completely lost, appears again inside the FoV after a certain period. This effect can be reproduced easily if we compare the OD results with the reference orbit. These test were performed on the same objects previously analyzed, therefore the same reference orbit were used. In particular, for the GLONASS 123 (10041B) we used the same reference orbit of the Paragraph 5.6.3, for the TOPEX (92052A), GLONASS 125 (11009A), and IRNSS1A (13034A) cases we used the same reference orbits of the Paragraph 5.6.4. The only exception was done for the LAGEOS 1 (76039A) for which we needed to generate a new reference orbit considering all data, both angular and ranges, available over a time interval of 15 days. All the reference orbits used contain the subset of observations used for these tests. Except for the TOPEX case for which, due to the use of CPF, only $\sim 7$ days of ephemerides were available; for all the other cases the reference orbit is propagated for a total period of 3 months starting from the epoch of the first observation used for the test. It must be said that the recovery time was calculated from the position difference extracted from the ephemerides if smaller than 90 days; while the longer recovery times (as shown in Table 5.19) were extrapolated by an interpolation of the position differences during the propagation period. Despite the complex shape of the position differences we assumed a linear growth of the error outside of the propagation period. Table 5.19 shows also the arc-length and the number of observations used in each case. As mentioned just above, only short observation arcs are used. In particular, for the Lageos 1 and TOPEX cases (namely 76039A and 92052A), the results obtained by 1, 2 and 3 passes within the same night are reported, while in the other cases the comparison between 1 and 2 nights of observation are shown. Looking now at the case of the 10041B, a further comparison is done changing the number of observations used in the case of 2 nights of observation arc. As one can see the first 3 tests were carried out using 3 tracklets of angular observations (14 observations in the table) varying the number of used range from 2 to 4. A second test was performed comparing the results given by the 4 tracklets (18 angular observations) case with the 4 tracklets and 4 ranges one.

Looking at the Table 5.19 we can see how in the angles-only 1 pass cases for the 76039A and the 92052A and the one-night cases for the 13034A and the 10041B, the recovery time is roughly 4 hours or even smaller (if one look at the results using the FoV of ZIMLAT). For 11009A even in the worst case scenario the recovery time is at least one day. The reason for it is in the length of the observed arc. In fact, the observations are distributed over $\simeq 4.5$ hours, which roughly coincide with one third of the orbital period. Already adding a couple of ranges the solution improves by at least one order of magnitude. As one can see from the results obtained with the smallest observation arc, the recovery time using few SLR measurements increases from few hours to almost one week (look at the 10041B) and even more, depending, of course, on the number of angular observations and their distribution. As shown in [44], extending the observation arc by adding follow-up observations, will produce an increase of the recovery time also using only angular measurements. Also in this case the improvement given by the ranges is noticeable but generally less pronounced. It is also interesting to highlight two cases where the angles-only solution of two nights of observations is compared with the merged one using only the range measurements acquired during the first night (namely the 2 nights cases for 10041B and 13034A marked with a *). These two examples highlight the importance of merging different kinds of observables since each one is acting differently on the estimated parameters. The combination of angular follow-up and a constant number of ranges produces a results 9 times better than the angles-only solution (see 13034A case). One last thing that can be noticed from the table is a general, quite obvious, trend in the improvement of the solution given by an increase of the observation time. There is only one case which goes against this trend: the 76039A. For this satellite the comparison between the one pass merged solution and the two passes one, shows that the one pass case has a longer recovery time. We do not deduce any general conclusion from this case, as we think that the distribution of the observations makes the system converge on a slightly worse solution. One last remark can be seen from the recovery times obtained for the TOPEX case which are sensitively smaller w.r.t. those obtained for the other satellites, this is probably due to the more complex orbital dynamics and the increasing difficulty in modeling all the forces acting on the LEO regime.

Table 5.19 Results of the recovery time tests.

| | | | # of Obs. | | Recovery Time [days] | |
|---|---|---|---|---|---|---|
| | | | 1D | 2D | ZIMLAT | ZimSMART |
| LEO | TOPEX<br>92052A | 1 Pass.* | – | 3 | 0.18 | 0.35 |
| | | 1 Pass. | 4 | 3 | 0.80 | 5.78 |
| | | 2 Pass. | – | 20 | 1.92 | 16.30 |
| | | 2 Pass. | 10 | 20 | 47.64 | 403.2 |
| | | 3 Pass. | – | 25 | 17.30 | 153.3 |
| | | 3 Pass. | 10 | 25 | 60.13 | 511.4 |
| MEO | LAGEOS1<br>76039A | 1 Pass. | – | 41 | $< 0.1667$ | 0.5417 |
| | | 1 Pass. | 3 | 41 | 917.2 | 7400 |
| | | 2 Pass. | – | 59 | 248.7 | 2006 |
| | | 2 Pass. | 10 | 59 | 674.1 | 5443 |
| | GLONASS<br>10041B | 1 Night | – | 9 | $< 0.1667$ | $< 0.1667$ |
| | | 1 Night | 2 | 9 | 5.83 | 45.83 |
| | | 2 Nights | – | 14 | 60 | 493.7 |
| | | 2 Nights | 2$*^1$ | 14 | 435.6 | 3515 |
| | | 2 Nights | 4 | 14 | 499.3 | 4032 |
| | | 2 Nights | – | 18 | 1177 | 9470 |
| | | 2 Nights | 4 | 18 | 1319 | 10650 |
| | GLONASS<br>11009A | 1 Night | – | 10 | 1.167 | 8 |
| | | 1 Night | 3 | 10 | 340.6 | 2749 |
| | | 2 Nights | – | 14 | 415.3 | 3350 |
| | | 2 Nights | 4 | 14 | 886.2 | 7153 |
| GEO | IRNSS1A<br>13034A | 1 Night | – | 19 | $< 0.1667$ | 0.5 |
| | | 1 Night | 2 | 19 | 29.83 | 310.2 |
| | | 2 Nights | – | 33 | 314.7 | 3039 |
| | | 2 Nights | 2$*^1$ | 33 | 2920 | 23660 |

$^*$ OD using the Gauss-method estimating a circular orbit (estimated parameters: $a$, $i$, $\Omega$ and $u_0$)

$*^1$ ranges belonging to the first observation night

## 5.7 Conclusions

The employment of laser ranging techniques in the space debris field is quite controversial. The problem rises from the fact that if on one hand the laser measurements are very attractive due to the high accuracy on the other hand, the FoV of a laser system is relatively small and to hit a space debris object a good a priori knowledge of its orbit is needed. Furthermore, usually the

SLR technique is applied to satellites which carry retroreflectors. These factors are partially limiting the applicability of SLR techniques in the space debris field. Studies proved that with the new generation of high-power laser it is possible to track big objects (as rocket stages or defunct satellites) even if they do not carry retroreflectors. The problem of the laser FoV can be overcome by mixing different instrumentations like tracking cameras to correct the ephemeris offset. It must be said that in both cases the attitude of the target has to be favorable to the reflection of laser pulses.

In this chapter we investigated the benefits that the high precision ranges provided by an SLR station, could be given to the OD process based on the classical angular measurements. First of all, we needed to adapt the tool used for the OD at the AIUB to handle the new observables. After the implementations of all model improvements needed to exploit the laser ranges, and after checking the proper application of the corrections to those measurements, we needed to validate the OD process. To do it: we selected four different satellites belonging to different orbital regimes, we estimated their orbit based on SLR measurements only and finally, we compared the generated ephemerides with those provided by the ILRS. Subsequently, a study was carried out to identify the proper relative weighting of the different observables within the LSQ adjustment. After the weights definition, some studies were performed to highlight the consequences of the use of the laser ranges in the OD process. First, we studied the influence of the length of the observed arc and the influence of the number of SLR observations used in the OD. Then we wanted to evaluate the influence of the relative object-observer geometry comparing the OD results obtained by different subsets of measurements acquired from different stations. Finally, we simulated a classical discovery and follow-up scenario and we highlighted the improvements given by a very small number of ranges. All these tests were performed using exclusively real angular and SLR measurements provided by the Zimmerwald observatory and the ILRS, respectively.

Those tests showed the huge improvements achievable using a relatively small number of ranges over a small observation arc. Furthermore, they showed that, since the SLR measurements are much more precise than the angular ones, a fine tuning of the measurements weights is needed so that the system will not ignore the angles. The tests on the influence of the arc-length show a plateau in the achievable accuracy highlighting the influence of the relative observer-object geometry. Furthermore, as expected, the improvements given by the SLR data on long observation arcs are less pronounced w.r.t. those obtained for short arcs. The tests made to investigate the geometry influence and those which simulated the discovery/follow-up scenario showed how each single observable is acting on the estimated parameters. Finally, the tests on the recovery time showed the benefits that merged SLR and angular measurements could bring to the catalog building and maintenance activities and to the planning of collision avoidance maneuvers.

Of course, this problem needs further investigation, but it already proved the benefit of the use of SLR measurements in the OD for space debris. However, to have more general outcomes one should analyze the results coming from the application to a wider set of observations concerning different orbital regimes. It would be interesting to investigate if there is a dependence of the achievable improvements, employing merged data, on the altitude of the orbit. Further improvements can be given by the investigation of the geometry influence in a more theoretical way. Further studies can be carried out using simulation and/or synthetic data in order to not have constraints given by the availability of the measurements. Otherwise one can follow and improve the approach proposed in Chapter 4.

# Chapter 6

# Summary

The increasing number of space debris objects, together with the risk associated for the active space missions, has as main consequence an increase of the working-load for the infrastructures dedicated to the space debris cataloging and orbit maintenance. Due to the high number of target objects and to the limitations of the observing systems, it is necessary to optimize the use of the time available for observations. The scheduling of the observations for the maintenance of the catalog depends on the quality of the orbit previously determined. Since the accuracy of the OD results depends on relative object-observer(s) geometry, on the type, the accuracy and the number of used observations, there are several methods to improve it. One can optimize the observation-geometry by adapting the scheduling of the network of sensors dedicated to the measurements acquisition. Then one could acquire as many observations as possible, but in this case the orbit accuracy will be limited by the accuracy of the measurements and, of course, this is time consuming. One could improve, to a certain extent, the accuracy of the measurements acquired by a generic sensor. Finally, one could merge different observables and exploit the advantages given by each one.

The main aim of this thesis was to study the ways of improvement of the results of the orbit determination process. After a brief introduction on the LSQ algorithm and its products, we focused our attention on the covariance matrix as index of the quality of the estimation. We needed first to understand how the covariance can be transformed according to the user needs focusing on the main advantages and disadvantages of the different covariance representations. Then we showed how it evolves in time and what are the parameters which influence its propagation. Successively we wanted to understand how the object-observer relative geometry and the different type of observables influence the OD results and improve the covariance.

The covariance matrix was used as evaluation criterion to investigate the effects due to the observation geometry. OD simulations were performed to evaluate the information gain given by a certain combination of small sets of observations. The isolation of the contribution given by a small set of observations is possible thanks to the stacking property of the NEQ. The simulations were carried out for different orbital regimes (LEO, MEO and GEO) and were used to evaluate the influence of the number of observations, of the time distance between the measurements, of the number of observers and their way of observing, and finally the type of processed measurements. We simulated also the typical discovery and follow-ups scenario. This approach allowed us to identify the key-factors determining the OD accuracy, and to understand how and why they influence the OD accuracy. These are: the distance of the object, the position of the observer w.r.t. the orbital plane, the position of the observations along the orbit, in the case of two observers the consequences of the parallax, and of course, the different types of observables. This is an information-gain problem and we approached it in a way that the object-specific results, together with some a priori information, can be used in an operational environment for the observation planning and scheduling. This study can be further improved by examining new scenarios and test cases, for example it is advisable to pay attention to the $S$-shaped uncertainty area in the covariance maps whose explanation needs further investigations.

Finally we investigated the effects of different observables in the OD results. There are two main types of observables which can be used for the OD of space debris: the angular and the distance measurements. We decided to perform this study using only real measurements provided by the ILRS and Zimmerwald observatory. In particular we analyzed the effects of the high-accuracy laser ranges on the OD process based on the classical angular measurements of RA and DE. We are fully conscious of the controversial opinions regarding the application of SLR in the space debris field. However, assuming that we are able to track a space debris with a laser system we implemented the capability to process laser ranges and we validated the software. Then, we performed several tests to study the influence of each observable in the OD process. When processing SLR and angular measurements, due to their huge accuracy difference, the relative weighting between the two observables becomes fundamental. In fact, the LSQ can converge on more laser-based solutions which, depending on the number of the laser observations and their distributions, could not coincide with the best ones. On the other hand, with the proper set up, the laser measurements improve the angular-only solution by orders of magnitude when processing short observations arcs ($1-2$ days). Since the main purpose of this study was not to obtain the best orbit but more to investigate the influence of the different observables, the level of accuracy achieved in the SATORB software can be considered sufficient. Nevertheless, further improvements are possible. For example we think that the discrepancies obtained comparing our laser-only LAGEOS solution with that provided by the BSW could be strongly reduced improving the background-dynamical model. Other improvements and checks have to be done for the atmospheric drag modeling and in the estimation of the ballistic coefficient.

In addition, it could be interesting to repeat the observation geometry study exploiting the possibility to constrain the NEQ system in order to analyze and discriminate which observation scenarios could be used for the improvements of certain orbital parameters. Especially for operational applications this capability has not to be underestimated since a poorly conditioned NEQ, used to estimate or improve the entire set of parameters, could produce a degradation of the solution which could be avoided allowing the improvements of only a subset of the unknowns. Furthermore, the constraint of the NEQ could be even more interesting when processing different observables. In our opinion it is worth analyzing the influence of each observable when, depending on the needs and the length of the arc of observations, the LSQ process is used to improve only certain elements.

# Bibliography

[1] D.A. Vallado. Covariance transformations for satellite flight dynamics operations. In *Proceedings of the AAS/AIAA Astrodynamics Specialist Conference*, number AAS 03-526, Big Sky Resort, Big Sky, Montana, USA, August 2003.

[2] M.R. Pearlman, J.J. Degna, and J.N. Bosworth. The International Laser Ranging Service. *Advances in Space Research*, 30(2):135–143, July 2013.

[3] ESA Website. Space debris by the numbers, June 2017.

[4] Office for Outer Space Affairs. Space debris mitigation guidelines of the committee on the peaceful uses of outer space. Technical report, United Nations, Vienna, Austria, January 2010.

[5] Office for Outer Space Affairs. Technical report on space debris. Technical Report A/AC.105/720, No. E.99.I.17, ISBN: 92-1-100813-1, United Nations, United Nations, New York, USA, 1999.

[6] N.L. Johnson. Orbital debris: the growing threat to space operations. In *Proceedings of the 33rd Annual AAS Guidance and Control conference*, number AAS 10-011, Breckenridge, Colorado, USA, February 2010.

[7] J.-C. Liou, N.L. Johnson, and N.M. Hill. Controlling the growth of future LEO debris populations with active debris removal. *Acta Astronautica*, 66:648–653, 2010.

[8] Committee on Space Debris. Orbital debris: a technical assessment. Technical Report ISBN: 0-309-05125-8, National Research Council (U.S.), Washington D.C., USA, 1995.

[9] J.-C. Liou. An active debris removal parametric study for LEO environment remediation. *Advances in Space Research*, 47:1865–1876, 2011.

[10] T. Schildknecht, J. Herzog, A. Vananti, M. Ploner, and E. Fletcher. Coordinated optical GEO survey for european SSA precursor services. In *Proceedings of Advanced Maui Optical and Space Surveillance Technologies Conference (AMOS)*, Maui, Hawaii, 2013.

[11] T. Schildknecht, A. Vananti, A. Hinze, J. Herzog, and M. Ploner. Long-term evolution of high area-to-mass ratio objects in different orbital regions. In *Proceedings of Advanced Maui Optical and Space Surveillance Technologies Conference (AMOS)*, Maui, Hawaii, 2012.

[12] T. Schildknecht, J. Herzog, A. Hinze, A. Vananti, and M. Ploner. AIUB efforts to survey, track, and characterize small-size objects at high altitudes. In *Proceedings of DLRK Conference*, Berlin, Germany, 2012.

[13] T. Schildknecht. Optical surveys for space debris. *The Astronomy and Astrophysics Review*, 14(1):41–111, 2007.

[14] G. Kirchner, F. Koidl, F. Friederich, I. Buske, U. Voelker, and W. Riede. Laser measurements to space debris from Graz SLR station. *Advances in Space Research*, 51:21–24, 2013.

[15] D.A. Vallado. *Fundamentals of Astrodynamics and Applications*. Number ISBN: 978-11881883180. Microcosm Press, 4th edition, March 2013.

[16] G. Beutler. *Methods of Celestial Mechanics, Vol. I and II*. Number ISBN: 978-3540407492 and ISBN: 978-3540407508. Springer-Verlag, Berlin, Germany, 2005.

[17] G. Beutler, A. Jäggi, L. Mervart, and U. Meyer. The celestial mechanics approach: theoretical foundations. *Journal of Geodesy*, 84(10):605–624, 2010.

[18] B.P. Gibbs. *Advanced Kalman Filtering, Least-Squares and Modeling: A Practical Handbook*. Wiley, 2011.

[19] D. Giza, P. Singla, and M. Jah. An approach for nonlinear uncertainty propagation: application to orbital mechanics. In *AIAA Guidance, Navigation, and Control Conference*, 2009.

[20] K. DeMars, M. Jah, D. Giza, and T. Kelecy. Orbit determination performance improvements for high area-to-mass ratio space object tracking using an adaptive Gaussian mixtures estimation algorithm. In *21st International Symposium on Space Flight Dynamics*, 2009.

[21] K.J. DeMars and M.K. Jah. Probabilistic initial orbit determination using gaussian mixture models. *Journal of Guidance, Control, and Dynamics*, 36(5):1324–1335, 2013.

[22] J.T. Horwood, A.B. Poore, and K.T. Alfriend. Orbit determination and data fusion in GEO. In *Proceedings of Advanced Maui Optical and Space Surveillance Technologies Conference (AMOS)*, Maui, Hawaii, 2011.

[23] W.H. Press. *Numerical Recipes 3rd Edition: The Art of Scientific Computing*. Cambridge University Press, 2007.

[24] E. Brockmann. *Combination of solutions for geodetic and geodynamic applications of the Global Positioning System (GPS)*, volume 55 of *Geod.-Geophys. Arb. Schweiz, Vol. 55,*. 1997.

[25] D. Thaller. *Inter-technique combination based on homogeneous normal equation systems including station coordinates, Earth orientation and troposphere parameters*. PhD thesis, Fakultät für Bauingenieur- und Vermessungswesen, TU München, 07 2008.

[26] B. Schutz, B. Tapley, and G.H. Born. *Statistical Orbit Determination*. Elsevier Science, 2004.

[27] A. Jäggi. Numerical methods in physics. Lecture Notes, University of Bern, Faculty of Physics, Astronomical Institut, 2013.

[28] I. Molotov, V. Agapov, V. Titenko, Z. Khutorovsky, Yu. Burtsev, I. Guseva, V. Rumyantsev, M. Ibrahimov, G. Kornienko, A. Erofeeva, V. Biryukov, V. Vlasjuk, R. Kiladze, R. Zalles, P. Sukhov, R. Inasaridze, G. Abdullaeva, V. Rychalsky, V. Kouprianov, O. Rusakov, E. Litvinenko, and E. Filippov. International scientific optical network for space debris research. *Advances in Space Research*, 41(7):1022 – 1028, 2008.

[29] H. Karttunen, P. Kröger, H. Oja, M. Poutanen, and K.J. Donner. *Fundamental Astronomy*. Springer Berlin Heidelberg, 2016.

[30] E. Cordelli, A. Vananti, and T. Schildknecht. Analysis of the orbit determination accuracy using laser ranges and angular measurements. In *Proceedings of 67th International Astronautical Congress (IAC)*, Guadalajara, Mexico, 2016.

[31] J. Sang and J.C. Bennett. Achievable debris orbit prediction accuracy using laser ranging data from a single station. *Advances in Space Research*, 54:119–124, 2014.

[32] J. Sang, J.C. Bennett, and C. Smith. Experimental results of debris orbit predictions using sparse tracking data from Mt. Stromlo. *Acta Astronautica*, 102:258–268, 2014.

[33] J.C. Bennett, J. Sang, C. Smith, and K. Zhang. An analysis of very short-arc orbit determination for low-earth objects using sparse optical and laser tracking data. *Advances in Space Research*, 55:617–629, 2015.

[34] U. Voelker, F. Friederich, I. Buske, D. Hampf, W. Riede, and A. Giesen. Laser based observation of space debris: taking benefits from the fundamental wave. In *6th European Conference on Space Debris*, Darmstadt, Germany, April 2013.

[35] J. Seago and D. Vallado. Coordinate frames of the US space object catalogs. In *Astrodynamics Specialist Conference*, number AIAA 2000-4025, Reston, VA, 2000. American Institute of Aeronautics and Astronautics.

[36] D.D. McCarthy. IERS conventions 1996, IERS Technical Note No. 21. Technical report, International Earth Rotation and Reference Systems Service (IERS), Paris, France, 1996.

[37] D.D. McCarthy and G. Petit. IERS conventions 2003, IERS Technical Note No. 32. Technical Report ISBN: 3-89888-884-3, International Earth Rotation and Reference Systems Service (IERS), Frankfurt am Main, Germany, 2004.

[38] G. Petit and B. Luzum. IERS Conventions 2010, IERS Technical Note No. 36. Technical Report ISBN: 3-89888-989-6, International Earth Rotation and Reference Systems Service (IERS), Frankfurt am Main, Germany, 2010.

[39] C. Sabol, T. Sukut, K. Hill, K.T. Alfriend, B. Wright, Y. Li, and P. Schumacher. Linearized orbit covariance generation and propagation analysis via simple Monte Carlo simulations. In *20th AAS/AIAA Space Flight Mechanics Conference*, number AAS 10-134, San Diego, California, 2010. American Institute of Aeronautics and Astronautics.

[40] Z. Folcik, A. Lue, and J. Vatsky. Reconciling covariances with reliable orbital uncertainty. In *Proceedings of Advanced Maui Optical and Space Surveillance Technologies Conference (AMOS)*, Maui, Hawaii, 2011.

[41] B.D. Tapley, B.E. Schiutz, and R.J. Eanes. Satellite laser ranging and its applications. *Celestial Mechanics*, 37(3):247–261, November 1985.

[42] J. Silha, T. Schildknecht, A. Hinze, and A. Vananti. Additional optical surveys for space debris on highly eccentric and inclined MEO orbits. In *Proceedings of 65th International Astronautical Congress (IAC)*, Toronto, Canada, 2014.

[43] A. Hinze, T. Schildknecht, , A. Vananti, H. Krag, and T. Flohrer. Observations strategies for space debris on highly-eccentric MEO orbit. In *Proceedings of 63rd International Astronautical Congress (IAC)*, Naples, Italy, 2012.

[44] R. Musci, T. Schildknecht, and M. Ploner. Orbit improvement for GEO objects using follow-up observations. *Advances in Space Research*, 34:912–916, 2004.

[45] R. Musci, T. Schildknecht, M. Ploner, and G. Beutler. Orbit improvement for GTO objects using follow-up observations. *Advances in Space Research*, 35:1236–1242, 2005.

[46] E. Cordelli, A. Vananti, and T. Schildknecht. Covariance study to evaluate the influence of optical follow-up strategies on estimated orbital parameters. *Acta Astronautica*, 122:76–89, 2016.

[47] K. Sośnica. *Determination of Precise Satellite Orbits and Geodetic Parameters using Satellite Laser Ranging*. Astronomical Institute, University of Bern, Switzerland, 2014.

[48] Wikipedia. Retroreflector — wikipedia, the free encyclopedia, 2017. [Online; accessed 22-January-2017].

[49] Wikipedia. Corner reflector — wikipedia, the free encyclopedia, 2016. [Online; accessed 9-November-2016].

[50] J. Degnan. A tutorial on retroreflectors and arrays for SLR. In *Proceedings of International Technical Laser Workshop 2012 (ITLW-12)*, Frascati (Rome), Italy, November 2012.

[51] E. Kaplan and C. Hegarty. *Understanding GPS: Principles and Applications*. Number ISBN: 9781580538954. Artech House, 2005.

[52] J. Silha, T. Schildknecht, J.-N. Pittet, D. Bodenmann, R. Kanzler, P. Kaerraeng, and H. Krag. Comparison of Envisat's attitude simulation and real optical and SLR observation in order to refine the satellite attitude model. In *Proceedings of Advanced Maui Optical and Space Surveillance Technologies Conference (AMOS)*, Maui, Hawaii, 2016.

[53] D. Kucharski, G. Kirchner, F. Koidl, C. Fan, R. Carman, C. Moore, A. Dmytrotsa, M. Ploner, G. Bianco, M. Medvedskij, A. Makeyev, G. Appleby, M. Suzuki, J.-M. Torre, Z. Zhongping, L. Grunwaldt, and Q. Feng. Attitude and spin period of space debris Envisat measured by satellite laser ranging. *IEEE Transactions on Geoscience and Remote Sensing*, 50(12):7651–7657, 2014.

[54] R. Dach, S. Lutz, P. Walser, and P. Friedez. *Bernese GNSS Software Version 5.2. User Manual*. Number ISBN: 978-3-906813-05-9. Astronomical Institute, University of Bern, Bern Open Publishing, Bern, Switzerland, 2015.

[55] G. Beutler, A. Jäggi, L. Mervart, and U. Meyer. The celestial mechanics approach: application to data of the GRACE mission. *Journal of Geodesy*, 84(11):661–681, 2010.

[56] V.B. Mendes and E.C. Pavlis. High-accuracy zenith delay prediction at optical wavelengths. *Geophysical Research Letters*, 31(LI14602), 2004.

[57] A. E. Hedin. Extension of the MSIS thermosphere model into the middle and lower atmosphere. *Journal of Geophysical Research: Space Physics*, 96(A2):1159–1172, 1991.

[58] F. Lyard, F. Lefevre, T. Letellier, and O. Francis. Modelling the global ocean tides: modern insights from FES2004. *Ocean Dynamics*, 56(5):394–415, 2006.

[59] R.D. Ray and R.M. Ponte. Barometric tides from ECMWF operational analyses. *Annales Geophysicae*, 21(8):1897–1910, 2003.

[60] N. K. Pavlis, S. A. Holmes, S. C. Kenyon, and J. K. Factor. The development and evaluation of the Earth Gravitational Model 2008 (EGM2008). *Journal of Geophysical Research: Solid Earth*, 117(B4):n/a–n/a, 2012. B04406.

[61] E.M. Standish. The observational basis for JPL′s DE200, the planetary ephemerides of the Astronomical Almanac. *Astronomy and Astrophysics*, 233(1):252–271, 1990.

[62] C. Bizouard and D. Gambis. The combined solution C04 for earth orientation parameters consistent with International Terrestrial Reference Frame 2008, 2011.

[63] P. M. Mathews, T. A. Herring, and B. A. Buffett. Modeling of nutation and precession: New nutation series for nonrigid Earth and insights into the Earth's interior. *Journal of Geophysical Research: Solid Earth*, 107(B4):ETG 3–1–ETG 3–26, 2002.

[64] Z. Altamimi, X. Collilieux, and L. Métivier. ITRF2008: an improved solution of the international terrestrial reference frame. *Journal of Geodesy*, 85(8):457–473, August 2011.

[65] J.W Marini and C.W. Murray. Correction of laser range tracking data for atmospheric refraction at elevation above 10 degrees. Technical Report 19740007037, National Research Council (U.S.), Greenbelt, MD, United States, 1973.

[66] Deutsches Geodätisches Forschungsinstitut Technische Universität München. Ilrs sinex file with data handling recommendations, 2017. [Online; accessed 27-January-2017].

[67] K. Sosnica, A. Jäggi, U. Meyer, D. Thaller, G. Beutler, D. Arnold, and R. Dach. Time variable Earth′s gravity field from SLR satellites. *J. Geod.*, 89:945–960, 2015.

[68] A.E. Hedin. MSIS-86 thermospheric model. *Journal of Geophysical Research: Space Physics (1978–2012)*, 92(A5):4649–4662, 5 1987.

[69] J. Griffiths and J.R. Ray. On the precision and accuracy of IGS orbits. *Journal of Geodesy*, 83(3):277–287, 2009.

[70] M. Ploner, E. Cordelli, D. Bodenmann, T. Schildknecht, P. Schlatter, and A. Jäggi. GNSS observations for calibration tasks at the Zimmerwald observatory. In *International Symposium on GNSS 2015*, Kyoto, Japan, November 2015.

[71] S.L.R. Ellison, T.J. Farrant, and V. Barwick. *Practical Statistics for the Analytical Scientist: A Bench Guide*. Number ISBN: 978-0854041312. Royal Society of Chemistry, Cambridge, United Kingdom, 2nd edition, 2009.

[72] D. Kucharski, J.C. Bennet, and G. Kirchner. Laser de-spin maneuver for an active debris removal mission a realistic scenario for Envisat. In *Proceedings of Advanced Maui Optical and Space Surveillance Technologies Conference (AMOS)*, Maui, Hawaii, 2016.

# Appendix A

# Subroutines for Processing SLR

## A.1 Perl Scripts

Here the list of implemented Perl scripts that were used for different purposes during the study of the merging of the laser range with the angular measurements. For each subroutine a short description of its purpose is given.

- **ReadCRD.pl**: used to read the Consolidated Range Data (CRD) both full-rate or quick-look files, store the data necessary for the SLR processing and converting them into the new observation data format.
- **LStaRen.pl**: called within ReadCRD.pl takes as input the station number and the observation epoch, searches within the station-information file (i.e. CODE_SLR.STA) the other part of the station-name, which identifies the station-configuration, according to the observation epoch.
- **ReadOBS.pl**: reads the standard SATORB observation file (e.g. procogs.OBS), stores the data and converts them into the new observation data format.
- **MergeObs.pl**: main scripts which converts from the standard observations formats (i.e. CRD and OBS) to the final observations file in the new format. It calls *ReadCRD.pl* and *ReadOBS.pl*, merges their output files and sorts the measurements in the chronological order from the oldest to the newest and finally calls the *CheckDoubleLines.pl*.
- **CheckDoublelines.pl**: checks the observations file obtained by merging laser and angular measurements and delete the lines which contain the same observations.
- **ScreenObservations.pl**: reads the SATORB orbit determination output file (e.g. procogs.OUT) and according to the selected threshold it comments the observations in the observation file whose residuals are higher than the threshold.
- **SelectStaObs.pl**: reads the observation file in the new format and stores or deletes all the observations coming from the specified station.
- **CreaFakeOBS.pl**: creates an observation file in the new or old SATORB observation format with the desired time epoch and interval. It is used for the generation of ephemerides.

- **ReadSP3.pl**: reads the SP3-format (i.e. file.EPH) downloaded from CODE, selects the coordinates of the position of the specified satellites, converts the position-epoch in MJD and stores time epoch and positions in a text file ready to be imported into another environment (e.g. MatLab).
- **ReduceFullRate.pl**: reads the output of the *MergObs.pl* and when it finds a full-rate data set, it selects only the observations with a time distance equal or bigger than the specified one. Finally, it writes the reduced set of observations in a new file.
- **ReadPRE.pl**: reads the file.PRE generated by the Bernese GNSS Software v. 5.2 [54] and stores the satellite positions in a text file ready to be imported into another environment.
- **RecOBSfromMJD.pl**: generates an observations files (in the new format) storing in it only the observations contained in a SLR RINEX file (i.e. file.XXO) or in a list of them. It was used to compare the orbit determination results with those obtained from the Bernese GNSS Software v. 5.2 [54].
- **RecoveryOBSfromOUT.pl**: reads the SATORB orbit determination output file (e.g. procogs.OUT), looks in the observations files containing all observations for the specified object and reconstructs a new observations file with only the measurements used in the orbit determination process.
- **AutoRunsoWeight.pl**: runs one after the other the orbit determination and the orbit propagation part of SATORB using each time different weights on the laser measurements (specified on a separated list) and stores the obtained orbital elements, output and ephemeris files (respectively OD.ELE, OD.OUT and PR.TAB).
- **ReadELE.pl**: reads all the elements files (i.e. .ELE) generated by *AutoRunsoWeight.pl* and stores all the orbital elements in a new file.

## A.2 Fortran Subroutines

### A.2.1 New Subroutines

As well as for the Perl scripts, here the list of Fortran routines implemented during the study of the merging of the laser range with the angular measurements. For each subroutine a short description of its purpose is given.

- **BUILDWEIGHTOBS.f**: calculates the weights for each measurement.
- **RGCORR.f**: main subroutine which applies all the corrections needed for the SLR measurements.
- **GTSFGMI.f**: reads the solar flux and geomagnetic indexes and combines them to be given as input to the MSISe90 atmospheric model for the calculation of the atmospheric drag.

- **WRTCOVM.f**: writes the covariance matrices w.r.t. the orbital elements and the state vector in the Earth Centered Inertial and Radial, Along- and Cross-track components at the end of the orbit determination process.

### A.2.2 Modified Subroutines

Finally the list of Fortran subroutines and/or programs that were modified and adapted for the processing of the laser measurements.

- **SATORB.f** adapted to handle the laser measurements and the correction of the light travel time for angular observations
- **OBSREA.f** adapted to read the new observation file
- **BNGOBS.f** adapted to read the new observation file, read station position and velocities, apply the station velocities and the station eccentricity correction for the laser measurements before the conversion of the station coordinates from Earth Centered Earth Fixed (ECEF) to Earth Centered Inertial (ECI, precisely the J2000 system).
- **SETNOR.f** adapted to handle the laser measurements, more details are given in the following Paragraph A.2.3.
- **DEQSOR.f** introduction of the subroutine *GTSFGMI.f* to improve the accuracy of the atmospheric density calculation.
- **TABPOS.f** introduction of the choice between generating the ephemerides in ECEF or in ECI coordinates
- **RDSORX.f** adapted to read all input files needed for the background model shown in Paragraph 5.3.1.

### A.2.3 Modification of the *SETNOR.f* Subroutine

The major modifications of the SATORB software were performed within the subroutine called *SETNOR.f*. This subroutine is responsible for the set up of the normal equation system (NEQ), the calculation of the observation residuals ($O-C$), the inversion of the NEQ, and the consequent estimation of the parameters, of the residuals and of the resulting covariance matrix.
First of all we needed to adapt it to handle the new observable and its relative weight. Then we needed to implement the partial derivatives shown in Paragraph 5.3.3, and finally we needed to modify the part which is responsible of the residuals calculation.
However, the most important modifications were needed to calculate the $O-C$ of the laser measurements. Since within the CelMech/Bernese GNSS softwares the corrections of the measurements are applied to the computed ones and not to the raw measurements, and in order to modify what is already existing as little as possible, we collected and applied almost all the corrections within the *RGCORR.f* subroutine and we called it within *SETNOR.f*. As just said and as shown in Figure A.1 not all the corrections are applied within *RGCORR.f*. Since

*SETNOR.f* takes as input the station coordinates already in the ECI system we were obliged to apply the correction due to the station eccentricity ($\delta_r$) before this transformation which is performed within the subroutine *BNGOBS.f*. The corrected station position, together with the satellite position (in the same ECI coordinates) and the meteorological data regarding the laser measurements are sent as input within *SETNOR.f* and then within *RGCORR.f*. Among these inputs there is also the measurement-epoch time fraction ($d_t$) which, as we will see in Appendix B, could not be taken into account within the MJD of the measurement because outside the significant digits. First of all, the position of the satellite is corrected according to the time fraction $d_t$, then it is sent as input, together with the station coordinates, into the subroutine *TOPSTA.f* which calculates the geometric range, the relativistic corrections (see Paragraph 5.3.1) and the light-travel-time correction (see Paragraph 5.3.2). The corrected satellite position together with the relative humidity, the temperature and the pressure of the observing site at the observation epoch are used by *TROPOS.f* to determine the tropospheric delay. Finally, within *RGCORR.f* the subroutine *GETRGB.f* is called twice to get the station range bias and, in the case of geodetic satellites, the center of mass corrections stored within the station information file. The just determined corrections ($\delta_{rel}$, $\delta_{ltt}$, $\delta_{atm}$, $\delta_{RB}$ and $\delta_{CoM}$) are then applied to the geometrical range to calculate the computed range which is the main output of *RGCORR.f* and will be then used for the $O-C$ derivation later within *SETNOR.f*.

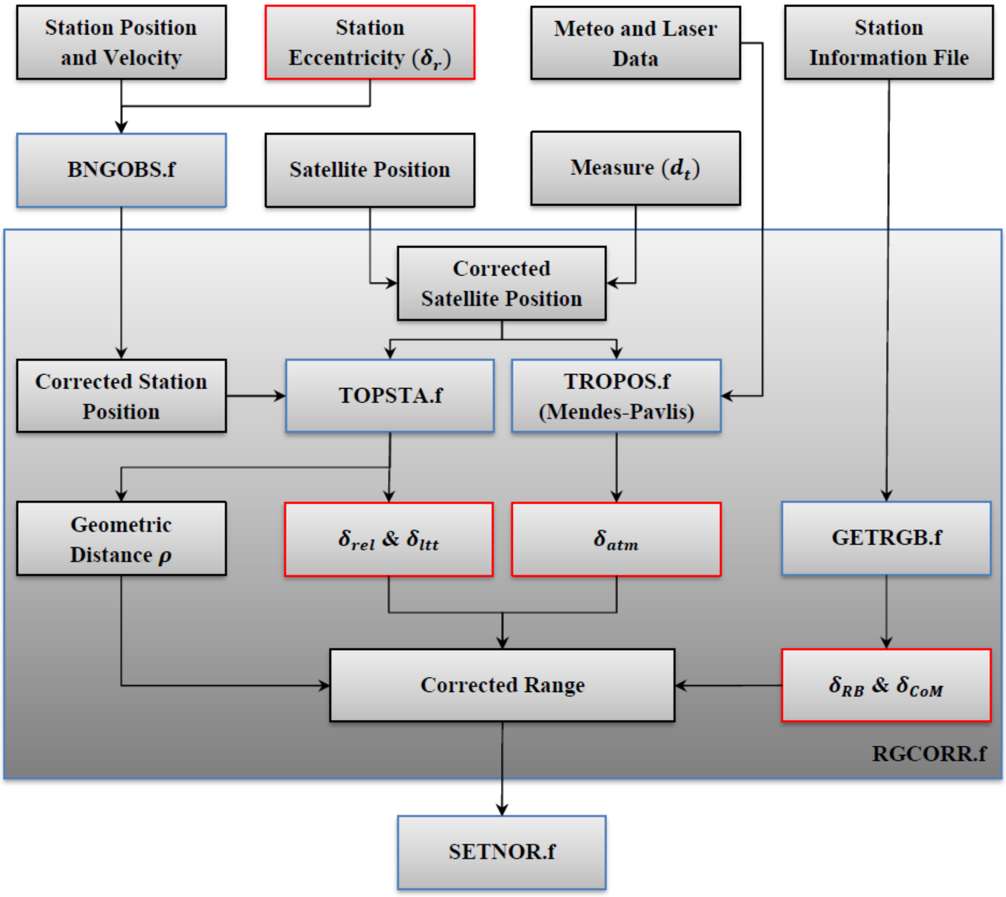

Figure A.1 Flowchart of the application of the corrections to the laser measurements

## A.3 Light Travel Time Correction for Angular Measurements

Finally we needed to correct a small error in the SATORB software which became evident only when we merged for the first time some range with angular observations. The tested object was the Lageos 1 satellite and the arc covered by the observations was 1 night. First we performed an OD using only the angles, then we repeated the OD process once using only ranges and a second time merging the two observables. If both ODs were good with separated observables, i. e. residuals of 0.27 arcsec for the angle-only solution and 1.64 cm for the laser-only one, we notice that when merging the two kinds of measurements the angular observations got a bias in the residuals of about 3 arcsec. This bias was corrected implementing the light travel time (LTT) correction for the angular measurement as shown in Figure A.2. This correction is needed since the angular position measured on the image does not represent the real position of the observed object at the time of the image acquisition, but it represents the position of the object at the time of the image acquisition minus the time needed by the light to travel from the object to the CCD camera [16]. Since at the image processing level the distance of the object is unknown this correction must be applied within the OD process. As said, this correction needs to be applied to the measurement epoch which is also the time used by the propagator to calculate the satellite state vector. Figure A.2 shows the application of this correction via a small iterative process. Finally, we compared again the sets of orbital elements estimated before and after the application of the correction. It was interesting to notice that the only difference between the two sets was visible for the argument of latitude. This means that the perigee passing time is absorbing entirely this error. Since this error for a geostationary satellite (altitude about $\sim$ 36000 km) is $\sim$ 0.12 sec and the angular velocity in the sky for a GEO is 15 arcsec/sec, neglecting the LTT produces an error of 1.8 arcsec. This corresponds to less than 3 pixels on the Zimlat CCD, which was unnoticeable without the use of highly precise external sources of information as the laser ranges, the GNSS orbits or other satellites whose orbit is accurate enough.

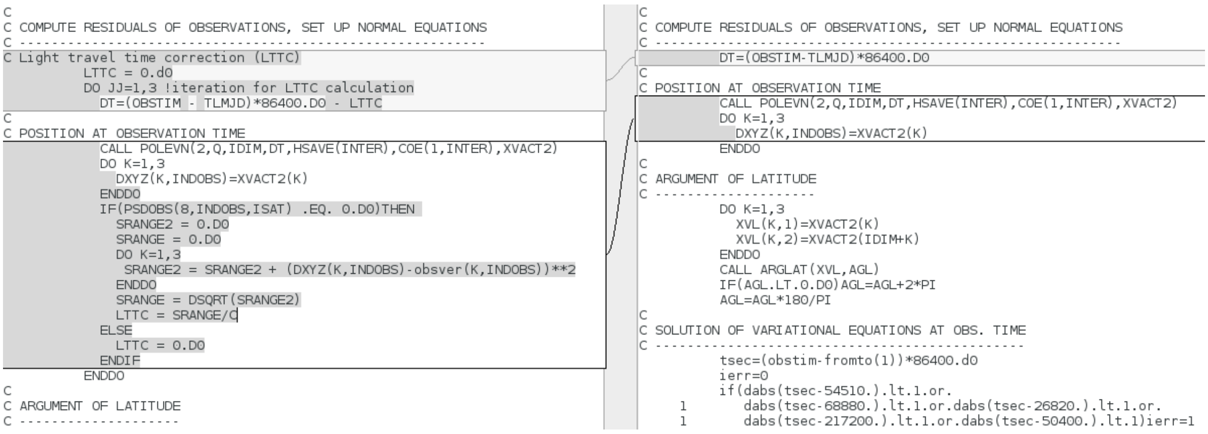

```fortran
C
C COMPUTE RESIDUALS OF OBSERVATIONS, SET UP NORMAL EQUATIONS
C ------------------------------------------------------------
C Light travel time correction (LTTC)
          LTTC = 0.d0
          DO JJ=1,3 !iteration for LTTC calculation
            DT=(OBSTIM - TLMJD)*86400.D0 - LTTC
C
C POSITION AT OBSERVATION TIME
            CALL POLEVN(2,Q,IDIM,DT,HSAVE(INTER),COE(1,INTER),XVACT2)
            DO K=1,3
              DXYZ(K,INDOBS)=XVACT2(K)
            ENDDO
            IF(PSDOBS(8,INDOBS,ISAT) .EQ. 0.D0)THEN
              SRANGE2 = 0.D0
              SRANGE = 0.D0
              DO K=1,3
               SRANGE2 = SRANGE2 + (DXYZ(K,INDOBS)-obsver(K,INDOBS))**2
              ENDDO
              SRANGE = DSQRT(SRANGE2)
              LTTC = SRANGE/C
            ELSE
              LTTC = 0.D0
            ENDIF
          ENDDO
C
C ARGUMENT OF LATITUDE
C --------------------
```

```fortran
C
C COMPUTE RESIDUALS OF OBSERVATIONS, SET UP NORMAL EQUATIONS
C ------------------------------------------------------------
          DT=(OBSTIM-TLMJD)*86400.D0
C
C POSITION AT OBSERVATION TIME
          CALL POLEVN(2,Q,IDIM,DT,HSAVE(INTER),COE(1,INTER),XVACT2)
          DO K=1,3
            DXYZ(K,INDOBS)=XVACT2(K)
          ENDDO
C
C ARGUMENT OF LATITUDE
C --------------------
          DO K=1,3
            XVL(K,1)=XVACT2(K)
            XVL(K,2)=XVACT2(IDIM+K)
          ENDDO
          CALL ARGLAT(XVL,AGL)
          IF(AGL.LT.0.D0)AGL=AGL+2*PI
          AGL=AGL*180/PI
C
C SOLUTION OF VARIATIONAL EQUATIONS AT OBS. TIME
C --------------------------------------------
          tsec=(obstim-fromto(1))*86400.d0
          ierr=0
          if(dabs(tsec-54510.).lt.1.or.
     1       dabs(tsec-68880.).lt.1.or.dabs(tsec-26820.).lt.1.or.
     1       dabs(tsec-217200.).lt.1.or.dabs(tsec-50400.).lt.1)ierr=1
```

Figure A.2 Light travel time correction implemented within the program *SATORB.f*.

# Appendix B

# The New Format of SATORB Files

## B.1 Observation Format

The SATORB software was not meant to deal with range measurements. So together with the modification described in the Paragraph 5.3 we needed also to implement the capability to read the new observations. For simplicity instead of import separately the angular observations file and the range one and then take care of sorting chronologically the measurements within the software, we decided to let SATORB read only one observation file with a new format where the just mentioned steps were performed outside the program. In the next paragraphs we will describe the starting observation formats (namely the CRD for the ranges and the OBS for the angles) and the new implemented one.

### B.1.1 Old Format - CRD Format

According with the ILRS standards, the laser ranges measurements are provided in the Consolidated Range Data format (CRD). This files usually contains:

- Header Record:
  Type ”H1” or ”h1” information about the version of the file,
  Type ”H2” or ”h2” information about the station,
  Type ”H3” or ”h3” information about the target,
  Type ”H4” or ”h4” information about the session (pass),
  Type ”H8” or ”h8” indicates the end of the session (pass),
  Type ”H9” or ”h9” indicates the end of file.
- Configuration Record:
  Type ”C” or ”c0” system configuration record,
  Type ”C1” or ”c1” laser configuration record,
  Type ”C2” or ”c2” detector configuration record,
  Type ”C3” or ”c3” timing system configuration record,
  Type ”C4” or ”c4” transponder (clock) configuration record.
- Data Record:
  Type ”10” Full-rate range record,

Type ”11” Normal Point range record,
Type ”12” Range supplement record,
Type ”20” Meteorological record,
Type ”21” Meteorological supplement record,
Type ”30” Pointing angles record,
Type ”40” Calibration record,
Type ”50” Session (Pass) statistics record,
Type ”60” Compatibility record.

We reported just a summary of the contents of the CRD format, for more information please look at the ILRS website [2]. It must be said also that not all data records are usually available in the CRD-files, and among CRD there are station dependent differences. Figure B.1 shows an example of CRD-file where normal point range data are stored. We reported this example to highlight the components that will be taken into account for conversion between CRD and the new observation file. From the CRD file we take into account: the measurements epoch in particular only the day, the month, the year of the measurement plus the seconds from midnight, the laser wavelength, the meteorological data, the time of flight of the laser pulse, the standard deviation (STD) of the normal point (which is given in picoseconds), and the epoch event flag which indicates the reference time of the normal point (e.g. spacecraft bounce epoch, ground receive time, ground transmit time etc.).

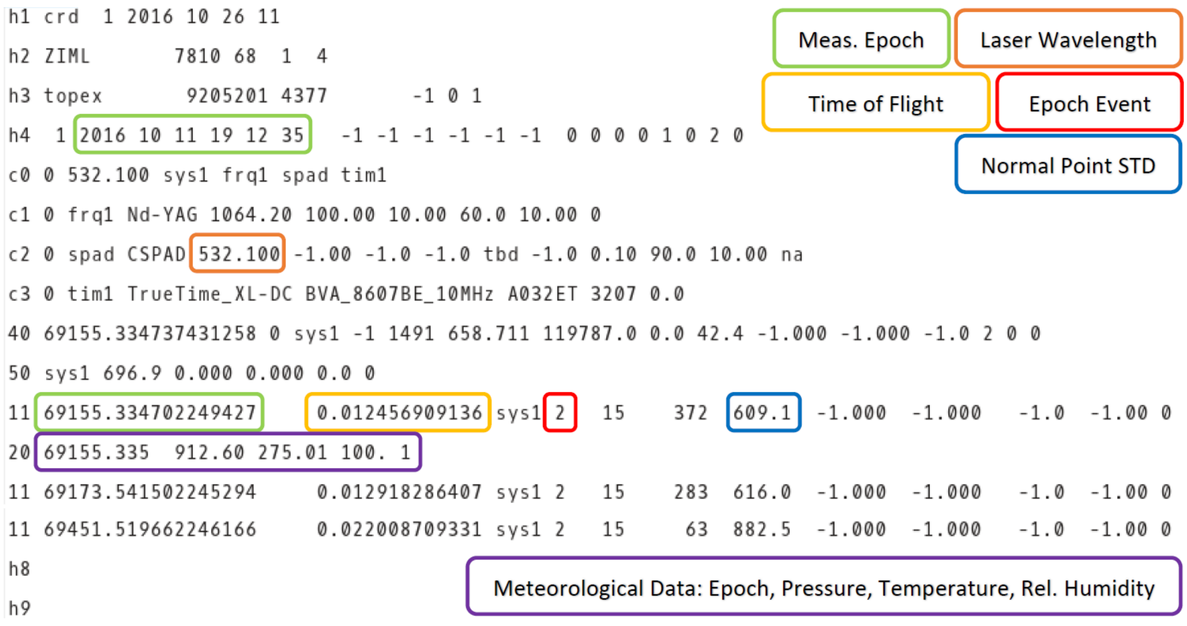

```
h1 crd  1 2016 10 26 11
h2 ZIML       7810 68  1  4
h3 topex       9205201 4377       -1 0 1
h4  1 2016 10 11 19 12 35  -1 -1 -1 -1 -1 -1  0 0 0 0 1 0 2 0
c0 0 532.100 sys1 frq1 spad tim1
c1 0 frq1 Nd-YAG 1064.20 100.00 10.00 60.0 10.00 0
c2 0 spad CSPAD 532.100 -1.00 -1.0 -1.0 tbd -1.0 0.10 90.0 10.00 na
c3 0 tim1 TrueTime_XL-DC BVA_8607BE_10MHz A032ET 3207 0.0
40 69155.334737431258 0 sys1 -1 1491 658.711 119787.0 0.0 42.4 -1.000 -1.000 -1.0 2 0 0
50 sys1 696.9 0.000 0.000 0.0 0
11 69155.334702249427    0.012456909136 sys1 2   15    372  609.1  -1.000  -1.000   -1.0  -1.00 0
20 69155.335  912.60 275.01 100. 1
11 69173.541502245294    0.012918286407 sys1 2   15    283  616.0  -1.000  -1.000   -1.0  -1.00 0
11 69451.519662246166    0.022008709331 sys1 2   15     63  882.5  -1.000  -1.000   -1.0  -1.00 0
h8
h9
```

Figure B.1 Example of CRD file.

### B.1.2 Old Format - OBS Format

The typical observation file used by SATORB when processing angular observations is the one shown in Figure B.2. As one can see, the first column is occupied with the telescope or the station name, the second can be occupied either by the tracklet ID or in the case where the tracklet is already associated to a known object by the object name. Nevertheless the tracklet-name is always reported also in the 9th column. Then comes the part regarding the data, in particular in the third column the modified Julian epoch (MJD) of the measurements is reported, then the Right Ascension (RA, in the format *hh.mmss*) and the Declination (DE, in the format *dd.mmss*). Successively the magnitude of the object, the astrometric uncertainty, and finally, the name of the picture from which the measure is extracted and some empty fields.

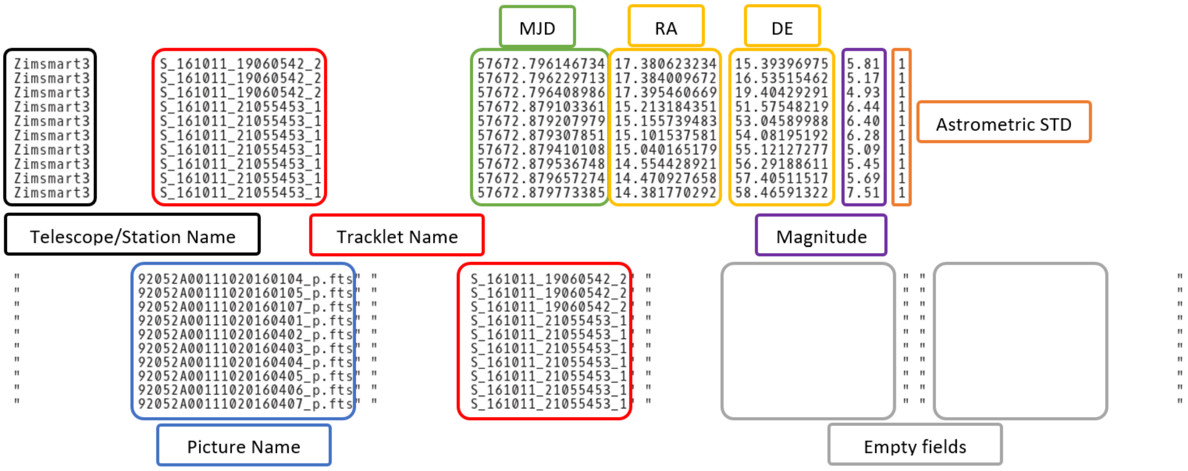

```
Zimsmart3   S_161011_19060542_2   57672.796146734 17.380623234 15.39396975 5.81 1
Zimsmart3   S_161011_19060542_2   57672.796229713 17.384009672 16.53515462 5.17 1
Zimsmart3   S_161011_19060542_2   57672.796408986 17.395460669 19.40429291 4.93 1
Zimsmart3   S_161011_21055453_1   57672.879103361 15.213184351 51.57548219 6.44 1
Zimsmart3   S_161011_21055453_1   57672.879207979 15.155739483 53.04589988 6.40 1
Zimsmart3   S_161011_21055453_1   57672.879307851 15.101537581 54.08195192 6.28 1
Zimsmart3   S_161011_21055453_1   57672.879410108 15.040165179 55.12127277 5.09 1
Zimsmart3   S_161011_21055453_1   57672.879536748 14.554428921 56.29188611 5.45 1
Zimsmart3   S_161011_21055453_1   57672.879657274 14.470927658 57.40511517 5.69 1
Zimsmart3   S_161011_21055453_1   57672.879773385 14.381770292 58.46591322 7.51 1

"        92052A00111020160104_p.fts" "    S_161011_19060542_2" "
"        92052A00111020160105_p.fts" "    S_161011_19060542_2" "
"        92052A00111020160107_p.fts" "    S_161011_19060542_2" "
"        92052A00111020160401_p.fts" "    S_161011_21055453_1" "
"        92052A00111020160402_p.fts" "    S_161011_21055453_1" "
"        92052A00111020160403_p.fts" "    S_161011_21055453_1" "
"        92052A00111020160404_p.fts" "    S_161011_21055453_1" "
"        92052A00111020160405_p.fts" "    S_161011_21055453_1" "
"        92052A00111020160406_p.fts" "    S_161011_21055453_1" "
"        92052A00111020160407_p.fts" "    S_161011_21055453_1" "
```

Figure B.2 Example of the classical SATORB observation file.

## B.1.3 New Format

The new observation format was studied essentially to collect different observables in the same files, but we also took the opportunity to introduce new features. Dealing with different kinds of observables the new format consists of a common part and then of an observation specific part. The first contains: the header, the flag specific of each kind of observation, the measurement epoch and the station name. The second contains: the measurement itself and the parameters related to that observable.

The header contains the name of the object whose observations refer to. The flag is observable-specific and within SATORB it is used as discriminant to understand which kind of observable we are dealing with. At the moment only three kind of observables can be distinguished: the normal point (L1), the full-rate data (L0) and the classical angular observations (O1). We introduced the flag mechanism so that if one wants to add a new observable it is sufficient to add a new flag in the file and in the *BNGOBS.f* subroutine, responsible for reading the observation file.

We introduced the possibility to comment out the measurements just by putting a # in front of the observation line.

We added digits to the MJD of the measurements in order to take into account up to tens of microseconds.

This accuracy it is not sufficient for the laser measurements so we needed to introduce another field ($d_t$) which contains the time fraction not considered in the MJD. The value of $d_t$ is expressed in milliseconds.

The last component of the common part is the name of the observing site to which correspond the geodetic coordinates used later by SATORB. We talked about observing site or "monument" and especially for angular observations we discriminate between telescope name and station name since different instruments were alternated in the same place. This separation allowed us to keep track of the used instrument and will not bring to ambiguous entries.
Continuing the description for the angular measurement we introduced the possibility to keep both the name of the object and the related tracklet, then the usual RA, DE coordinates, their respective STD (which could be different), and finally the magnitude of the observed object.
For the laser observations, after the MJD of the measurement, we report the station name, which is made by two part: the first identifies the place, and the second the version of the system. Then, we have the target name, the measured range, the range STD, a data quality alert indicator (Qf), the laser wavelength ($\lambda$), the before mentioned time fraction not considered by the MJD ($d_t$), the atmospheric pressure expressed in millibar ($p$), the temperature in Kelvin degree ($K$) and the relative humidity ($RH$). As said in Paragraph 5.3.2 the laser wavelength together with the meteorological data are needed to calculate the tropospheric correction. It must be said that the range STD is expressed in meters and in the case of normal points is obtained by the conversion of the STD expressed in picoseconds in the CRD file. In the case of full rate data, since it is not available in the CRD file, is assumed to be equivalent to 0.5 m. Finally the data quality alert indicator is reported directly from the CRD file, indicates when the quality of the measurement is good($= 0$), suspicious ($= 1$) in the sense that can be used with caution or poor ($= 2$) when it is advisable to not use it for geodetic purposes. We decided to keep this flag to better understand the results.

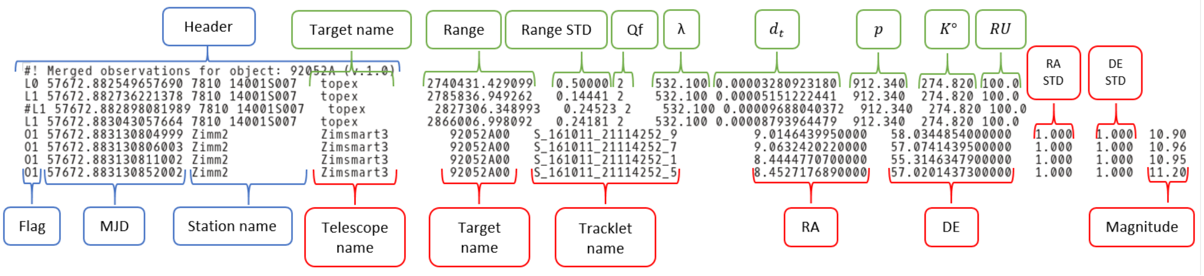

```
#! Merged observations for object: 92052A (v.1.0)
L0 57672.882549657690 7810 14001S007   topex       2740431.429099   0.50000 2     532.100 0.00003280923180  912.340  274.820 100.0
L1 57672.882736221378 7810 14001S007   topex       2785836.949262   0.14441 2     532.100 0.00005151222441  912.340  274.820 100.0
#L1 57672.882898081989 7810 14001S007   topex       2827306.348993   0.24523 2     532.100 0.00009688040372  912.340  274.820 100.0
L1 57672.883043057664 7810 14001S007   topex       2866006.998092   0.24181 2     532.100 0.00008793964479  912.340  274.820 100.0
01 57672.883130804999 Zimm2            Zimsmart3      92052A00   S_161011_21114252_9        9.0146439950000   58.0344854000000   1.000   1.000  10.90
01 57672.883130806003 Zimm2            Zimsmart3      92052A00   S_161011_21114252_7        9.0632420220000   57.0741439500000   1.000   1.000  10.96
01 57672.883130811002 Zimm2            Zimsmart3      92052A00   S_161011_21114252_1        8.4444770700000   55.3146347900000   1.000   1.000  10.95
01 57672.883130852002 Zimm2            Zimsmart3      92052A00   S_161011_21114252_5        8.4527176890000   57.0201437300000   1.000   1.000  11.20
```

Figure B.3 Example of the new SATORB observation file.

## B.2 Output File

For completeness, we report also a small description of the fields that were modified within the SATORB output file. The new fields of the SATORB output file are the ones within the red rectangles in the Figures B.4, B.5 and B.6. The changes strictly related to the introduction of the ranges measurements were essentially 3: we added a column in the list of the observations and of the residuals paying attention to put a 0 on the range column when only the angles are present and vice versa. Then we needed to adapt the unit of measurements and the residual computation according to the kind of measurements processed.
The other modifications introduced to the output file were done to display other results useful during the study, and to better understanding the outcomes. We then introduced the residuals

computed during the first iteration of the LSQ adjustment. Finally, we reported the obtained covariance w.r.t. the estimated orbital elements and its conversion w.r.t. the state vector in Earth Centered Inertial (ECI) and in radial, along- and cross-track (RSW) coordinates. To better understand the effects of the different observables we displayed also the STD of the position and the velocity plus the correlation matrix in RSW components. For completeness, the last change was performed to show, together with the scaling parameter, the new estimated value of the AMR (see Figure B.6).

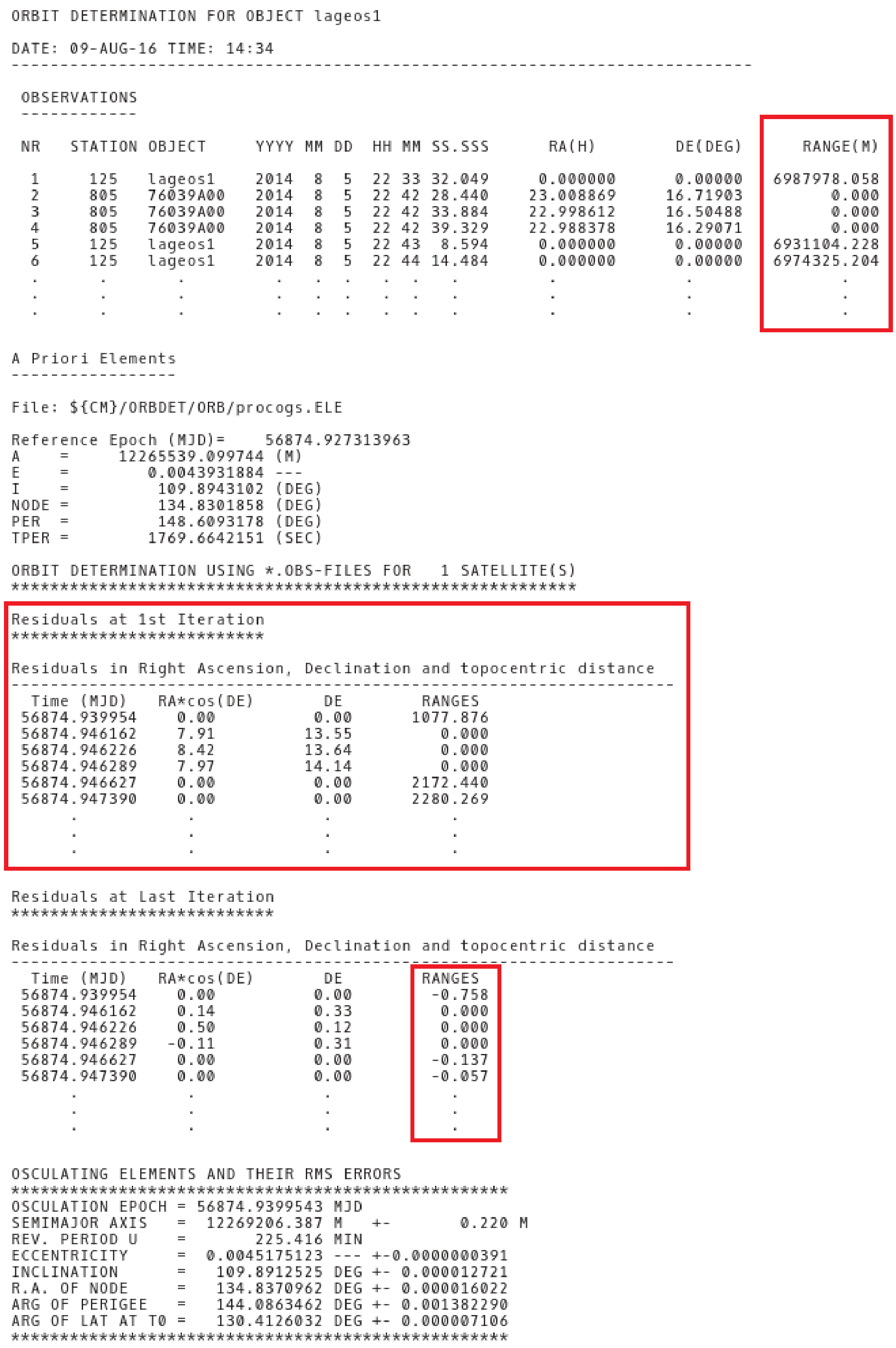

```
ORBIT DETERMINATION FOR OBJECT lageos1

DATE: 09-AUG-16 TIME: 14:34
----------------------------------------------------------------------------

 OBSERVATIONS
 ------------

 NR    STATION OBJECT     YYYY MM DD  HH MM SS.SSS      RA(H)        DE(DEG)      RANGE(M)

  1     125   lageos1    2014  8  5  22 33 32.049     0.000000      0.00000  6987978.058
  2     805   76039A00   2014  8  5  22 42 28.440    23.008869     16.71903        0.000
  3     805   76039A00   2014  8  5  22 42 33.884    22.998612     16.50488        0.000
  4     805   76039A00   2014  8  5  22 42 39.329    22.988378     16.29071        0.000
  5     125   lageos1    2014  8  5  22 43  8.594     0.000000      0.00000  6931104.228
  6     125   lageos1    2014  8  5  22 44 14.484     0.000000      0.00000  6974325.204
  .      .       .         .   .  .   .  .   .          .            .                .
  .      .       .         .   .  .   .  .   .          .            .                .
  .      .       .         .   .  .   .  .   .          .            .                .

A Priori Elements
-----------------

File: ${CM}/ORBDET/ORB/procogs.ELE

Reference Epoch (MJD)=    56874.927313963
A    =     12265539.099744 (M)
E    =        0.0043931884 ---
I    =         109.8943102 (DEG)
NODE =         134.8301858 (DEG)
PER  =         148.6093178 (DEG)
TPER =        1769.6642151 (SEC)

ORBIT DETERMINATION USING *.OBS-FILES FOR   1 SATELLITE(S)
**********************************************************
Residuals at 1st Iteration
**************************

Residuals in Right Ascension, Declination and topocentric distance
--------------------------------------------------------------------
  Time (MJD)    RA*cos(DE)        DE         RANGES
 56874.939954    0.00          0.00      1077.876
 56874.946162    7.91         13.55         0.000
 56874.946226    8.42         13.64         0.000
 56874.946289    7.97         14.14         0.000
 56874.946627    0.00          0.00      2172.440
 56874.947390    0.00          0.00      2280.269
      .           .             .            .
      .           .             .            .
      .           .             .            .

Residuals at Last Iteration
***************************

Residuals in Right Ascension, Declination and topocentric distance
--------------------------------------------------------------------
  Time (MJD)    RA*cos(DE)        DE         RANGES
 56874.939954    0.00          0.00        -0.758
 56874.946162    0.14          0.33         0.000
 56874.946226    0.50          0.12         0.000
 56874.946289   -0.11          0.31         0.000
 56874.946627    0.00          0.00        -0.137
 56874.947390    0.00          0.00        -0.057
      .           .             .            .
      .           .             .            .
      .           .             .            .

OSCULATING ELEMENTS AND THEIR RMS ERRORS
***************************************************
OSCULATION EPOCH = 56874.9399543 MJD
SEMIMAJOR AXIS    =  12269206.387 M   +-       0.220 M
REV. PERIOD U     =       225.416 MIN
ECCENTRICITY      =  0.0045175123 --- +-0.0000000391
INCLINATION       =   109.8912525 DEG +- 0.000012721
R.A. OF NODE      =   134.8370962 DEG +- 0.000016022
ARG OF PERIGEE    =   144.0863462 DEG +- 0.001382290
ARG OF LAT AT T0 =    130.4126032 DEG +- 0.000007106
***************************************************
```

Figure B.4 First part of the modified SATORB output file.

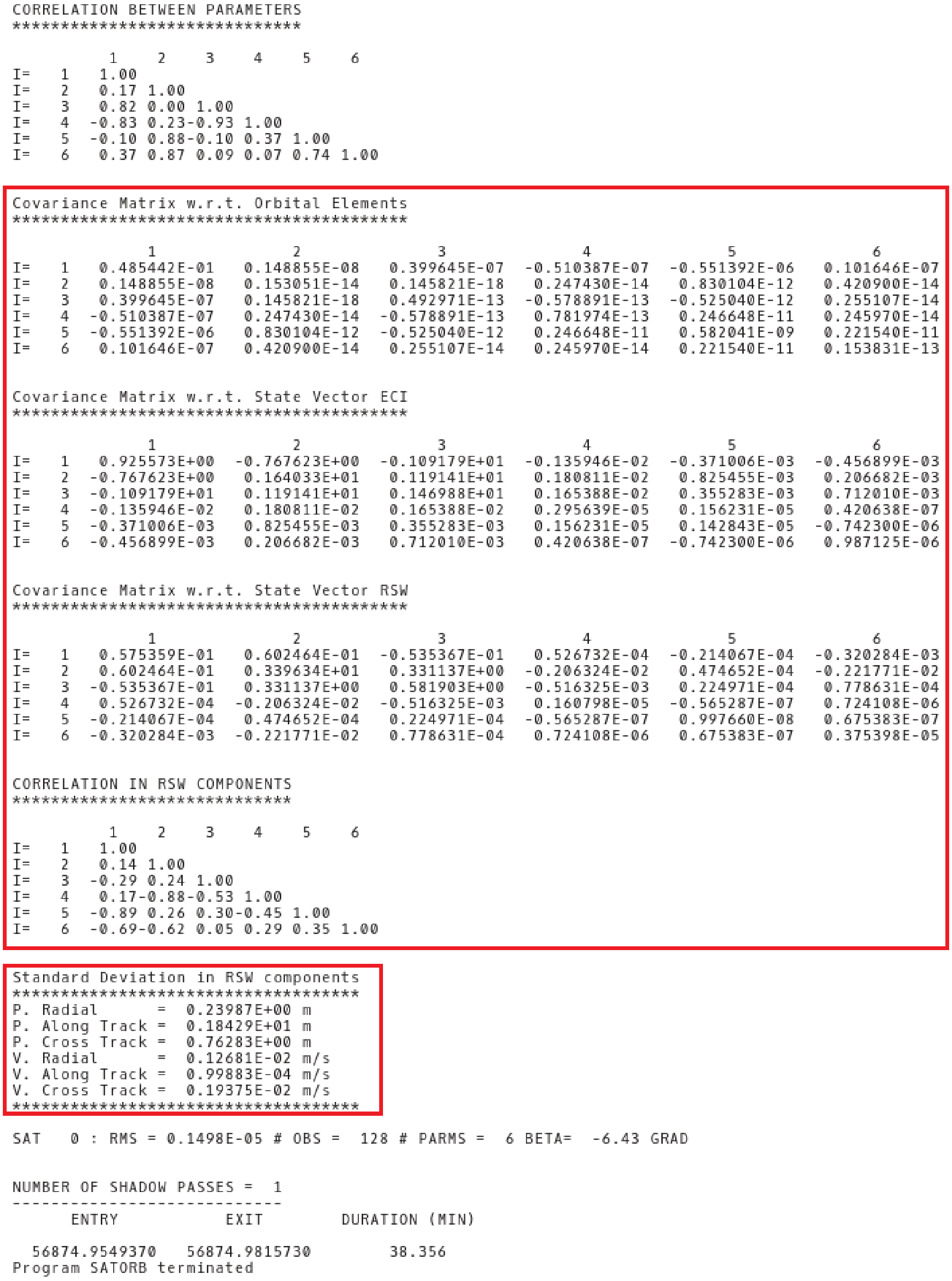

```
CORRELATION BETWEEN PARAMETERS
******************************

          1    2    3    4    5    6
I=   1   1.00
I=   2   0.17 1.00
I=   3   0.82 0.00 1.00
I=   4  -0.83 0.23-0.93 1.00
I=   5  -0.10 0.88-0.10 0.37 1.00
I=   6   0.37 0.87 0.09 0.07 0.74 1.00

Covariance Matrix w.r.t. Orbital Elements
*****************************************

              1              2              3              4              5              6
I=   1   0.485442E-01   0.148855E-08   0.399645E-07  -0.510387E-07  -0.551392E-06   0.101646E-07
I=   2   0.148855E-08   0.153051E-14   0.145821E-18   0.247430E-14   0.830104E-12   0.420900E-14
I=   3   0.399645E-07   0.145821E-18   0.492971E-13  -0.578891E-13  -0.525040E-12   0.255107E-14
I=   4  -0.510387E-07   0.247430E-14  -0.578891E-13   0.781974E-13   0.246648E-11   0.245970E-14
I=   5  -0.551392E-06   0.830104E-12  -0.525040E-12   0.246648E-11   0.582041E-09   0.221540E-11
I=   6   0.101646E-07   0.420900E-14   0.255107E-14   0.245970E-14   0.221540E-11   0.153831E-13

Covariance Matrix w.r.t. State Vector ECI
*****************************************

              1              2              3              4              5              6
I=   1   0.925573E+00  -0.767623E+00  -0.109179E+01  -0.135946E-02  -0.371006E-03  -0.456899E-03
I=   2  -0.767623E+00   0.164033E+01   0.119141E+01   0.180811E-02   0.825455E-03   0.206682E-03
I=   3  -0.109179E+01   0.119141E+01   0.146988E+01   0.165388E-02   0.355283E-03   0.712010E-03
I=   4  -0.135946E-02   0.180811E-02   0.165388E-02   0.295639E-05   0.156231E-05   0.420638E-07
I=   5  -0.371006E-03   0.825455E-03   0.355283E-03   0.156231E-05   0.142843E-05  -0.742300E-06
I=   6  -0.456899E-03   0.206682E-03   0.712010E-03   0.420638E-07  -0.742300E-06   0.987125E-06

Covariance Matrix w.r.t. State Vector RSW
*****************************************

              1              2              3              4              5              6
I=   1   0.575359E-01   0.602464E-01  -0.535367E-01   0.526732E-04  -0.214067E-04  -0.320284E-03
I=   2   0.602464E-01   0.339634E+01   0.331137E+00  -0.206324E-02   0.474652E-04  -0.221771E-02
I=   3  -0.535367E-01   0.331137E+00   0.581903E+00  -0.516325E-03   0.224971E-04   0.778631E-04
I=   4   0.526732E-04  -0.206324E-02  -0.516325E-03   0.160798E-05  -0.565287E-07   0.724108E-06
I=   5  -0.214067E-04   0.474652E-04   0.224971E-04  -0.565287E-07   0.997660E-08   0.675383E-07
I=   6  -0.320284E-03  -0.221771E-02   0.778631E-04   0.724108E-06   0.675383E-07   0.375398E-05

CORRELATION IN RSW COMPONENTS
*****************************

          1    2    3    4    5    6
I=   1   1.00
I=   2   0.14 1.00
I=   3  -0.29 0.24 1.00
I=   4   0.17-0.88-0.53 1.00
I=   5  -0.89 0.26 0.30-0.45 1.00
I=   6  -0.69-0.62 0.05 0.29 0.35 1.00

Standard Deviation in RSW components
************************************
P. Radial       =  0.23987E+00 m
P. Along Track =  0.18429E+01 m
P. Cross Track =  0.76283E+00 m
V. Radial       =  0.12681E-02 m/s
V. Along Track =  0.99883E-04 m/s
V. Cross Track =  0.19375E-02 m/s
************************************

SAT    0 : RMS = 0.1498E-05 # OBS =   128 # PARMS =   6 BETA=  -6.43 GRAD

NUMBER OF SHADOW PASSES =  1
----------------------------
      ENTRY           EXIT         DURATION (MIN)

  56874.9549370   56874.9815730        38.356
Program SATORB terminated
```

Figure B.5 Second part of the modified SATORB output file.

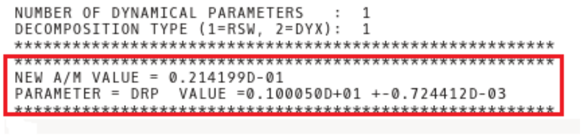

```
NUMBER OF DYNAMICAL PARAMETERS    :  1
DECOMPOSITION TYPE (1=RSW, 2=DYX):  1
*****************************************************
*****************************************************
NEW A/M VALUE = 0.214199D-01
PARAMETER = DRP  VALUE =0.100050D+01 +-0.724412D-03
*****************************************************
```

Figure B.6 Part of the SATORB output file modified to display the new AMR value.

# Appendix C

# List of Publications

| | |
|---|---|
| **7th ESDC** | *Fusion of laser ranges and angular measurements data for LEO and GEO space debris orbit determination*, E. Cordelli, A. Vananti, T. Schildknecht, 7th European Conference on Space Debris Priority, 18 - 21 April 2017, ESA ESOC, Darmstadt, Germany |
| **Stardust Final Conference** | *Orbit Improvement Merging Angular and Laser Range Measurements*, E. Cordelli, A. Vananti, T. Schildknecht, Stardust Final Conference on Asteroids and Space Debris, 31 October - 3 November 2016, ESA ESTEC, Noordwijk, Netherlands |
| **67th IAC** | *Analysis of the Orbit Determination Accuracy Using Laser Ranges and Angular Measurements*, E. Cordelli, A. Vananti, T. Schildknecht, 67th International Astronautical Congress (IAC), 26 - 30 September 2016, Guadalajara, Mexico, IAC-16-A6.9.8. |
| **Acta Astronautica** | *Covariance study to evaluate the influence of optical follow-up strategies on estimated orbital parameters*, E. Cordelli, A. Vananti, T. Schildknecht, Acta Astronautica, 122 (2016) 76-89, DOI: 10.1016/j.actaastro.2016.01.020. |
| **ISGNSS** | *GNSS Observations for Calibration Tasks at the Zimmerwald Observatory*, M. Ploner, E. Cordelli, D. Bodenmann, T. Schildknecht, A. Jaeggi, International Symposium on GNSS 2015, 16 - 19 November 2015, Kyoto, Japan, Paper nr. 165. |
| **66th IAC** | *A Covariance Analysis to Optimize the Optical Follow-up Strategies*, E. Cordelli, A. Vananti, T. Schildknecht, 66th International Astronautical Congress (IAC), 12 - 16 October 2015, Jerusalem, Israel, IAC-15-A6.9.9. |
| **6th EUCASS** | *Optimization of Optical Follow-up Strategies Based on Covariance Analysis*, E. Cordelli, A. Vananti, T. Schildknecht, 6th European Conference for Aeronautics and Space Sciences, 29 June - 3 July 2015, Krakow, Poland, SI-479. |
| **Kolloquiums der Universitaet Bern** | *SMARTnet - First Results of a Test Campaign*, H. Fiedler, T. Schildknecht, M. Wiegel, M. Meinel, R. Hempel, M. Prohaska, M. Ploner, E. Cordelli, University of Bern, November 2014, Bern, Switzerland. |

# List of Publications

| | |
|---|---|
| **40th COSPAR** | *A Covariance Study to Optimize the Optical Observation Strategy for Earth-orbiting Objects*, E. Cordelli, A. Vananti, T. Schildknecht, 40th COSPAR Scientific Assembly, 2 August 2014, Moskow, Russia, PEDAS. 1-0043-14, TFS-S-445. |
| **Journal of Spacecraft and Rockets** | *Determination of Disposed Upper Stage Attitude Motion by Ground-Based Optical Observations*, F. Santoni, E. Cordelli, F. Piergentili, Journal of Spacecraft and Rockets, Vol. 50, No. 3, pp. 701-708, May 2013. |
| **63rd IAC** | *Rocket Body Rotational State Estimation by Remote Optical Observations*, F. Santoni, E. Cordelli, F. Piergentili, 63rd International Astronautical Congress, 1 October 2012, Naples, Italy, IAC-12-A6.5.22. |
| **ENCGNSS** | *Navigation Applications of Vehicles Mobility*, M. Leonardi, G. Gargiulo, E. Cordelli, M. Zanzi, M. Pace, G. Varacalli, C. Facchinetti, The European Navigation Conference on Global Navigation Satellite System, 19 October 2010, Braunschweig, Germany. |
| **Journal of Navigation** | *A New Method for DGPS Ambiguity Resolution*, F. Piergentili, E. Cordelli, The Journal of Navigation, 63 (2010), 645-661. The Royal Institute of Navigation, DOI: 10.1017/S0373463310000299. |
| **ASI Workshop** | *Design and Manufacture of a Low Cost Educational Hexapod Rover Prototype*, F. Piergentili, G. P. Candini, J. Piattoni, E. Paolini, E. Cordelli, D. Ferraresi, T. Cardona, S. Donati, F. Romei, A. Spadanuda, M. Valdatta, Robotica Mobile per Esplorazione Lunare Unmanned, 1 - 2 July 2009, Italian Space Agency (ASI), Rome, Italy. |

# Curriculum Vitae

## Personal Information

| | |
|---|---|
| *Name:* | Emiliano Cordelli |
| *Date of Birth:* | 14 June 1986 |
| *Place of Birth:* | Acquapendente, VT, Italy |
| *Nationality:* | Italian |

## Education

*2013-2017* PH.D. CANDIDATE IN PHYSICS/ASTRONOMY

Astronomical Institute, University of Bern, Bern, Switzerland
Thesis: *Algorithms for Orbit Determination and Propagation of Space Debris*

*2009-2012* M.SC. IN ASTRONAUTICAL ENGINEERING

*La Sapienza*, University of Rome, Rome, Italy
Thesis: *Determination of Orbiting Objects Motion from Optical Observations*

*2005-2009* B.SC. IN AEROSPACE ENGINEERING

*Alma Mater Studiorum*, University of Bologna, Forlí, Italy
Thesis: *Experimentation of a Navigation System Based on Differential GPS*

*2000-2005* HIGH SCHOOL DIPLOMA

*Liceo Scientifico L. Da Vinci*, Acquapendente (VT), Italy

## Work Experience

*2009-2010* SOFTWARE ENGINEER

*ARCES*, University of Bologna, Forlí, Italy
Italian Space Agency (ASI) INFOSAT Project

## Certification

| | |
|---|---|
| *06/2017* | DEUTSCH ALS FREMDSPRACHE NIVEAU A2.2 |
| *12/2016* | DEUTSCH ALS FREMDSPRACHE NIVEAU A2.1 |
| *06/2016* | DEUTSCH ALS FREMDSPRACHE NIVEAU A1.2 |
| *12/2015* | DEUTSCH ALS FREMDSPRACHE NIVEAU A1.1 |
| *01/2015* | WRITING RESEARCH ARTICLES IN THE NATURAL SCIENCES, COURSE IN ACADEMIC ENGLISH AT B2-C1 LEVEL |
| *09/2014* | BERNESE GNSS SOFTWARE INTRODUCTORY COURSE |

## Award

*06/2015* BEST STUDENT PAPER AWARD

6th European Conference for Aeronautics and Space Sciences,
29 June - 3 July 2015, Krakow, Poland
Paper: *Optimization of Optical Follow-up Strategies Based on Covariance Analysis*, E. Cordelli, A. Vananti, T. Schildknecht, $SI-479$.